
Ph.D. Dissertation

# Evaluation of the LTE Positioning Capabilities in Realistic Navigation Channels

Author: José A. del Peral-Rosado

Thesis Advisors: Gonzalo Seco-Granados
José A. López-Salcedo
Francesca Zanier

Department of Telecommunications and Systems Engineering
Universitat Autònoma de Barcelona (UAB)

Bellaterra, March 2014

# Abstract

The provision of high-data rates leads the advances of new technologies in mobile communications. One of these advances is the use of multicarrier signals that allow a flexible allocation of resources in time and frequency, thus the spectrum can be efficiently shared for different applications. This feature is used by several systems to combine communications and positioning capabilities, due to the increasing demand of data and location services. However, the presence of mobile devices in harsh environments, such as indoor or urban scenarios, prevents these systems to achieve the required accuracy with conventional ranging techniques. The main impairment in these conditions is the effect of the multipath channel, which induces a considerable bias on the ranging estimation. Thus, countermeasures against multipath are necessary to achieve the ultimate positioning performance.

This thesis deals with the ranging capabilities of multicarrier signals in mobile communications over harsh environments, characterized by dense multipath. For this purpose, the practical case of the Long Term Evolution (LTE) mobile communications standard is considered. The LTE standard is of special interest because its downlink transmission is based on the orthogonal frequency-division multiplexing (OFDM), which is a multicarrier format. In addition, LTE specifies a multicarrier signal dedicated to support the observed time difference of arrival (OTDoA) positioning, which is based on ranging estimates with respect to the reference base stations. This pilot signal is called positioning reference signal (PRS), and it is used for time-delay estimation (TDE) in the procedure to locate the mobile device. Thus, the first part of the thesis is aimed to assess the achievable localization capabilities of LTE conventional receivers using the PRS. These conventional receivers are based on the matched filter or correlation-based techniques. The study focuses on two main impairments for TDE in LTE networks: inter-cell interference and multipath. The inter-cell interference can be mostly removed by the coordinated transmission of the PRS. However, multipath notably degrades the positioning accuracy of these conventional estimators, as it could be expected.

The main contribution of this thesis is provided in the second part, by introducing the joint estimation of time delay and channel response. This is an optimum solution for multicarrier signals, due to the straightforward implementation of the channel estimation in the frequency domain. However, most of the joint estimation algorithms are focused on communication applications, without considering the extreme accuracy of the TDE required for positioning. Typically, multipath appears close to the line-on-sight ray in urban and indoor environments. Thus, a novel channel parameterization is proposed in this thesis to characterize close-in multipath. This channel estimation model is based on the time delay and equi-spaced taps together with an arbitrary-tap with variable position between the first two equi-spaced taps. This new hybrid approach is adopted in the joint maximum likelihood (JML) time-delay estimator to improve the ranging performance in the presence of short-delay multipath. The optimality of this estimator is confirmed because its variance attains the Cramér-Rao bound. The ranging performance of this estimator is then compared to conventional estimators in realistic navigation conditions. These conditions are characterized by standard channel models adopted in LTE, additive white Gaussian noise (AWGN) and the LTE signal bandwidths. Considering the resulting time-delay estimations, the cumulative density function (CDF) in the absence of noise is used to determine the optimum model order of the estimators, and the root-mean-square error (RMSE) and bias is used to assess the achievable ranging accuracy. A notable improvement is shown by the JML estimator proposed in close-in multipath scenarios.

In the last part of the thesis, the goal is to validate the ranging performance of the proposed estimator using real LTE signals. For this purpose, a software-defined radio (SDR) receiver is developed for OTDoA positioning in LTE. A preliminary scenario with four synchronized base stations is used to validate the positioning engine. Then, the multipath error envelope (MPEE) of the JML estimators is obtained for the emulated and simulated signal cases. The work is completed with the validation of the ranging performance of the new JML time-delay and channel estimator, by using the SDR receiver in an emulated urban channel. The results obtained show the improvement on the ranging accuracy of the new JML estimator over realistic navigation channels.

# Resumen

En comunicaciones móviles, los avances de nuevas tecnologías están principalmente impulsados por el incremento en las velocidades de transmisión. Uno de estos avances es el uso de senales multiportadora que permiten una distribución flexible de recursos en tiempo y frecuencia, por lo tanto, el espectro se puede compartir eficientemente para diferentes aplicaciones. Diversos sistemas utilizan esta característica para combinar funcionalidades de comunicaciones con posicionamiento, debido a la creciente demanda de servicios de datos y localización. Sin embargo, la presencia de dispositivos móviles en entornos severos, como interiores o escenarios urbanos, no permite a las técnicas convencionales alcanzar la precisión requerida en la estimación de distancias. La principal degradación en estas condiciones se produce por el efecto del canal multicamino, que induce un considerable sesgo en la estimación de distancias. Por lo tanto, es necesario contrarrestar el multicamino para alcanzar el máximo rendimiento en posicionamiento.

Esta tesis aborda el potencial de las senales multiportadora en comunicaciones móviles para la estimación de distancias en canales severos, caracterizados por denso multicamino. Para ello, se considera el caso práctico del estándar de comunicaciones *Long Term Evolution* (LTE). El estándar de LTE es de especial interés ya que define las senales en el canal de bajada mediante la multiplexación por división de frecuencias ortogonales (OFDM), que es un tipo de senal multiportadora. Además, LTE especifica una senal multiportadora dedicada para posicionamiento mediante diferencias en los tiempos de llegada observados (OTDoA), que se basa en estimaciones de distancias respecto a estaciones base de referencia. Esta senal piloto se llama senal de referencia de posicionamiento (PRS), y se utiliza para la estimación del tiempo de retardo (TDE) en el procedimiento de localización del dispositivo móvil. Por lo tanto, la primera parte de la tesis evalúa la precisión de posicionamiento alcanzable en LTE con receptores convencionales utilizando la PRS. Estos receptores convencionales se basan en el filtro adaptado o técnicas basadas en la correlación. El estudio se centra en dos principales degradaciones de la TDE en redes LTE: la interferencia entre celdas y el multicamino. La interferencia entre celdas se puede eliminar

prácticamente mediante la transmisión coordinada de PRS. Sin embargo, el multicamino degrada notablemente la precisión de posicionamiento de los receptores convencionales, como se podía preveer.

La contribución principal de la tesis se encuentra en la segunda parte, con la introducción de la estimación conjunta del tiempo de retardo y la respuesta del canal. Ésta es una solución óptima para senales multiportadora, ya que la estimación de canal se puede implementar fácilmente en el dominio frecuencial. Sin embargo, la mayoría de los algoritmos de estimación conjunta se centran en aplicaciones de comunicaciones, sin considerar la precisión extrema de la TDE requerida para posicionamiento. Normalmente, el multicamino aparece cerca del rayo en visión directa en entornos urbanos e interiores. Por lo tanto, en esta tesis se propone una innovadora parametrización del canal para caracterizar el multicamino cercano. Este modelo de estimación de canal se basa en el tiempo de retardo y términos equiespaciados junto a un término arbitrario, con una posición variable entre los dos primeros términos equiespaciados. Este nuevo método híbrido se adopta en el estimador de máxima verosimilitud conjunto (JML) del tiempo de retardo para mejorar la estimación de la distancia en presencia de multicamino cercano. La optimalidad del estimador se confirma ya que su varianza alcanza la cota de Cramér-Rao. El rendimiento de este estimador de distancias se compara con los estimadores convencionales en condiciones realistas de navegación. Estas condiciones se caracterizan mediante modelos de canal estándar adoptados en LTE, ruido Gaussiano blanco aditivo (AWGN) y los anchos de banda de LTE. Considerando las estimaciones del tiempo de retardo resultantes, la función de densidad acumulada (fda) en absencia de ruido se utiliza para determinar el orden óptimo del modelo de los estimadores, y la raíz cuadrada del error cuadrático medio (RMSE) y el sesgo se utilizan para evaluar la máxima precisión en la estimación de distancias. Se muestra una mejora importante mediante el estimador JML propuesto en entornos con multicamino cercano.

En la última parte de la tesis, el objetivo es validar el rendimiento del estimador de distancias con senales LTE reales. Para ello, se desarrolla un receptor *software-defined radio* (SDR) para el posicionamiento OTDoA en LTE. Se utiliza un escenario preliminar con cuatro estaciones base sincronizadas para validar el sistema de posicionamiento. A continuación, se obtiene la envolvente del error producido por multicamino (MPEE) en los estimadores JML para los casos de senal emulada y simulada. El trabajo se completa con la validación del rendimiento del nuevo estimador conjunto de distancias, utilizando el receptor SDR en un canal urbano emulado. Los resultados obtenidos muestran la mejora en la precisión de las distancias del nuevo estimador en canales de navegación realistas.

# Acknowledgements

This Ph.D. dissertation ends a journey full of good experiences and joyful moments. At the same time, it has triggered new ideas to expand and goals to pursue, while enjoying the path towards them.

First of all, I would like to express my deepest gratitude to my advisors (from UAB) Prof. Gonzalo Seco-Granados and Prof. José A. López-Salcedo for their guidance, patience and generosity throughout this thesis. They have always found time to discuss results and doubts, and they have provided countless suggestions and corrections. I am also really thankful to my advisor (from ESA) Ph.D. Francesca Zanier for her great support and supervision during my research stays at ESTEC, and her commitment to track the status of the thesis during the research periods at UAB. I would like to thank Ph.D. Massimo Crisci, head of TEC-ETN section at ESTEC, for his support on my research stays and for granting me access to the outstanding facilities and resources of the European Navigation Laboratory.

This Ph.D. thesis has also allowed me to meet lovely people, such as my current and former colleagues of the SPCOMNAV group and of the Dept. of Telecommunications at UAB or the Spanish trainee community at ESTEC. I would like to especially thank Rafael Montalbán, Moisés Navarro, Juan Manuel Parro, and Mariano Vergara for the fruitful discussions, conversations and help that they have offered me.

Last but not least, I really thank the support provided by my family and friends during these years at the university, helping me to overcome any adversities and to enjoy life outside work and research.

José A. del Peral-Rosado
March 21, 2014

This work was supported by the ESA under the PRESTIGE programme ESA-P-2010-TEC-ETN-01 and by the Spanish Ministry of Economy and Competitiveness project TEC2011-28219.

# Contents

# Acronyms

| | |
|---|---|
| 1D, 2D | One-Dimensional, Two-Dimensional |
| 3G, 4G | Third Generation, Fourth Generation |
| 3GPP | Third Generation Partnership Project |
| A-GNSS | Assisted GNSS |
| ADC | Analog-to-Digital Converter |
| AFLT | Advanced Forward Link Trilateration |
| AoA | Angle of Arrival |
| AoD | Angle of Departure |
| ALI | Automatic Location Identification |
| ANI | Automatic Number Identification |
| ARQ | Automatic Repeat reQuest |
| AUC | Area Under the ROC Curve |
| AWGN | Additive White Gaussian Noise |
| BS | Base Station |
| $C/N_0$ | Carrier-to-Noise-Density Ratio |
| CDF | Cumulative Density Function |
| CDMA | Code Division Multiple Access |
| CEPT | Conférence Européenne des Administrations des Postes et Télécommunications |
| CFO | Carrier-Frequency Offset |
| CGALIES | Coordination Group on Access to Location Information by Emergency Services |
| CIR | Channel Impulse Response |
| CP | Cyclic Prefix |
| CRB | Cramér-Rao Bound |
| CRS | Cell-specific Reference Signal |
| CSI | Channel State Information |
| DFT | Discrete Fourier Transform |
| DLL | Delay Lock Loop |

| | |
|---|---|
| DVB | Digital Video Broadcasting |
| DwPTS | Downlink Pilot Timeslot |
| E911 | Enhanced 911 |
| E-CID | Enhanced Cell ID |
| E-OTD | Enhanced OTD |
| E-SMLC | Evolved Serving Mobile Location Centre |
| E-UTRA | Evolved Universal Terrestrial Radio Access |
| EARFCN | E-UTRA Absolute Radio Frequency Channel Number |
| ECRB | Expected CRB |
| EDGE | Enhanced Data rates for GSM Evolution |
| EIA | Electronic Industries Alliance |
| EMILY | European Mobile Integrated Location sYstem |
| ENL | European Navigation Laboratory |
| EPA | Extended Pedestrian A |
| ETSI | European Telecommunications Standards Institute |
| ETU | Extended Typical Urban |
| EVA | Extended Vehicular A |
| FCC | Federal Communications Commission |
| FDD | Frequency Division Duplexing |
| FIM | Fisher Information Matrix |
| FFT | Fast Fourier Transform |
| FPGA | Field-Programmable Gate Array |
| GERAN | GSM/EDGE Radio Access Network |
| GNSS | Global Navigation Satellite Systems |
| GP | Guard Period |
| GPS | Global Positioning System |
| GSA | Global mobile Suppliers Association |
| GSCM | Geometric-based Stochastic Channel Model |
| GSM | Global System for Mobile communications |
| IC | Interference Cancellation |
| iDEN | Integrated Dispatch Enhanced Network |
| IMS | IP Multimedia Subsystem |
| INS | Inertial Navigation Systems |
| IPDL | Idle Period in Downlink |
| ISD | Inter-site Distance |
| ISI | Intersymbol Interference |

| | |
|---|---|
| JML | Joint Maximum Likelihood |
| LBS | Location-Based Services |
| LCS | Location Services |
| LIS | Low-Interference Subframe |
| LoS | Line-of-Sight |
| LPP | LTE Positioning Protocol |
| LTE | Long Term Evolution |
| MBSFN | Multimedia Broadcast Single Frequency Network |
| MC | Multicarrier |
| MCL | Minimum Coupling Loss |
| MDL | Minimum Description Length |
| ML(E) | Maximum Likelihood (Estimation) |
| MoU | Memorandum of Understanding |
| NDA | Non-Data-Aided |
| NLoS | Non-Line-of-Sight |
| NLS | Nonlinear Least Squares |
| NNR | Noise-to-Noise Ratio |
| OFDM | Orthogonal Frequency Division Multiplexing |
| OFDMA | Orthogonal Frequency Division Multiple Access |
| OTD | Observed Time Difference |
| OTDoA | Observed TDoA |
| PAPR | Peak-to-Average Power Ratio |
| PBCH | Physical Broadcast CHannel |
| PCFICH | Physical Control Format Indicator CHannel |
| PDCCH | Physical Downlink Control CHannel |
| PDF | Probability Density Function |
| PDP | Power-Delay Profile |
| PDSCH | Physical Downlink Shared CHannel |
| PHICH | Physical Hybrid-ARQ Indicator CHannel |
| PMCH | Physical Multicast CHannel |
| PLL | Phase Lock Loop |
| PRS | Positioning Reference Signal |
| PSAP | Public Safety Answering Point |
| PSD | Power Spectral Density |
| PSS | Primary Synchronization Signal |
| QuaDRiGa | Quasi Deterministic Radio channel Generator |

| | |
|---|---|
| RAN | Radio Access Network |
| RB | Resource Block |
| RE | Resource Element |
| RMSE | Root-Mean-Square Error |
| ROC | Receiver Operating Characteristic |
| RS | Reference Signal |
| RSRP | Reference Signal Received Power |
| RSRQ | Reference Signal Received Quality |
| RSTD | Reference Signal Time Difference |
| RTD | Round-Trip Delay |
| SC-FDMA | Single Carrier FDMA |
| SCM | Spatial Channel Model |
| SDR | Software-Defined Radio |
| SF | Subframe |
| SFN | Single-Frequency Network |
| SINR | Signal-to-Interference plus Noise Ratio |
| SMG | Special Mobile Group |
| SMR | Signal-to-Multipath Ratio |
| SNR | Signal-to-Noise Ratio |
| SON | Self-Organizing Network |
| SoO | Signals-of-Opportunity |
| SSS | Secondary Synchronization Signal |
| TA | Timing Advance |
| TDE | Time-delay Estimation |
| TDD | Time Division Duplexing |
| TDL | Tapped-Delay Line |
| TDMA | Time Division Multiple Access |
| TDoA | Time Difference of Arrival |
| TIA | Telecommunications Industry Association |
| ToA | Time of Arrival |
| TS | Technical Specification |
| TR | Technical Report |
| UDP | Undetected Direct Path |
| UE | User Equipment |
| UE-RS | UE-specific Reference Signal |
| UHD | USRP Hardware Driver |

| | |
|---|---|
| UMTS | Universal Mobile Telecommunication System |
| UpPTS | Uplink Pilot Timeslot |
| USRP | Universal Software Radio Peripheral |
| UTDoA | Uplink TDoA |
| UWB | Ultra-wideband |
| WG | Working Group |
| WI | Working Item |
| WINNER | Wireless World Initiative New Radio |
| WLAN | Wireless Local Area Network |
| ZC | Zadoff-Chu |

# Notation

In general, letters or symbols formatted in upper-case boldface denote matrices, in lower-case boldface denote vectors, and in italics denote scalars. The rest of the notation is described as follows:

| | |
|---|---|
| $\mathbf{A}^*, \mathbf{A}^{\mathrm{T}}, \mathbf{A}^{\mathrm{H}}$ | Complex conjugate, transpose, and conjugate transpose (Hermitian) of matrix $\mathbf{A}$, respectively. |
| $\mathbf{A}^{\dagger}$ | Moore-Penrose pseudo-inverse of matrix $\mathbf{A}_{\tau}$. |
| $[\mathbf{A}]_{n,k}$ | The $[n,k]$ element of matrix $\mathbf{A}$. |
| $\|\mathbf{a}\|$ | $\sqrt{\mathbf{a}^{\mathrm{H}}\mathbf{a}}$, Euclidean norm of vector $\mathbf{a}$. |
| $\|a\|$ | Absolute value of scalar $a$. |
| $\mathbf{1}$ | Vector of ones. |
| $\mathbf{I}$ | Identity matrix. |
| $\mathbf{P}_{\mathbf{A}}$ | $\mathbf{A}\mathbf{A}^{\dagger}$, orthogonal projection matrix onto the subspace spanned by the columns of matrix $\mathbf{A}$. |
| $\mathbf{P}_{\mathbf{A}}^{\perp}$ | $\mathbf{I} - \mathbf{P}_{\mathbf{A}}$, orthogonal projection matrix onto the subspace orthogonal to that spanned by the columns of matrix $\mathbf{A}$. |
| $\mathrm{tr}\,(\mathbf{a})$ | Trace of vector $\mathbf{a}$. |
| $\mathrm{diag}\,(\mathbf{a})$ | Diagonal matrix with the given elements of vector $\mathbf{a}$ on its diagonal. |
| $\mathrm{E}\,[\cdot]$ | Expectation operator. |
| $\mathcal{F}\,\{\cdot\}$ | Discrete Fourier transform operator. |
| $\mathrm{Re}\,(\cdot)\,, \mathrm{Im}\,(\cdot)$ | Real and imaginary parts. |
| $\max(a,b)$ | Maximum between $a$ and $b$. |
| $\min(a,b)$ | Minimum between $a$ and $b$. |
| $\doteq$ | Defined as. |
| $\circledast$ | Circular convolution operation. |
| $*$ | Convolution operation. |
| $\mathbb{Z}_{\neq 0}$ | Integer number different than zero. |
| $\mathbb{N}$ | Natural number. |

| | |
|---|---|
| $\mathcal{A}$ | Subset of scalars. |
| $\mathcal{A} \cup \mathcal{B}$ | Union of subsets $\mathcal{A}$ and $\mathcal{B}$. |
| $\mathcal{A} \cap \mathcal{B}$ | Intersection of subsets $\mathcal{A}$ and $\mathcal{B}$. |
| $\log_a$ | Logarithm to the base $a$. |
| $\delta(t)$ | Dirac delta. |
| $\operatorname{sinc}(x)$ | $\frac{\sin(\pi \cdot x)}{\pi \cdot x}$, sinc function. |
| $\operatorname{sinc}_{\mathrm{d}}(N; x)$ | $\frac{\sin(\pi \cdot N \cdot x)}{\sin(\pi \cdot x)}$, discrete sinc function. |
| $\arg\max_x f(x)$ | Value of $x$ that maximizes $f(x)$. |
| $\arg\min_x f(x)$ | Value of $x$ that minimizes $f(x)$. |

# Chapter 1

# Introduction

Navigation and positioning technologies are every day more important in civil applications, demanding enhancements on accuracy, availability, and reliability. Positioning improvements are mainly achieved thanks to the advances in Global Navigation Satellite Systems (GNSS) and the introduction of new systems, such as Galileo. These advances have led to the incorporation of GNSS receivers even into small and portable devices, such as mobile phones. However, a myriad of possible working conditions are faced in ubiquitous positioning, where the GNSS nominal performance is highly degraded, such as in urban environments or indoors. In these circumstances, the presence of blocking obstacles and propagation disturbances prevent mass-market GNSS receivers from observing the expected perfect clear-sky conditions that were assumed in the nominal design of the system. Thus, the use of complementary terrestrial localization systems is envisaged as a major step towards the realization of anywhere and anytime positioning.

Several technological solutions have been proposed to complement GNSS. The use of inertial sensors is widely adopted in mobile devices due to their cheap, efficient and easy implementation. Inertial navigation systems (INS) are typically formed by accelerometers, gyroscopes and magnetometers. However, the inertial drift of the sensors have to be continuously corrected, otherwise a significant error is produced on the position. Thus, instead of being used standalone, inertial sensors are loosely- or tightly-coupled with GNSS modules, known as GNSS/INS integration. Given that many GNSS receivers are integrated in mobile phones, cellular networks are traditionally used to provide assistance data, resulting in the so-called assisted-GNSS (A-GNSS). The assistance data aids the GNSS receiver to speed up the acquisition of the signal, and thus to achieve positioning in a reduced time. Nevertheless, both A-GNSS and GNSS/INS solutions still have difficulties to provide accurate positioning in less benign environments, such as urban or indoor

scenarios, due to the poor reception of satellite signals. An alternative solution in those challenging conditions is the location fingerprinting with map-matching techniques. This method is typically based on the received signal strength (RSS) measurements from a wireless local area network (WLAN) associated to positions in a map. These fingerprints are saved in a database that the users will access to determine their position. Despite this solution is widely extended, it suffers from reliability and accuracy issues due to the calibration and update of the database.

The ranging principles of GNSS can also be applied to terrestrial systems. Thus, the time-delay estimation (TDE) of wireless signals, transmitted in broadcast television, radio or cellular communication systems, can be used for positioning purposes. As an example, the ultra-wideband (UWB) technology is widely adopted in proprietary localization systems for indoor scenarios. This technology is of special interest because it achieves very accurate positioning, due to the wide bandwidths used. In addition, the terrestrial systems may not need to be dedicated for positioning, but they can still be used for this purpose. This is the concept of navigation using signals-of-opportunity (SoO). For instance, the digital video broadcasting (DVB) systems can be used for navigation, given the known position of the radio transmitters. Still, the support of dedicated positioning can be found in some wireless communication standards. This is the case of the Long Term Evolution (LTE) standard. The most attractive features of LTE for ranging are based on wideband and low-interference signals, along with a tight synchronisation between base stations. The high deployment of this technology worldwide increases the potential availability of this positioning solution. Thus, LTE is a good candidate to complement GNSS.

Considering the TDE with LTE signals, the major source of ranging errors is certainly multipath. The multiple reflections of the transmitted signal introduce interference on the received signal. The TDE is expecting only the line-of-sight (LoS) propagation of the signal. Thus, the delayed reflections induce a notable bias on the TDE, if nothing is done against multipath. This effect is especially critical in indoor and urban areas, where non-line-of-sight (NLoS) conditions are predominant. This topic has received special attention for years within the GNSS community, due to the limitation imposed in terms of TDE accuracy. However, multipath mitigation techniques are barely implemented in LTE, using only simple extensions of the conventional estimators. The LTE standard is based on multicarrier signals, which offers flexible resource allocation, efficient spectrum shaping and low-complexity channel estimation, among other advantages with respect to traditional single-carrier signals. Thus, the multicarrier features of LTE should be exploited for ranging purposes, by counteracting the effect of multipath in harsh environments.

## 1.1 Motivation and objectives

Multipath channel has a critical impact on the ranging performance of conventional receivers. This effect prevents those receivers from achieving the accurate positioning required in many localization applications. Thus, advanced TDE techniques have to be proposed in order to counteract the effect of multipath. As a practical case, these new ranging approaches can be studied in LTE. This standard is of interest due to the use of multicarrier signals, which may be transmitted with a high bandwidth. The multicarrier signals can easily adopt channel estimation models to compensate the effect of multipath.

The aim of this thesis is to explore the capabilities of multicarrier signals in order to enhance the time-delay estimation in harsh environments with dense multipath. For this purpose, the joint estimation of time delay and channel response is studied, considering a new estimation model to counteract the presence of multipath. The practical case of LTE is used to specify realistic navigation conditions and signal formats. In addition, the proposed TDE approach should keep a low complexity, in order to be applicable in mobile devices, typically equipped with mass-market receivers. To complete these goals, the research contribution is focused in the following points:

- Detailed review of the LTE technology highlighting its positioning features.
- Assessment of the achievable LTE positioning capabilities using conventional receivers.
- Design of joint time-delay and channel estimation techniques to counteract the effect of multipath exploiting the format of LTE multicarrier signals.
- Validation of the joint estimation techniques by implementing a software receiver and using real LTE signals.

## 1.2 Thesis outline

The outline of the thesis is presented in this section. The introduction to positioning with LTE is in Chapter 2, and its achievable localization is analysed in Chapter 3. The main contribution of the thesis is presented in Chapter 4, by proposing a novel time-delay estimator to counteract the effect of multipath for ranging applications. The validation of LTE positioning with a real receiver is shown in Chapter 5. Finally, conclusions and future work are drawn in Chapter 6. Next, a brief summary of each chapter is provided.

**Chapter 2**

This chapter provides an overview of the positioning features specified in the LTE standard. It is noted that the LTE technology does not only include new features for communication applications, but they can also support positioning. To understand this evolution, a brief historical review on the use of cellular communication systems for positioning applications is presented. Then, the positioning methods and protocols are summarized. The accuracy limits of these methods mainly depend on the physical layer of the technology. Thus, the signal formats and physical configurations of LTE are also introduced.

**Chapter 3**

This chapter studies the achievable localization capabilities of LTE using a conventional receiver, which is based on the matched filter. Since the matched filter is characterized by the correlation between the received signal and the known pilots, the correlation properties of the LTE signal formats are studied. Then, the performance of this conventional estimator is assessed in Gaussian noise with the Cramér-Rao bound (CRB). Once the nominal performance is analysed, the main sources of ranging errors are introduced. First, the inter-cell interference is studied for three general scenarios in a macro-cell layout, considering the impact of this interference on the ranging and position accuracy. Second, the conventional estimator is evaluated in the presence of multipath. Although its performance is expected to be poor, this scenario is also included in order to complete the analysis of the achievable positioning capabilities. Finally, both interference and multipath are considered, and the positioning accuracy of LTE using a conventional receiver is provided for the 67% and 95% of the cases in a urban macro-cell environment.

**Chapter 4**

This chapter proposes a new model for the joint estimation of time delay and channel response, which is the main contribution of this thesis. The most typical channel estimation models are presented, along with the novel estimation model. Then, the Cramér-Rao bound of this joint estimation is introduced for every model. Using these channel estimation models, the corresponding time-delay estimators are derived. Given that the presence of multipath induces a notable bias in conventional estimators, the timing errors of the joint estimators are computed first in absence of noise. The assessment of their bias is completed using different signal bandwidths and standard channel models of LTE. This study provides insights on the design of the joint estimators in general scenarios.

The effect of multipath and noise over the joint estimators is then studied to assess the achievable ranging accuracy of LTE in realistic navigation channels.

**Chapter 5**

This chapter describes the software receiver implemented to validate the joint time-delay and channel estimators with real LTE signals. The architecture of the receiver is detailed according to the cell acquisition, signal tracking and position calculation. These three main parts are validated for a preliminary scenario by emulating four synchronised base stations, and obtaining results of the time delay, frequency and position accuracy. Then, the ranging performance of the joint estimators is assessed by computing their bias with real LTE signals in a two-ray multipath scenario. Finally, the achievable ranging performance of the joint time-delay and channel estimators is validated with the emulation of an urban channel.

## 1.3 Research contributions

The work of this dissertation has been presented in several publications, such as journals and international conference papers. These research contributions are listed for every chapter.

**Chapter 3**

The main result of this chapter is the achievable localization accuracy of LTE using a conventional receiver, and considering the presence of inter-cell interference, Gaussian noise and multipath. The results in this chapter have been published in the following international conference papers:

- J. A. del Peral-Rosado, J. A. López-Salcedo, G. Seco-Granados, F. Zanier, M. Crisci, Preliminary Analysis of the Positioning Capabilities of the Positioning Reference Signals of 3GPP LTE , *5th European Workshop on GNSS Signals and Signal Processing*, Toulouse, France, 8-9 December 2011.
- J. A. del Peral-Rosado, J. A. López-Salcedo, G. Seco-Granados, F. Zanier, M. Crisci, Achievable Localization Performance Accuracy of the Positioning Reference Signal of 3GPP LTE , *Proc. International Conference on Localization and GNSS (ICL-GNSS)*, Starnberg, Germany, 25-27 June 2012.

- J. A. del Peral-Rosado, J. A. López-Salcedo, G. Seco-Granados, F. Zanier, M. Crisci, Evaluation of the LTE Positioning Capabilities Under Typical Multipath Channels , *Proc. 6th Advanced Satellite Multimedia Systems Conference and 12th Workshop on Signal Processing for Space Communications (ASMS/SPSC)*, Baiona, Spain, 5-7 September 2012.

- J. A. del Peral-Rosado, J. A. López-Salcedo, G. Seco-Granados, F. Zanier, M. Crisci, Analysis of Positioning Capabilities of 3GPP LTE , *Proc. 25th International Technical Meeting of The Satellite Division of the Institute of Navigation (ION GNSS)*, Nashville, Tennessee, USA, 17-21 September 2012.

**Chapter 4**

The main result of this chapter is the derivation and assessment of a new joint time-delay and channel estimator to counteract the effect of multipath, especially of the critical close-in multipath. The results of this chapter has been presented in one international conference and in one journal paper:

- J. A. del Peral-Rosado, J. A. López-Salcedo, G. Seco-Granados, F. Zanier, M. Crisci, Joint Channel and Time Delay Estimation for LTE Positioning Reference Signals , *6th ESA Workshop on Satellite Navigation Technologies and European Workshop on GNSS Signals and Signal Processing (NAVITEC)*, Noordwijk, The Netherlands, 5-7 December 2012.

- J. A. del Peral-Rosado, J. A. López-Salcedo, G. Seco-Granados, F. Zanier, M. Crisci, Joint Maximum Likelihood Time-Delay Estimation for LTE Positioning in Multipath Channels , *EURASIP Journal on Advances in Signal Processing, special issue on Signal Processing Techniques for Anywhere, Anytime Positioning*, Vol. 2014, nº 33, pags. 1 13, 2014.

**Chapter 5**

The main result of this chapter is the validation of the joint estimation techniques with real LTE signal. Part of the results of this chapter have been published in the following international conference paper:

- J. A. del Peral-Rosado, J. A. López-Salcedo, G. Seco-Granados, F. Zanier, P. Crosta, R. Ioannides, M. Crisci, Software-Defined Radio LTE Positioning Receiver Towards

Future Hybrid Localization Systems , *Proc. AIAA International Communication Satellite Systems Conference (ICSSC)*, Florence, Italy, 14-17 October 2013.

**Other contributions not directly related with this dissertation**

During the PhD studies, other research contributions have been produced apart from the topic of positioning with LTE. The following conference and journal paper have been published related to robust carrier tracking:

- J. A. del Peral-Rosado, J. A. López-Salcedo, G. Seco-Granados, J. M. López-Almansa, J. Cosmen, Kalman Filter-Based Architecture for Robust and High-Sensitivity Tracking in GNSS Receivers , *5th ESA Workshop on Satellite Navigation Technologies and European Workshop on GNSS Signals and Signal Processing (NAVITEC)*, Noordwijk, The Netherlands, 8-10 December 2010.
- J. A. López-Salcedo, J. A. del Peral-Rosado, G. Seco-Granados, Survey on Robust Carrier Tracking Techniques , *IEEE Communications Surveys & Tutorials*, pags. 1 19, December 2013.

# Chapter 2

# Overview of LTE Positioning

The main application of cellular networks for wireless communications is the provision of packet data and voice services to mobile devices. Significant efforts are devoted to improve these services, by creating new technologies and systems. A relevant example is the LTE standard that introduces major advances with respect to its predecessors, i.e. the Global System for Mobile communications (GSM) and the Universal Mobile Telecommunication System (UMTS). Among all the new features, LTE technology offers a tight synchronisation among base stations with the possibility to use wideband signals. These are two main enabling features to achieve accurate ranging. In addition, this standard specifies a dedicated support for positioning to enhance the localization performance. Thus, LTE networks may provide promising positioning capabilities. In order to assess this potential, the main positioning features of LTE are described in this chapter.

## 2.1 Introduction

LTE technology is the last evolution of third generation (3G) mobile communications systems, being its new releases already fourth generation (4G) technologies. LTE achieves higher data rates with a flexible and efficient use of the spectrum, and provides a reduced latency with respect to previous cellular technologies. Most of its standard, which is driven by the Third Generation Partnership Project (3GPP), has been inherited from UMTS in order to maintain backward compatibility. One of the main new features of LTE is the multicarrier (MC) transmission on the downlink access, by defining an orthogonal frequency division multiple access (OFDMA) between base station (BS) and user equipment (UE).

The concept of multicarrier transmission has been known since it was first introduced in the 1960s. However, its potential was not fully exploded until it was efficiently implemented by means of the fast Fourier transform (FFT). Nowadays, as well as in LTE, MC communications are widely implemented in different standards and products, such as is the case of OFDM in ADSL, WiFi 802.11n, WiMAX 802.16e, DVB-T, DVB-SH, etc. The flexibility of multicarrier signals offers spectral efficiency and robustness against frequency-selective fading introduced by multipath, among other advantages with respect to traditional single-carrier signals. However, MC signals have a high sensitivity to frequency offsets and high peak-to-average power ratio (PAPR). PAPR can be mitigated with high compression point power amplifiers and amplifier linearization techniques, but such methods become expensive on mobile devices. Thus, LTE moves this complexity to the BS by using OFDMA for the downlink access, and introduces the single carrier FDMA (SC-FDMA) for the uplink access.

The rapid commercial deployment of LTE around the world leads to the description of LTE as the fastest developing mobile system technology ever , according to the Global mobile Suppliers Association (GSA) in [GSA14a]. LTE has expanded from 7 commercial networks launched in 6 countries by 26 October 2010, to 274 networks in 101 countries by 17 February 2014 [GSA14a], which are mapped in Figure 2.1. But, LTE is not only able to rapidly improve current cellular networks, it may have a key role on the evolution of terrestrial navigation technologies by introducing a dedicated positioning support, as a continuation of the efforts done in UMTS. LTE can be a perfect multicarrier testbed for positioning in practical scenarios. This interest is also triggered by the potential application of MC signals to next-generation GNSS, as it is already suggested in [Zan08, Dai10, Ver10, Emm11, Wan12a].

## 2.2 Brief historical review of cellular positioning

Despite the issue of legal mandates and the potential revenue foreseen, mobile positioning is still an optional feature in current cellular networks. This can be justified by the slow deployment of location-based services (LBS), affected by business and technological challenges [Dha11]. One of these technological challenges is to achieve ubiquitous positioning with mobile terminals being operated either outdoors or indoors in heterogeneous networks [Dam11]. An historical review of cellular positioning is given in this section, to understand the capabilities of current networks and the aspects to be improved in the future.

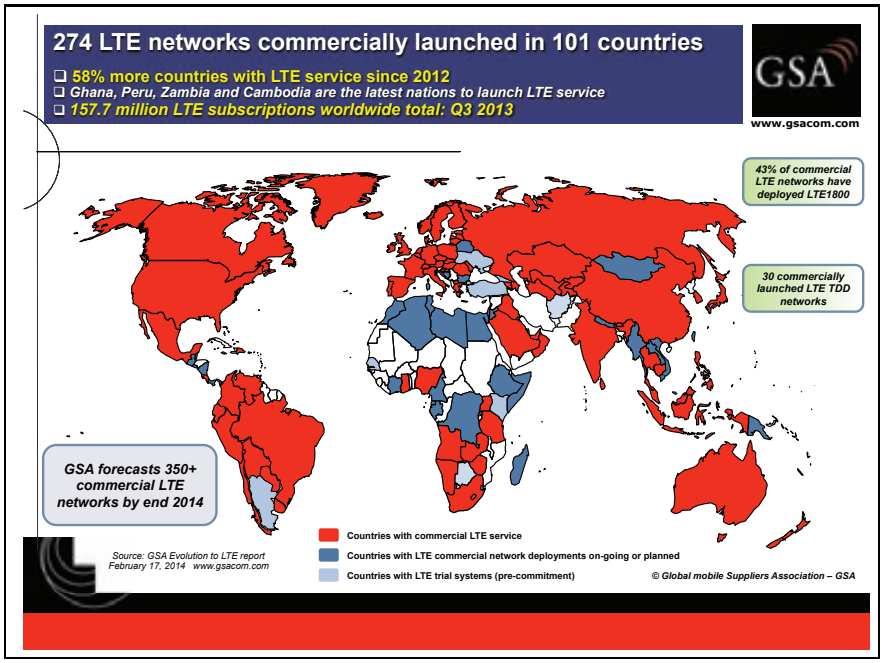


Figure 2.1: Status of LTE around the world [GSA14a].

### 2.2.1 Fundamental positioning techniques

Most of the positioning techniques used in wireless communications are based on the same principles defined several decades ago. A receiver computes signal measurements with respect to single or multiple reference transmitters, and then calculates the position according to a certain model. The positioning methods can be defined according to three main categories:

- **Mobile-based**: The mobile device computes by itself both signal measurements and position calculation.
- **Network-based**: The network computes signal measurements with respect to the mobile device, and calculates the position of the mobile device.
- **Mobile-assisted**: The mobile device computes both signal measurements and position calculation using assistance data from the network, or the mobile device computes (aided or non-aided) signal measurements and sends them to the network, which calculates the position of the mobile device.

As we will see in the following section, network-based wireless location can be considered as the preferred option in cellular networks, because of its centralized nature that (in some cases) does not require any modification on the mobile device. However, the

adoption of network-based methods may have produced the failure of positioning services in mobile devices, due to the following points:

- Many network providers are reluctant to assume the costs implied on the implementation complexity of this kind of methods, given the reduced profit expected on the positioning services.
- The fact that the network can know the user location generates privacy issues that complicate the introduction of applications using this information.

Regardless of the positioning method, different techniques can be used to compute the location of the mobile device, by considering different measurements or references. The localization algorithms can be classified as:

- **Lateration**: The position solution is obtained by computing the intersection between geometric forms, such as circles or hyperbolas, created by distance measurements from the terminal to the reference transmitters. Several signal measurements can be used, such as time of arrival (ToA), time difference of arrival (TDoA) or RSS.
- **Angulation**: The direction of arrival of the different signals received is used to estimate the position. Angle of arrival (AoA) is an example method used for angulation.
- **Proximity**: The known transmitter position is assigned to be the position of the terminal. An example is the cell-ID method, where the position provided is the one of the serving base station. This is the most widely adopted method in conventional GSM networks.
- **Scene analysis**: Also known as pattern matching, the algorithm is based on finding the best match for a certain signal measurement, such as RSS, from a database of *fingerprints*. Each fingerprint has associated a specific position.
- **Hybrid**: A combination of the previous localization algorithms can be implemented to improve the overall performance, or to support an algorithm that cannot be computed standalone given the lack of signal measurements.

Wireless location systems have been widely studied in the literature. For instance, further information on the positioning designs and challenges in cellular networks and

WLAN can be found in [Say05, Sun05]. A comprehensive review of the indoor positioning techniques and systems is presented in [Liu07]. The fundamental limits of mobile positioning are studied in [Gus05, Gez08] using the CRB. In [Guv09], a survey of ToA localization algorithms is presented considering NLoS mitigation techniques. Given the context of LTE, a survey on cellular positioning is presented in the following sections, considering the standard systems from the past to the future.

### 2.2.2 Initial studies and standards

Although the first cellular systems were introduced in the early 1970s, the widespread use of cellular networks did not happen until the late 1990s [Far05]. One of the main enablers of this transition was the evolution of mobile communications, from many independent systems towards standard systems among countries. Such a commitment was first held in Europe by the Conférence Européenne des Administrations des Postes et Télécommunications (CEPT) in 1982 [Hil13], which resulted on a common European cellular system in 1987 [Eur87], now known as GSM. The development of the GSM standard was then driven by the European Telecommunications Standards Institute (ETSI) Special Mobile Group (SMG). By that time, very few trials had studied mobile location in cellular systems, such as in [Hat80]. Thus, Phase 1 of GSM specification only included a radio subsystem synchronisation to improve handover transitions by removing the propagation delay, using the round-trip delay (RTD) perceived by the base station. The RTD resulted on the timing advance (TA) that the mobile device should apply to synchronize its transmission. In Phase 2, the observed timing difference (OTD) was added as an optional synchronisation feature, based on the time difference between BSs measured by the mobile device [ETS92], as in TDoA-based techniques. However, these synchronisation methods were not used yet for positioning purposes.

It was not until 1996 that a major step in cellular positioning took place. The Federal Communications Commission (FCC) of the United States approved a national mandate for enhanced 911 (E911) services [FCC96]. The deployment of the new E911 services should be achieved in two phases:

- **Phase I**: By the end of 1997, carriers were required to provide a caller s automatic number identification (ANI) and the location of the base station or cell site receiving a 911 call to the designated public safety answering point (PSAP).
- **Phase II**: By the end of 2001, carriers were required to provide the location of a 911 caller, with a root-mean-square error (RMSE) of 125 meters in 67% of all cases.

The E911 mandate motivated intensive efforts in United States to achieve the location requirements on the existing TDMA (Time Division Multiple Access) cellular systems, formed by the integrated dispatch enhanced network (iDEN) from Motorola, IS-54 [EIA90] (later substituted by IS-136) and GSM, and CDMA (Code Division Multiple Access) cellular systems, formed by IS-95 or cdmaOne [EIA92] from Qualcomm. As an example, in April 1998, several survey articles [Ree98, Zag98, Tek98, Caf98, Dra98] reviewed the challenges and performance of cellular positioning in a dedicated issue of the IEEE Communications Magazine. The positioning techniques were mobile- or handset-based solutions, such as the Global Positioning System (GPS), and network-based solutions, such as ToA, TDoA, AoA, cell-ID, fingerprinting or hybrid methods. But, mobile-assisted methods could also be found, such as assisted-GPS (A-GPS), where the GPS receiver is aided with the navigation message and differential correction data provided by a network, as it was proposed in [Moe98] by SnapTrack (a company acquired by Qualcomm in 2000). Later, in 1999, the FCC approved that carriers were required to provide an automatic location identification (ALI) as a part of E911 Phase II by 1 October 2001 [FCC99]. The accuracy requirements adopted in the Third Report and Order of E911 [FCC99] for **mobile-based** or **handset-based solutions** are:

- 50 meters for 67% of calls,
- 150 meters for 95% of calls, and

for **network-based** solutions are:

- 100 meters for 67% of calls,
- 300 meters for 95% of calls.

Due to the tighten requirements and the incompatibility of handset-based solutions with legacy phones, the FCC provided waivers to several companies on the application of this E911 mandate. Following the trend of enhanced emergency services, in 1999, the European Commission filled a report requiring to the carriers, the provision of location information of 112 callers, i.e. enhanced 112 (E112), by 1 January 2003 [Com99].

Meanwhile, digital cellular networks were evolving towards 3G mobile standards. ETSI members were developing the specification of both GSM Phase 2+, i.e. Enhanced Data rates for GSM Evolution (EDGE), and UMTS. However, companies of non-European countries could barely contribute to these standards. Thus, the 3GPP was created in 1998 as a partnership of international members to standardise the evolutions of GSM

and UMTS, being ETSI one of the main sponsors and contributors [Hil13]. In 1999, the cooperation between ETSI and the American standardization group T1P1 resulted in the specification of the functional description of location services (LCS) in GSM [3GP99a] and in UMTS [3GP99b]. The positioning schemes specified in GSM were uplink ToA, enhanced OTD (E-OTD), and A-GPS. The timing advance and the cell-ID of the serving cell were used as fall-back positioning procedures. The standard location methods in UMTS were cell-ID, observed TDoA (OTDoA) with network configurable idle periods, and A-GPS, being uplink TDoA (UTDOA) added in later versions of the standard. In 2000, the 3GPP became responsible for the specifications of the GSM/EDGE radio access network (GERAN) and UMTS terrestrial radio access network (UTRAN) technologies. In the same sense, the 3GPP2 consortium continued the standardisation of IS-95 and CDMA2000 technologies from the Telecommunications Industry Association (TIA) and the Electronic Industries Alliance (EIA). In 2001, the 3GPP2 produced the standard C.S0022-0 as a continuation of IS-801 (from TIA/EIA) to determine signalling of positioning services in CDMA systems [3GP01]. The positioning technologies specified in this standard were advanced forward link trilateration (AFLT) and A-GPS, considering also the combination of AFLT and GPS.

The use of TDoA-based positioning may result in a sufficient accuracy to fulfil legal mandates. However, several sources of ranging errors have to be considered, as it is described in [Hei00, Zha02, Sol02]. In GSM and UMTS networks, the BSs are not tightly synchronized, thus the relative time delay between BSs produces a certain error. The standard solves this problem by adding a location measurement unit (LMU) to the network in order to estimate the BS synchronization errors. In contrast, the BSs in CDMA2000 networks are accurately synchronized to the GPS time reference. Another important source of error is the inter-cell interference between neighbour BSs due to the single-frequency transmission, such as in UMTS. The TDoA-based position can be successfully estimated if the UE receives from three or more BSs. However, only at the cell edge a good reception of several BSs is ensured. This limitation is due to the near-far effect or hearability problem, where the nearest BS masks the neighbour BSs. In order to overcome this problem, an idle period in downlink (IPDL) was specified in UTRAN [3GP99b] for OTDoA positioning. Nevertheless, multipath is certainly the major source of ranging errors, producing a critical degradation in GSM [Hei00]. Since the initial specification of these TDoA-based methods, many contributions have proposed techniques to counteract the multipath effect, such as in [Fis98] by means of channel estimation in GSM, but multipath is still a major issue for ranging applications.

In parallel to the technology standardisation, the regulation of E112 continued in Europe with the coordination group on access to location information by emergency services (CGALIES), created by the European Commission in May 2000. CGALIES is a partnership between members of the public and private sector that aim to assess feasible location requirements and solutions for E112. Although location accuracy requirements were described by CGALIES in [Lud02], the European Commission recommendation of 25 July 2003 in [Com03] did not mandate specific location performance, but it encouraged the providers to use their best effort to ensure E112 services. For this purpose, the European Memorandum of Understanding (MoU) for the realisation of an interoperable in-vehicle emergency call service (eCall) was presented in 28 May 2004 [eSa04]. In order to support this legislation, the European Commission have continuously called for European research projects. For instance, the European mobile integrated location system (EMILY) project investigated the hybridisation of terrestrial (i.e. E-OTD and OTDOA) and satellite-based GNSS positioning, as it described in [ME02] and the references therein. In United States, the FCC strongly supervised the implementation of E911 services, and approved in 2007 a stricter order of the Phase II standard, where the location accuracy and reliability requirements have to be fulfilled at the PSAP local region by 11 September 2012 [FCC07]. This order avoids the carriers from achieving the Phase II requirements by averaging locations across the entire national network. Considering this legislation, hybrid A-GPS and AFLT systems and UTDoA technologies has been deployed in American networks, while E-OTD has failed to fulfil the accuracy requirements and OTDOA has not been adopted by any carrier in UMTS by 2011 [CSR11], since carriers are expecting to migrate directly to LTE positioning technologies.

### 2.2.3 Present and future cellular positioning

The standardization development of LTE started in 2004, proposed by NTT DOCOMO of Japan [Abe10], under the name of Super 3G . But, it was not until December 2008 that the first specification of LTE was frozen by 3GPP with Release 8. By that time, the radio access network (RAN) #42 plenary approved in [RP-08a] (proposed by Qualcomm Europe) and [RP-08b] the work items (WIs) of the LTE positioning service and the support for IMS emergency calls over LTE. The objective of these WIs was mainly based on providing a positioning protocol and a downlink terrestrial positioning method to act as a backup to A-GNSS, in regions where full visibility of GNSS satellites cannot be ensured and emergency calls are subject to strong regulation [3GP12a]. The downlink positioning method was suggested to be analogous to well-known techniques, such as OTDoA in

UTRAN, E-OTD in GERAN and AFLT in CDMA2000 (from 3GPP2). Following the evolution of UMTS, OTDoA positioning method was evaluated by RAN working group (WG) 1 and the positioning protocol was developed by RAN WG2 considering the performance requirements of RAN WG4. Focusing on the positioning method, Nortel earlier pointed out in RAN WG1 meeting #55 [R1-08] that LTE positioning could support emergency services, but also, the user equipment location could help BSs to optimize RF deployment parameters, e.g. in the support of self-organizing networks (SON). In the following meeting (i.e. #55bis), the issue of neighbour cell hearability was introduced. As an evolution of the IPDL method in UTRAN, two main solutions were proposed by Qualcomm Europe in [R1-09b] and Alcatel-Lucent in [R1-09a]: a dedicated reference signal and the serving cell muting. In RAN WG1 meeting #56, simulations assumptions and performance evaluations were presented, such as by Alcatel-Lucent in [R1-09c] or by Ericsson in [R1-09d]. RAN WG1 meeting #56bis had many contributions on the topic, and the way forward on the definition of a positioning reference signal (PRS) allocated in a low-interference positioning subframe was agreed in [R1-09e]. Then, RAN WG1 meetings #57 and #57bis served to specify the general definition of the PRS selecting the preferred option among all the proposals. Several performance assessments could be found, such as in [R1-09f], [R1-09g] or [R1-09h]. For instance, in [R1-09h], system and propagation errors are also considered to assess the LTE positioning performance with a sensitivity analysis. Finally, the OTDoA specification was stated in RAN WG1 meetings #58 and 58bis, and was included in the LTE standard with Release 9 by December 2009. From the end of 2009 up to nowadays, 3GPP meetings have focused on the conformance test specification [3GP12d]. They also have discussed other positioning procedures, such as RF-matching or UTDoA. The RF-matching is still under study. UTDOA finally has been standardised in Release 11 in 2012 with some controversy, due to a lawsuit between TruePosition (precursor of the UTDoA technology) and Ericsson, Alcatel-Lucent, and Qualcomm.

Apart from the 3GPP reports, the LTE research community has been active on the study of LTE positioning. The wireless hybrid enhanced mobile radio estimators (WHERE) project, funded by the European Commission, can be highlighted, since it is aimed to enhance communications by using location information [Rau08]. This project studies mobile positioning by means of the hybridisation of LTE OTDoA and GNSS, such as in [Men10, Men13] and [Gen12]. The research and development of the WHERE project is continued by the WHERE2 project [Dam13], which is aimed to exploit synergies between heterogeneous cooperative positioning and communications. These research projects have also produced contributions on positioning with LTE PRS and signals of opportunity in [Dam10], or on resource allocation for cooperative positioning in [Rau13].

Further research can be found in academic and private studies. The LTE PRS ranging performance is assessed by Ericsson AB in [Med09] with measurements of a channel campaign. The results show a LTE OTDoA positioning accuracy better than 20 m for 50% of the cases and 63 m for 95% of the cases, using the PRS over a bandwidth of 20 MHz. The time synchronisation of LTE is studied with an interference cancellation technique in [Zhu11], and using the PRS over multipath channels in [Pan13]. A comprehensive review and comparison of the the location technologies found in LTE is provided in [Che13]. Most of these contributions mainly use the matched filter or correlation-based techniques as the conventional estimator for ranging in LTE, following the trend of CDMA systems.

Regarding to the legislative regulations, the FCC created, by 19 March 2011, the Communications Security, Reliability and Interoperability Council (CSRIC) III WG3, in order to mainly address E911 location accuracy testing. The CSRIC III WG3 tested, during winter of 2012 2013, the indoor location accuracy of three technologies: network beacons by NextNav, RF fingerprinting by Polaris Wireless, and hybrid A-GPS and AFLT by Qualcomm. According to the resulting report in [CSR13], none of these technologies proved to identify the specific building and floor where the mobile device was located. This report suggests future improvements by means of the deployment of LTE PRS ranging and its hybridisation with A-GNSS. Recently, the FCC has proposed in [FCC14] specific measures to regulate indoor location, such as by requiring 50 m of horizontal accuracy and 3 m of vertical accuracy for 67% of 911 calls. This notice also provides a comprehensive summary of the current status of indoor positioning. In Europe, the European Commission has required full deployment of the eCall in-vehicle system by 1 October 2015 [Eur13], which affects new models of passenger cars and vans. Similarly to the eCall system, Russian Federation is developing the ERA-GLONASS in-vehicle system [GOS12, Gla14]. Thus, cellular positioning is envisaged to supplement GNSS in order to fulfil legislative regulations, e.g. using LTE PRS ranging in challenging environments.

## 2.3 LTE positioning features

### 2.3.1 Positioning methods

The review on cellular positioning has shown that the positioning techniques specified in LTE have been inherited from its predecessor standards (i.e. GSM and UMTS). Although these methods are based on the same principles, LTE includes additional support to enhance the positioning performance. Thus, this section further describes the positioning methods standardised in Release 9, which are summarized in Figure 2.2.

The overall description of LCS can be found in the technical specification (TS) 22.071 (Stage 1) [3GP05], and the mechanisms to support the services can be found in TS 23.271 (Stage 2) [3GP13a]. The specific positioning methods in LTE are described in TS 36.305 [3GP13b], and a general summary of the specifications is shown in Figure 2.3. The standard already defines that the provision of UE positioning is optional, and the positioning information obtained by the network can be used to improve system performance [3GP13b]. According to Release 9 [3GP13b], the LTE positioning methods supported are:

- A-GNSS based positioning methods, where ranging measurements from navigation satellite are aided with assistance data, such as ephemeris, almanac, ionospheric model or UTC model [VD09]. The assistance data helps the receiver to reduce the acquisition time, and thus it accelerates the availability of the position information.
- enhanced cell ID (E-CID) method, which is based on the position and cell coverage of the BS (i.e. eNodeB), enhanced with uplink or downlink signals measurements, such as timing advance. The signal measurements can be the reference signal received power (RSRP), reference signal received quality (RSRQ), round trip time (RTT), AoA or a combination of them.
- OTDoA positioning method, which is based on the difference in the arrival times of downlink radio signals from multiple base stations.

The primary location method in LTE is A-GNSS, because of its accuracy and availability. However, its robustness is compromised in challenging environments, such as indoor or urban scenarios. In these circumstances, the presence of blocking obstacles and propagation disturbances prevent them from observing the expected perfect clear-sky conditions that were assumed in the nominal design of the GNSS system. Thus, the E-CID and OTDoA are specified as fall-back methods. The E-CID results in a coarse estimation of the user location. Thus, the OTDoA positioning is added in Release 9 to improve the accuracy of the complementary methods. This positioning technology has a high potential accuracy due to two main enabling features of LTE: tight synchronisation among base stations, and wideband signals. In addition, the hybridisation of these standard methods is supported. Finally, and although it is not specified in the standard, fingerprinting or scene analysis methods can also be implemented with LTE, by means of signal measurements based on the received power or on the time-delay estimation.

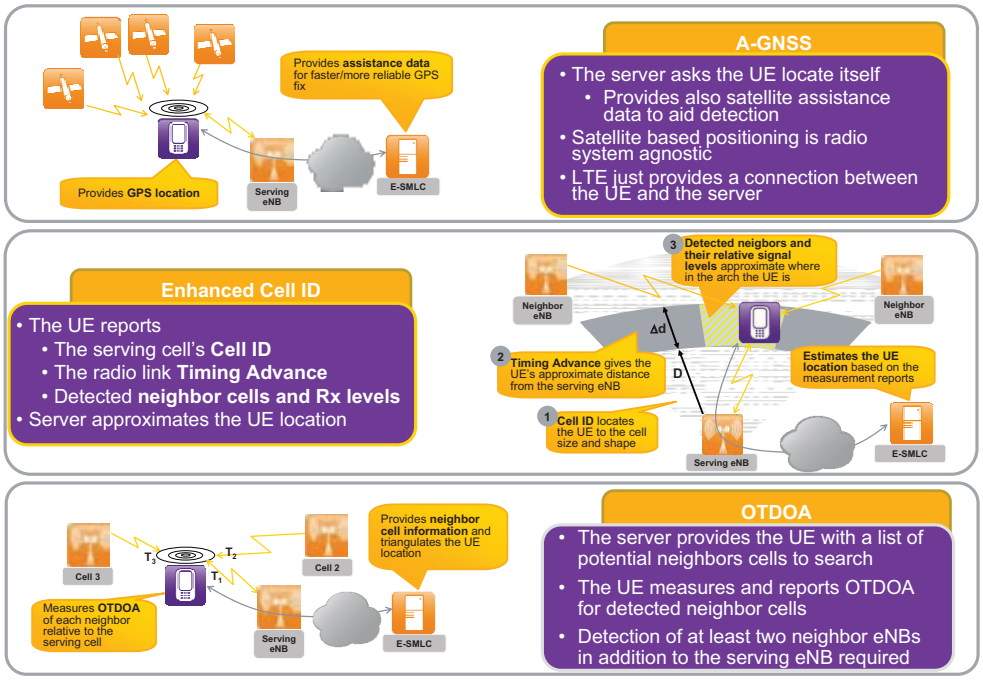


Figure 2.2: LTE positioning procedures [RA10].

### 2.3.2 Positioning protocols

LTE positioning methods can be classified in network-based and UE-based, depending on whether the position is computed by the network or by the UE, respectively. The UE can only compute its position standalone by means of satellite-based methods, but GNSS measurements can also be sent to the enhanced serving mobile location center (E-SMLC), in order to compute the location. The location procedure can also be initiated either by the UE or by the network. The positioning class or service determines the algorithm selection, also considering hybrid approaches. The LTE positioning protocol (LPP) provides the necessary messaging to support a location service. The LTE location architecture is defined by the target device or UE, reference sources (i.e. GNSS satellites or eNodeB), and E-SMLC, as it is shown in Figure 2.4. The LTE protocol is structured into a control plane, which uses the transport channel, and user plane, which uses the data channel.

The E-SMLC location server manages the configuration and coordination among BSs and UE involved in a positioning service. Since the OTDoA method relies on a network-based strategy, the eNodeB locations are not provided to the user. This centralised method may hinder its use for other purposes, such as positioning using SoO. The OTDoA positioning procedure can be described in three steps:

| | |
|---|---|
| **Requirements** | |
| 22.071 | LCS Service Description |
| **Architecture and Feature Description** | |
| 23.271 | Functional Description of LCS |
| 36.305 | Functional Spec of UE Positioning |
| **Core Network Interfaces and Services** | |
| 29.171 | LCS-AP MME ↔ E-SMLC; SLs Interface |
| 29.172 | ELP GMLC ↔ MME; SLg Interface |
| 29.173 | Diameter-based SLh interface for CP LCS |
| 24.030 | Supplementary Service Operations |
| **Operations and Maintenance** | |
| 32.171 | Telecom Mgt; Charging Mgt; LCS Charging |
| **LTE Physical Layer (impacted by LCS)** | |
| 36.211 | Physical Channels and Modulation |
| 36.214 | Physical Layer Measurements |
| **RAN Protocols (impacted by LCS)** | |
| 36.331 | RRC Protocol Specification |
| **RAN ↔ Core Network Protocols** | |
| 36.355 | LTE Positioning Protocol (LPP) |
| 36.455 | LTE Positioning Protocol A (LPPa) |
| 24.301 | NAS protocol for EPS |
| 24.413 | S1-Application Protocol (S1-AP) |
| **Performance Requirements** | |
| 36.133 | Requirements for support of RRM |
| 36.171 | Requirements for Support of A-GNSS |

Figure 2.3: 3GPP standards for LTE localisation [Fly10].

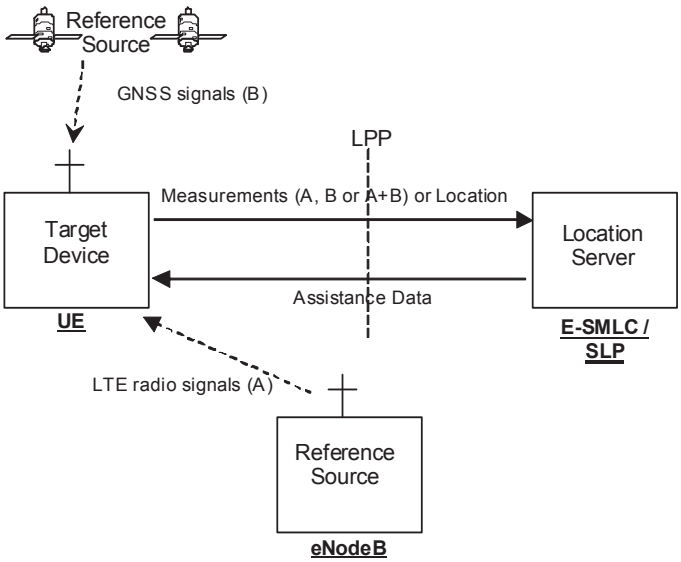


Figure 2.4: LPP configuration for control- and user-plane positioning in LTE [3GP14c].

1. **Assistance data**: The UE may request assistance information to proceed with the timing measurements. Otherwise, the network initiates the OTDoA positioning, and the assistance data is directly provided to the user [3GP14b, p.82]. The information provided to the UE is the cell-ID of the nearest base stations, PRS information, slot number offset, and PRS-subframe offset in a positioning occasion.

2. **Ranging measurements**: The OTDoA measurements are then produced by the UE with time differences between the received signals of different synchronized BSs. If the BSs are not perfectly synchronized, a time bias will be added to the estimation and corrections should be applied a posteriori by the E-SMLC. If the PRS is enabled, one or several positioning subframes of a certain period are transmitted in every positioning occasion, characterized by its low inter-cell interference. The reported measurement, called reference signal time difference (RSTD), is delivered in multiples of the basic time unit $T_{\mathrm{s,min}}$. Then, the LPP transfers the UE measurements to the location server, i.e. E-SMLC.

3. **Position computation**: Based on the ranging measurements obtained by the UE, the E-SMLC estimates the UE position using a lateration technique and correcting the BS synchronisation errors. This position information is finally sent to the UE.

## 2.4 Downlink physical layer of LTE

The current description of the downlink physical layer is based on Release 9 of the LTE standard, because Release 10 and beyond are part of LTE-Advanced, and this variant of LTE is out of the scope of the present work. The downlink transmission resources in LTE possess dimensions of time, frequency and space. The spatial dimension is exploited by multi-antenna techniques. In frequency, scalable channel bandwidths from 1.4 to 20 MHz are allowed, being the actual FFT size and sampling frequency not specified. In time, one or two of the following types of radio frame structure are supported [3GP10]:

- Type 1, applicable to both full-duplex and half-duplex FDD (Frequency Division Duplexing), where uplink and downlink are separated in frequency, and the 10-ms radio frame is divided in subframes of 1 ms and slots of 0.5 ms,

- Type 2, applicable to TDD (Time Division Duplexing), consisting of two half-frames of 5 ms assigning the uplink or downlink transmissions in subframes of 1 ms and slots of 0.5 ms. There are two special subframes formed by the DwPTS (Downlink Pilot Timeslot), GP (Guard Period), and UpPTS (Uplink Pilot Timeslot).

In order to reduce complexity, a minimum resource allocation is defined. It is called resource block (RB) and its smallest unit is a resource element (RE), which consists of one subcarrier for a duration of one OFDM symbol. The size of the RB depends on the subcarrier spacing and the cyclic prefix (CP) length designed. These two parameters are defined according to the channel environment. First, the spacing among subcarriers allows a certain tolerance against Doppler shifts caused by user mobility. Second, the CP introduces a redundancy on the transmission, by adding the end of the OFDM symbol at the beginning, in order to avoid the effects of intersymbol interference (ISI). The CP length is intended to be equal or larger than the delay spread of the channel, that is, the CP should be larger than the delay between the first and the last arriving ray. As it can be seen, the design of these parameters produces an overhead on the transmission. Thus, there is a trade-off between the optimal performance of the system in a certain environment and the amount of time and frequency resources allocated. LTE specifies a `normal CP length of around 5 µs and an `extended CP length of 16.7 µs with a subcarrier spacing $F_{\text{sc}}$ of 15 kHz, and a halved subcarrier spacing of 7.5 kHz with an extended CP of 33 µs. This last mode is defined for multi-cell broadcast, known as multimedia broadcast single frequency network (MBSFN). These modes and their corresponding parameters are summarized in Figure 2.5. Current networks are deployed with the normal configuration, thus the RB contains 12 subcarriers and 7 OFDM symbols, which occupies a bandwidth of 180 kHz and one slot. The basic time unit specified in LTE is $T_{\text{s,min}} = 1/\left(F_{\text{sc}} \cdot 2048\right) =$ 32.55 ns, which results in a sampling frequency $F_{\text{s}}$ equal to 30.72 MHz. This basic unit allows backward compatibility with predecessor technologies.

According to TS 36.211 [3GP10] subclause 6.2.1, the number of RBs or downlink bandwidth configuration $N_{\text{RB}}$ depends on the downlink transmission bandwidth configured in the cell and shall fulfil

$$N_{\text{RB}}^{\text{min}} \leq N_{\text{RB}} \leq N_{\text{RB}}^{\text{max}}, \tag{2.4.1}$$

where $N_{\text{RB}}^{\text{min}} = 6$ and $N_{\text{RB}}^{\text{max}} = 110$ are the smallest and largest downlink bandwidth, respectively. Although the standard is flexible enough to support up to 110 RBs, the maximum transmission bandwidth is set to 100 RBs [3GP14a]. The $N_{\text{RB}}$ values allowed in TS 36.104 [3GP12c] subclause 5.6 are summarized in Table 2.1, with examples of FFT and sampling frequency for efficient implementation. Guard bands are left at the edges of the spectrum, approximately 10% of the channel bandwidth, which is scalable from 1.4 to 20 MHz. There is also no transmission on the DC subcarrier in order to avoid undesirable DC offsets that may induce a bias on the carrier-frequency offset (CFO) estimator.

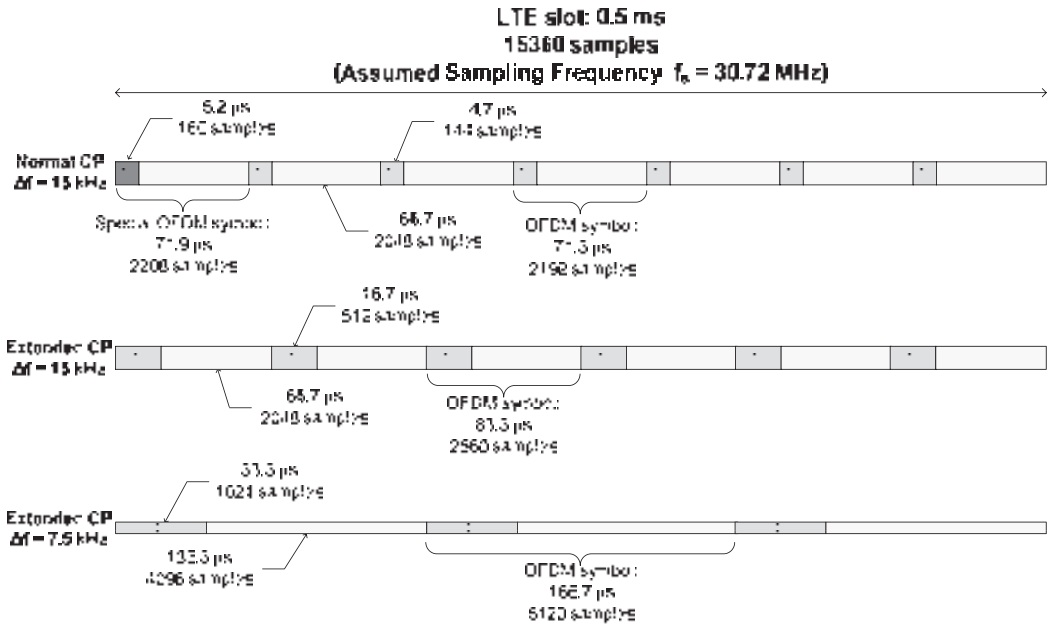


Figure 2.5: LTE OFDM symbol and CP lengths [Ses11, p.141].

| Channel Bandwidth (MHz) | 1.4 | 3 | 5 | 10 | 15 | 20 |
|---|---|---|---|---|---|---|
| Number of Resource Blocks ($N_{\mathrm{RB}}$) | 6 | 15 | 25 | 50 | 75 | 100 |
| Number of occupied subcarriers | 72 | 180 | 300 | 600 | 900 | 1200 |
| FFT size | 128 | 256 | 512 | 1024 | 1536 | 2048 |
| Occupied Bandwidth (MHz) | 1.08 | 2.7 | 4.5 | 9.0 | 13.5 | 18.0 |
| Sampling Frequency (MHz) | 1.92 | 3.84 | 7.68 | 15.36 | 23.04 | 30.72 |
| Samples per slot | 960 | 1920 | 3840 | 7680 | 11520 | 15360 |

Table 2.1: LTE bandwidth and resource configuration.

### 2.4.1 Physical channels and modulation

LTE signals are constituted by synchronisation signals, reference signals, data signals and control signals, which are defined in TS 36.211 [3GP10]. The synchronisation signals and the reference signals are pilot signals (i.e. signals completely known), thus they will be of main interest for ranging. The pilots signals defined in LTE are:

- The primary synchronization signal (PSS) and the secondary synchronization signal (SSS) allow cell search and signal acquisition.
- The reference signals (RS) are mainly aimed to aid data demodulation and achieve fine synchronisation. The following reference signals are specified in Release 9:
  - The cell-specific reference signal (CRS) is used for downlink channel estimation in a cell supporting PDSCH transmission.
  - The MBSFN reference signal is only transmitted in the MBSFN transmission mode and are only defined for extended CP. These reference symbols are spaced more closely in the frequency domain than in the non-MBSFN transmission, thus improving the channel estimation accuracy in large delay spread scenarios.
  - The UE-specific reference signal (UE-RS) may be added to the transmission of CRS in resource blocks with PDSCH. It is used to derive the channel estimation for demodulating the data in the corresponding PDSCH RBs.
  - The PRS is a dedicated signal for positioning purposes based on the time-delay estimation.

The transmission of transport and control data is not allowed in the synchronisation symbols, neither in the DC subcarrier. This data is allocated in the following channels:

- The physical broadcast channel (PBCH) is the physical channel that carries the main information of the cell, such as the downlink system bandwidth, used for initial network access.
- The physical downlink shared channel (PDSCH) is the physical channel that carries the traffic data.
- The physical downlink control channel (PDCCH) is the physical channel that carries the channel allocation and control information.
- The physical multicast channel (PMCH) is the physical channel that carries information to multiple users for point-to-multipoint broadcast services.

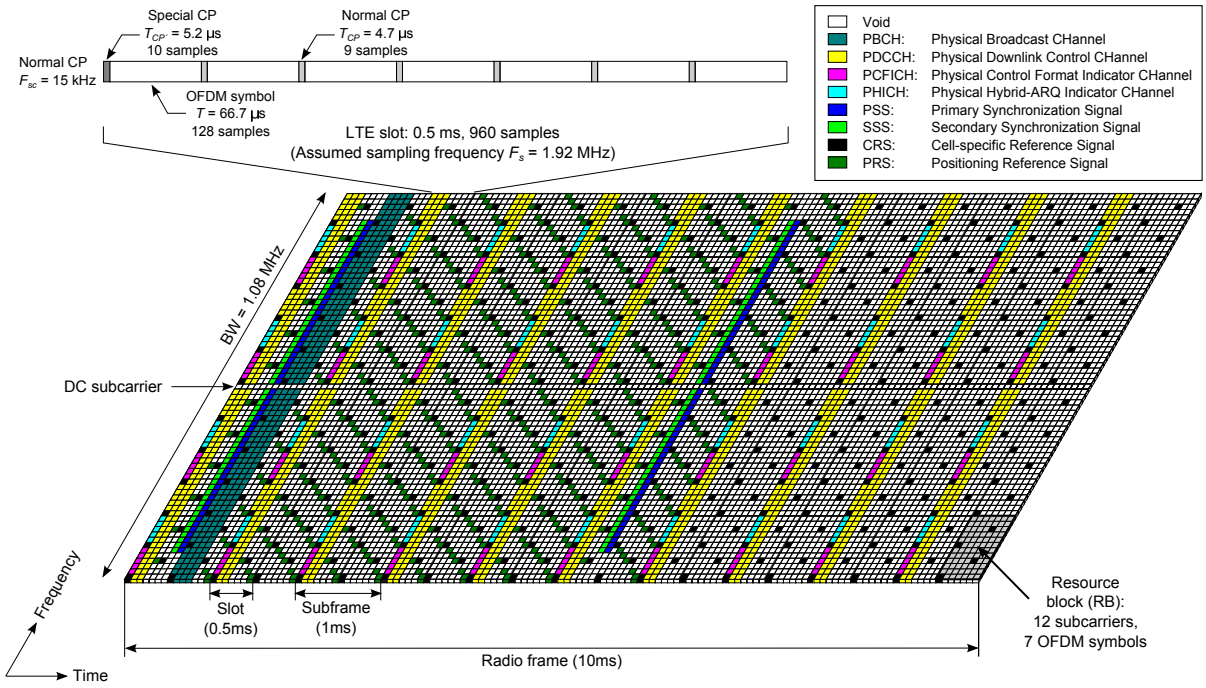


Figure 2.6: Time-frequency grid of the LTE signals specified in Release 9 of the standard for 6 RB, frame structure type 1 (applicable to FDD) and normal CP, assuming a sampling frequency of 1.92 MHz and unicast transmission without user data.

- The physical control format indicator channel (PCFICH) is the physical channel that carries the number of OFDM symbols used for transmission of PDCCHs in a subframe.
- The physical hybrid automatic repeat request (ARQ) indicator channel (PHICH) that carries the hybrid ARQ indicator, to inform to the UE whether its uplink transmission has been correctly received.

Further information on the data-transport channels (i.e. PBCH and PDSCH) and data-control channels (i.e. PDCCH, PCFICH and PHICH) can be found in [Ses11]. An example of the time-frequency transmission grid of a BS is shown in Figure 2.6.

### 2.4.2 Synchronization signals

In LTE, the system access is based on the acquisition of two physical signals that are periodically broadcast with specific codes for each cell, i.e. the synchronization signals. The network admits 504 unique cell identities $N_{\mathrm{ID}}^{\mathrm{cell}}$ (cell ID) grouped into 168 groups of three identities, as shown in Figure 2.7. Each cell group is usually controlled by the same BS, and three PSS sequences are used to identify each sector cell within the group $N_{\mathrm{ID}}^{(2)}$.

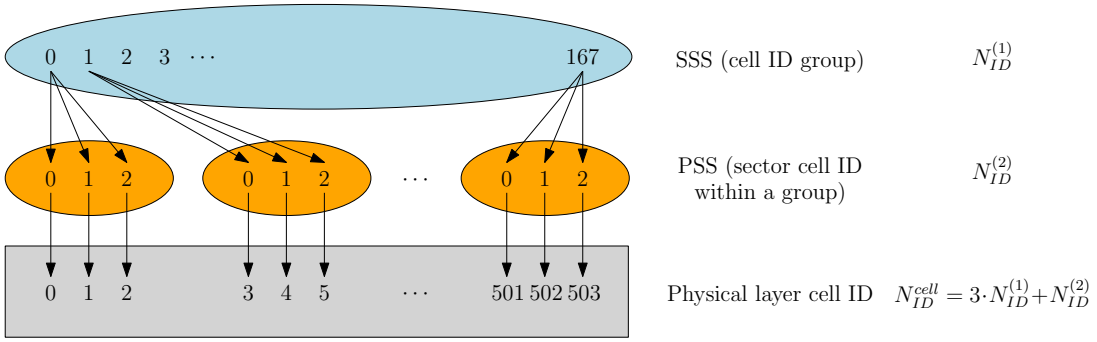


Figure 2.7: Cell distribution in LTE.

These PSS sequences are defined by three length-63 Zadoff-Chu (ZC) sequences in the frequency domain, which have the middle element punctured to avoid transmitting on the DC subcarrier. In order to distinguish each group, 168 SSS sequences indicate the identity of the group $N_{\mathrm{ID}}^{(1)}$ (cell ID group). These SSS sequences are constructed by interleaving, in the frequency-domain, two length-31 BPSK-modulated secondary synchronization codes. These sequences are described in TS 36.211 [3GP10] clause 6.11.1, and briefly discussed in the following subsections.

### Primary synchronization signal

The PSS uses a frequency-domain ZC sequence defined in TS 36.211 [3GP10] as

$$d_u(n) = \begin{cases} \exp\left(-j\dfrac{\pi u n(n+1)}{63}\right) & \text{if } n = 0, 1, \ldots, 30, \\ \exp\left(-j\dfrac{\pi u (n+1)(n+2)}{63}\right) & \text{if } n = 31, 32, \ldots, 61, \end{cases} \tag{2.4.2}$$

where the indexes $u$ of the ZC root sequence are 25, 29 and 34 for $N_{\mathrm{ID}}^{(2)} = 0, 1, 2$, respectively. Given the normalized periodic auto-correlation defined by

$$R(k) \doteq \frac{1}{N_{\mathrm{ZC}}} \sum_{n=0}^{N_{\mathrm{ZC}}-1} d_u^*(n) \cdot d_u(n+k), \tag{2.4.3}$$

where $N_{\mathrm{ZC}}$ is the sequence length (i.e. equal to 63), the periodic auto-correlation of the ZC sequences is ideal, i.e.

$$R(k) = \begin{cases} 1 & \text{if } k = 0, \\ 0 & \text{otherwise}, \end{cases} \tag{2.4.4}$$

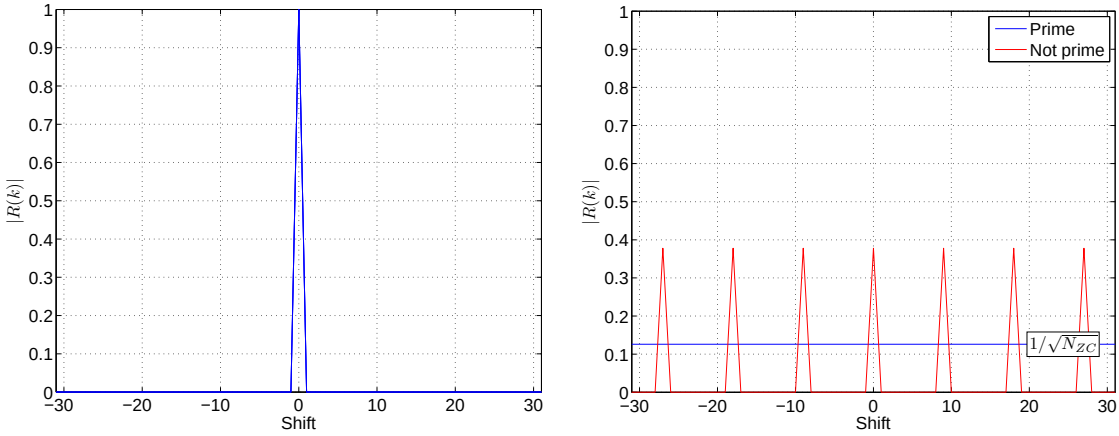


(a) Normalized periodic auto-correlation (b) Normalized periodic cross-correlation

Figure 2.8: Correlation properties of the ZC sequences.

as it is shown in Figure 2.8(a). Although these sequences are not orthogonal, they exhibit a low cross-correlation, which is equal to $1/\sqrt{N_{\text{ZC}}}$ if the difference between both root indexes is relatively prime to $N_{\text{ZC}}$ [Pop92] (e.g. the cross-correlation between roots 25 and 34), as it can be seen in Figure 2.8(b).

### Secondary synchronization signal

The SSS is an interleaved concatenation of two length-31 binary sequences. Its generation is based on scrambling two length-31 $m$-sequences (maximal length sequences), which differs between subframe 0 and subframe 5 [3GP10]. The periodic auto-correlation of the $m$-sequence is 1 for zero-lag, and nearly zero ($-1/M$, where $M$ is the sequence length) for all other lags, as it is shown in Figure 2.9. Due to the scrambling of $m$-sequences and the avoidance of the DC subcarrier, the ideal properties of the $m$-sequences are not achieved by the SSS sequences, resulting on the auto-correlation and cross-correlation shown in Figures 2.10(a) and 2.10(b).

### Mapping to resource elements

In the time domain, the PSS and SSS mapping structure is shown in Figure 2.11(a) for the FDD case and in Figure 2.11(b) for the TDD case. The specific structure is designed to facilitate the synchronization of the signal. For instance, in the FDD case, the location of the PSS symbols enables the UE to detect the slot boundary independently of the CP length. In the frequency domain, the mapping of the PSS and SSS to subcarriers is shown in Figure 2.12. The PSS and SSS are allocated in the center of the spectrum

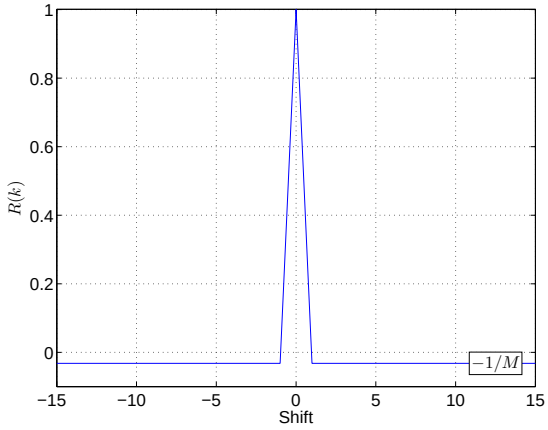


Figure 2.9: Normalized periodic auto-correlation of a $m$-sequence.

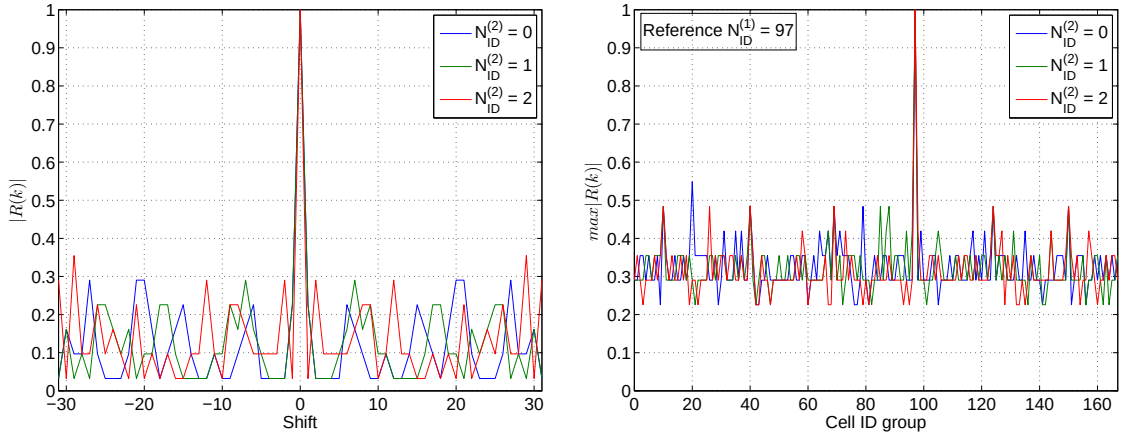


(a) Normalized periodic auto-correlation (b) Normalized periodic cross-correlation

Figure 2.10: Correlation of the SSS sequences as a function of shift and cell ID group $N_{ID}^{(1)}$ (excluding DC component).

with 62 contiguous pilot subcarriers, and avoiding the DC subcarrier, thus the mapping of these signals is invariant with respect to the system bandwidth.

### 2.4.3 Reference signals

The reference signals are mainly used for channel estimation in order to improve the data demodulation. But, they can also help to track the signal or obtain time-delay measurements for positioning purposes. The current study focuses only on the cell-specific RS and the positioning RS. In contrast to the UE-specific RS, they are independent of the traffic data transmitted in the network. Although the CRS and PRS are mapped in different resource elements, they are characterized by the same code sequences, which are

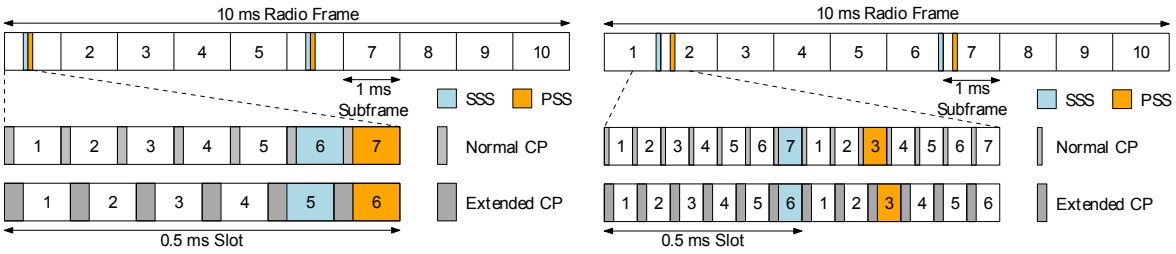


(a) FDD case (b) TDD case

Figure 2.11: PSS and SSS frame and slot structure in the time domain [Ses11, p.153].

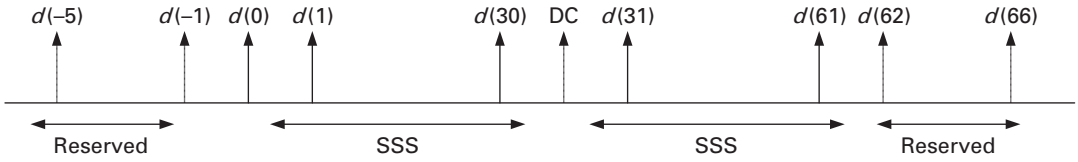


Figure 2.12: Frequency-domain mapping of the synchronization signals [Ses11, p.157].

unique for each slot, OFDM symbol, cell ID, and CP configuration. Their RS sequence $d_{l,n_s}(m)$ is defined by

$$d_{l,n_s}(m) = \frac{1}{\sqrt{2}}\left(1 - 2c(2m)\right) + j\frac{1}{\sqrt{2}}\left(1 - 2c(2m+1)\right), \quad m = 0, 1, \ldots, 2N_{\mathrm{RB}}^{\max} - 1, \quad (2.4.5)$$

where $n_s$ is the slot number within a radio frame, $l$ is the OFDM symbol number within the slot, and $N_{\mathrm{RB}}^{\max}$ is the maximum number of RBs in the downlink. As it can be noticed, the index $m$ is used to allocate the chip codes to every subcarrier, starting from the most negative subcarrier in a symmetric spectrum and excluding the DC subcarrier. The CRS and PRS introduce a frequency reuse factor of six according to the cell identity, i.e. a shift from one to six subcarriers is applied to their frequency pattern given by $N_{\mathrm{ID}}^{\mathrm{cell}} \bmod 6$. Thus, pilot sequences from different base stations typically do not overlap. In (2.4.5), $c(i)$ is a pseudo-noise sequence used for scrambling and defined by a length-31 Gold sequence [3GP10, p.81]. This sequence is constructed by EXOR-ing two $m$-sequences of the same length as shown in Figure 2.13. According to TS 36.211 [3GP10], the pseudo-noise sequence generator shall be initialised with

$$c_{\mathrm{init}} = 2^{10} \cdot (7 \cdot (n_s + 1) + l + 1) \cdot \left(2 \cdot N_{\mathrm{ID}}^{\mathrm{cell}} + 1\right) + 2 \cdot N_{\mathrm{ID}}^{\mathrm{cell}} + N_{\mathrm{CP}}, \quad (2.4.6)$$

at the start of the OFDM symbol, where the cell ID is $N_{\mathrm{ID}}^{\mathrm{cell}} = 3 \cdot N_{\mathrm{ID}}^{(1)} + N_{ID}^{(2)}$ and $N_{\mathrm{CP}}$ is equal to 1 for normal CP and equal to 0 for extended CP. The results obtained with the periodic auto-correlation and cross-correlation of the RS sequence are shown in Figure

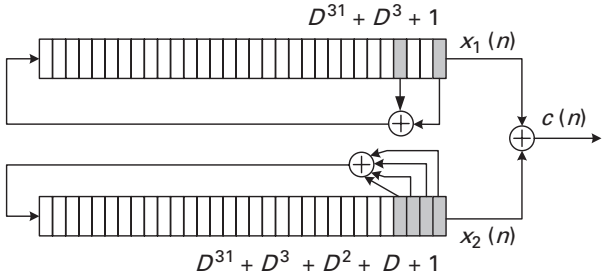


Figure 2.13: Pseudo-noise scrambling code generation [Kha09, p.189].

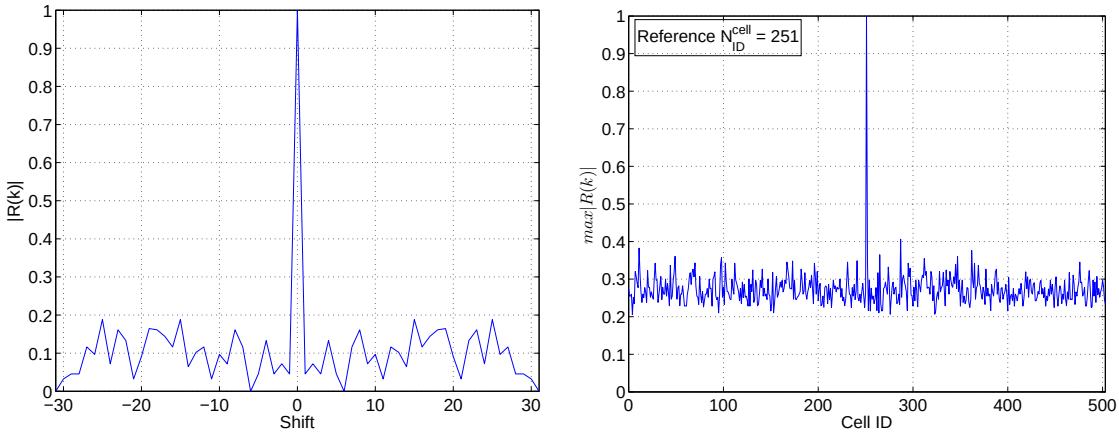


(a) Normalized periodic auto-correlation (b) Normalized periodic cross-correlation

Figure 2.14: Correlation of the RS sequences using 31 RBs and excluding the DC component.

2.14 by using 31 RBs, which results in a length-62 sequence. The RS sequence shows a slightly poorer auto-correlation than the ZC sequence, but it has better cross-correlation properties than the $m$-sequences. Moreover, the RS generation procedure provides a higher number of different sequences than with the PSS and SSS procedures.

The pilot distribution of the CRS and PRS is shown in Figure 2.15. The total number of subcarriers depicted is $N_{\mathrm{t}} = 12 \cdot N_{\mathrm{RB}} + 1$, including the DC subcarrier. But, the LTE physical layer is typically implemented with $N_{\mathrm{t}} = 2^{\lceil \log_2(12 \cdot N_{\mathrm{RB}}) \rceil}$ filled by empty subcarriers at the edges of the bandwidth, in order to leave guard bands and to efficiently use the FFT. As it can be noticed, the bandwidth occupied by the active subcarriers, i.e. effective bandwidth, is lower than the bandwidth formed by the total number of subcarriers $N_t$. Thus, the effective bandwidth is considered to be equal to the distance between the first and last active subcarriers. Transmitting only reference signals, the number of subcarriers equivalent to the effective bandwidth is $N = 12 \cdot N_{\mathrm{RB}} - 4$. Considering this example, let us assume the transmission of 6 RB and uniform power distribution among PRS subcarriers.

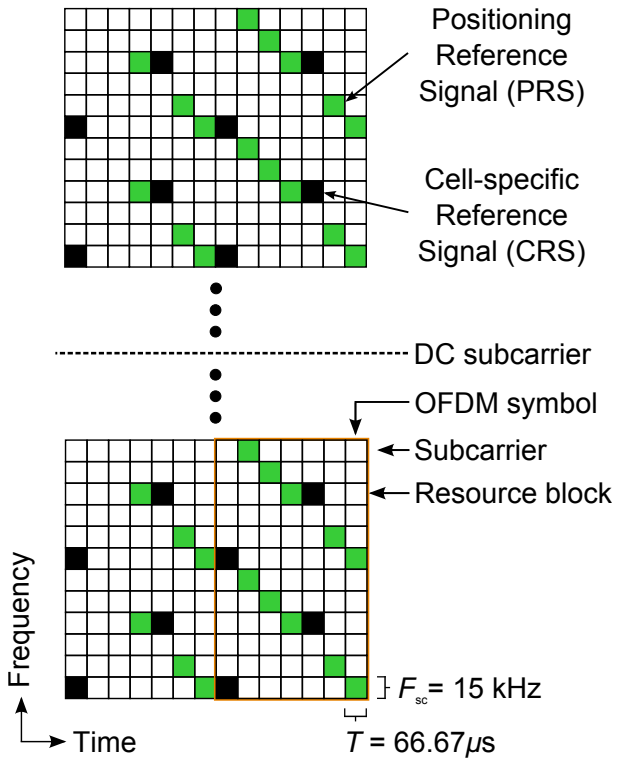


Figure 2.15: Time and frequency distribution of the LTE CRS and PRS pilot signals.

Then, the normalised power spectral density (PSD) for one symbol is shown in Figure 2.16. In this case, the number of subcarriers $N$ is equal to 68, and the sampling period $T_{\mathrm{s}}$ is

$$T_{\mathrm{s}} = \frac{T}{N} = \frac{1}{F_{\mathrm{sc}} \cdot N} = \frac{1}{15 \cdot 10^3 \cdot 68} = \frac{1}{1020 \cdot 10^3} = 0.98 \ \mu\mathrm{s}. \tag{2.4.7}$$

### Cell-specific reference signal

The cell-specific reference signal are mapped in a optimal distribution for channel estimation. The distance between their resource elements in time and frequency is designed according to the most extreme channel supported. These pilots can also be used to generate the channel state information (CSI) feedback or to track the time-delay and frequency offset components of the signal.

### Positioning reference signal

The PRS is defined as a pilot signal exclusively dedicated for positioning purposes in LTE. Their specification appears in 3GPP Release 9 [3GP10, p.71] in order to improve the timing measurements by decreasing the inter-cell interference. Before its definition,

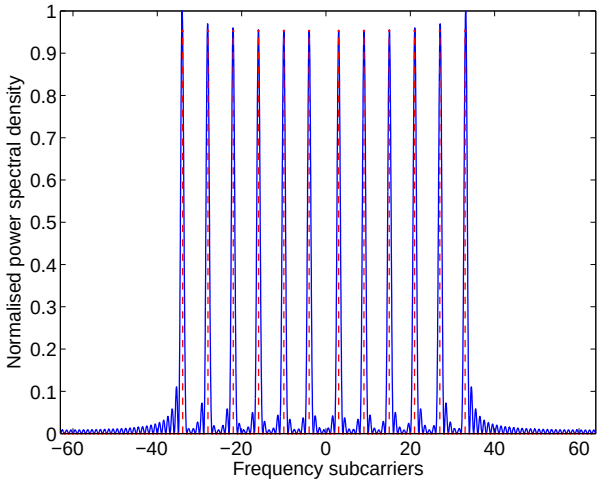


Figure 2.16: Normalised PSD of the 6-RB PRS without data transmission.

the most suitable LTE pilots for ranging were the synchronization signals and the cell-specific reference signals. However, the flexibility of cellular networks allows sharing the same spectrum among neighbour base stations, such as in single-frequency networks (SFN) characterized by a frequency reuse factor of one. This leads to the overlapping between pilot signals and data channels, which results in the well-known near-far effect or hearability problem, and prevents accurate signal measurements. Thus, the PRS solves the interference between pilots and traffic data by setting the possibility to avoid the transmission of data on the RBs allocated for positioning. For instance, the PDSCH may not be transmitted on the positioning subframe. The sophistication of this signal is even higher when the network mutes the PRS transmissions of certain base stations, i.e. PRS muting, in order to further reduce the inter-cell interference. Given this flexible standard, the proper configuration of a positioning situation is left up to the network operator.

The PRS is only transmitted in downlink subframes configured for positioning, which are called positioning occasions. Each positioning occasion may include from one to six consecutive positioning subframes with a periodicity of 160, 320, 640 or 1280 subframes (of 1 ms) [3GP10, p.74]. The complex-valued symbols of the PRS follow the mapping of the normal CP configuration shown in Figure 2.15. It is only configured for a subcarrier spacing equal to 15 kHz, and can be extended in the frequency domain occupying the whole available bandwidth. However, the positioning reference signals should not be mapped in resource elements allocated to PBCH, PSS or SSS. In addition, the PRS is defined by a subframe offset to the start of the radio frame, defined by a configuration index $I_{\mathrm{PRS}}$. The main parameters for PRS configuration are shown in Table 2.2.

Table 2.2: Main parameters of the PRS.

| | |
|---|---|
| PRS bandwidth | 1.4, 3, 5, 10, 15 and 20 MHz |
| PRS periodicity | 160, 320, 640 or 1280 ms |
| Consecutive subframes | 1, 2, 4, or 6 |
| PRS muting information[1] | 2, 4, 8, 16 bits |
| PRS pattern | 6-reuse in frequency |
| PRS sequence | Length-31 Gold sequence |

[1] Number of positioning occasion configured for PRS muting (i.e. bit equal to 0 when PRS is muted).

Further details can be found in several books with comprehensive information about LTE. The book of Sesia et al. [Ses11] is truly recommended for understanding the LTE standard, particularly Chapter 19 that describes the LTE positioning. In addition, the book of Zekavat and Buehrer [Zek11] provides a general understanding on position location, but also gives specific values on the LTE accuracy (see Section 32.8). Further review on cellular localisation can be found in [Gen13].

# Chapter 3

# Achievable Localization Capabilities of LTE Conventional Receivers

Despite the significant advances in the 3GPP standard and the research studies on OTDoA positioning, a detailed assessment of the achievable localization capabilities of LTE is not available yet. The 3GPP consortium has presented results of the LTE positioning performance, but with few details on the techniques implemented. The rest of the LTE research community has produced studies on specific scenarios. This chapter provides an analysis of the positioning capabilities of LTE on the main working scenarios. This assessment is obtained with a conventional receiver based on the matched filter. The use of the matched filter in LTE for ranging purposes is inherited from CDMA systems (e.g. UMTS or CDMA2000). Thus, the positioning performance of this conventional and low-complexity implementation is assessed in a standard cell layout with Gaussian noise and inter-cell interference. Although the matched filter is expected to perform poorly in multipath environments, the study also considers the presence of multipath to complete the analysis of the positioning performance.

## 3.1 Signal model

As a first step to analyse the positioning performance of LTE, we present the signal model to be used in this study. The downlink transmission of the LTE standard is based on the OFDM modulation. The OFDM transmission and reception scheme is shown in Figure

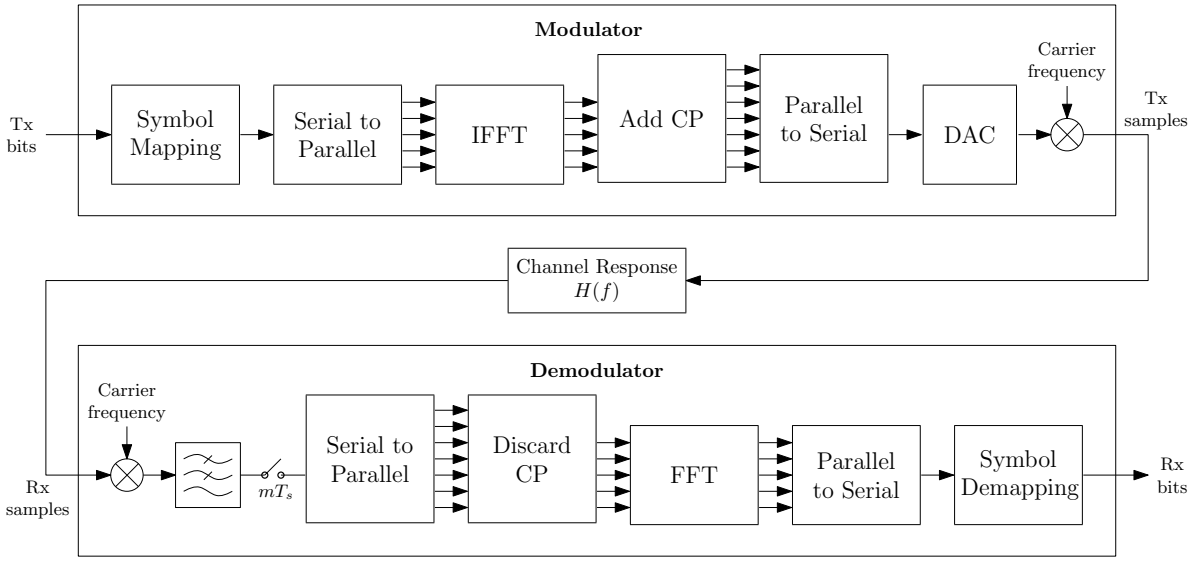


Figure 3.1: OFDM transmission/reception block diagram.

3.1. Let us define the OFDM complex-valued baseband signal for one OFDM symbol as

$$x_{\mathrm{c}}(t) = \sqrt{\frac{2C}{N}} \sum_{n=0}^{N-1} b(n) \cdot \exp\left(j \frac{2\pi n t}{T}\right), \tag{3.1.1}$$

where $C$ is the power of the band-pass signal, $N$ is the total number of subcarriers, $b(n)$ is the complex-valued symbol transmitted at the $n$-th subcarrier, and $T$ is the OFDM symbol period. The symbol $b(n)$ is defined by $b(n) = d(n) \cdot p(n)$, being $d(n)$ the data or pilot symbol assigned with a relative power weight $p(n)^2$, which is constrained by $\sum_{n=0}^{N-1} p(n)^2 = N$. The symbol period $T$ is defined according to the subcarrier spacing as $T = 1/F_{\mathrm{sc}}$.

Assuming the successful removal of the cyclic prefix and perfect carrier-frequency synchronisation, the baseband received signal is

$$y_{\mathrm{c}}(t) = x_{\mathrm{c}}(t) \circledast h_{\mathrm{c}}(t) + n_{\mathrm{c}}(t), \tag{3.1.2}$$

where $\circledast$ is the circular convolution operation (due to circular effect introduced by the cyclic prefix), $h_{\mathrm{c}}(t)$ is an unknown channel impulse response (CIR), and the additive white Gaussian noise (AWGN) $n_{\mathrm{c}}(t)$ is statistically uncorrelated with $n_{\mathrm{c}}(t) \sim \mathcal{N}(0, \sigma_{\mathrm{n}}^2)$. If the LTE receiver applies a sampling frequency $F_{\mathrm{s}}$, defined by the sampling period

$T_\mathrm{s} = 1/F_\mathrm{s} = T/N$, the discrete-time signal model is

$$x\left(m\right) \doteq x_\mathrm{c}\left(mT_\mathrm{s}\right) = \sqrt{\frac{2C}{N}} \sum_{n=0}^{N-1} b\left(n\right) \exp\left(j\frac{2\pi nm}{N}\right), \tag{3.1.3}$$

and the discrete received signal is $y\left(m\right) \doteq y_\mathrm{c}\left(mT_\mathrm{s}\right)$ for $m = 0, 1, \ldots, N-1$ (thanks to the circular convolution of $N$ samples), whereas the discrete CIR is $h\left(m\right) \doteq h_\mathrm{c}\left(mT_\mathrm{s}\right)$. After applying an $N$-point discrete Fourier transform (DFT) to $y\left(m\right)$, we have

$$r\left(n\right) = \sqrt{2C} \cdot b\left(n\right) \cdot H\left(n\right) + w\left(n\right), \tag{3.1.4}$$

where $n$ is the index of the subcarriers, $H\left(n\right) = \mathcal{F}\left\{h\left(m\right)\right\}$ is the channel frequency response, being $\mathcal{F}\left\{\cdot\right\}$ the discrete Fourier transform operator, and $w\left(n\right)$ are the noise frequency samples, which are statistically uncorrelated with $w\left(n\right) \sim \mathcal{N}\left(0, \sigma_\mathrm{w}^2\right)$.

## 3.2 Time-delay estimation for the AWGN channel

The performance of the time-delay estimation is first assessed considering the impact of the AWGN channel only. Thus, let us define the propagation channel model as

$$h_\mathrm{c}\left(t\right) = h_0 \cdot \delta\left(t - t_\epsilon\right), \tag{3.2.1}$$

where $h_0$ is the complex channel coefficient, $\delta\left(t\right)$ is the Dirac delta, and $t_\epsilon$ is the time delay introduced by the channel. Using a bandlimited representation for the channel, the discrete CIR of this model is

$$h\left(m\right) = h_0 \cdot \mathrm{sinc}\left(m - \tau\right), \tag{3.2.2}$$

where $\mathrm{sinc}\left(x\right) \doteq \frac{\sin(\pi \cdot x)}{\pi \cdot x}$ is the sinc function, and $\tau \doteq t_\epsilon/T_\mathrm{s}$ is the discrete-time symbol-timing error, which is the time delay to estimate for positioning purposes. For sake of simplicity, and without loss of generality, the channel coefficient $h_0$ is assumed equal to one.

### 3.2.1 Maximum likelihood estimation

The maximum likelihood estimation (MLE) of the time delay in AWGN channels is based on the matched filter, being widely studied in the literature, such as in [Kay98, p.192].

Considering a pilot signal, the MLE is based on the maximization of the correlation between the received signal and the transmitted pilots (i.e. the matched filter in this case), resulting in the time-delay estimation

$$\tau = \arg\max_{\tau} \left\{ \left| R_{\mathrm{yx}}(\tau) \right|^2 \right\}, \tag{3.2.3}$$

where $R_{\mathrm{yx}}(\tau)$ is the correlation function. Since the cyclic prefix introduces a circular symmetry in the signal at the output of the channel, the correlation between the received signal and the pilots is a circular correlation, which is defined as

$$R_{\mathrm{yx}}(\tau) \doteq \sum_{m=0}^{N-1} y(m) \cdot x_{\mathrm{s}}^{*}(m-\tau), \tag{3.2.4}$$

where $x_{\mathrm{s}}^{*}(m)$ is a circular shifted and conjugate version of the original $x(m)$. This operation results in the matched filter of the received signal. The MLE can be efficiently implemented by using the FFT operation, as it is shown in Figure 3.2. This implementation is typically adopted for the bi-dimensional search of time-delay and carrier-frequency errors in GNSS receivers [Bor07, p.79].

As it has been described in (3.2.3), the MLE is obtained by measuring the time delay corresponding to the maximum of the correlation function of (3.2.4), or correlation peak. Let us analyse the correlation function by considering only the transmitted signal, resulting on the auto-correlation function (ACF) of the discrete signal $x(m)$, defined as

$$R_{\mathrm{xx}}(\tau) \doteq \sum_{m=0}^{N-1} x(m) \cdot x_{\mathrm{s}}^{*}(m-\tau). \tag{3.2.5}$$

Assuming an equipowered data and pilot structure, i.e. power is uniformly distributed among all the subcarriers, the relative power weight at the $n$-th subcarrier is $p(n) =$

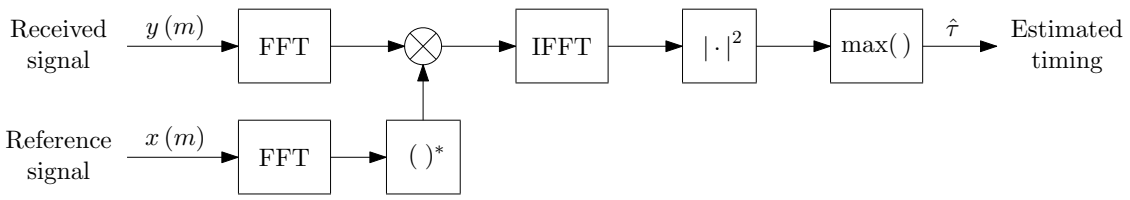


Figure 3.2: FFT implementation of the correlation at the receiver.

$\sqrt{1/N}$. Thus, the circular auto-correlation of (3.2.5) results in

$$R_{\mathrm{xx}}(\tau) = \frac{2C}{N}\sum_{n=0}^{N-1} b(n)\cdot b^{*}(n)\cdot \exp\left(j\frac{2\pi n\tau}{N}\right) = \frac{2C}{N^{2}}\sum_{n=0}^{N-1}\exp\left(j\frac{2\pi n\tau}{N}\right), \tag{3.2.6}$$

where $d(n)\cdot d^{*}(n) = 1$. Let us consider the allocation of LTE pilot signals, which defines the following subcarriers allocation sets:

- Synchronisation signals:

$$\mathcal{N}_{\mathrm{SS}} = \{-31,-30,\ldots,-2,-1,1,2,\ldots,30,31\}, \tag{3.2.7}$$

- Reference signals:

$$\mathcal{N}_{\mathrm{RS}} = \{-N_{\mathrm{RB}}\cdot(\lambda_{\mathrm{RS}}+1), N_{\mathrm{RB}}\cdot\lambda_{\mathrm{RS}}+1\} + \theta_{\mathrm{RS}}, \tag{3.2.8}$$

  where $N_{\mathrm{RB}}$ is the number of resource blocks, i.e. $N_{\mathrm{RB}} = \{6,15,25,50,75,100\}$, the vector of indexes is $\lambda_{\mathrm{RS}} = [0,1,\ldots,N_{\mathrm{RB}}-1]$, and $\theta_{\mathrm{RS}}$ is the subcarrier shift, i.e. $\theta_{\mathrm{RS}} = \{0,1,3,4,5\}$.

The number of subcarriers equivalent to the effective bandwidth, i.e. bandwidth occupied by the active subcarriers, when only transmitting the synchronisation signals is $N_{\mathrm{SS}} = 63$, and when only transmitting the reference signals is $N_{\mathrm{RS}} = 12\cdot N_{\mathrm{RB}} - 4$. Thus, the circular auto-correlation function of the synchronisation signals results in

$$R_{\mathrm{xx,SS}}(\tau) = \frac{2C}{{N_{\mathrm{SS}}}^{2}}\sum_{n\in\mathcal{N}_{\mathrm{SS}}} e^{j2\pi n\tau/N_{\mathrm{SS}}} = \frac{2C}{{N_{\mathrm{SS}}}^{2}}\left(\sum_{n=1}^{31} e^{j2\pi n\tau/N_{\mathrm{SS}}} + \sum_{n=1}^{31} e^{-j2\pi n\tau/N_{\mathrm{SS}}}\right), \tag{3.2.9}$$

where the geometric progression, i.e. $\sum_{n=m}^{N} r^{n} = \dfrac{r^{m}-r^{N+1}}{1-r}$ for $m < N$, is expressed as

$$\begin{aligned}\sum_{n=m}^{N} e^{j2\pi n\tau/N} &= \frac{e^{j2\pi m\tau/N} - e^{j2\pi(N+1)\tau/N}}{1-e^{j2\pi\tau/N}} = \frac{e^{j2\pi m\tau/N}\cdot\left(1-e^{j2\pi(N+1-m)\tau/N}\right)}{e^{j\pi\tau/N}\cdot\left(e^{-j\pi\tau/N}-e^{j\pi\tau/N}\right)} = \\ &= \frac{e^{j2\pi m\tau/N}e^{j\pi(N+1-m)\tau/N}\cdot\left(e^{-j\pi(N+1-m)\tau/N}-e^{j\pi(N+1-m)\tau/N}\right)}{e^{j\pi\tau/N}\cdot\left(e^{-j\pi\tau/N}-e^{j\pi\tau/N}\right)} = \\ &= e^{j\pi(N+m)\tau/N}\cdot\frac{\sin\left(\pi\left(N+1-m\right)\tau/N\right)}{\sin\left(\pi\tau/N\right)}.\end{aligned} \tag{3.2.10}$$

Substituting (3.2.10) in (3.2.9), we obtain

$$R_{\mathrm{xx,SS}}(\tau) = \frac{2C}{{N_{\mathrm{SS}}}^2} \cdot \left(e^{j\pi 32\tau/N_{\mathrm{SS}}} + e^{-j\pi 32\tau/N_{\mathrm{SS}}}\right) \cdot \frac{\sin(\pi 31\tau/N_{\mathrm{SS}})}{\sin(\pi\tau/N_{\mathrm{SS}})} = \\ = \frac{4C}{{N_{\mathrm{SS}}}^2} \cdot \cos(\pi 32\tau/N_{\mathrm{SS}}) \cdot \mathrm{sinc_d}(31; \tau/N_{\mathrm{SS}}), \tag{3.2.11}$$

where $\mathrm{sinc_d}(N; x) \doteq \frac{\sin(\pi \cdot N \cdot x)}{\sin(\pi \cdot x)}$ is the discrete sinc function, which is a periodic function, unlike the traditional sinc function, and corresponds to the Fourier transform of a rectangular pulse of $N$ samples when $x = f$, being $f$ the frequency. Following the same procedure, the ACF of the reference signals can be obtained as

$$R_{\mathrm{xx,RS}}(\tau) = \frac{2C}{{N_{\mathrm{RS}}}^2} \sum_{n \in \mathcal{N}_{\mathrm{RS}}} e^{j2\pi n\tau/N_{\mathrm{RS}}} = \\ = \frac{2C}{{N_{\mathrm{RS}}}^2} \cdot e^{j2\pi\theta\tau/N_{\mathrm{RS}}} \cdot \left(\sum_{n=1}^{N_{\mathrm{RB}}} e^{-j2\pi 6n\tau/N_{\mathrm{RS}}} + \sum_{n=0}^{N_{\mathrm{RB}}-1} e^{j2\pi(6n+1)\tau/N_{\mathrm{RS}}}\right), \tag{3.2.12}$$

where

$$\sum_{n=1}^{N_{\mathrm{RB}}} e^{-j2\pi 6n\tau/N_{\mathrm{RS}}} = \frac{e^{-j2\pi 6\tau/N_{\mathrm{RS}}} - e^{-j2\pi 6(N_{\mathrm{RB}}+1)\tau/N_{\mathrm{RS}}}}{1 - e^{-j2\pi 6\tau/N_{\mathrm{RS}}}} = \\ = e^{-j\pi 6(N_{\mathrm{RB}}+1)\tau/N_{\mathrm{RS}}} \cdot \mathrm{sinc_d}(N_{\mathrm{RB}}; 6\tau/N_{\mathrm{RS}}), \tag{3.2.13}$$

and

$$\sum_{n=0}^{N_{\mathrm{RB}}-1} e^{j2\pi(6n+1)\tau/N_{\mathrm{RS}}} = \frac{e^{j2\pi\tau/N_{\mathrm{RS}}} - e^{j2\pi(6N_{\mathrm{RB}}+1)\tau/N_{\mathrm{RS}}}}{1 - e^{j2\pi 6\tau/N_{\mathrm{RS}}}} = \\ = e^{j\pi(6N_{\mathrm{RB}}-4)\tau/N_{\mathrm{RS}}} \cdot \mathrm{sinc_d}(N_{\mathrm{RB}}; 6\tau/N_{\mathrm{RS}}). \tag{3.2.14}$$

Substituting (3.2.13) and (3.2.14) in (3.2.12), we obtain

$$R_{\mathrm{xx,RS}}(\tau) = \frac{2C}{{N_{\mathrm{RS}}}^2} \cdot e^{j2\pi\theta\tau/N_{\mathrm{RS}}} \cdot \left(e^{j\pi(6N_{\mathrm{RB}}-4)\tau/N_{\mathrm{RS}}} + e^{-j\pi 6(N_{\mathrm{RB}}+1)\tau/N_{\mathrm{RS}}}\right) \cdot \\ \cdot \mathrm{sinc_d}(N_{\mathrm{RB}}; 6\tau/N_{\mathrm{RS}}) = \\ = \frac{4C}{{N_{\mathrm{RS}}}^2} \cdot e^{j(5+2\theta)\pi\tau/N_{\mathrm{RS}}} \cdot \cos(\pi(6N_{\mathrm{RB}}+1)\tau/N_{\mathrm{RS}}) \cdot \\ \cdot \mathrm{sinc_d}(N_{\mathrm{RB}}; 6\tau/N_{\mathrm{RS}}). \tag{3.2.15}$$

From (3.2.11) and (3.2.15), the ACF is described by the number and distribution of the

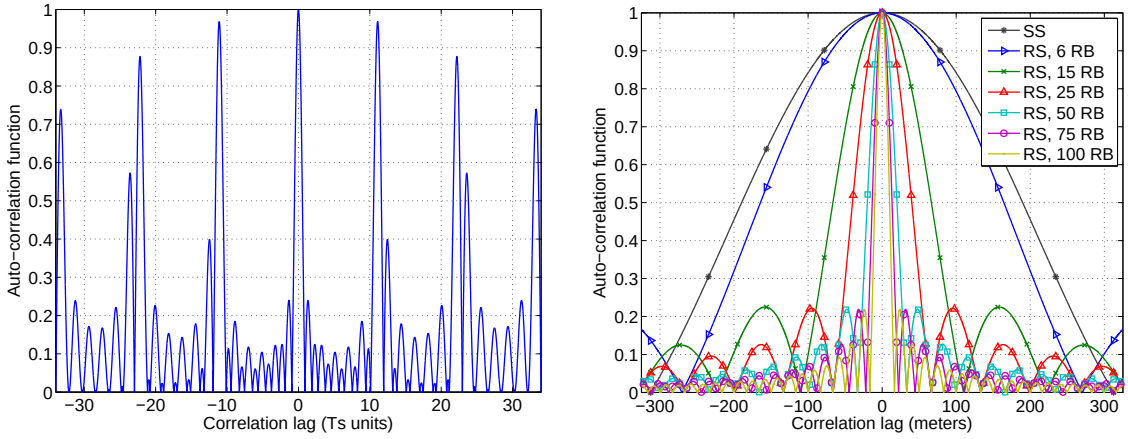


(a) ACF of the 6-RB RS, $T_{\mathrm{s}} = 66.67$ µs

(b) ACF of the SS and RS

Figure 3.3: Auto-correlation function of the LTE synchronization signals and reference signals for the different signal bandwidths.

pilots subcarriers. Focusing on the reference signals, the equispacing between pilot subcarriers mainly determines the ACF. For instance, the spacing of six subcarriers introduces a multiplicative factor of six in the discrete sinc of (3.2.15). This factor introduces periodic peaks on the ACF, approximately around $\tau = 2k \cdot N_{RB}$ for $k \in \mathbb{Z}$, as it is shown in Figure 3.3(a). The equispaced pilots of the reference signal also affect the zeros of the ACF, as it can be seen by finding the values of $\tau$ that make the cosine and the discrete sinc of (3.2.15) equal to zero:

$$\left.\begin{aligned} \tau &= \frac{k \cdot N_{\mathrm{RS}}}{2 \cdot (6N_{\mathrm{RB}} + 1)} \qquad \text{for } k = 2\ell + 1, \text{ and } \ell \in \mathbb{Z}_{\neq 0} \\ \tau &= \frac{k \cdot N_{\mathrm{RS}}}{6N_{\mathrm{RB}}} \qquad \text{for } k \in \mathbb{Z}_{\neq 0} \end{aligned}\right\} \Longrightarrow R_{\mathrm{xx,RS}}(\tau) = 0. \tag{3.2.16}$$

Moreover, any variation on the uniform pattern (i.e. contiguous or equispaced) modifies the ACF, as it is produced by the avoidance of the DC subcarrier that adds the cosine term in (3.2.11) and (3.2.15). However, a shift of the subcarrier allocation, such as the term $\theta_{\mathrm{RS}}$ in the reference signals, only adds a phase shift in the ACF. In Figure 3.3(b), the ACF $R_{\mathrm{xx}}(\tau)$ is shown for the SS and the RS with different LTE bandwidth configurations using only one OFDM symbol. As it can be noticed, the RS-bandwidth is denoted according to the number of resource blocks allocated in the frequency domain (i.e. 180 kHz per RB). As it could be expected from (3.2.16), the main lobe of the ACF is narrower as the bandwidth increases.

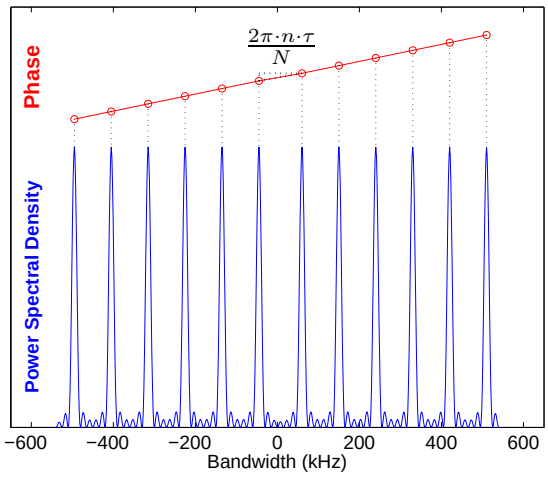


Figure 3.4: Time delay in the frequency domain.

### 3.2.2 Adaptation of Fitz estimator

Mobile devices are every day more powerful. However, and despite the low complexity of the matched filter, some mass-market receivers may require even lower computational burden. This can be achieved with approximations of the MLE that result in a near-ML performance. For instance, if we take advantage of the time-delay property of the Fourier transform, $\mathcal{F}\{x(m \pm \tau)\} = X(n)\, e^{\pm j2\pi n\tau/N}$, the time delay can be entirely estimated in the frequency domain, as it is depicted in Figure 3.4. Thus, the time-delay estimation becomes a frequency-like estimation problem, and well-known ML and near-ML frequency estimators can be adopted for time-delay estimation after the FFT operation. Examples of low-complexity open-loop carrier-frequency estimators are proposed by Kay [Kay89], Fitz [Fit91], Luise and Reggiannini (L&R) [Lui95], and Xiao et al. [Xia04]. Our interest is not focused on the analysis of the performance and complexity among them or other carrier frequency-estimators, this can be found in [Men97, Section 3.2] or [Mor98], but on their feasibility for a low-complexity application. For this purpose, Fitz estimator is adopted as an example.

As it is described in [Fit91], the Fitz estimator is an approximation of the ML estimator of the frequency of a sinusoid in white noise, which is the maximum of the periodogram [Kay89]. From the likelihood function derivation, a practical estimator can be found with the unnormalized auto-correlation function, being its mathematical derivation in [Fit91]. Nevertheless, the distribution of pilots is scattered over the spectrum, and only few samples of the FFT-output signal can be used. Thus, the application of the Fitz estimator requires a modification on the summation indexes. Let us express the received signal correlated with the pilot subcarriers in the frequency domain, and in absence of

frequency and phase offsets, as

$$s\left(n\right)=\mathcal{F}\left\{y\left(m\right)\right\}\cdot b^{*}\left(n\right)=e^{j2\pi n\tau/N}+w'\left(n\right), \tag{3.2.17}$$

where $w'\left(n\right)$ is the frequency noise contribution at the $n$-th subcarrier. Then, the modified auto-correlation function is described as

$$R'_{\mathrm{xx}}\left(\ell\right)=\sum_{n\in\mathcal{A}_0}s\left(n\right)\cdot s^{*}\left(n-\ell\right), \tag{3.2.18}$$

where the subset of available pilot subcarriers $n$ for correlation lag $\ell$ is expressed as $\mathcal{A}_0=\{z\in\mathbb{N}|z,(z-\ell)\in\mathcal{N}_{\mathrm{a}}\}$, which results in $R\left(\ell\right)=e^{j2\pi\tau\ell/N}+w''\left(\ell\right)$, being $w''\left(\ell\right)$ the noise contribution. The indexes of the $N_{\mathrm{a}}$ available pilot subcarriers are denoted in the subset $\mathcal{N}_{\mathrm{a}}$. Then, the adaptation of Fitz estimator for time-delay estimation using the LTE PRS is expressed as

$$\tau=\cdot\frac{\sum_{\ell\in\mathcal{A}_1,}\arg\left\{R\left(\ell\right)\right\}}{\sum_{\ell\in\mathcal{A}_1}\ell}, \tag{3.2.19}$$

where the subset of correlation lags for the PRS pilot distribution is $\mathcal{A}_1=(\mathcal{A}_2\cup\mathcal{A}_3)\cap\mathcal{A}_4$, defined by

$$\mathcal{A}_2=\{z\in\mathbb{N}\mid z=6i \qquad i=1,\ldots,N_{\mathrm{a}}/2-1\}, \tag{3.2.20}$$

$$\mathcal{A}_3=\{z\in\mathbb{N}\mid z=6i+1 \qquad i=1,\ldots,N_{\mathrm{a}}-1\}, \tag{3.2.21}$$

$$\mathcal{A}_4=\{z\in\mathbb{N}\mid z\leq M \qquad M\leq N-1\}. \tag{3.2.22}$$

The value $M$ limits the number of lags, e.g. resulting in

$$\sum_{\ell\in\mathcal{A}_1}\ell=\begin{cases}6 & \text{if } M=6,\\ \left(3N_{\mathrm{a}}^{2}-5N_{\mathrm{a}}-2\right)/2 & \text{if } M=N/2,\\ N_{\mathrm{a}}\left(15N_{\mathrm{a}}-14\right)/4-1 & \text{if } M=N.\end{cases} \tag{3.2.23}$$

### 3.2.3 Cramér-Rao bound

The Cramér-Rao bound is a well-known lower bound that describes the maximum achievable accuracy of any unbiased estimator for a moderate to high signal-to-noise ratio (SNR). Since the time delay is estimated with pilot sequences, the CRB can be easily computed. Thus, the CRB expression for TDE, $\tau$, applied to the LTE signal formats can be derived

from the general definition given by [Kay98],

$$\mathrm{var}\,(\tau) \geq \mathrm{CRB}(\tau) = \frac{1}{\dfrac{E_\mathrm{s}}{N_0/2} \cdot \bar{F}^2}, \tag{3.2.24}$$

where $E_\mathrm{s} = C \cdot T$ and $\mathrm{SNR} = (C/N_0)/B$, being $C/N_0$ the carrier-to-noise-density ratio and $B$ the bandwidth of the signal. The mean square bandwidth or Gabor bandwidth of the OFDM signal in the frequency domain $X\,(f)$ is defined by

$$\bar{F}^2 \doteq \frac{\displaystyle\int_{-\infty}^{\infty} (2\pi f)^2 \cdot |X(f)|^2 \, df}{\displaystyle\int_{-\infty}^{\infty} |X(f)|^2 \, df}, \tag{3.2.25}$$

and can be approximated as follows,

$$\begin{aligned} \bar{F}^2 &\simeq \frac{\dfrac{1}{N} \displaystyle\sum_{n \in \mathcal{N}_\mathrm{a}} (2\pi n \cdot F_\mathrm{sc})^2 \cdot |X(n \cdot F_\mathrm{sc})|^2}{\dfrac{1}{N} \displaystyle\sum_{n \in \mathcal{N}_\mathrm{a}} |X(n \cdot F_\mathrm{sc})|^2} = \\ &= 4\pi^2 \frac{F_\mathrm{sc}^2}{N} \sum_{n \in \mathcal{N}_\mathrm{a}} p_n^2 \cdot n^2, \end{aligned} \tag{3.2.26}$$

by considering a rectangular PSD. Thus, disregarding the presence of CP, the CRB for TDE using LTE signal pilots, and in general any OFDM signal for one symbol, is

$$\mathrm{CRB}(\tau) = \frac{T^2}{8\pi^2 \cdot \mathrm{SNR} \cdot \displaystyle\sum_{n \in \mathcal{N}_\mathrm{a}} p_n^2 \cdot n^2}. \tag{3.2.27}$$

### 3.2.4 TDE performance assessment

The timing performance of a certain estimator can be evaluated by using the root-mean-square error, which is defined as

$$\mathrm{RMSE}(\tau) = \sqrt{\mathrm{E}\left[(\tau - \tau)^2\right]}, \tag{3.2.28}$$

and the bias, expressed as

$$\mathrm{b}(\tau) = \mathrm{E}\,[\tau] - \tau, \tag{3.2.29}$$

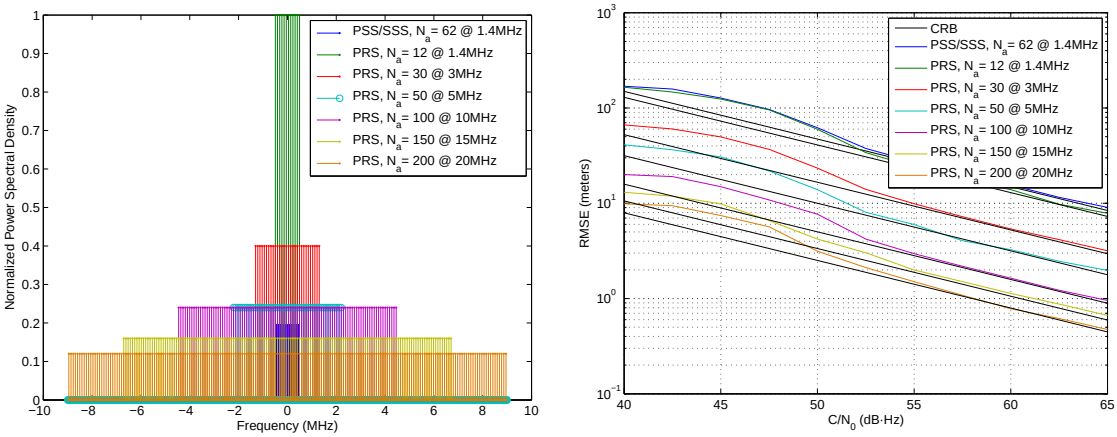


(a) Normalized PSD of LTE pilots

(b) ML for LTE signal bandwidths

Figure 3.5: Normalized PSD and corresponding RMSE of the MLE for the LTE pilot signals (i.e. PSS, SSS and PRS), considering only one OFDM symbol and the maximum BS power specified in TR 36.942 [3GP12b].

being $\mathrm{E}[\cdot]$ the expectation operator. For the case under study, the maximum likelihood estimation and the adaptation of the Fitz estimator are unbiased. Thus, only the RMSE is computed for the LTE pilot signals, considering the maximum transmission power. According to the standard in [3GP12b, Section 4.6], the maximum power of the BS is:

- 43 dBm for a bandwidth equal to or lower than 5 MHz, and
- 46 dBm for 10, 15 and 20 MHz bandwidth.

For this analysis, the pilot signals are transmitted only, thus the power is spread over all the active subcarriers by assuming an equipowered pilot structure, as it shown in Figure 3.5(a) with the normalized PSD of the LTE pilot signals for every bandwidth configuration. The resulting RMSE of the ML estimation, which is computed with 1000 Monte-carlo simulations, attains the CRB for TDE above a $C/N_0$ of 55 dB-Hz, as it shown in Figure 3.5(b). Considering the case of 12 PRS subcarriers distributed over 1.02 MHz, the RMSE is computed with 10000 Monte-carlo simulations for the matched filter (i.e. ML estimator) and the adaptation of Fitz estimator. As it can be seen in Figure 3.6, the Fitz estimator approximates the ML approach and attains the CRB when increasing the number of lags $M$ up to $N$. In addition, $M = N/2$ is not yet optimal in our application due to the scattered pilot subcarriers.

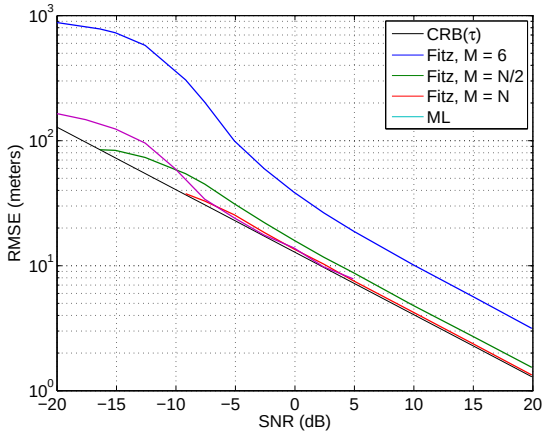


Figure 3.6: RMSE of the MLE and the Fitz estimator compared with CRB for TDE using a PRS of 1.02 MHz (i.e. $N = 68$) and only one OFDM symbol.

## 3.3 Impact of inter-cell interferences

The LTE localization performance can be deeply deteriorated due to the inter-cell interference among base stations transmitting in the same frequency band. In this section, the simulation of the LTE scenario is presented by using the PRS in an AWGN channel, and three main interference scenarios are identified. The base stations are assumed to be fully synchronised and no clock offsets are considered.

### 3.3.1 System simulation scenario

The LTE scenario is assumed to follow the typical layout of a cellular network. Thus, a hexagonal grid with three-sectorial base stations (i.e. 3-dB beamwidth of 65-degree) and inter-site distance (ISD) of 750 meters is created, as it is shown in Figure 3.7. This cell layout is complying with the coordinated macro cellular deployment specified in [3GP12b]. The simulation of this LTE scenario is implemented in MATLAB. The main consideration for the system simulation scenario is the signal-to-interference plus noise ratio (SINR), which is defined as the ratio of signal power to the combined noise and interference power,

$$\mathrm{SINR} = \frac{P_{\mathrm{signal}}}{P_{\mathrm{noise}} + P_{\mathrm{interference}}}, \tag{3.3.1}$$

where $P$ is the averaged power. In order to compute the SINR, the transmitter and macroscopic pathloss formulas specified in the standard are considered. The scenario simulation parameters are summarized in Table 3.1.

Table 3.1: Simulation parameters according to [3GP12b].

| Parameter | Characteristic/value |
|---|---|
| *System* | |
| Carrier frequency | 2 GHz |
| Bandwidth | 1.4, 3, 5, 10, 15 and 20 MHz |
| Cell layout | Hexagonal |
| Inter-site distance | 750 m |
| *Transmitter* | |
| Maximum BS power | 43 and 46 dBm |
| BS antenna model | 3 dB-beamwidth of 65-degree |
| BS antenna gain | 15 dBi |
| *Receiver* | |
| UE antenna model | Omnidirectional, 0 dBi |
| UE noise figure | 9 dB |
| Thermal noise density | -174 dBm/Hz |
| *Channel* | |
| Path loss model[1] | $128.1 + 37.6\log_{10}(R)$ dB |

[1] $R$ is the propagation distance in kilometres.

### Transmitter

According to the technical report (TR) 36.942 [3GP12b], the BS has a maximum power of 43 dBm and an antenna gain of 15 dBi transmitting at a carrier frequency of 2 GHz for a bandwidth equal to or lower than 5 MHz. The radiation pattern of the BS antenna is defined in [3GP12b, p.11] for each sector in 3-sector cell sites as

$$A(\theta) = -\min\left[12\left(\frac{\theta}{\theta_{3\text{dB}}}\right)^2, A_{\min}\right], \quad \text{for } -180 \leq \theta \leq 180, \tag{3.3.2}$$

where $\theta_{3\text{dB}}$ is the 3-dB beamwidth which corresponds to 65 degrees, and $A_{\min} = 20$ dB is the minimum attenuation, as it is shown in Figure 3.8(a).

### Macroscopic pathloss

Considering a carrier frequency of 2 GHz and a BS height of 15 meters above average rooftop level, the propagation model is based on a distance-dependent path loss model

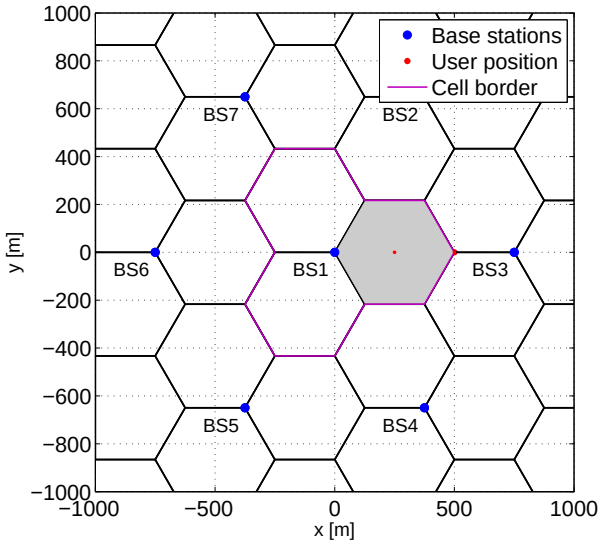


Figure 3.7: LTE simulation cell layout.

defined in [3GP12b, p.15] as

$$L = 128.1 + 37.6 \log_{10}(R), \tag{3.3.3}$$

where $R$ is the distance between the BS and the UE in kilometres. For sake of simplicity, shadowing effect is not added in (3.3.3). The resulting macroscopic losses for a certain cell are shown in Figure 3.8(b).

### SINR calculation

The signal power received from a BS $i$ is expressed in [3GP12b, p.14] as

$$P_{\mathrm{rx},i} = P_{\mathrm{tx},i} - \max\left(L_i - G_{\mathrm{tx},i} - G_{\mathrm{rx},i}, \mathrm{MCL}\right), \tag{3.3.4}$$

where $P_{\mathrm{tx},i}$ is the transmitted signal power, $L_i$ is the macroscopic pathloss, $G_{\mathrm{tx},i}$ is the transmitter antenna gain, $G_{\mathrm{rx},i}$ is the receiver antenna gain and MCL is the minimum coupling loss (MCL), defined as the minimum path loss between UE and BS antenna connectors. The receiver noise floor is defined as

$$N_{\mathrm{rx}} = 10 \cdot \log_{10}(k_{\mathrm{B}} \cdot T_{\mathrm{N}} \cdot B) + \mathrm{NF} = N_0 + 10 \cdot \log_{10}(B) + \mathrm{NF}, \tag{3.3.5}$$

where $k_{\mathrm{B}}$ is the Boltzmann constant ($1.381 \times 10^{23}$ J/K, Joules per Kelvin), $T_{\mathrm{N}}$ is the noise temperature (K), which results in the noise spectral density $N_0$ (dBm/Hz), $B$ is

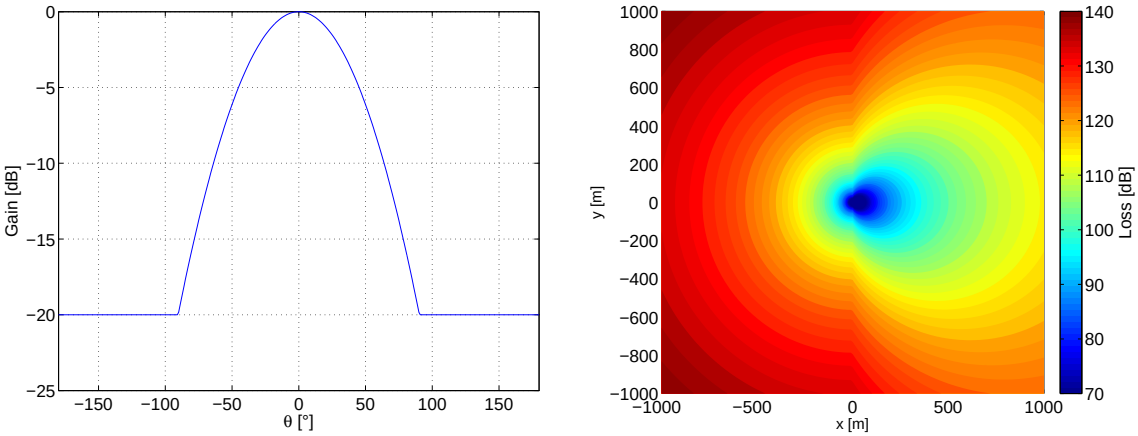


(a) Antenna pattern for 3-sector cells.

(b) Macroscopic pathloss for only one sector.

Figure 3.8: Antenna pattern and macroscopic pathloss.

the system bandwidth, and NF denotes the UE noise figure. Thus, the SINR can be calculated with the resulting expression

$$\boxed{\text{SINR} = \frac{P_{\text{rx},i}}{\sum_{j \neq i} P_{\text{rx},j} + N_{\text{rx}}},} \tag{3.3.6}$$

where $P_{\text{rx},j}$ is the received power from other antenna sectors, which causes the interference. Similar power budget calculations can be found implemented in MATLAB-based simulators, such as in [Meh11].

### 3.3.2 Non-coordinated network

The inter-cell interference is produced due to the single-frequency transmission of the neighbour base stations, as it may be planned in cellular networks for spectral efficiency. The received signal from neighbour cells is heavily masked by the strong signal of the serving cell, leading to the so-called near-far effect. Since the network provider decides if data is transmitted during positioning occasions, the PRS pattern can be used inefficiently by interfering the PRS pilots with data of neighbour cells, resulting on a non-coordinated network from the positioning point of view. Our analysis is based on the PRS over 6 RB, i.e. 12 pilot subcarriers scattered over 1.08 MHz, and using only one OFDM symbol.

This LTE interference scenario is implemented by means of a MATLAB simulator. Then, the SINR is computed with (3.3.6) in an AWGN channel. As it is shown in Figure 3.9(a) for BS 1 and in Figure 3.9(b) for BS 2, the SINR drastically decreases near the neighbour base stations, which shows the near-far effect produced by the serving BS.

Considering an UE location $\mathbf{x} = (250, 0)^T$ in meters, the SINR of the serving BS (i.e. BS 1) is approximately 10 dB, while the SINR of the neighbour BSs is equal to -17.3 dB, as it is shown in Figure 3.9(a) and 3.9(b). For the later case, the time-delay estimator is almost saturated according to Figure 3.6, producing a significant deterioration on the position accuracy.

### 3.3.3 Interference cancellation

In order to reduce the interference impact, the LTE research community is investigating on inter-cell interference coordination techniques to increase data transmission performance at critical positions of the cell layout, such as at the cell edge. An overview of these techniques can be found in [Bou09], where the interference cancellation (IC) technique can be highlighted for 4G in general. The IC technique is based on reconstructing the signal from the strongest BS and subtracting it from the received signal, in order to obtain a superposition of the signals from the weaker base stations. Thus, we approximate the resulting SINR as

$$\text{SINR} = \frac{P_{\text{rx},i}}{\sum_{\substack{j \neq i \\ j \neq m}} P_{\text{rx},j} + N_{\text{rx}}}, \tag{3.3.7}$$

where $P_{\text{rx},m}$ is the received power from the strongest BS. Supposing the IC technique is ideal (e.g. over the PRS), the SINR obtained for BS 1 and BS 2 have increased with respect to the non-coordinated scenario, as it is shown in Figure 3.9(c) and Figure 3.9(d). For instance, with an UE at $\mathbf{x} = (250, 0)^T$ in meters, the SINR of BS 1 slightly increases to 10.9 dB, and the SINR of BS 2 is improves to -4.8 dB. In the later case, the SINR level of -4.8 dB is at the threshold of attaining the CRB of the time delay using the MLE, as it was shown in Figure 3.6.

In [Men09], the IC technique is also applied for positioning, obtaining results that improve the accuracy performance in interference scenarios. Nevertheless, errors on the demodulation of the strongest BS signal may deteriorate the cancellation or even increase the interference. This is avoided when the interference source is a pilot signal (i.e. PSS, SSS or CRS) because the demodulation process is not necessary, as it is studied in [Zhu11, Zhu12].

### 3.3.4 Coordinated network

In general, a coordinated network is defined by the avoidance of data transmission from multiple base stations in the same frequency/slot, thus definitely reducing the interfer-

ences. The PRS characteristics are flexible enough in the LTE standard to create a coordinated network, by assuming no transmission of data on the PRS subframe. Particularly, the surrounding base stations have to transmit the corresponding PRS pattern during the same positioning occasion, and have to avoid the data transmission on the PRS bandwidth. This coordinated scheme is completed by providing assistance data to the user. Although this coordinated scheme comes at the expense of decreasing the spectral efficiency, the interference avoidance is such that the SINR may be considered equal to the SNR, as is shown in Figure 3.9(e) and Figure 3.9(f). For instance, SINR values above 40 dB can be found from both BS 1 and BS 2 at the UE location $\mathbf{x} = (250, 0)^T$ in meters. At these SINR levels, the MLE attains the CRB for TDE.

The wording of coordinated network is used in this work to characterize the scenario where the network is synchronised and coordinated. In the 3GPP consortium, this coordination is referred by the so-called low-interference subframes (LIS). The LIS were inherited from the OTDoA positioning proposals in UMTS. The LIS concept is hidden on the design of the non-overlapping pattern of the positioning reference signal, introduced in Release 9 of LTE. In addition, in LTE-Advanced (Release 10 and beyond), the concept of the coordinated transmissions and precoding between multiple BSs is introduced for inter-cell interference mitigation. This is referred as active interference avoidance or as coordinated multi-point (CoMP) transmission or reception, and it can also be used for positioning, as it is discussed in Chapter 15.1 of [Mar11].

### 3.3.5 Other possible scenarios

The previous scenarios have been considered to study the general interference cases of LTE, but other possible scenarios can be found. We have studied a synchronous LTE network in the coordinated case, where there is no overlapping among PRS of different BSs due they frequency shifts among PRS patterns (controlled by BS cell ID). However, the network might be asynchronous, thus the loss of orthogonality between received PRSs generates continuous interferences. This situation can also be reproduced when the time-difference measurements are obtained between different system or network providers, which are probably not synchronised among them. The study of this type of scenarios is out of the scope of this sections, thus it is left for future work.

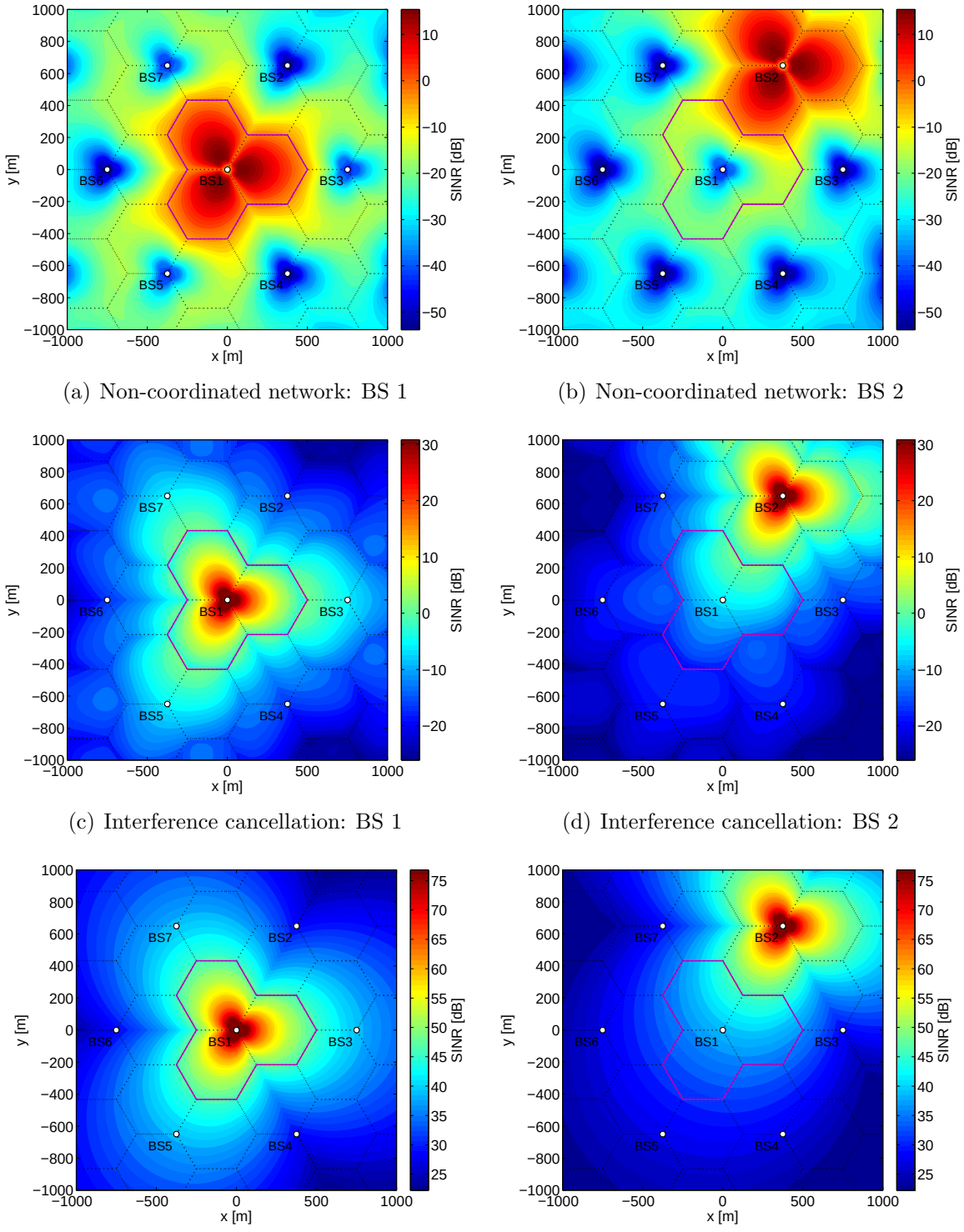


(a) Non-coordinated network: BS 1

(b) Non-coordinated network: BS 2

(c) Interference cancellation: BS 1

(d) Interference cancellation: BS 2

(e) Coordinated network: BS 1

(f) Coordinated network: BS 2

Figure 3.9: SINR of BS 1 and BS 2 computed for three general cases using a 6-RB PRS.

## 3.4 Impact of interferences on the OTDoA accuracy

Assuming the interferences to be Gaussian, the estimation of the user position, $\mathbf{x} = (x, y)^T$, can be assessed by means of the CRB for OTDoA localization. For this purpose, the $K$ most powerful base stations with respect to position $\mathbf{x}$ are considered, defining their locations by $\mathbf{x}_i = (x_i, y_i)^T$, where $i = 1, \ldots, K$. The range between these base stations and the user is computed with the Euclidean distance of their positions as

$$d_i = |\mathbf{x} - \mathbf{x}_i| = \sqrt{(x - x_i)^2 + (y - y_i)^2}. \tag{3.4.1}$$

The OTDoA localization is computed by the difference of these range measurements. For this computation, the most powerful BS, whose location is $\mathbf{x}_1$, is considered the reference BS. Thus, assuming no clock offsets, the LTE network can estimate range differences as

$$\mathbf{d} = \mathbf{d} + \mathbf{n}, \quad \mathbf{n} \sim \mathcal{N}(0, \mathbf{R}), \tag{3.4.2}$$

where $\mathbf{d}$ is defined as the true range differences vector,

$$\mathbf{d} = |\mathbf{x} - \mathbf{x}_1| - |\mathbf{x} - \mathbf{x}_j|, \quad j = 2, \ldots, K, \tag{3.4.3}$$

and $\mathbf{n}$ is a noise vector assumed to be AWGN with constant covariance matrix $\mathbf{R}$,

$$\mathbf{R} = \begin{pmatrix} \sigma_1^2 + \sigma_2^2 & \sigma_1^2 & \cdots & \sigma_1^2 \\ \sigma_1^2 & \sigma_1^2 + \sigma_3^2 & \cdots & \sigma_1^2 \\ \vdots & \vdots & \ddots & \vdots \\ \sigma_1^2 & \sigma_1^2 & \cdots & \sigma_1^2 + \sigma_K^2 \end{pmatrix}, \tag{3.4.4}$$

being $\sigma_i$ the standard deviation, which is defined by the RMSE of the time delay for the signal transmitted from BS $i$. The general derivation of the CRB in AWGN channel can be found in [Kay98, p.47], and it is applied for TDoA in [Cha94, Kau11]. Although incurring in a penalty, as noted in [Kau11] and [Wan09], the covariance matrix $\mathbf{R}$ is approximated to be constant or non-dependent on the user position, thus the CRB for OTDoA localization results in

$$\mathrm{CRB}(\mathbf{x}) = \left(\mathbf{D}^T \mathbf{R}^{-1} \mathbf{D}\right)^{-1}, \tag{3.4.5}$$

where

$$\mathbf{D} = \begin{pmatrix} \frac{x-x_1}{d_1} - \frac{x-x_2}{d_2} & \frac{y-y_1}{d_1} - \frac{y-y_2}{d_2} \\ \frac{x-x_1}{d_1} - \frac{x-x_3}{d_3} & \frac{y-y_1}{d_1} - \frac{y-y_3}{d_3} \\ \vdots & \vdots \\ \frac{x-x_1}{d_1} - \frac{x-x_K}{d_K} & \frac{y-y_1}{d_1} - \frac{x-x_K}{d_K} \end{pmatrix}. \tag{3.4.6}$$

The position error in meters with respect to the true position $\mathbf{x}$ is finally computed as

$$\varepsilon_{\mathbf{x}} = \sqrt{\mathrm{tr}\left(\mathrm{CRB}(\mathbf{x})\right)}. \tag{3.4.7}$$

Using (3.4.7), the position error can be computed for every interference case studied in Section 3.3, and using the CRB for TDE in (3.2.27) with the SINR values, considering five base stations for OTDoA with 6-RB PRS. First, in a non-coordinated network, the position errors exceed 100 meters around the bases stations due to the near-far effect. At the cell edge, the mutual interference between BSs is lower, thus positions errors between 20 and 40 meters can be achieved, as it can be seen in Figure 3.10(a). Second, and assuming an ideal performance of the IC technique, the SINR obtained for BS 1, in Figure 3.9(c), results on a notable improvement of the position errors, which are shown in Figure 3.10(c) with values between 10 and 40 meters. Finally, considering the interference avoidance obtained by a coordinated network, the SINR is practically equal to the SNR, and the resulting position error is below 1 meter, as it is shown in Figure 3.10(e). Given a SNR of 57.5 dB and 46.1 dB at the center and the edge of the cell for BS 1, respectively, the corresponding $C/N_0$ is 117.5 dB-Hz and 106.2 dB-Hz for a 6-RB PRS bandwidth of 1.02 MHz. Thus, the position errors are obtained well below 1 meter, showing the maximum achievable accuracy of positioning reference signals for 6 RB during one symbol.

Nevertheless, the positioning results have been obtained assuming that a certain estimator can always attain the CRB for TDE. This assumption is not fulfilled for low and moderate SNR because the estimator is saturated due to noise. For instance, the Fitz estimator studied in Section 3.2.2 attains the CRB for values of SNR above -5 dB using a 6-RB PRS (i.e. 1.02 MHz of bandwidth), which corresponds to 55 dB-Hz of $C/N_0$. Thus, considering that the pseudorange estimation is not valid for signals received below -5 dB of SNR, we can obtain a realistic achievable accuracy with the LTE PRS, as it is shown for the different interference cases in Figure 3.10(b), 3.10(d) and 3.10(f). As a result, the accuracy obtained is practically the same, but the coverage of the position determination has been reduced. The areas of the layout painted in white refer to those points where the receiver is not able to compute the position, because there are not enough strong base stations available.

The position errors for the coordinated-network case can also be obtained for higher bandwidths than 1.4 MHz. Results obtained using the PRS for system bandwidths of 5 MHz, 10 MHz and 20 MHz are shown in Figure 3.11(b), 3.11(c) and 3.11(d), respectively. As it can be seen, the position errors are in the order of centimetres when increasing the bandwidth, avoiding interference and supposing no multipath impact. Some assumptions and concerns about these results of this section have to be remarked:

- perfect synchronization between base stations has been considered,
- maximum power transmitted has been assumed,
- interference cancellation technique is assumed ideal,
- impact of multipath channels is studied in the following section, and
- impact of shadowing is left as future work.

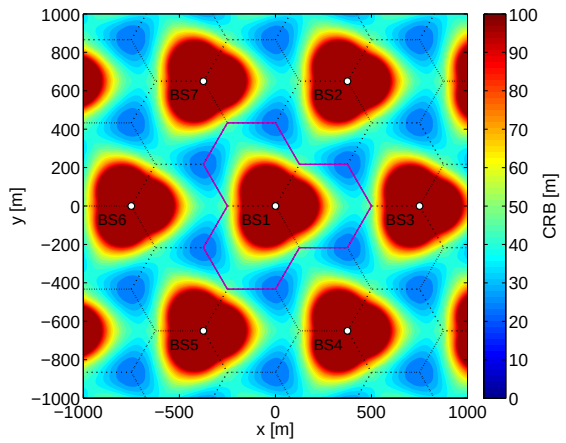


(a) Non-coordinated network: CRB for TDE

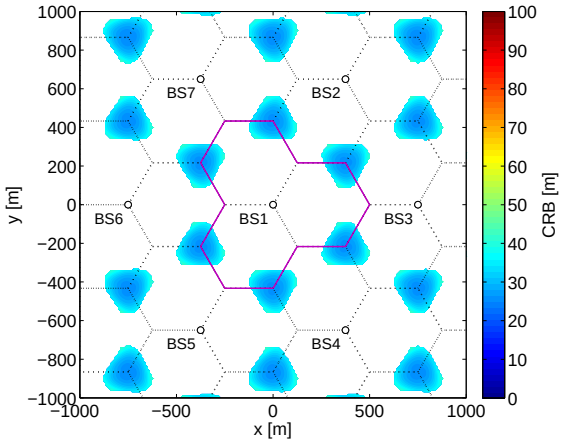


(b) Non-coordinated network: Fitz estimator

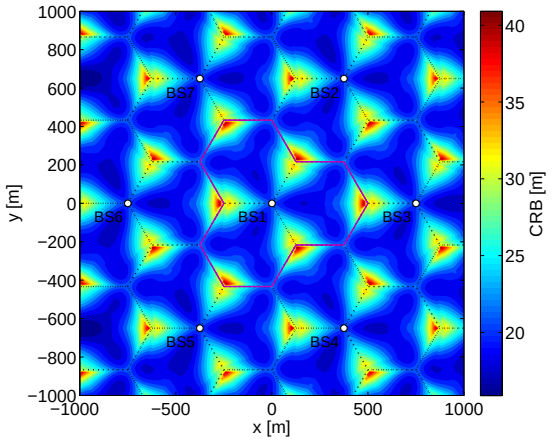


(c) Interference cancellation: CRB for TDE

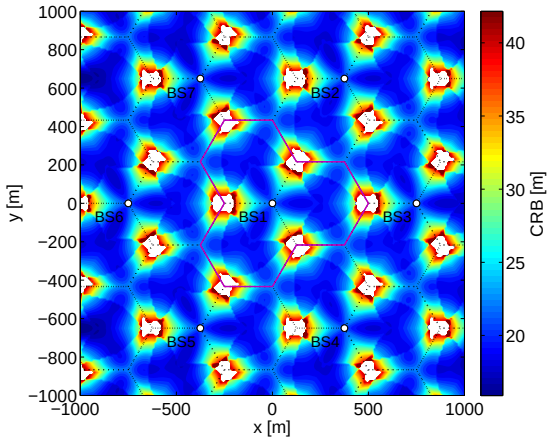


(d) Interference cancellation: Fitz estimator

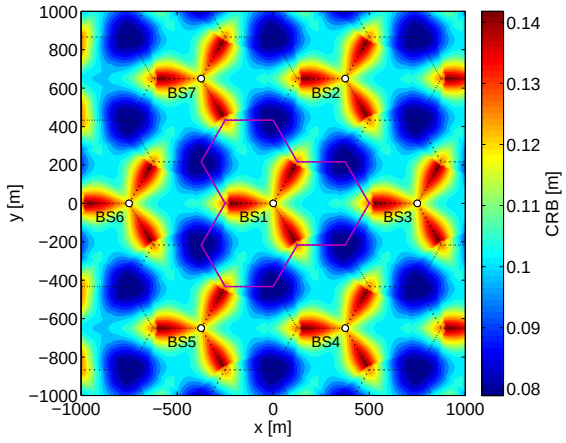


(e) Coordinated network: CRB for TDE

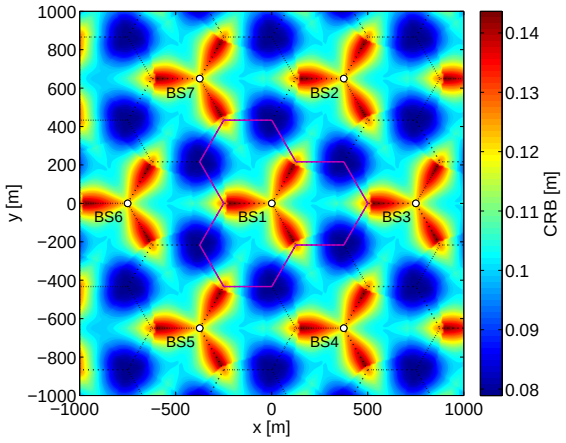


(f) Coordinated network: Fitz estimator

Figure 3.10: Position error maps computed with the CRB for OTDoA localization considering the CRB for TDE and Fitz estimator, using a 6-RB PRS (i.e. 1.02 MHz of bandwidth) transmitted by BS 1.

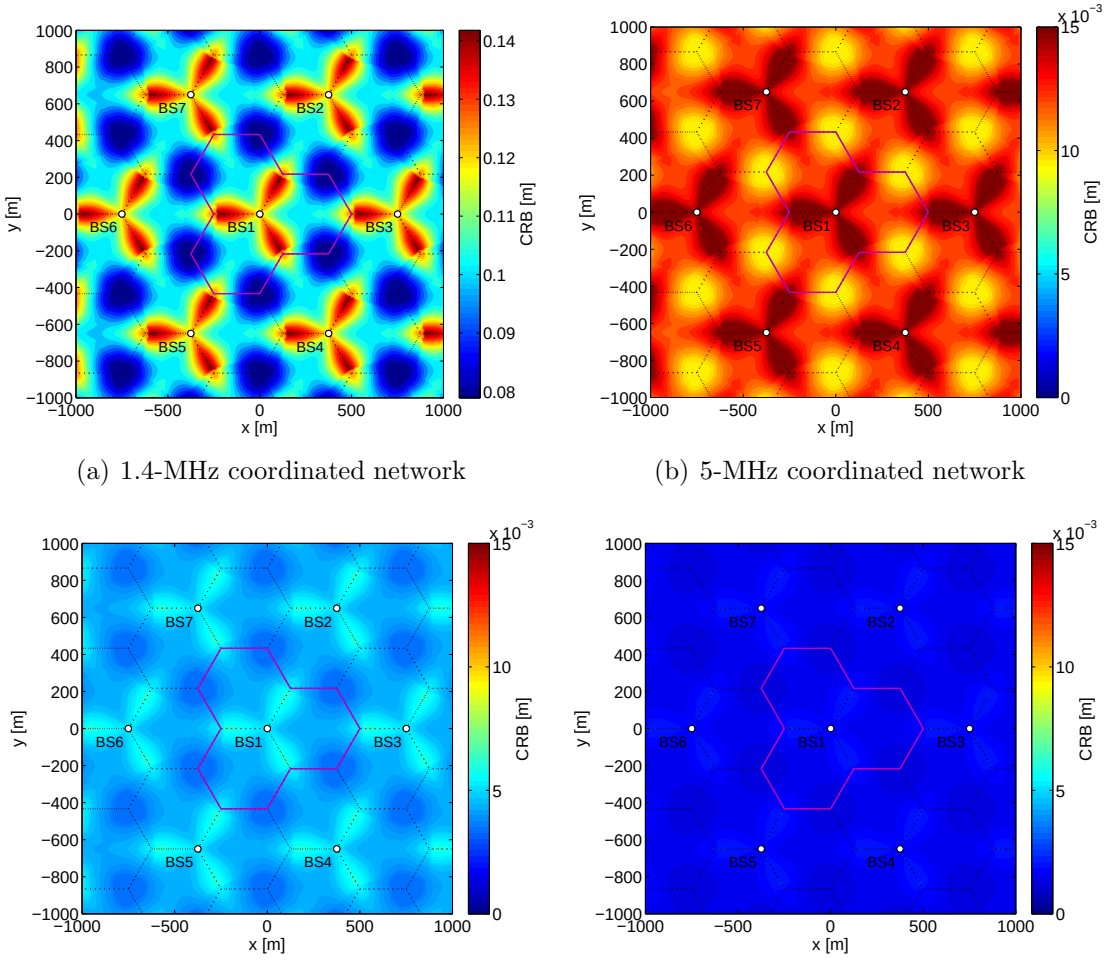


(a) 1.4-MHz coordinated network

(b) 5-MHz coordinated network

(c) 10-MHz coordinated network

(d) 20-MHz coordinated network

Figure 3.11: Position errors computed with the CRB for OTDoA localization on a coordinated network using signal bandwidths from 1.4 MHz to 20 MHz.

## 3.5 Impact of multipath on time-delay estimation

The results obtained in the previous sections have been computed for an AWGN channel, which is not realistic for a mobile communications scenario characterized by the presence of multipath. Thus, it is necessary to assess the performance of conventional estimators in this kind of environment. It can be already suggested that their performance will be poor, which will motivate later the proposal of specific estimators to consider the presence of multipath.

Propagation channel models are essential parts for simulation and testing of wireless transmission systems. The literature is extensive on this topic, and many standards have recommended channel models for specific propagation environments. These models may characterize path-loss attenuation, shadowing and multipath effects. Our interest is focused on the multipath propagation conditions present in typical LTE channels, and their impact on the time-delay estimation of the PRS.

### 3.5.1 Typical channel models

#### Tapped-delay line (TDL) channel models

Propagation channel models are aimed to realistically represent the physical channel. In this sense, the multipath CIR is typically modelled defining a tap for each physical ray. Every tap is determined by a complex amplitude and a time delay. In mobile communications, the standard multipath models for single-antenna transmission are the so-called tapped-delay line (TDL) models [Pro00]. Indeed, the LTE technology adopts specific TDL models inherited from second- and third-generation mobile communications, i.e. GSM and UMTS, based on the ITU-R M.1225 [ITU97] recommendation and the 3GPP TS 05.05 [3GP11] specification for GSM. But, they are extended to be applied with the wide bandwidth of LTE signals. The TDL models are based on several multipath reflections characterized by fixed taps delays $t_k$, relative average power $\overline{\mathrm{RP}}_k$ for every tap, and Doppler spectrum. Their channel impulse response is defined as

$$h_{\mathrm{c}}(t) = \sum_{k=0}^{L_{\mathrm{c}}-1} h_k \delta\left(t - t_k - t_{\epsilon}\right), \tag{3.5.1}$$

where $L_{\mathrm{c}}$ is the number of taps of the channel, $h_k$ is the complex gain for the $k$-th path, $t_k$ is the tap delay relative to the first tap (i.e. $t_0 = 0$), and $t_{\epsilon}$ is the time delay introduced by the channel (i.e. the time delay of the first arriving ray). The channel coefficients $h_k$

of these models are typically time-varying with a Rayleigh distribution, and following a classical Jakes Doppler spectrum $S(f)$,

$$S(f) \propto \sqrt{\frac{1}{1-(f/f_{\mathrm{D}})^2}}, \quad \text{for } f \in [-f_{\mathrm{D}}, f_{\mathrm{D}}]\,, \tag{3.5.2}$$

being $f_{\mathrm{D}}$ the maximum Doppler shift. Considering the highest speed to be supported in LTE as $v = 500$ km/h [3GP06] and a carrier frequency $f_{\mathrm{c}} = 2$ GHz, the maximum Doppler shift expected is $f_{\mathrm{D}} = f_{\mathrm{c}} \cdot v/c \simeq 927$ Hz, being $c$ the speed of light. Thus, the 50% coherence time is computed using Clarke s model [Rap02], and results in

$$T_{\mathrm{coh},50\%} = \sqrt{\frac{9}{16\pi}} \cdot \frac{1}{f_{\mathrm{D}}} \simeq 0.46\text{ms}. \tag{3.5.3}$$

Particularly, the 3GPP consortium agreed, in [R4-07], on the use of the Pedestrian A and Vehicular A channels from [ITU97], and the Typical Urban (TU) channel from [3GP11], in order to model three reference environments characterized by a low, medium and large delay spread, respectively. Nevertheless, they were designed for a 5 MHz operating bandwidth, and an apparent periodicity appears in their frequency correlation properties for higher bandwidths [Sor05]. Thus, the LTE standard has adopted since 2007 an extension of the ITU and 3GPP models by following the procedure described in [Sor05], resulting in the Extended Pedestrian A (EPA), Extended Vehicular A (EVA) and Extended Typical Urban (ETU) channel models. The main parameters of these models, i.e. fixed delay $t_k$ and relative average power $\overline{\mathrm{RP}}_k$, are specified in Annex B of TS 36.101 [3GP14a] and TS 36.104 [3GP12c], and shown in Table 3.2. These specifications also define maximum Doppler shifts for each model to represent low, medium and high mobile conditions, e.g. EPA 5 Hz, EVA 5 Hz, EVA 70 Hz, ETU 30 Hz, ETU 70 Hz, and ETU 300 Hz. Finally, the TDL models can be applied to multiple antenna schemes by introducing spatial correlation matrices, as it is discussed in [R4-06], resulting on a simple LTE MIMO channel model.

#### Geometric-based stochastic channel models (GSCM)

The LTE channel can also be modelled with geometric-based stochastic channel models (GSCM). These are more complex models based on the geometry between base station, mobile station and scatterers following a stochastic construction, as is shown in Figure 3.12. The GSCM models are widely adopted for MIMO channel modelling, e.g. COST

Table 3.2: LTE tapped-delay line channel model parameters.

| Tap | **EPA channel** | | **EVA channel** | | **ETU channel** | |
|---|---|---|---|---|---|---|
| $k$ | $t_k$ (ns) | $\overline{\text{RP}}_k$ (dB) | $t_k$ (ns) | $\overline{\text{RP}}_k$ (dB) | $t_k$ (ns) | $\overline{\text{RP}}_k$ (dB) |
| 1 | 0 | 0.0 | 0 | 0.0 | 0 | -1.0 |
| 2 | 30 | -1.0 | 30 | -1.5 | 50 | -1.0 |
| 3 | 70 | -2.0 | 150 | -1.4 | 120 | -1.0 |
| 4 | 90 | -3.0 | 310 | -3.6 | 200 | 0.0 |
| 5 | 110 | -8.0 | 370 | -0.6 | 230 | 0.0 |
| 6 | 190 | -17.2 | 710 | -9.1 | 500 | 0.0 |
| 7 | 410 | -20.8 | 1090 | -7.0 | 1600 | -3.0 |
| 8 | | | 1730 | -12.0 | 2300 | -5.0 |
| 9 | | | 2510 | -16.9 | 5000 | -7.0 |

259 channel model [Mol06], COST 273 channel model [Cor06], COST 2100 channel model [Ver11], 3GPP spatial channel model (SCM) [3GP03], or the WINNER channel model [Kyo07]. Indeed, the ITU-R M.2135-1 [ITU08] recommendation for the evaluation of IMT-Advanced systems is based on the WINNER channel model, which is able to operate on bandwidths from 5 MHz to 100 MHz. According to this recommendation, the deployment scenarios are classified as indoor hotspot, urban micro-cell, urban macro-cell and rural macro-cell. Depending on the scenario selected, large-scale parameters, such as delay spread, angle spread or shadow fading, are randomly generated following the distributions specified in Table A1-7 of [ITU08]. Then, the small-scale parameters, such as delay, power, AoA and angle of departure (AoD), are randomly distributed for each cluster of propagation rays (i.e. rays with similar delay and directions). Both large- and small-scale parameters are fixed during each channel segment (i.e. the so-called *drop*). Finally, the time-variant channel realisations of a drop are generated according to the random initial phases of the scatterers. Using the MATLAB software described in [Hen07], the power-delay profile (PDP) density is computed for WINNER B1 and C2 scenarios, as it is shown in Figure 3.13, by using 1000 realisations and NLoS propagation conditions.

### Limitations of current channel models

Given the previous two examples of channel models, the LTE (i.e. EPA, EVA and ETU) and the WINNER channel models are compared in Table 3.3. The TDL and GSCM models represent the most typical channel models of current literature. Nevertheless,

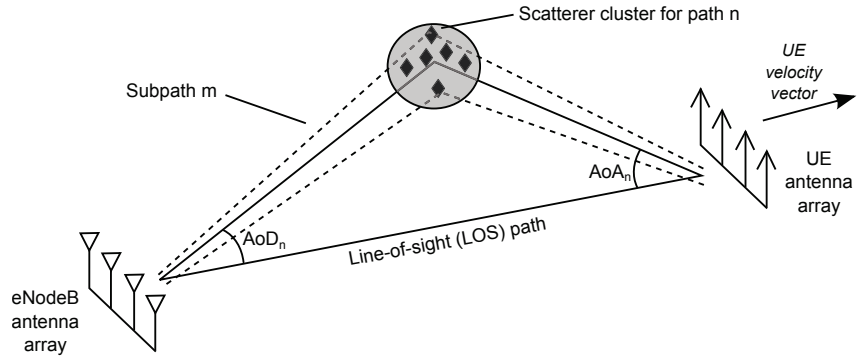


Figure 3.12: Scheme of the geometry-based stochastic channel model [Ses11, p.443].

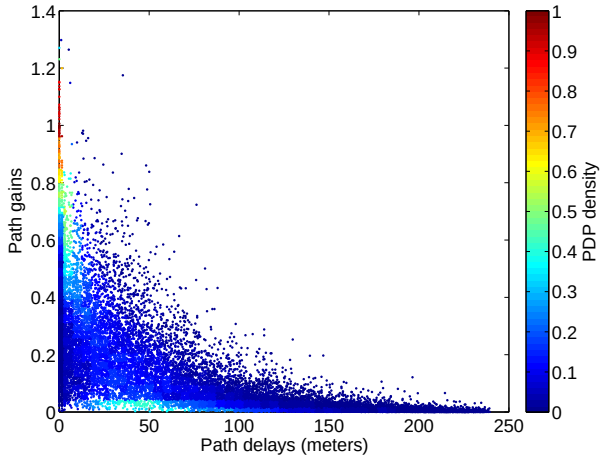


(a) B1 scenario

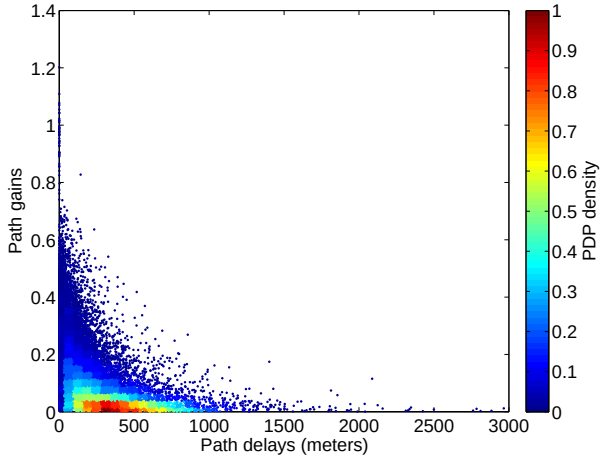


(b) C2 scenario

Figure 3.13: Example of power-delay profile density of the WINNER B1 and C2 scenarios.

they are designed for communications purposes, and do not cover important features for positioning applications. First, the time-delay offset between the base station and the user is not considered in these models, thus the bias produced in NLoS conditions is not modelled. And second, the channel impulse response is not time-continuous, thus the time evolution of the CIR is not completely implemented. Recently, extensions of the WINNER channel model are being studied to jointly model satellite and terrestrial scenarios including these missing features, such as the quasi deterministic radio channel generator (QuaDRiGa) described in [Bur14] and developed under ESA MIMOSA activity (see [Ebe13]), or as proposed by Wang et al. in [Wan12b].

### 3.5.2 Multipath error envelope

The impact of the multipath channel on the positioning error can be preliminary studied by means of the multipath error envelope (MPEE). This metric is based on the evaluation of the time-delay error produced when adding to the LoS signal an artificial multipath signal, which is generated with specific delay, power and phase.

The maximum likelihood estimation is used to compute the MPEE, by considering a two-ray multipath model (i.e. LoS and multipath signal), as it is shown in Figure 3.14. Firstly, the signal-to-multipath ratio (SMR) is changed for the smallest PRS bandwidth, in Figure 3.14(a), to assess the increase of the time-delay error due to the impact of the multipath power. The results are obtained for the destructive and constructive contribution of the multipath, that is, when the multipath ray is in-phase (solid line) and counter-phase (dashed line), respectively. Secondly, PRS bandwidths are tested for an SMR equal to 1 dB, in Figure 3.14(b), to confirm the multipath error reduction as the bandwidth increases.

As it can be seen, the maximum delay error produced by a single multipath ray can be found easily for different scenarios with the multipath error envelope. Nevertheless, the multipath error assessment is more complicated in a realistic channel due to the increase on the number of multipath rays. This observation suggests that another metric should be found in order to measure the impact of a certain multipath channel on the time delay.

### 3.5.3 Mean delay error

Realistic propagation channels are not just formed by two rays, such as in the MPEE scenario, but they are characterized by several taps at different delay positions, as it is

Table 3.3: Comparison between LTE and WINNER channel models.

| Description | LTE models | WINNER model |
|---|---|---|
| Type | Statistical | Statistical (ray-based double-directional) |
| Amplitude distribution | Rayleigh | Driven by scenario |
| Delay distribution | Fixed | Exponential |
| Bandwidth | 20 MHz | 100 MHz |
| Multipath taps | 6 to 9 | Up to 20 |
| Path loss and shadowing | Not included | Optional |
| Environments | Pedestrian, vehicular and typical urban | Indoor, urban, suburban and rural |
| **Pros** | • Low computational cost<br>• Magnitude driven by Doppler shift | • Realistic<br>• Scatterers driven by user movement |
| **Cons** | • Fixed PDP<br>• Lack of delay resolution<br>• NLoS bias not modelled | • Non-continuous PDP<br>• Random tap delay (independent of the user movement)<br>• NLoS bias not modelled |

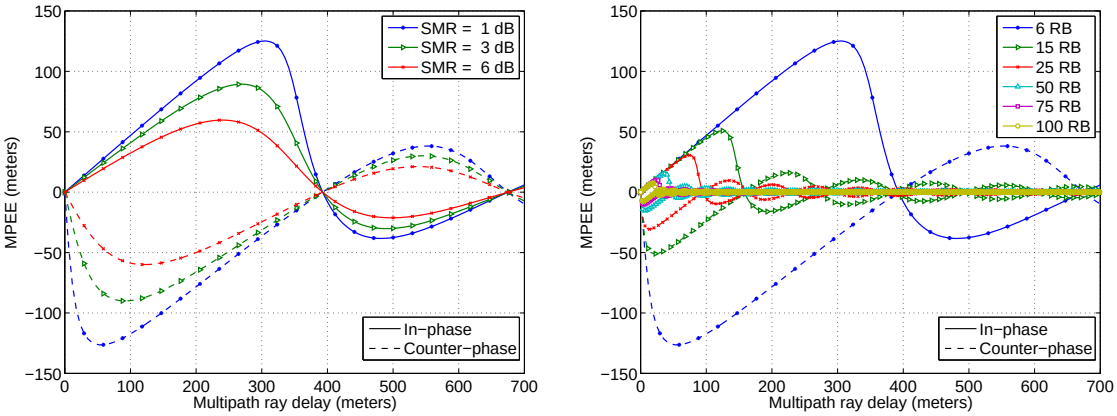


(a) 6-RB bandwidth and different SMR (b) LTE signal bandwidths and 1-dB SMR

Figure 3.14: Multipath error envelope for the LTE PRS considering different SMR values and signal bandwidths.

introduced in Section 3.5.1. The MPEE has already suggested that the contribution of the multipath rays on the time-delay error mainly depends on their delay and relative power. Thus, some authors, such as [R1-09h] and [Men08], have used the mean delay, or the so-called *center of gravity*, of the PDP to provide an approximation of the delay error by computing a weigthed average of the taps delays using the taps squared amplitude, defined by

$$\bar{\tau} = \frac{\sum_{k=1}^{K} \tau_k \left|a_k\right|^2}{\sum_{k=1}^{K} \left|a_k\right|^2}. \tag{3.5.4}$$

The mean delays of EPA, EVA and ETU models for the span of interest are 13, 47 and 59 meters, respectively. Nevertheless, this metric has to be carefully used because it may not characterize the typical timing estimate obtained for the actual multipath channel. The main constraint is posed by the signal bandwidth, which is not considered in the metric, but it determines the ultimate shape of the correlation function. As it is shown in Figure 3.3(b), the main lobe of the correlation function is narrowed when increasing the bandwidth, and thus the multipath rays can have (among them) an independent contribution to the timing error. This effect can be especially noticed for high bandwidths, such as for 75-RB and 100-RB bandwidths.

Another metric, which may indeed vary due to the bandwidth, can be obtained by measuring the center of gravity of the probability density function (PDF) $f(\tau_\varepsilon)$ of the

timing error $\tau_\varepsilon$. This metric results in the mean delay error, expressed as

$$\overline{\tau}_\varepsilon = \frac{\int_{\tau_\mathrm{a}}^{\tau_\mathrm{b}} \tau_\varepsilon \cdot f(\tau_\varepsilon)\, d\tau_\varepsilon}{\int_{\tau_a}^{\tau_b} f(\tau_\varepsilon)\, d\tau_\varepsilon} = \int_{\tau_a}^{\tau_b} \tau_\varepsilon \cdot f(\tau_\varepsilon)\, d\tau_\varepsilon = \mathrm{E}[\tau_\varepsilon], \tag{3.5.5}$$

where $[\tau_\mathrm{a}, \tau_\mathrm{b}]$ is the search interval of the time-delay $\tau$.

### 3.5.4 Timing error histogram

#### Conventional estimation

As it has been introduced in the previous section, the impact of the multipath channel can be assessed by computing the PDF of the time-delay errors. For that purpose, a large number of channel realisations is necessary to cover the majority of possible timing errors produced by multipath, from the statistical point of view. The timing errors are computed with a conventional estimator, such as the matched filter. This estimator is the MLE for AWGN channel, where the time delay is estimated by finding the maximum peak of the correlation between the received signal and the pilots. The histogram of the resulting timing errors finally shows the impact of the channel on the ranging accuracy. This analysis is also of interest because it allows the assessment of the actual effect of multipath when nothing is done to compensate it. Particularly, since the multipath delays of the channel models specified in LTE (i.e. EPA, EVA and ETU) are constant over time, we measure the impact produced by the complex amplitude variation of every multipath ray.

The Communications System Toolbox™ provided in MATLAB is used to perform the simulations. This toolbox contains the `stdchan` function to simulate multipath fading channels, where the LTE channel parameters of Table 3.2 can be introduced. In order to cover the maximum number of multipath ray combinations, a fast fading scenario is selected by defining a maximum Doppler shift of 300 Hz. The resulting histograms are shown in Figure 3.15 for 20000 channel realisations and using a Savitzky-Golay FIR smoothing filter. The PDP of the EPA, EVA and ETU channels is also added in order to identify which ray or group of rays may have caused a certain timing error.

As it could be expected, the PDP distribution characterizes the impact of the channel on the timing error. For instance, the histograms for EPA channel, in Figure 3.15(a), are centred on the multipath rays that concentrate more energy. This effect is more evident

Table 3.4: Maximum and mean time delay error for LTE PRSs in TDL channel models, for histograms of Figure 3.15.

| Bandwidth | **EPA channel** | | **EVA channel** | | **ETU channel** | |
|---|---|---|---|---|---|---|
| (RB) | $\tau$ (m) | $\overline{\tau}_\varepsilon$ (m) | $\tau$ (m) | $\overline{\tau}_\varepsilon$ (m) | $\tau$ (m) | $\overline{\tau}_\varepsilon$ (m) |
| 6 | 13 | 13 | 45 | 55 | 50 | 61 |
| 15 | 13 | 13 | 7 | 49 | 36 | 58 |
| 25 | 12 | 13 | 8 | 46 | 55 | 55 |
| 50 | 7 | 13 | 3 | 44 | 150 | 55 |
| 75 | 2 | 13 | 3 | 44 | 150 | 58 |
| 100 | 3 | 13 | 111 | 42 | 150 | 60 |

for EVA and ETU channels, shown in Figure 3.15(b) and 3.15(c), respectively, due to their larger delay spread with respect to EPA channel. For high bandwidths, one can easily identify the multipath rays in the timing error distributions. Using the timing error histogram, the mean delay error $\overline{\tau}_\varepsilon$ is around 13 meters for EPA channel, 47 meters for EVA channel and 58 meters for ETU channel, which approximately coincides with the mean delay $\overline{\tau}$. Let us define $\tau$ as the timing error corresponding to the maximum peak of the PDF. The values of $\tau$ for every scenario are compared with the mean delay error $\overline{\tau}_\varepsilon$ in Table 3.4. As it can be seen, $\tau$ varies significantly due to the bandwidth, while the mean delay error has a softer variation.

### First-peak estimation

Our interest is based on the analysis of the typical timing errors achieved with the LTE PRS. In the presence of multipath, the matched is not just applied, but extended to mitigate the effect of multipath. This enhanced time-delay estimation is based, such as in [Che03], on finding the first peak (above the noise level) of the correlation function, as it is shown in Figure 3.16(a). Thus, the impact of both noise and multipath is considered in this procedure, hereby called *first-peak estimation*.

Using the procedure described, we can compute the cumulative density function (CDF) of the timing errors for a certain SNR, channel model and signal bandwidth. The resulting CDFs of the timing errors for EPA and ETU channels models with a SNR equal to 25 dB are shown in Figure 3.16(b) and 3.16(c), respectively. As it can be seen, the ETU case produces larger timing errors than the EPA case, especially for low signal bandwidths (e.g. 6 RB). At low bandwidths, the current procedure is equal to the conventional estimation,

because all the multipath rays jointly contribute on the timing error, forming a single peak on the correlation function. Thus, the mean delay of the PDP $\bar{\tau}$ is around the 50% of the cases of the CDF, as it can be seen in Figure 3.16(c). The large pseudorange errors obtained in the ETU case are mainly produced by the disperse contribution of multipath, due to a larger delay spread than EPA case.

In order to have a measure of the typical timing or pseudoranges errors obtained with LTE in these scenarios, the 67% and 95% of the cases of the computed CDF are chosen. These values can also be compared with those stated within E911 requirements.

Further literature of the first-peak estimation can be found considering undetected direct path (UDP) conditions, such as in [Als04, Ala05, Sch07] and [Dar09], as well as the references therein.

### 3.5.5 Variation of taps delays

The timing error histograms have shown that the delay position of the multipath ray have a significant impact on the ranging performance. Using the tapped-delay line models, the complex amplitude of the taps changes every channel realisation, but a fixed tap delay distribution is maintained. Thus, the variation of the taps delays is introduced to assess the impact of the tap delay position and resolution. For this purpose, more complex models, such as GSCM models, are used to compare fixed and non-fixed tap delays, with a certain variance on the tap delay distribution.

The WINNER channel models [Kyo07] are chosen for this evaluation because they have more flexibility on the simulation test. These models increase the number of paths (i.e. up to 20 paths) leading to rich power-delay profiles that can help us to assess different situations. Particularly, the B2 propagation or bad urban micro-cell scenario is used for this study. The WINNER B2 scenario is characterized by a Manhattan-like urban area, where transmitter and receiver are located outdoors surrounded by buildings with the eventual presence of far scatterers. NLoS conditions are predominant with user velocities up to 70 km/h.

In order to produce the WINNER channel realisations, the MATLAB code provided in [Hen07] is used. The simulation is simplified to a single link between transmitter and receiver with single isotropic antennas. Although the code computes path losses and shawoding coefficients, they are not applied to the channel in order to focus on the

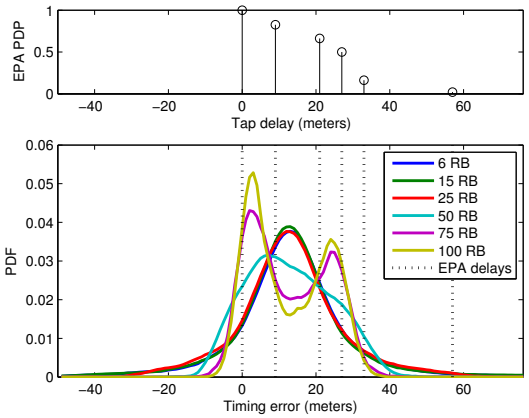


(a) EPA channel model

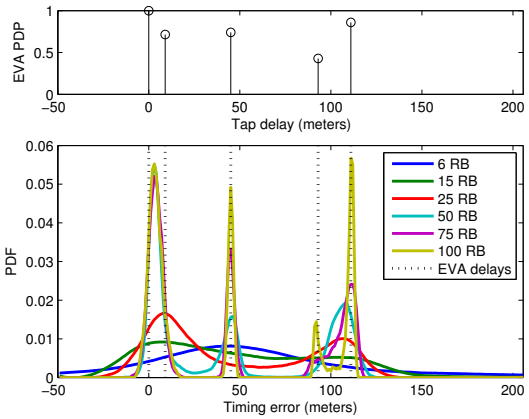


(b) EVA channel model

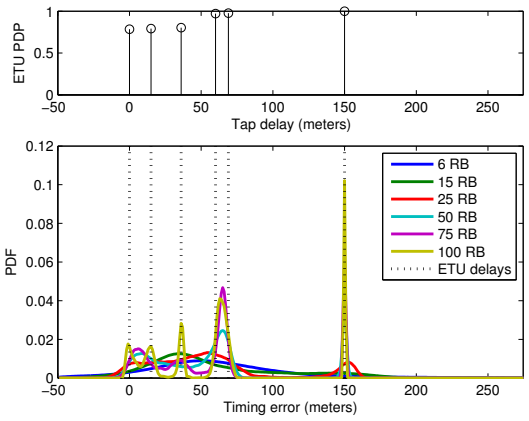


(c) ETU channel model

Figure 3.15: Timing error histograms of the MLE for TDL channel models.

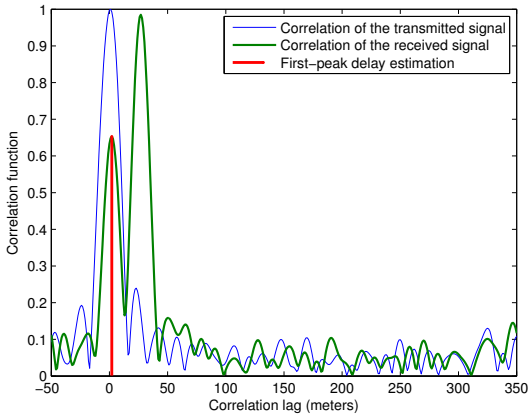


(a) EPA channel model, 100 RB

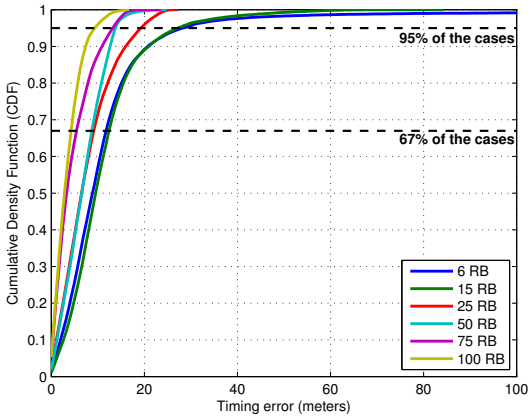


(b) CDF for EPA channel model

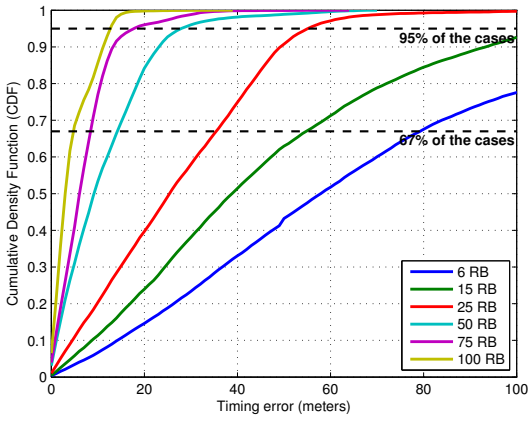


(c) CDF for ETU channel model

Figure 3.16: Pseudoranges results using first-peak estimation using EPA and ETU models for a SNR equal to 25 dB.

analysis of the multipath components. Time evolution of the delay taps is described in the WINNER specification [Kyo07, p.33] by defining simulations of multiple and correlated channel segments. Since a channel segment is a group of realisations with fixed parameters, where phases of rays are only varying, smooth transition between segments allow time evolution of propagation parameters. Nevertheless, the evaluation of tap delay variations is simplified in our study by applying a Gaussian distribution to the fixed tap delay positions. The use of the time evolution option specified by WINNER recommendation is left for future work.

A single channel segment of 40000 realisations is computed, and a sampling grid of 0.25 meters is defined in the delay domain. Since the path delays are fixed during the whole simulation, a Gaussian-distributed delay is artificially added to every existing path for each realisation. Thus, tap delay variations are defined as $\tau_k(i) \sim \mathcal{N}(\overline{\tau}_k, \sigma_\tau^2)$, where $i$ is the channel realisation, $\overline{\tau}_k$ is the mean tap delay defined by the channel model, and $\sigma_\tau$ is the standard deviation of the artificial delays. Two standard deviations, i.e. $\sigma_\tau$ equal to 5 and 20 meters, are defined to assess two cases with low and high variations, respectively. These standard deviations do not intend to model a specific mobile scenario, but to assess the impact of the delay variation statistically.

Following the same procedure of the previous section, timing error histograms for fixed and non-fixed taps delays cases are simulated considering the WINNER B2 channel model and the different LTE PRS bandwidths, using the conventional estimator. The power-delay profile of the three cases is depicted in Figure 3.17(a), 3.17(b) and 3.17(c), where the Gaussian distribution of the artificial variation is also introduced. At first glance, the histograms for the fixed case and the first non-fixed case (i.e. $\sigma_\tau = 5$ meters) are very similar, and they follow the same behaviour studied in the previous section for a certain PDP and signal bandwidth. But, evaluating the second non-fixed case (i.e. $\sigma_\tau = 20$ meters), one can notice that the timing error distributions have expanded in the delay domain, and it happens in both non-fixed delay cases. This effect is stressed for high bandwidths where the timing error peaks are wider than in the fixed delay case.

Using the conventional estimator, the same behaviour is found in the timing histogram error for the EVA channel, where a standard deviation $\sigma_\tau$ of 0, 10 and 30 meters is applied over the taps delays, as it is shown in Figure 3.18. In this case, the timing error distribution also reproduces the Gaussian variation of the taps delays. Thus, the tap delay positions of the propagation channel can be identified as the main source of timing error.

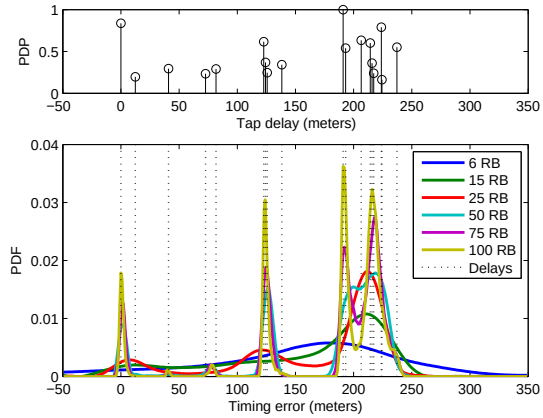


(a) Fixed tap delays

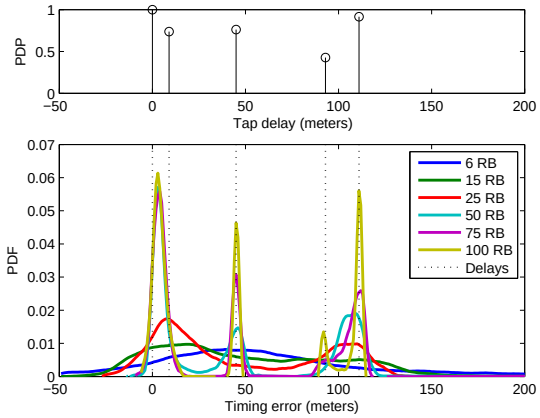


(a) Fixed tap delays

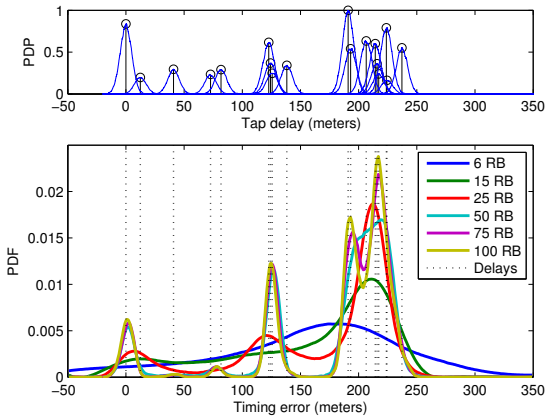


(b) Non-fixed tap delays ($\sigma_\tau = 5$ m)

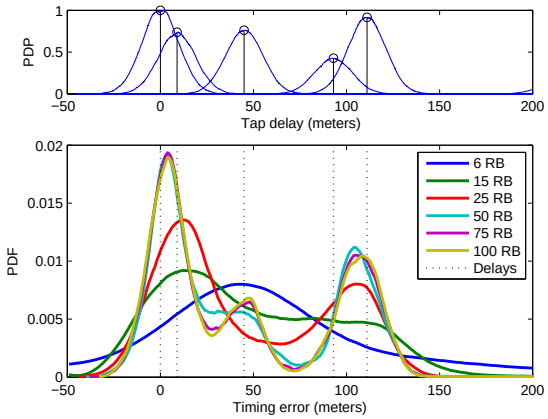


(b) Non-fixed tap delays ($\sigma_\tau = 10$ m)

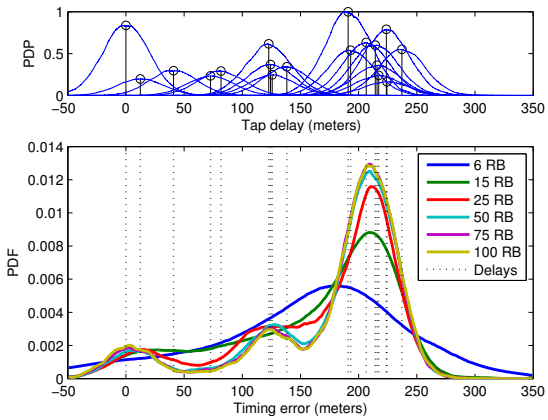


(c) Non-fixed tap delays ($\sigma_\tau = 20$ m)

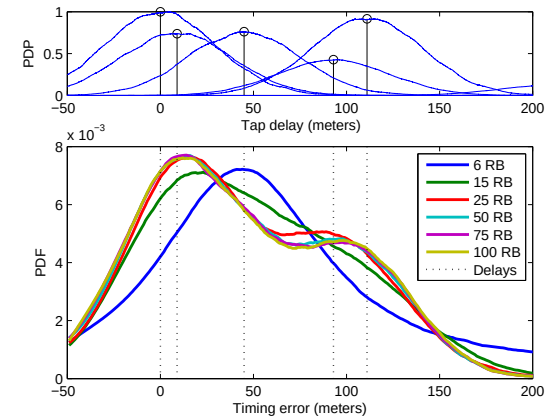


(c) Non-fixed tap delays ($\sigma_\tau = 30$ m)

Figure 3.17: Timing error histograms for WINNER B2 channel model.

Figure 3.18: Timing error histograms for EVA channel model.

## 3.6 Impact of both interference and multipath

The analysis of the LTE PRS has just been focused on the impact of noise and multipath, but interference is a major impairment in LTE that must be definitely taken into account. For that purpose, the tools previously described are combined to compute the typical position errors for an LTE coordinated network (i.e. from the interference point of view) in a pedestrian and urban scenario, characterized by EPA and ETU channel models, respectively.

If we assume that the signals transmitted from the five most powerful base stations with respect to the user position are received and used for OTDoA localisation, the link budget for every base station and user location can be computed following the procedure described in Section 3.3. Thus, five SINR values are obtained for every user location considering a certain bandwidth, and are used to determine the noise level for a certain link between BS and UE. Once the signal is passed through the multipath and AWGN channel, the received signal is cross-correlated with the PRS. Then, the first-peak estimation technique is used to compute the CDF of the pseudorange errors. Finally, the 67% or 95% values of the CDF are taken for the specific SINR, channel model and signal bandwidth to obtain the final user position error with the CRB for OTDoA localisation.

Following the procedure just described, the resulting position errors are shown in a two-dimensional map at every user location in Figure 3.19, and they can be compared with the results in the absence of multipath presented in Section 3.4. As it can be seen, the best position accuracy is around the barycentre of every three close base stations. For an EPA channel using a bandwidth of 6 RB (i.e. 1.08 MHz), the lowest position error is around 12 and 30 meters in the 67% and 95% of the cases, as is shown in Figure 3.19(a) and 3.19(b), respectively. These position errors can be improved if the signal bandwidth is increased up to 100 RB (i.e. 18 MHz), resulting in position errors around 4 and 10 meters in the 67% and 95% of the cases for an EPA channel, as it is shown in Figure 3.19(c) and 3.19(d), respectively. Similar results can only be obtained for an ETU channel when using high bandwidths, as it is shown in Figure 3.19(e) and 3.19(f), because of the higher mean delay of the channel impulse response, as commented in the previous section. In order to achieve the ultimate positioning performance of LTE, ranging techniques able to counteract the effect of multipath should be considered, as it is proposed in the following chapter.

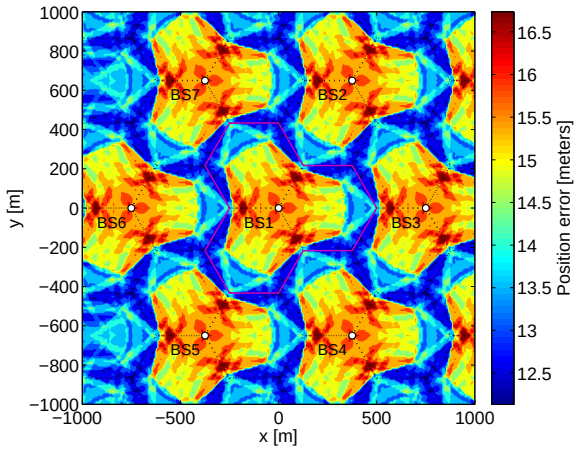


(a) 67% of the CDF of EPA channel, 6 RB

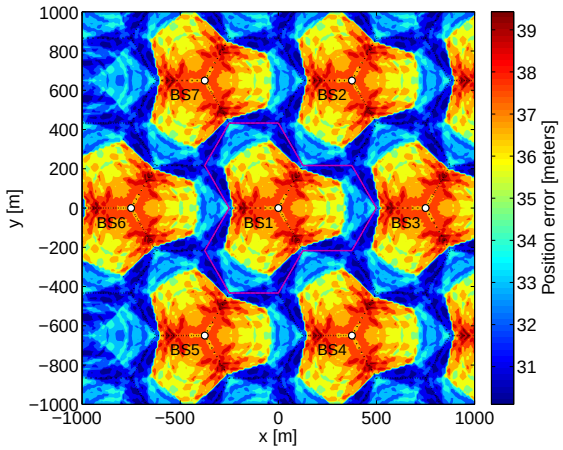


(b) 95% of the CDF of EPA channel, 6 RB

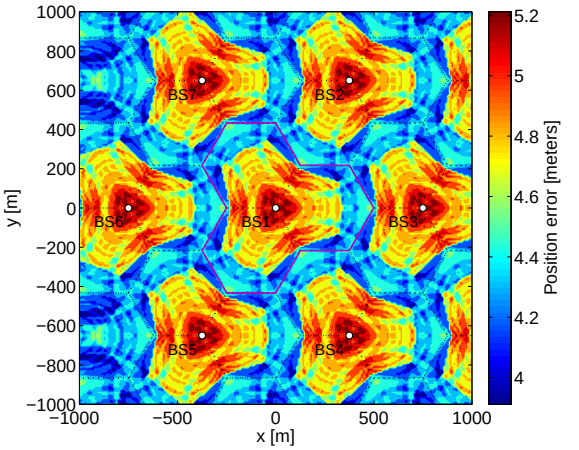


(c) 67% of the CDF of EPA channel, 100 RB

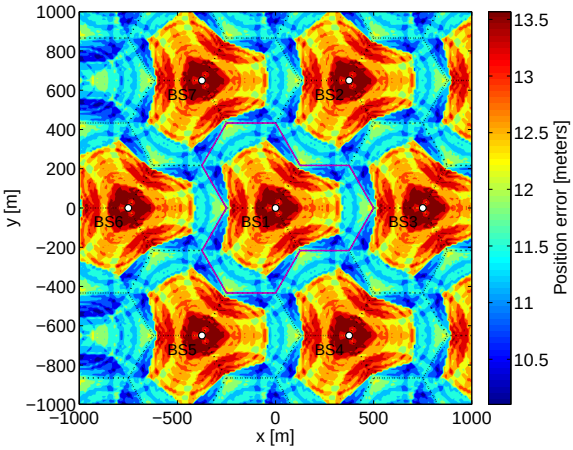


(d) 95% of the CDF of EPA channel, 100 RB

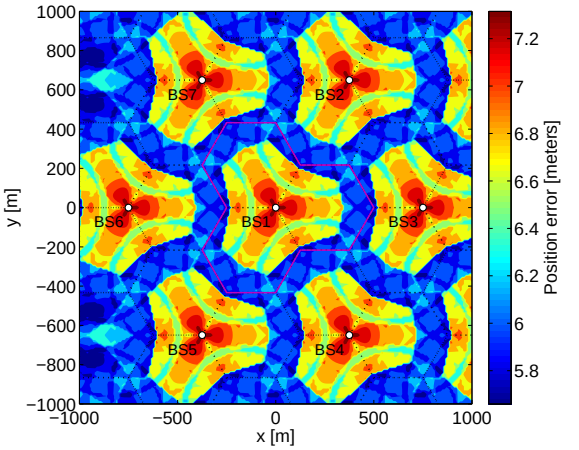


(e) 67% of the CDF of ETU channel, 100 RB

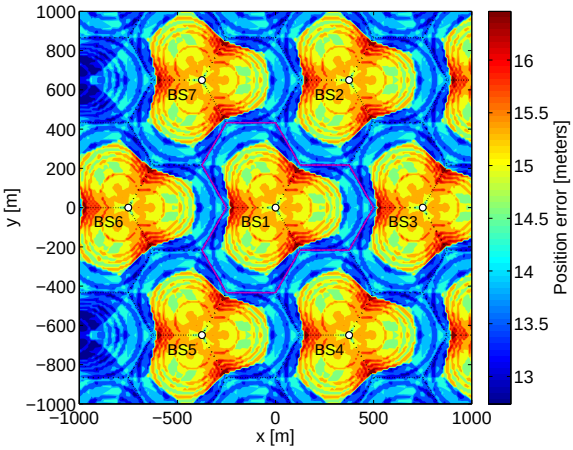


(f) 95% of the CDF of ETU channel, 100 RB

Figure 3.19: Typical position errors for the PRS in an LTE coordinated network.

# Chapter 4

# Joint Maximum Likelihood Time-Delay and Channel Estimation

The evolution of cellular positioning, from CDMA systems (e.g. UMTS or CDMA2000) to OFDM systems, has inherited the use of the matched filter or correlation-based techniques for ranging in LTE. This adoption is shown in recent research studies on LTE OTDoA positioning, such as those in [Med09] and [Gen12]. In order to assess the main working scenarios, the potential of LTE to provide accurate positioning has been studied using this conventional estimator in the previous chapter. The matched filter is the maximum likelihood estimator in AWGN channels, being also a low-complexity estimator. But, in multipath channels, the delayed reflections of the signal induce a notable bias on this conventional estimation. In addition, multipath is the main limiting factor in urban environments, once inter-cell interference is removed. Therefore, countermeasures against multipath have to be introduced in order to achieve the ultimate positioning performance in LTE. The optimum solution to this problem necessarily lies in the joint estimation of the time-delay and channel response, as the way to counteract the effect of the multipath channel.

Timing synchronization for data transmission does not need to achieve the extreme accuracy required for positioning. This is the reason why, in communications applications, the ML approach is widely applied to channel estimation assuming the time delay to be coarsely corrected in a previous stage, and the residual time delay is considered negligible. There are still some contributions that propose the joint maximum likelihood (JML) estimation of the time delay and channel response in OFDM systems, considering a model based on equi-spaced or periodic taps, but few of them deal with the specific case of ranging applications. The authors of [Lar01] propose an algorithm based on the JML approach

and on the channel length estimation, but providing only coarse timing estimates. In [Pun06], two JML estimators are applied for synchronisation of multiple users. The first one is a joint frequency and channel estimator, while the second one is a joint time-delay and channel estimator. A similar JML approach is used for ranging purposes considering an IEEE 802.16 system [San11]. An approximation of the JML algorithm is proposed in [Zho09] using early and late estimations in a delay-locked loop. The JML estimation has also been studied for multicarrier ranging considering the optimal placement of pilot subcarriers in [Lar11], and applied without data-aiding after the definition of a unified signal model in [LS13]. Therefore, the joint estimation algorithms found in the literature have mainly focused on communication applications, where a very accurate time-delay estimation is not critical in general. In our ranging application, the representation of the channel has to be improved, especially for those scenarios where multipath highly deteriorates the time-delay estimation. Thus, the channel estimation models have to be adapted to these harsh environments.

The periodic-tap estimation model is suitable for mass-market receivers, such as mobile phones, because it has a low complexity. However, this model may lead to significant ranging errors with close-in multipath. Typically, multipath appears close to the line-on-sight ray in urban and indoor environments, producing a critical degradation in ranging applications. This multipath, which is ignored in communications, significantly affects the performance of the periodic-tap estimation model for low-sampling rates, because short-delay multipath may not be properly modelled between samples. Therefore, a hybrid estimation model is proposed in this thesis by using equi-spaced taps together with an arbitrary tap between the first two. This solution improves the characterization of the channel, while only adding the complexity of one more estimation parameter. Thus, the introduction of this arbitrary tap with a variable position helps to increase the ranging accuracy in close-in multipath environments. This new hybrid JML approach, as well as the periodic JML approach, is studied in this chapter and used to assess the achievable positioning performance of LTE, considering a low-complexity time-delay estimation that exploits the structure of the LTE OFDM signals.

## 4.1 Channel estimation models

The time-delay estimation can be enhanced by model-based estimators. These estimators use channel estimation models in order to counteract the effect of multipath. There are many possibilities for these channel estimation models. On the one hand, the most

accurate model corresponds to the estimation of amplitude, phase and delay of every propagation ray. However, it is also the most complex model because of the many unknowns to estimate. Despite its complexity, this estimation model has been widely studied, for instance, with super-resolution techniques in [Vid02, Li04], with the ML criterion in [Bia12], or in a two-step approach in [Sch12]. On the other hand, channel estimation models can be simplified by defining equi-spaced or periodic taps relative to the time delay of the first path. Since this model is based on the uniform sampling of the channel, it has been used with the compressed sampling theory for channel estimation, such as in [Baj08, Ged10], but it can also be found in multipath interference cancellation [Yan12].

It is important to note that channel estimation models should be distinguished from propagation channel models. The first ones consider the response of the channel in order to later counteract its effect. The second ones model the physical channel and they are used to understand the behaviour of the channel itself from a propagation point of view. Thus, the propagation channel models are used to simulate the actual channel, while the channel estimation models are used to represent the effect of the channel on the time-delay estimation. Next, we describe those channel estimation models that are typically used, as well as a new model presented in this work.

### 4.1.1 Single-tap model

The most simple and used channel estimation model is the single-tap model. It assumes that the signal is mainly attenuated and delayed by the channel. Thus, this estimation model is only defined by a single-channel coefficient $h_0$, which can be complex-valued, associated to the propagation time delay $t_\epsilon$. Using a bandlimited representation for the channel, the discrete CIR of this model is

$$h_{\mathrm{ST}}(m) = h_0 \cdot \mathrm{sinc}(m - \tau), \tag{4.1.1}$$

where $\mathrm{sinc}(x) = \frac{\sin(\pi \cdot x)}{\pi \cdot x}$ is the sinc function, and $\tau \doteq t_\epsilon / T_\mathrm{s}$ is the discrete-time symbol-timing error, which is the time delay to estimate. The main characteristics of this channel model are summarized in Table 4.1. This estimation model is typically applied in AWGN channels. Using this model, the derivation of the ML estimator results in the matched filter or correlation-based estimator. As it has been discussed, the matched filter may have a considerable bias in multipath channels. For instance, in multipath channels with a large delay spread, the maximum average energy of the CIR may be located far from the time delay of the first arriving path. This deviation causes a notable degradation

on the performance of this conventional TDE. The reason is that the matched filter estimates the time delay based on the maximum peak of the correlation, which coincides with the maximum energy of the CIR. However, the stronger correlation peak may not necessarily correspond to the first arriving path, and thus a bias is produced in the time-delay estimation.

### 4.1.2 Arbitrary-tap model

The most accurate model is constituted by the amplitude, phase and delay of every physical multipath ray. But, this model is also the most complex because these parameters have to be estimated for every tap. Since the taps delays are in positions to be determined, this model is hereafter called the arbitrary-tap model. Its discrete CIR is written as

$$h_{\mathrm{AT}}(m) = \sum_{k=0}^{L-1} h_k \cdot \mathrm{sinc}(m - \tau_k - \tau), \tag{4.1.2}$$

where $L$ is the number of taps, $h_k$ is the channel coefficient for the $k$-th tap, $\tau_k$ is the relative delay to the first tap (i.e. $\tau_0 = 0$), and $\tau$ is the time delay. As it is shown in Table 4.1, the arbitrary-tap model is represented, in that case, by matching the $L_{\mathrm{c}}$ propagation taps at delay positions $\tau_{\mathrm{c},k}$. Although the channel response can be accurately reconstructed using this model, the implementation complexity is a major concern. For instance, the number of unknowns substantially increase (without *a priori* statistics) in dense multipath, due to the high number of rays to estimate. Thus, the iterative methods used for the TDE, such as super-resolution techniques [Li04], have a high computational burden.

### 4.1.3 Periodic-tap model

The complexity of the channel estimation model is reduced by placing the estimation taps in equi-spaced or periodic delay positions. The aim is to avoid the tap delay estimation for every physical ray, and focus on the propagation time-delay estimation. Thus, the actual physical tap positions are not estimated, and the resulting model is a sampled version of the channel impulse response. The discrete CIR of the periodic-tap model is

$$h_{\mathrm{PT}}(m) = \sum_{k=0}^{L-1} h_k \cdot \mathrm{sinc}(m - k - \tau), \tag{4.1.3}$$

where $L$ is the number of taps, $h_k$ is the channel coefficient for the $k$-th tap, and $\tau$ is the time delay. Ideally, the sampled model would require an infinite number of taps in order to perfectly represent the channel. The solution described in (4.1.3) is to truncate the number of taps to $L$, by assuming that the rest of taps have a negligible contribution. However, this assumption may produce an incorrect characterization of the channel response, leading to the so-called problem of model mismatch. The periodic-tap model is represented in the example of Table 4.1 considering six taps. Since the tap positions are assumed to be equi-spaced, the close-in multipath, i.e. multipath close to the LoS signal, is not properly modelled if it coincides between the first two samples at delay 0 and $T_\mathrm{s}$. Thus, the multipath energy missed between samples may severely degrade the performance of the time-delay estimation. In the opposite case, if the sampling period $T_\mathrm{s}$ is small enough, the number of taps $L$ have to expand a similar interval to the multipath dispersion. The design of $L$ is beyond the scope of this work, but it can be obtained by means of model order selection techniques, such as minimum description length (MDL) or Akaike [Lar01], or by considering the delay spread of the channel, which can be estimated as in [Yuc08] and the references therein.

### 4.1.4 Novel hybrid-tap model

A novel hybrid solution is proposed in this work by using the equi-spaced taps together with an additional tap in a position to be determined between the first two. Thus, the equi-spaced taps allow the estimator to capture most of the multipath energy present in the propagation model, while the additional tap models close-in multipath with only the added complexity of having one more variable. The CIR of the hybrid-tap model is defined as

$$h_{\mathrm{HT}}(m) = \sum_{k=0}^{L-2} h_k \cdot \mathrm{sinc}(m-k-\tau) + h_{L-1} \cdot \mathrm{sinc}(m-\tau'-\tau), \quad 0<\tau'<1, \qquad (4.1.4)$$

where $L$ is the number of taps, $h_k$ is the channel coefficient for the $k$-th periodic tap, $h_{L-1}$ and $\tau'$ denote the channel coefficient and delay of the arbitrary tap, respectively, and $\tau$ is the time delay. As an example, the hybrid-tap model is represented in Table 4.1, where the arbitrary-tap delay values of $\tau'$ are fixed within 0 and 1 with respect to $\tau$.

Table 4.1: Summary of channel estimation models.

$$H(n) = \sum_{k=0}^{K-1} h_k \cdot e^{-j\frac{2\pi}{N}\cdot n\cdot(\tau+\tau_k)}$$

Single-tap estimation model:

$$\tau_k = 0 \quad , \quad K = 1$$

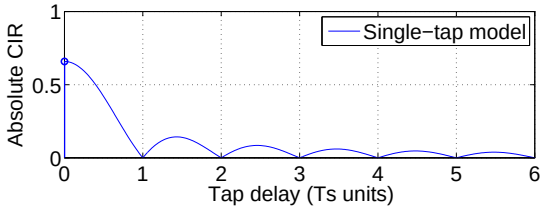


Arbitrary-tap estimation model:

$$\tau_k = \tau_{c,k} \quad , \quad K = L_c$$

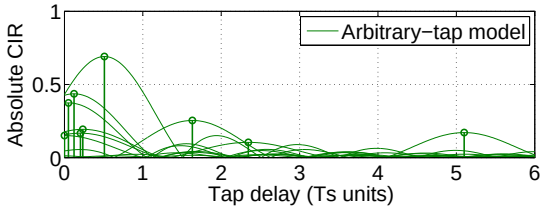


Periodic-tap estimation model:

$$\tau_k = \{0, 1, \cdots, L-1\} \quad , \quad K = L$$

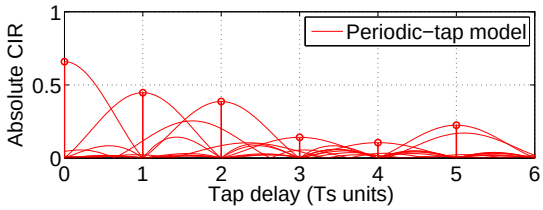


Hybrid-tap estimation model:

$$\tau_k = \{0, \tau', 1, \cdots, L-2\} \quad , \quad K = L$$
$$0 < \tau' < 1$$

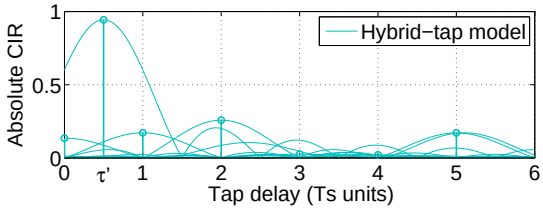


## 4.2 Cramér-Rao bound

The achievable accuracy of any unbiased estimator can be assessed (in the moderate- to high-SNR region) by means of the Cramér-Rao bound, as it was introduced in Section 3.2.3. The CRB was derived in (3.2.27), but only considering the time-delay estimation, and not the channel coefficients. Thus, the CRB for the joint time-delay and channel estimation has to be introduced. This section derives the CRB for every channel estimation model described in Table 4.1, except the arbitrary-tap model, which is not considered in this work due to the high computational burden introduced on the joint estimation.

Let us rewrite the frequency-domain model of the received signal of (3.1.4) in matrix notation as in [Lar11, LS13],

$$\mathbf{r} = \mathbf{B}\boldsymbol{\Gamma}_\tau \mathbf{F}_L \mathbf{h} + \mathbf{w}, \tag{4.2.1}$$

where

$$\mathbf{r} = \left[r\left(-N/2+1\right), \ldots, r\left(N/2\right)\right]^{\mathrm{T}}, \tag{4.2.2}$$

$$\boldsymbol{\Gamma}_\tau = \mathrm{diag}\left(e^{-j\frac{2\pi}{N}(-N/2+1)\tau}, \ldots, e^{-j\frac{2\pi}{N}(N/2)\tau}\right), \tag{4.2.3}$$

$$\mathbf{B} = \sqrt{2C} \cdot \mathrm{diag}\left(b\left(-N/2+1\right), \ldots, b\left(N/2\right)\right), \tag{4.2.4}$$

$$\mathbf{h} = \left[h_0, \ldots, h_{L-1}\right]^{\mathrm{T}}, \tag{4.2.5}$$

$$\mathbf{w} = \left[w\left(-N/2+1\right), \ldots, w\left(N/2\right)\right]^{\mathrm{T}}, \tag{4.2.6}$$

and the Fourier matrix $\mathbf{F}_L$ is composed of the first $L$ columns of the zero-frequency-centered $N \times N$ DFT matrix, whose entries at the $n$-th subcarrier and the $k$-th tap are

$$\left[\mathbf{F}\right]_{n,k} = \frac{1}{\sqrt{N}} \cdot e^{-j\frac{2\pi}{N} \cdot n \cdot \tau_k}, \tag{4.2.7}$$

for $n = -N/2+1, \ldots, N/2$ and $k = 0, \ldots, L-1$, being $\tau_k$ the tap delay positions of the channel estimation model. Assuming only the PRS transmission, the number of subcarriers is $N = 12 \cdot N_{\mathrm{RB}} - 4$, as it was discussed in Section 2.4.3.

Given the estimation of the parameter vector $\boldsymbol{\theta} = [\theta_1, \theta_2, \ldots, \theta_p]$, the minimum variance of any unbiased estimator $\theta_i$ is lower bounded by the CRB, as it is discussed in [Kay98]. This minimum variance is defined by the $[i,i]$ element of the inverse of the Fisher information matrix (FIM) $\mathbf{J}\left(\boldsymbol{\theta}\right)$ as

$$\mathrm{var}\left(\theta_i\right) \geq \mathrm{CRB}_{i,i} = \left[\mathbf{J}^{-1}\left(\boldsymbol{\theta}\right)\right]_{i,i}. \tag{4.2.8}$$

Since $\mathbf{w}$ in (4.2.6) is a complex Gaussian vector, the $[i,j]$ element of the FIM is

$$\begin{aligned}\left[\mathbf{J}\left(\boldsymbol{\theta}\right)\right]_{i,j} = \mathrm{tr}&\left[\mathbf{C}^{-1}\left(\boldsymbol{\theta}\right)\frac{\partial \mathbf{C}\left(\boldsymbol{\theta}\right)}{\theta_i}\mathbf{C}^{-1}\left(\boldsymbol{\theta}\right)\frac{\partial \mathbf{C}\left(\boldsymbol{\theta}\right)}{\theta_j}\right] \\ &+2\mathrm{Re}\left[\frac{\partial \boldsymbol{\mu}^{\mathrm{H}}\left(\boldsymbol{\theta}\right)}{\theta_i}\mathbf{C}^{-1}\left(\boldsymbol{\theta}\right)\frac{\partial \boldsymbol{\mu}\left(\boldsymbol{\theta}\right)}{\theta_j}\right],\end{aligned} \tag{4.2.9}$$

where the mean vector is $\boldsymbol{\mu}\left(\boldsymbol{\theta}\right) = \mathbf{B}\boldsymbol{\Gamma}_\tau \mathbf{F}_L \mathbf{h}$, and the covariance matrix is assumed to be $\mathbf{C}\left(\boldsymbol{\theta}\right) = \mathrm{E}\left[\mathbf{w}\mathbf{w}^{\mathrm{H}}\right] = \sigma_{\mathrm{w}}^2 \mathbf{I}$. The expression in (4.2.9) is known as the Bangs-Slepian s formula, and its proof can be found in Appendix 15C of [Kay98].

### 4.2.1 Periodic-tap model

Considering the periodic-tap estimation model, the taps delays are defined by $\tau_k = \{0, 1, \cdots, L-1\}$, and the Fourier matrix $\mathbf{F}_L$ is written as

$$\mathbf{F}_L = \frac{1}{\sqrt{N}} \begin{bmatrix} 1 & \omega^{-\frac{N}{2}+1} & \cdots & \omega^{\left(-\frac{N}{2}+1\right)(L-1)} \\ \vdots & \vdots & \ddots & \vdots \\ 1 & 1 & \cdots & 1 \\ 1 & \omega & \cdots & \omega^{L-1} \\ \vdots & \vdots & \ddots & \vdots \\ 1 & \omega^{\frac{N}{2}} & \cdots & \omega^{\frac{N}{2}(L-1)} \end{bmatrix}, \tag{4.2.10}$$

where $\omega = e^{-j\frac{2\pi}{N}}$. Thus, the parameter vector to estimate is

$$\boldsymbol{\theta}_{\mathrm{PT}} = \left[\ \tau\ ,\ \mathrm{Re}\left[\mathbf{h}^{\mathrm{T}}\right]\ ,\ \mathrm{Im}\left[\mathbf{h}^{\mathrm{T}}\right]\ \right]^{\mathrm{T}}, \tag{4.2.11}$$

where the real and imaginary part of the channel coefficients $\mathbf{h}$ are considered separately to obtain a real parameter vector $\boldsymbol{\theta}_{\mathrm{PT}}$. The FIM for the periodic-tap model is then computed with the Bangs-Slepian s formula using the signal model in (4.2.1) as

$$\mathbf{J}\left(\boldsymbol{\theta}_{\mathrm{PT}}\right) = \frac{2}{\sigma_{\mathrm{w}}^2} \begin{bmatrix} J_{11} & \mathbf{J}_{21}^{\mathrm{T}} \\ \mathbf{J}_{21} & \mathbf{J}_{22} \end{bmatrix}, \tag{4.2.12}$$

where

$$J_{11} = \mathbf{h}^{\mathrm{H}}\mathbf{F}_L^{\mathrm{H}}\mathbf{B}^{\mathrm{H}}\mathbf{D}^2\mathbf{B}\mathbf{F}_L\mathbf{h}, \tag{4.2.13}$$

$$\mathbf{J}_{21} = \begin{bmatrix} \mathrm{Im}\left[\mathbf{F}_L^{\mathrm{H}}\mathbf{B}^{\mathrm{H}}\mathbf{D}\mathbf{B}\mathbf{F}_L\mathbf{h}\right] \\ -\mathrm{Re}\left[\mathbf{F}_L^{\mathrm{H}}\mathbf{B}^{\mathrm{H}}\mathbf{D}\mathbf{B}\mathbf{F}_L\mathbf{h}\right] \end{bmatrix}, \tag{4.2.14}$$

$$\mathbf{J}_{22} = \begin{bmatrix} \mathrm{Re}\left[\mathbf{F}_L^{\mathrm{H}}\mathbf{B}^{\mathrm{H}}\mathbf{B}\mathbf{F}_L\right] & -\mathrm{Im}\left[\mathbf{F}_L^{\mathrm{H}}\mathbf{B}^{\mathrm{H}}\mathbf{B}\mathbf{F}_L\right] \\ \mathrm{Im}\left[\mathbf{F}_L^{\mathrm{H}}\mathbf{B}^{\mathrm{H}}\mathbf{B}\mathbf{F}_L\right] & \mathrm{Re}\left[\mathbf{F}_L^{\mathrm{H}}\mathbf{B}^{\mathrm{H}}\mathbf{B}\mathbf{F}_L\right] \end{bmatrix}, \tag{4.2.15}$$

being

$$\mathbf{D} = \frac{2\pi}{N} \cdot \mathrm{diag}\left(-N/2+1, \ldots, N/2\right). \tag{4.2.16}$$

The CRB using the periodic-tap estimation model is calculated in [Lar11] as

$$\mathbf{CRB}_{\mathrm{PT}} = \frac{\sigma_{\mathrm{w}}^2}{2} \begin{bmatrix} \gamma_\tau^{-1} & \mathbf{CRB}_{21}^{\mathrm{T}} \\ \mathbf{CRB}_{21} & \mathbf{CRB}_{22} \end{bmatrix} \tag{4.2.17}$$

where

$$\gamma_\tau = \mathbf{h}^{\mathrm{H}} \mathbf{F}_L^{\mathrm{H}} \mathbf{B}^{\mathrm{H}} \mathbf{D} \mathbf{\Pi}^{\perp}_{\mathbf{BF}_L} \mathbf{D} \mathbf{B} \mathbf{F}_L \mathbf{h}, \tag{4.2.18}$$

$$\mathbf{\Pi}^{\perp}_{\mathbf{BF}_L} = \mathbf{I} - \mathbf{BF}_L \left(\mathbf{F}_L^{\mathrm{H}} \mathbf{B}^{\mathrm{H}} \mathbf{B} \mathbf{F}_L\right)^{-1} \mathbf{F}_L^{\mathrm{H}} \mathbf{B}^{\mathrm{H}}. \tag{4.2.19}$$

Thus, the CRB with respect to $\tau$ is

$$\mathrm{CRB}_{\tau,\mathrm{PT}} = \sigma_{\mathrm{w}}^2/2 \cdot \gamma_\tau^{-1}. \tag{4.2.20}$$

The resulting CRB is dependent on the channel coefficients $\mathbf{h}$, being independent of $\tau$. The effect of the channel information on the time-delay estimation is denoted by the projection matrix $\mathbf{\Pi}^{\perp}_{\mathbf{BF}_L}$, as it can be seen in the right part of (4.2.19). In case the channel response $\mathbf{h}$ is assumed to be known, the corresponding bound is obtained by introducing $\mathbf{\Pi}^{\perp}_{\mathbf{BF}_L} = \mathbf{I}$ in (4.2.20), which results in a lower bound than $\mathrm{CRB}_{\tau,\mathrm{PT}}$.

### 4.2.2 Single-tap model

As it could be noticed in Section 4.1, the single-tap estimation model is a particular case of the periodic-tap model for $L = 1$. Thus, the parameter vector for this model is

$$\boldsymbol{\theta}_{\mathrm{ST}} = \left[\, \tau \,,\, \mathrm{Re}\left[h_0\right] \,,\, \mathrm{Im}\left[h_0\right] \,\right]^{\mathrm{T}}. \tag{4.2.21}$$

Since the Fourier matrix is actually a vector in this case, i.e. $\mathbf{F}_1 = \mathbf{1}/\sqrt{N}$, the CRB with respect to $\tau$ using the single-tap model is just a particularization of (4.2.20), resulting in

$$\mathrm{CRB}_{\tau,\mathrm{ST}} = \frac{\sigma_{\mathrm{w}}^2 \cdot N}{2 \cdot h_0^{\mathrm{H}} \cdot h_0} \cdot \left(\mathbf{b}^{\mathrm{H}} \mathbf{D} \mathbf{\Pi}^{\perp}_{\mathbf{b}} \mathbf{D} \mathbf{b}\right)^{-1}, \tag{4.2.22}$$

where

$$\mathbf{b} = \sqrt{2C} \cdot \left[ b\left(-N/2+1\right), \ldots, b\left(N/2\right) \right]^{\mathrm{T}}, \tag{4.2.23}$$

$$\mathbf{\Pi}_{\mathbf{b}}^{\perp} = \mathbf{I} - \mathbf{b}\left(\mathbf{b}^{\mathrm{H}}\mathbf{b}\right)^{-1}\mathbf{b}^{\mathrm{H}}. \tag{4.2.24}$$

If the channel coefficient $h_0$ is considered to be known and equal to one, the CRB derived in (3.2.27) is obtained by substituting the projection matrix $\mathbf{\Pi}_{\mathbf{b}}^{\perp}$ by the identity matrix $\mathbf{I}$ in (4.2.22).

### 4.2.3 Hybrid-tap model

Considering the hybrid-tap estimation model, the parameter vector is

$$\boldsymbol{\theta}_{\mathrm{HT}} = \left[\ \tau\ ,\ \mathrm{Re}\left[\mathbf{h}^{\mathrm{T}}\right]\ ,\ \mathrm{Im}\left[\mathbf{h}^{\mathrm{T}}\right]\ ,\ \tau'\ \right]^{\mathrm{T}}. \tag{4.2.25}$$

This parameter vector includes one more estimate than $\boldsymbol{\theta}_{\mathrm{PT}}$, i.e. the delay $\tau'$ of the arbitrary tap introduced between the first two periodic taps. Thus, the Fourier matrix depends on $\tau'$ as follows:

$$\mathbf{F}_{L,\tau'} = \frac{1}{\sqrt{N}} \begin{bmatrix} 1 & \omega^{-\frac{N}{2}+1} & \cdots & \omega^{\left(-\frac{N}{2}+1\right)(L-2)} & \omega^{\left(-\frac{N}{2}+1\right)\tau'} \\ \vdots & \vdots & \ddots & \vdots & \vdots \\ 1 & 1 & \cdots & 1 & 1 \\ 1 & \omega & \cdots & \omega^{L-2} & \omega^{\tau'} \\ \vdots & \vdots & \ddots & \vdots & \vdots \\ 1 & \omega^{\frac{N}{2}} & \cdots & \omega^{\frac{N}{2}(L-2)} & \omega^{\frac{N}{2}\tau'} \end{bmatrix}. \tag{4.2.26}$$

Since the hybrid-tap model is an extension of the periodic-tap model, the Fourier matrix $\mathbf{F}_L$ is substituted by $\mathbf{F}_{L,\tau'}$ in (4.2.12)-(4.2.15), and the FIM using the hybrid-tap model results in the following partitioned matrix:

$$\mathbf{J}\left(\boldsymbol{\theta}_{\mathrm{HT}}\right) = \frac{2}{\sigma_{\mathrm{w}}^2} \begin{bmatrix} J_{11} & \mathbf{J}_{21}^{\mathrm{T}} & J_{31}^{\mathrm{T}} \\ \mathbf{J}_{21} & \mathbf{J}_{22} & \mathbf{J}_{23} \\ J_{31} & \mathbf{J}_{23}^{\mathrm{T}} & J_{33} \end{bmatrix} = \left[\begin{array}{cc|c} \multicolumn{2}{c|}{\multirow{2}{*}{$\mathbf{J}\left(\boldsymbol{\theta}_{\mathrm{PT}}\right)$}} & J_{31}^{\mathrm{T}} \\ & & \mathbf{J}_{23} \\ \hline J_{31} & \mathbf{J}_{23}^{\mathrm{T}} & J_{33} \end{array}\right], \tag{4.2.27}$$

where

$$J_{31} = \mathrm{Re}\left[\mathbf{h}^{\mathrm{H}}\mathbf{d}\mathbf{d}^{\mathrm{T}}\mathbf{F}_{L,\tau'}^{\mathrm{H}}\mathbf{B}^{\mathrm{H}}\mathbf{D}^{2}\mathbf{B}\mathbf{F}_{L,\tau'}\mathbf{h}\right], \tag{4.2.28}$$

$$\mathbf{J}_{23} = \begin{bmatrix} \mathrm{Im}\left[\mathbf{F}_{L,\tau'}^{\mathrm{H}}\mathbf{B}^{\mathrm{H}}\mathbf{D}\mathbf{B}\mathbf{F}_{L,\tau'}\mathbf{d}\mathbf{d}^{\mathrm{T}}\mathbf{h}\right] \\ -\mathrm{Re}\left[\mathbf{F}_{L,\tau'}^{\mathrm{H}}\mathbf{B}^{\mathrm{H}}\mathbf{D}\mathbf{B}\mathbf{F}_{L,\tau'}\mathbf{d}\mathbf{d}^{\mathrm{T}}\mathbf{h}\right] \end{bmatrix}, \tag{4.2.29}$$

$$J_{33} = \mathbf{h}^{\mathrm{H}}\mathbf{d}\mathbf{d}^{\mathrm{T}}\mathbf{F}_{L,\tau'}^{\mathrm{H}}\mathbf{B}^{\mathrm{H}}\mathbf{D}^{2}\mathbf{B}\mathbf{F}_{L,\tau'}\mathbf{d}\mathbf{d}^{\mathrm{T}}\mathbf{h}, \tag{4.2.30}$$

being $\mathbf{d} = [0, \ldots, 0, 1]^{\mathrm{T}}$. The $L \times 1$ vector $\mathbf{d}$ is obtained from the derivative of the Fourier matrix $\mathbf{F}_{L,\tau'}$ with respect to $\tau'$, which is written as

$$\frac{\partial \mathbf{F}_{L,\tau'}}{\partial \tau'} = -j\frac{2\pi}{N\sqrt{N}} \begin{bmatrix} 0 & \cdots & 0 & \left(-\frac{N}{2}+1\right)\omega^{\left(-\frac{N}{2}+1\right)\tau'} \\ \vdots & \ddots & 0 & \vdots \\ 0 & \cdots & 0 & 0 \\ 0 & \cdots & 0 & \omega^{\tau'} \\ \vdots & \ddots & 0 & \vdots \\ 0 & \cdots & 0 & \frac{N}{2}\omega^{\frac{N}{2}\tau'} \end{bmatrix} = -j\mathbf{D}\mathbf{F}_{L,\tau'}\mathbf{d}\mathbf{d}^{\mathrm{T}}. \tag{4.2.31}$$

The CRB with respect to $\tau$ using the hybrid-tap model is computed numerically as follows:

$$\mathrm{CRB}_{\tau,\mathrm{HT}} = \left[\mathbf{J}^{-1}\left(\boldsymbol{\theta}_{\mathrm{HT}}\right)\right]_{1,1}. \tag{4.2.32}$$

Given the CRB for the channel estimation models derived in this section, the expectation of the CRB for multiple channel realizations results in the expected CRB (ECRB), i.e.

$$\mathrm{ECRB}_{\tau} = \mathrm{E}\left[\mathrm{CRB}_{\tau}\right]. \tag{4.2.33}$$

The computation of the ECRB can be done numerically as in this work, or it can be obtained analytically as it has been presented in [Mon13].

## 4.3 Joint maximum likelihood estimation

### 4.3.1 One-dimensional joint ML (1D-JML) estimator

In order to derive a low-complexity time-delay estimator, the periodic-tap model is first selected. Thus, the estimation parameters are the time delay $\tau$ and the channel coefficients $\mathbf{h} = [h_0, \cdots, h_{L-1}]^{\mathrm{T}}$. Let us define a matrix $\mathbf{A}$ of dimensions $N \times L$ as a function of $\tau$ as follows:

$$\mathbf{A}_\tau = \mathbf{B}\boldsymbol{\Gamma}_\tau \mathbf{F}_L. \tag{4.3.1}$$

Hence, the received signal is expressed as

$$\mathbf{r} = \mathbf{A}_\tau \mathbf{h} + \mathbf{w}. \tag{4.3.2}$$

Given this formulation, the maximum likelihood criterion is applied, which results in

$$\begin{bmatrix} \tau \\ \mathbf{h} \end{bmatrix} = \arg\max_{\tau,\mathbf{h}} \Lambda\left(\mathbf{r}; \tau, \mathbf{h}\right), \tag{4.3.3}$$

where $\Lambda\left(\mathbf{r}; \tau, \mathbf{h}\right)$ is the likelihood function of the received samples parametrized by the unknowns $\tau$ and $\mathbf{h}$, which is defined by a multivariate Gaussian distribution,

$$\Lambda\left(\mathbf{r}; \tau, \mathbf{h}\right) = C_0 \exp\left(-\frac{1}{\sigma_{\mathrm{w}}^2}\|\mathbf{r} - \mathbf{A}_\tau \mathbf{h}\|^2\right), \tag{4.3.4}$$

being $C_0$ an irrelevant constant. Substituting the log-likelihood function in (4.3.3) leads to the following minimization problem:

$$\begin{bmatrix} \tau \\ \mathbf{h} \end{bmatrix} = \arg\min_{\tau,\mathbf{h}} \left\{\|\mathbf{r} - \mathbf{A}_\tau \mathbf{h}\|^2\right\}, \tag{4.3.5}$$

which coincides with the nonlinear least squares (NLS) criterion, since $\tau$ depends nonlinearly on the received signal model. The resulting two-dimensional optimization can be separated by minimizing first with respect to $\mathbf{h}$ and then with respect to $\tau$ as in [Gol73], which can be written as

$$\tau = \arg\min_{\tau} \left\{\min_{\mathbf{h}} \|\mathbf{r} - \mathbf{A}_\tau \mathbf{h}\|^2\right\}. \tag{4.3.6}$$

Then, the well-known least-squares solution can be applied to obtain the ML estimate of the unknown channel coefficients as

$$\mathbf{h} = \mathbf{A}_\tau^\dagger \mathbf{r}, \tag{4.3.7}$$

where $\mathbf{A}_\tau^\dagger$ denotes the Moore-Penrose pseudo-inverse of $\mathbf{A}_\tau$, which is defined as

$$\mathbf{A}_\tau^\dagger \doteq \left(\mathbf{A}_\tau^{\mathrm{H}} \mathbf{A}_\tau\right)^{-1} \mathbf{A}_\tau^{\mathrm{H}}, \tag{4.3.8}$$

being the superindex $^{\mathrm{H}}$ the Hermitian conjugate. Introducing the least-squares solution into (4.3.6), the ML estimation of the time delay results in

$$\tau = \arg\min_\tau \left\{ \|\mathbf{r} - \mathbf{A}_\tau \mathbf{A}_\tau^\dagger \mathbf{r}\|^2 \right\} = \arg\min_\tau \left\{ \|\mathbf{P}_{\mathbf{A},\tau}^\perp \mathbf{r}\|^2 \right\}, \tag{4.3.9}$$

where $\mathbf{P}_{\mathbf{A},\tau}^\perp = \mathbf{I} - \mathbf{A}_\tau \left(\mathbf{A}_\tau^{\mathrm{H}} \mathbf{A}_\tau\right)^{-1} \mathbf{A}_\tau^{\mathrm{H}}$ is the orthogonal projection matrix onto the subspace orthogonal to that spanned by the columns of $\mathbf{A}_\tau$. Thus, the decoupling of $\tau$ and $\mathbf{h}$ leads to the proposed ML time-delay estimator of (4.3.9). It is hereafter called **one-dimensional joint ML (1D-JML)** time-delay and channel estimator. The 1D-JML estimation is computed numerically by minimizing the cost function of $\|\mathbf{P}_{\mathbf{A},\tau}^\perp \mathbf{r}\|^2$ as a function of $\tau$. This optimization is not complex because it is a one-dimensional function that is simply evaluated within the range $[-1/2, 1/2]$ and then minimized. This range is defined to find the residual time delay after a coarse estimation. The minimum could be obtained by solving the function with a grid of points sufficiently fine. However, the `fminbnd` function of MATLAB [Mat13b] is used for an efficient computation, which finds the minimum in the search interval. Instead of doing an exhaustive evaluation, this function searches the minimum by means of the Golden section technique followed by a parabolic interpolation.

Let us study the particular case of $L$ equal to one. In this case, the channel is formed only by one ray, thus $\mathbf{a}_\tau$ is a $N \times 1$ vector defined as $\mathbf{a}_\tau = \mathbf{B}\boldsymbol{\Gamma}_\tau \mathbf{F}_1$. Developing further the expression of (4.3.9), the one-dimensional optimization problem results into the following maximization of the cost function

$$\tau = \arg\max_\tau \left\{ |\mathbf{a}_\tau^{\mathrm{H}} \mathbf{r}|^2 \right\} = \arg\max_\tau \left\{ |R(\tau)|^2 \right\}, \tag{4.3.10}$$

where $R(\tau)$ is the cross-correlation of the received signal $\mathbf{r}$ with the pilot symbols $\mathbf{b}$,

defined in the scalar notation as

$$R(\tau) = \sum_{n=0}^{N-1} r(n) \cdot b^*(n) \cdot \exp\left(j\frac{2\pi n\tau}{N}\right). \tag{4.3.11}$$

Thus, the particular case of the joint ML estimation for $L = 1$ reduces to the estimation based on the correlation or matched filter output. This confirms the optimality of the matched filter for time-delay estimation in the absence of multipath. In addition, if the range of the time-delay estimation is bounded close to $\tau = 0$, the 1D-JML estimator for $L = 1$ can be compared to those correlation-based estimators that use an energy-threshold to find the first arriving path, such as the first-peak estimation introduced in Section 3.5.4. These threshold-based estimators are widely adopted for multipath mitigation due to their low-complexity, as it is further described in [Dar09].

### 4.3.2 Two-dimensional joint ML (2D-JML) estimator

The derivation of the JML estimator, using the periodic-tap channel estimation model described in (4.1.3), results in a low-complexity implementation by decoupling the problem of joint time-delay and channel estimation. Now, the hybrid-tap estimation model of (4.1.4) is applied to enhance the characterization of the physical channel response. Using this novel channel parameterization, the model mismatch is reduced at the expense of adding one more estimation parameter, the arbitrary tap delay $\tau'$. Considering the derivation of the 1D-JML estimator obtained in (4.3.9), the problem at hand is solved following the same procedure. This leads to the **two-dimensional joint ML (2D-JML)** estimator, which can be expressed as

$$\begin{bmatrix}\tau \\ \tau'\end{bmatrix} = \arg\min_{\tau,\tau'} \left\{ \|\mathbf{P}^{\perp}_{\mathbf{A},\tau,\tau'}\mathbf{r}\|^2 \right\}, \tag{4.3.12}$$
$$\text{s.t. } 0 < \tau' < 1 \,,$$

where $\mathbf{P}^{\perp}_{\mathbf{A},\tau,\tau'} = \mathbf{I} - \mathbf{A}_{\tau,\tau'}\left(\mathbf{A}^{\mathrm{H}}_{\tau,\tau'}\mathbf{A}_{\tau,\tau'}\right)^{-1}\mathbf{A}^{\mathrm{H}}_{\tau,\tau'}$, and $\mathbf{A}_{\tau,\tau'} = \mathbf{B}\boldsymbol{\Gamma}_{\tau}\mathbf{F}_{L,\tau'}$. The two-dimensional optimization of (4.3.12) is computed by an exhaustive search in the $\tau \times \tau'$ region of $[-1/2, 1/2] \times [0, 1]$. The `patternsearch` function of MATLAB [Mat13a] is used for an efficient computation of the 2D optimization. This function is configured with a direct search algorithm, which is called generalized pattern search. The pattern search is implemented in two phases per iteration [Aud02]: first, a global search of the minimum in a grid of points over the search region, and second, a local search with a grid of points around

the tentative solution, called local poll. This exhaustive evaluation will likely convergence to the global minimum in the search region, instead of any local minima.

## 4.4 Multipath error envelope

### 4.4.1 General assessment

As it was discussed in Section 3.5.2, the main properties of a certain estimator in the presence of multipath can be studied through the MPEE. This metric evaluates the impact of a two-ray multipath model on the time-delay estimation. In absence of noise, the MPEE represents the time-delay error produced by a multipath reflection (with specific delay, power and phase) when it is added to the LoS component. Thus, the received signal in the MPEE analysis is defined as

$$y(m) = x(m-\tau) + a_1 \cdot e^{j\phi_1} \cdot x(m-\tau-\tau_1), \tag{4.4.1}$$

where $a_1$, $\phi_1$ and $\tau_1$ are the amplitude, phase and delay of the multipath ray, respectively. The MPEE is computed considering $-1$ dB of relative power to the LoS ray (i.e. SMR = 1 dB) within a delay range between 0 and $3{\cdot}T_s/2$. The multipath ray is added constructively and destructively to the LoS component, i.e. the multipath contribution is in-phase (i.e. $\phi_1 = 0$) and counter-phase (i.e. $\phi_1 = \pi$), respectively. In this scenario, the LTE PRS is configured for the lowest bandwidth of 6 RB, and assuming no data allocation on the transmitted symbol. As it was discussed in Section 2.4.3, the 6-RB PRS bandwidth is defined by $N = 12 \cdot N_{\text{RB}} - 4 = 68$ subcarriers, which results in $T_s = T/N = 980.39$ ns and a signal bandwidth equal to $1/T_s = 1.02$ MHz. The OFDM signal is considered to be successfully acquired, being the receiver in signal tracking mode, thus the time-delay estimation range is defined within $[-T_s/2, T_s/2]$, or $[-1/2, 1/2]$ since $\tau$ is in $T_s$ units.

The resulting MPEE is shown in Figure 4.1, by comparing the 1D-JML estimator for $L = \{1, 8\}$ with the 2D-JML estimator for $L = \{2, 8\}$, using expressions (4.3.10), (4.3.9) and (4.3.12), respectively. As it can be seen, the multipath errors are normalized with respect to the sampling period $T_s$. Three main results can be identified:

- The effect of increasing the number of taps from $L = 1$ to $L = 8$ in the 1D-JML estimator, that is, from using a single-tap model to a periodic-tap model, improves the TDE performance, but there is still a significant bias in both cases.

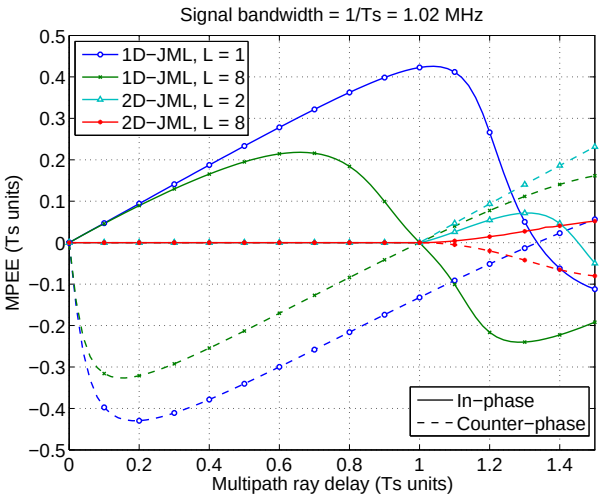


Figure 4.1: MPEE of the 1D- and 2D-JML estimators using the single-tap, periodic-tap and hybrid-tap models for the 6-RB PRS without data transmission.

- While the 1D-JML estimator for $L = \{1, 8\}$ is only unbiased at certain instants (e.g. $\tau = \{1.34, 1\}$, respectively), the 2D-JML estimator is completely unbiased for values of $\tau_1$ within 0 and 1, due to the matching between the channel estimation model and the propagation channel model.
- The effect of decreasing the number of taps from $L = 8$ to $L = 2$ in the 2D-JML estimator does not have the same behaviour as in the 1D-JML estimator, because the hybrid approach is still unbiased for values of $\tau_1$ within 0 and 1.

### 4.4.2 Analysis of the 1D-JML cost function

The impact of the model mismatch can be further assessed by studying the cost function of the estimators described in (4.3.10), (4.3.9) and (4.3.12). Let us first consider the 1D-JML estimator and only the LoS signal, corresponding to a multipath delay equal to zero (i.e. $\tau_1 = 0$). The cost function of the 1D-JML for $L = \{1, 8\}$ is computed using $\|\mathbf{P}^{\perp}_{\mathbf{A},\tau}\mathbf{r}\|^2/\|\mathbf{r}\|^2$, and the channel coefficients $\mathbf{h}$ are estimated as in (4.3.7). As it is shown in Figure 4.2(a), the 1D-JML estimator for $L = 1$ has a global minimum, while the 1D-JML estimator for $L = 8$ has eight local minima. These multiple local solutions for $L = 8$ are natural and inherent in the time-delay estimation when the channel is also unknown. In this case, we have to deal with two unknowns that are related among them, and this

produces that inevitably, the result is coupled between the time delay and the channel. In fact, there is no ambiguity, because the total delay of the signal, which is of main interest for positioning, is unique. Thus, the solution to the problem is unique too. But, since the solution is formed by two coupled elements, one has to interpret first which is the time delay with respect to the channel estimation, and which is the channel estimated. Then, the total delay of the signal has to be determined, resulting in a unique solution without any ambiguity. Taking this into account, two cases can be considered in order to estimate the time delay for $L > 1$:

1. If the value of $\tau$ is around 0, which corresponds to the blue dot in Figure 4.2(a), the resulting channel estimation is depicted in blue in Figure 4.2(b).

2. If the value of $\tau$ is around 1 or around 2, which corresponds to the red square or the purple triangle in Figure 4.2(a), respectively, the resulting channel estimation is depicted in red or purple in Figure 4.2(b), respectively. These values of $\tau$ would only be chosen if the search interval of $\tau$ is wider than $[-1/2, 1/2]$, such as $[-8, 2]$, and one of these values corresponds to the global minimum of the cost function.

In both cases, if the value of $\tau$ is compensated considering the delay of the first relevant tap (e.g. the first tap with an estimated amplitude exceeding a certain threshold) in the channel estimation, the resulting time delay is the same (approximate) value of the total delay of the signal. The second case is equivalent to delay the channel estimation and advance $\tau$, thus the effects cancel. This shows that the time-delay estimation in a unknown channel is coupled with the channel estimation. That is, there are multiple solutions of the time delay with respect to multiple channel estimations, but at the end, all of these combinations coincide into one solution, which is the total delay of the signal. Therefore, given that a change in $\tau$ equal to a $T_\mathrm{s}$ unit or a multiple of it can be counter compensated with a shift in the channel impulse response, it is reasonable to limit the search range of $\tau$ to $[-1/2, 1/2]$, as in this work.

Being applicable the search range of $\tau$ under use, the value of $\tau$ should be first compensated, and then estimated again in the search range with the compensation applied. When the multipath delay is larger than zero (i.e. $\tau_1 > 0$), the local minima correspond to slightly different time-delay solutions, even if these solutions of $\tau$ are compensated. In order to prove this statement, the time delay is estimated by minimizing the cost function for every local minimum, e.g. within a range of $\tau$ between $[k - 3/8, k + 3/8]$, where $k = 0, \ldots, L - 1$. As an example, the first, second and third local minimum are shown in Figure 4.2(a). Once the compensation is applied, the MPEE for every local solution is

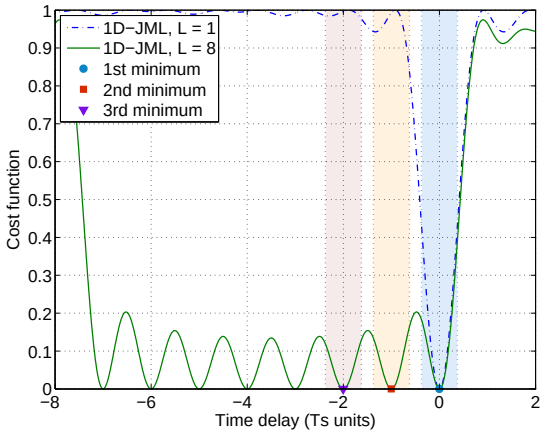


(a) Cost function for $\tau_1 = 0$

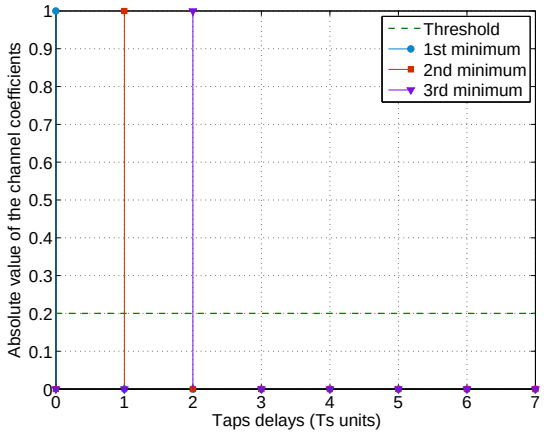


(b) CIR for $\tau_1 = 0$ and $L = 8$

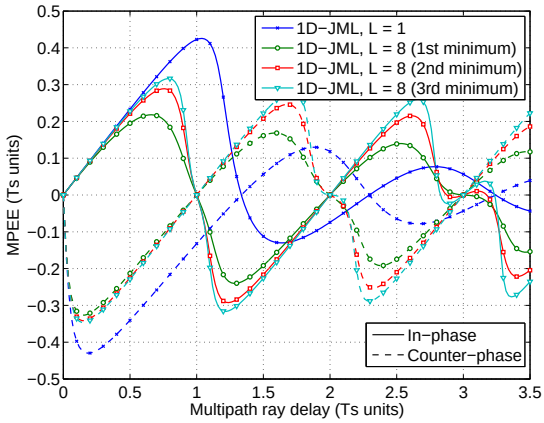


(c) MPEE for different local minima

Figure 4.2: Comparison of the different solutions of the 1D-JML cost function for a 6-RB PRS bandwidth (i.e. BW $= 1/T_s = N \cdot F_{sc} = 1.02$ MHz).

depicted in Figure 4.2(c), resulting in slightly different multipath errors for every solution. The optimum solution is the first local minimum (close to $\tau = 0$), because it produces the lowest multipath error.

The 1D-JML cost function can also be depicted for every multipath delay, i.e. delay of the multipath ray (with respect to the LoS ray) used to compute the MPEE, as it is shown in Figure 4.3. The two-dimensional plot shows the logarithm of the cost function, and the resulting MPEE is highlighted in red. The ideal case corresponds to a time delay equal to zero for every multipath delay. As it can be seen in Figure 4.3(a), this case is obtained by using the known propagation delays into the 1D-JML estimator for $L = 2$. In contrast, the 1D-JML estimator for $L = \{1, 8\}$ using single- and periodic-tap models results in a model mismatch that produces a certain time-delay error in most of the cases, as it is shown in Figure 4.3(b) and 4.3(c). The periodic-tap 1D-JML estimator is then not able to counteract completely the channel response, and part of the error produced in the channel estimation ends into the time-delay estimation.

Let us also analyse the relation between the cost function of the JML estimator and the CIR estimated for a certain $\tau$. For this purpose, a multipath delay $\tau_1$ equal to 2.5 is considered in the two-ray channel model. The resulting cost function using the 1D-JML estimator for $L = 8$ is shown in Figure 4.4(a), which corresponds to a cut in the y-axis at $\tau_1 = 2.5$ of Figure 4.3(c). The local minimum of the cost function for values of $\tau$ within $[-1/2, 1/2]$ is depicted in a blue dot, and the global minimum is depicted with a red square. Considering these solutions, their absolute CIR is shown in Figure 4.4(b). By using the delay of the first relevant tap, the solution of the global minimum can be compensated, resulting in a value close to the solution of $\tau$ around 0. As it can be seen, the number of relevant taps (i.e. two taps out of eight estimated taps) can be related to the number of local minima in the cost function (i.e. six minima). In both cases, the relevance of a certain tap or a certain local minimum should be assessed with the adequate threshold.

Another important aspect on the JML estimation is the number of taps $L$ to estimate. Let us compute the MPEE of the 1D-JML estimator for $L = \{2, 3, 8\}$, as it can be seen in Figure 4.5(a). The 1D-JML estimation for $L > 1$ becomes biased at a multiple of a sample when the delay spread is higher than the number of taps, i.e. $\tau_1 > L-1$. At these large delays, the channel is under-estimated, thus producing a higher bias on the TDE in most of the cases. This effect can also be seen in the 2D plot of Figure 4.3(c), and it could be avoided by determining the model order of the channel.

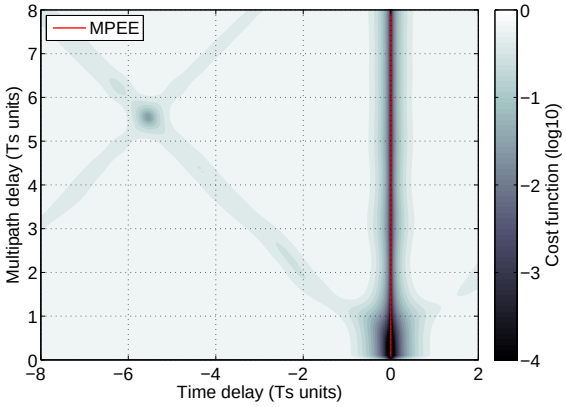


(a) 1D-JML estimator for $L = 2$ with known delays

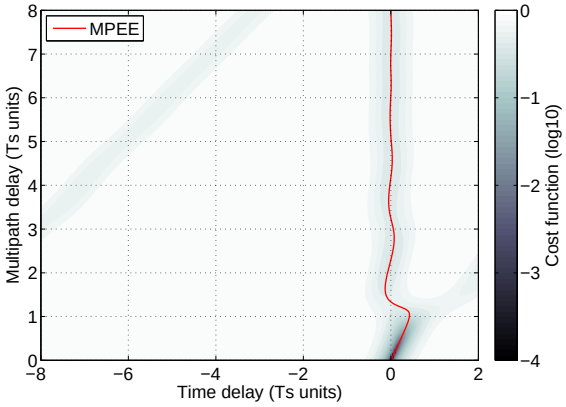


(b) Single-tap 1D-JML estimator for $L = 1$

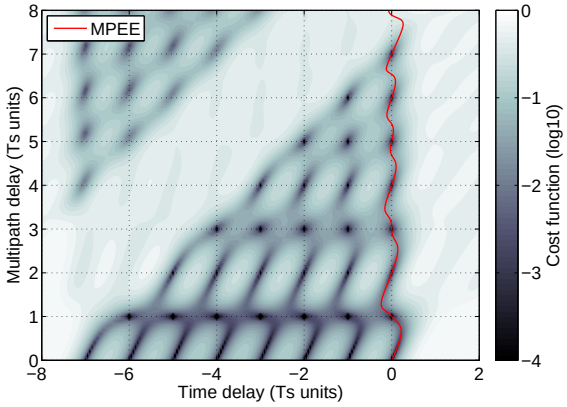


(c) Periodic-tap 1D-JML estimator for $L = 8$

Figure 4.3: Logarithm of the cost function of the 1D-JML estimator using the known propagation delays, the single-tap model and the periodic-tap model as function of the multipath delay in a two-ray channel with $\phi_1 = 0$ and 6-RB PRS bandwidth.

Finally, the signal bandwidth, which is directly related to the sampling period $T_s$, may affect the bias of the time delay. In Figure 4.5(b), the MPEE of the 1D-JML for $L = \{1, 8\}$ is computed using the PRS with a signal bandwidth from 6 RB to 100 RB. In absolute terms, a higher signal bandwidth implies a reduction on the multipath error of the estimators, as it was shown in Figure 3.14(b) of Section 3.5.2. However, the impact of the bandwidth is very small when scaling the results by the sampling period $T_s$. This is shown in Table 4.2 by normalizing over $T_s$ the maximum (absolute) errors $\epsilon_{max}$ obtained in the MPEE. Then, $\epsilon_{max}$ (in $T_s$ units) for 6-RB bandwidth is extrapolated to obtain the maximum errors for the rest of bandwidths. In this case, a scaling error $\gamma$ is produced due to the impact of the signal bandwidth, and it is added in Table 4.2 as a percentage between the true value of $\epsilon_{max}$ and its extrapolation. The results of the scaling error prove the minor differences on the multipath error due to a change of the signal bandwidth.

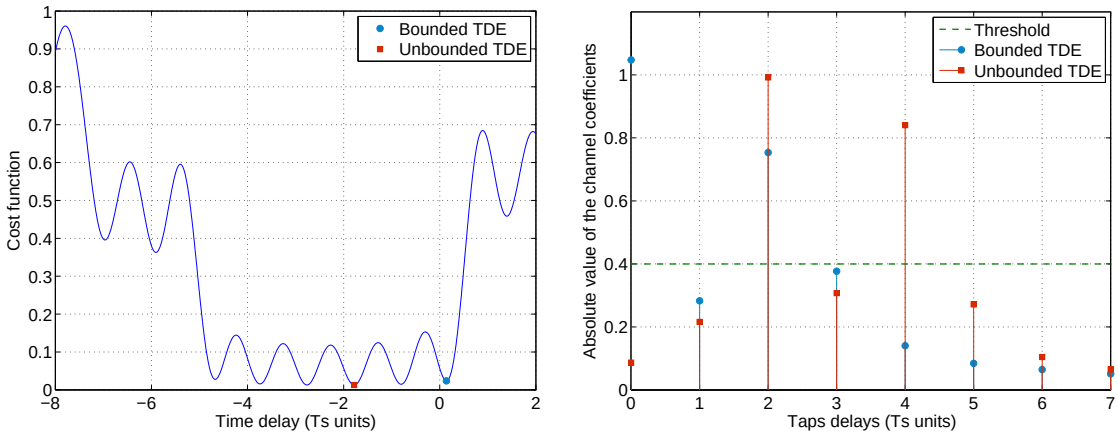


(a) Cost function for $\tau_1 = 0$ (b) CIR for $\tau_1 = 0$ and $L = 8$

Figure 4.4: Cost function and CIR of the bounded and unbounded 1D-JML estimator for $L = 8$ using a 6-RB PRS bandwidth (i.e. 1.02 MHz) in a two-ray multipath channel, where the multipath delay $\tau_1$ is equal to $2.5 \cdot T_s$ and $\phi_1 = 0$.

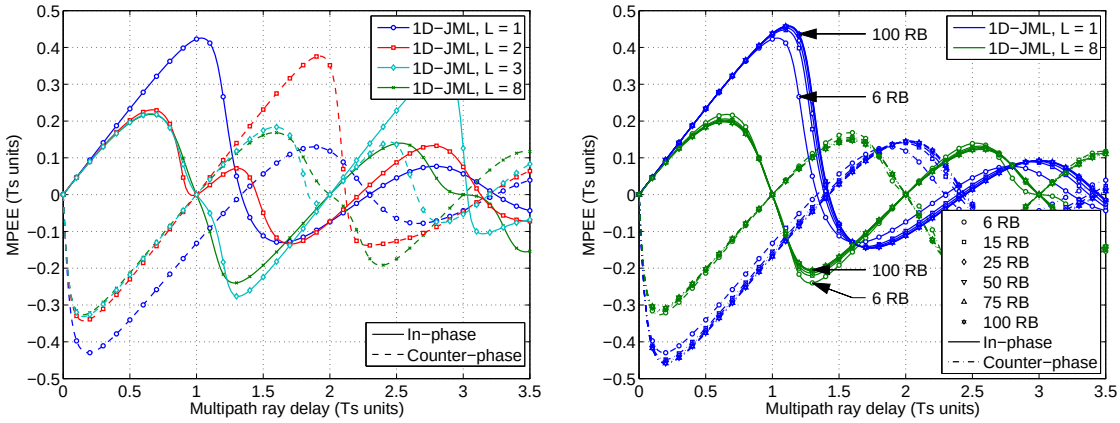


(a) MPEE depending on $L$ for a 6-RB bandwidth (b) MPEE depending on the signal bandwidth

Figure 4.5: MPEE of the 1D-JML estimators for different number of taps and signal bandwidth using the PRS without data transmission.

Table 4.2: Maximum TDE errors of the 1D-JML in the MPEE.

| | | $\epsilon_{\max,L=1}$ (m) / $\gamma$ (%) | | $\epsilon_{\max,L=8}$ (m) / $\gamma$ (%) | |
|---|---|---|---|---|---|
| Bandwidth (RB) | $T_s/2$ (m) | $\phi_1 = 0$ | $\phi_1 = \pi$ | $\phi_1 = 0$ | $\phi_1 = \pi$ |
| 6 | 147.06 | 125.16 / 0.00 | -126.37 / 0.00 | 64.14 / 0.00 | -96.01 / 0.00 |
| 15 | 56.82 | 50.83 / 4.86 | -50.93 / 4.14 | 23.38 / 5.99 | -36.17 / 2.56 |
| 25 | 33.78 | 30.61 / 6.05 | -30.63 / 5.21 | 13.67 / 7.81 | -21.34 / 3.37 |
| 50 | 16.78 | 15.33 / 6.86 | -15.34 / 6.00 | 6.69 / 9.32 | -10.53 / 4.03 |
| 75 | 11.16 | 10.23 / 7.14 | -10.23 / 6.26 | 4.43 / 9.85 | -6.99 / 4.26 |
| 100 | 8.36 | 7.67 / 7.28 | -7.68 / 6.39 | 3.31 / 10.13 | -5.23 / 4.38 |

### 4.4.3 Analysis of the 2D-JML cost function

The 2D-JML estimator is the new approach proposed to counteract close-in multipath, while still preserving a low-complexity on the time-delay estimation. The 2D-JML estimator can be further assessed by analysing its two-dimensional cost function for values of $\tau$ within $[-1/2, 1/2]$ and values of $\tau'$ within $[0, 1]$. Considering a two-ray channel model, the multipath delays $\tau_1 = \{0.4, 0.8, 1.2\}$ and the multipath phases $\phi_1 = \{0, \pi\}$ are used to compute the 2D-JML cost function for $L = 8$, as it is shown in Figure 4.6. This cost function have several local minima in most of the cases, thus the implementation of the 2D-JML estimator should avoid the convergence to a local minimum. As it was discussed in Section 4.3.2, the problem can still be solved by an exhaustive search in the region of interest with a grid of points sufficiently fine. Then, the 2D-JML estimator results unbiased for the cases with $\tau_1 < 1$, which represent close-in multipath. For those cases, a global minimum is found at $\tau = 0$ for the arbitrary-tap delay equal to the multipath delay, i.e. $\tau' = \tau_1$, as it can be seen with a red dot in Figure 4.6(a), 4.6(b), 4.6(c) and 4.6(d). If the multipath delay is larger than one (i.e. $\tau_1 > 1$), the time-delay estimation is biased in most of the cases due to the model mismatch, as it is shown in Figure 4.6(e) and 4.6(f).

## 4.5 Bias induced by LTE channel models

The MPEE has shown the bias introduced by a particular multipath ray on the TDE. The results shown in Figure 4.1 indicate the potential of the JML approach to improve the TDE performance with respect to the matched filter. However, the two-ray multipath model does not represent general urban channels. Thus, the channel models specified in LTE are used to assess the performance of the estimators in more realistic conditions.

As it was introduced in Section 3.5.1, the LTE standard adopts tapped-delay line channel models, where each tap corresponds to a multipath ray characterized by a fixed delay, relative average power and Doppler spectrum. These models are the EPA, EVA and ETU channel models, and their main parameters, i.e. tap delay $t_k$ and relative average power $\overline{\mathrm{RP}}_k$, were described in Table 3.2. In Section 3.5.3, the mean delay of the PDP was introduced to approximately characterize the channel impact on the ranging error. Since every channel realisation may produce a different mean delay, the PDF of the mean delay is computed for the EPA, EVA and ETU channel models, as it is shown in Figure 4.7. The mean delay is in units of microseconds, and the sampling period $T_\mathrm{s}$ is indicated

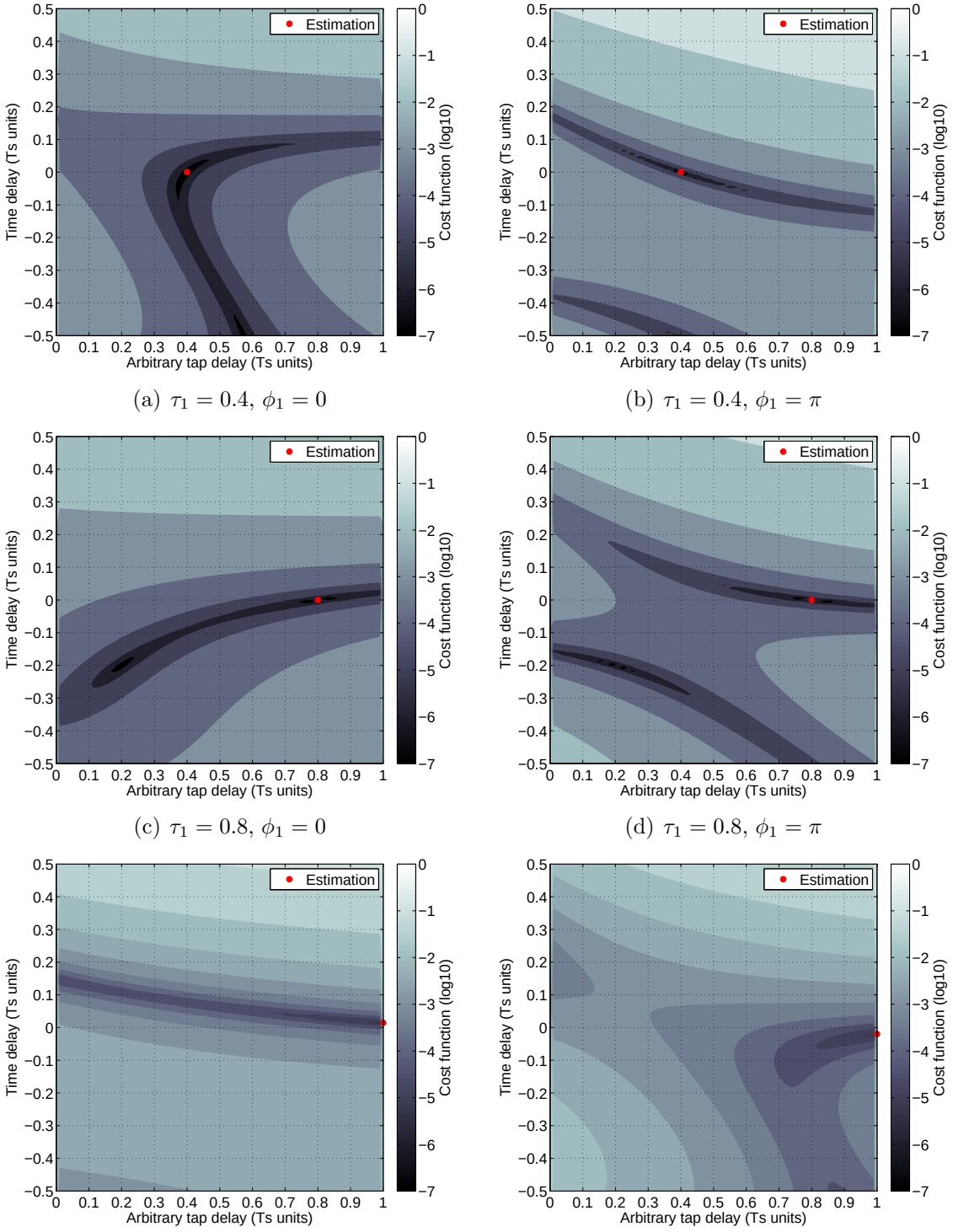


(a) $\tau_1 = 0.4$, $\phi_1 = 0$

(b) $\tau_1 = 0.4$, $\phi_1 = \pi$

(c) $\tau_1 = 0.8$, $\phi_1 = 0$

(d) $\tau_1 = 0.8$, $\phi_1 = \pi$

(e) $\tau_1 = 1.2$, $\phi_1 = 0$

(f) $\tau_1 = 1.2$, $\phi_1 = \pi$

Figure 4.6: Logarithm of the cost function of the 2D-JML estimator for $L = 8$, considering different delays and phases of a multipath ray with SMR = 1 dB added to the LoS signal.

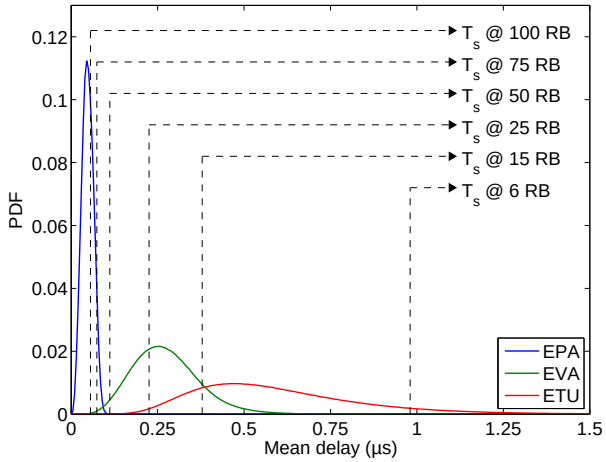


Figure 4.7: Probability density function of the mean delay for the LTE channel models, indicating the sampling period $T_\mathrm{s}$ for every signal bandwidth.

for every LTE signal bandwidth. The PDF of the mean delay describes those tap delays with a major contribution for a certain channel. Thus, this metric can be used to define close-in multipath scenarios, if most of the channel contribution is within a sampling period $T_\mathrm{s}$ with respect to the LoS ray, such as the EPA model or the ETU model with a 6-RB bandwidth. Considering the LTE standard models, the bias of the 1D- and 2D-JML estimators is assessed in this section.

### 4.5.1 Particular assessment of the signal bandwidth impact

#### Low signal bandwidth (i.e. 1.4 MHz)

The effect of multipath on the time-delay estimation is first assessed statistically considering the ETU model and the lowest LTE bandwidth of 1.4 MHz, which can be considered a close-in multipath scenario. Within this bandwidth, the PRS is allocated along 6 RB without data transmission, which results in a signal bandwidth equal to $1/T_\mathrm{s} = 1.02$ MHz. For this case, 1000 ETU realisations are computed with a Doppler shift of 500 Hz. The resulting channel is represented with the average power-delay profile $\overline{\mathrm{PDP}}$ in Figure 4.8. The average PDP is calculated with the mean absolute value of the discrete CIR for every $\ell-$th realisation $h_\ell(m)$ in the interval $[\tau, \tau+8]$, that is,

$$\overline{\mathrm{PDP}}(m) = \frac{1}{N_\ell} \cdot \sum_{\ell=0}^{N_\ell-1} |h_\ell(m)|^2, \quad \tau < m < \tau + 8, \tag{4.5.1}$$

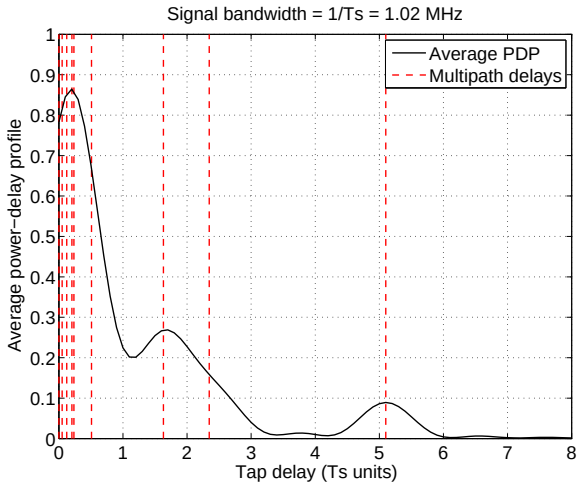


Figure 4.8: Average power-delay profile for the ETU model with a signal bandwidth of 6 RB (i.e. 1.08 MHz and $T_s = 980.39$ ns). [1000 channel realisations are used.]

where $N_\ell$ is the number of realisations. In Figure 4.8, the multipath delays of the channel are highlighted with vertical red lines. As it can be seen, this channel model is mainly characterised by the presence of LoS signal and strong multipath in short-delays. Thus, most of the multipath energy is concentrated for delays between 0 and $T_s/2$, approximately. In addition, it can be seen (as specified in Table 3.2) that the delay spread of the ETU model is equal to $5.1 \cdot T_s$. Then, if the periodic-tap estimation model is used, one can notice as the estimation taps at positions larger than the delay spread have a negligible multipath contribution. Thus, we use this prior information in order to correctly assume the truncation of the number of taps to the delay spread of the ETU model, which in the 1D-JML estimator corresponds to $L = 6$ and in the 2D-JML estimator corresponds to $L = 7$. Using a higher number of taps, the estimators do not capture more channel energy, thus they obtain the same TDE performance (in absence of noise).

Given the generated ETU channel, time-delay errors are computed in the absence of AWG noise using the 1D- and 2D-JML estimators. The PDF of the time-delay errors is shown in Figure 4.9(a). The performance of the 1D-JML estimator for $L = 1$ is poor, producing the highest number of outliers. The outlier estimations are defined as those time-delay estimations with an absolute error higher or equal to $T_s/2$, which are then truncated to $T_s/2$. In this sense, the application of the periodic-tap estimation model (with six taps) reduces the number of outliers. Nevertheless, the low sampling rate avoids this channel estimation model to properly characterize close-in multipath. Thus, using the new hybrid-tap estimation model, an additional arbitrary tap is introduced within 0 and $T_s$ to reduce the model mismatch. The resulting 2D-JML estimator shows a notable

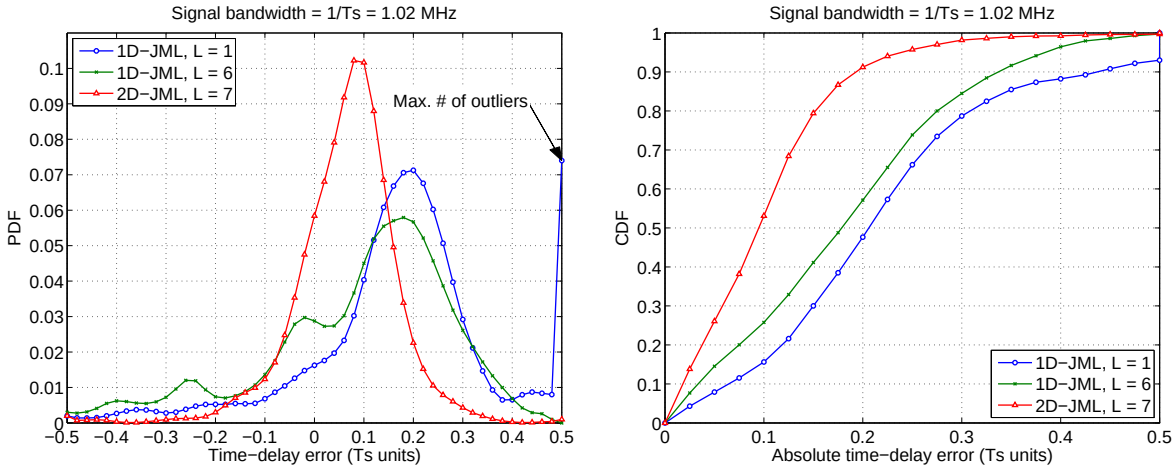


(a) PDF of the time-delay estimations.

(b) CDF of the time-delay estimations.

Figure 4.9: Performance of the 1D- and 2D-JML estimators using the ETU model with a LTE PRS bandwidth of 6 RB. [1000 channel realisations are used.]

improvement with respect to the 1D-JML estimators. This enhancement is highlighted by the CDF of the absolute time-delay error, as it is shown in Figure 4.9(b). For instance, the 2D-JML estimator for $L = 7$ produces an absolute TDE error of $0.12{\cdot}T_s$ (i.e. 35.3 meters) for 67% of the cases, while the 1D-JML estimators obtain (for the same percentage of the cases) an error of $0.25{\cdot}T_s$ (i.e. 73.5 meters) with $L = 1$ and $0.23{\cdot}T_s$ (i.e. 67.7 meters) with $L = 6$. Thus, the 2D-JML estimator provides an important reduction of the multipath error.

### Typical signal bandwidths (i.e. 5 MHz and 10 MHz)

The most usual working modes of LTE are based on the 5 MHz and 10 MHz operating bandwidths, because they are specified for most of the LTE bands, as it is shown in Table 5.6.1-1 of TS 36.101 [3GP14a]. The signal bandwidths associated to these typical modes are 25 RB (i.e. 4.5 MHz) and 50 RB (i.e. 9 MHz), respectively. Thus, the ETU model is applied with these typical bandwidths in order to represent usual LTE positioning conditions.

Using the ETU model realisations of the previous section, the average PDP is shown for both bandwidths in Figure 4.10. The range of the tap delay is defined between 0 and 1.96 microseconds, which coincides with $2{\cdot}T_s$ for 6-RB bandwidth. For the current bandwidths, the sampling period $T_s$ is 225.23 ns for 25 RB and 111.86 ns for 50 RB, given a total number of $N$ subcarriers equal to 296 and 596, respectively. Thus, the time-delay estimation can be focused on the short-delay multipath. Given a higher channel

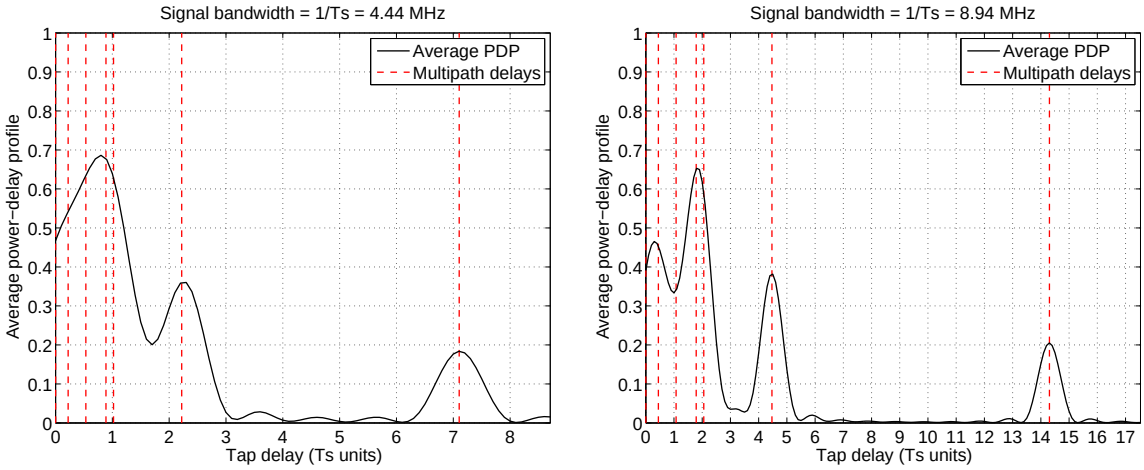


(a) 25 RB (i.e. 4.5 MHz), $T_s = 225.23$ ns. (b) 50 RB (i.e. 9 MHz), $T_s = 111.86$ ns.

Figure 4.10: Average power-delay profile for the ETU model with typical signal bandwidths. [1000 channel realisations are used.]

bandwidth, the contribution of every multipath ray is more independent. In the same way, the sampling rate of the estimation model is higher, and more multipath energy can be captured by every estimation tap. Therefore, the 1D- and 2D-JML estimators can use a lower number of taps, and the value of $L$ may not need to increase up to the delay spread of the channel. For a 25-RB bandwidth, we should consider $L = 8$ for the 1D-JML estimator and $L = 9$ for the 2D-JML estimator, while for a 50-RB bandwidth, we should consider $L = 4$ for the 1D-JML estimator and $L = 5$ for the 2D-JML estimator. *A priori* information of the average PDP should be used to minimize the number of taps $L$ according to the most significant amount of energy of the channel, in order to alleviate the computational burden of the estimation.

The cumulative density function of the TDE errors obtained with the 1D- and 2D-JML estimators are compared using both bandwidths in Figure 4.11. As it can be seen, the 1D- and 2D-JML estimators for $L > 1$ improve the TDE performance with respect to the 1D-JML estimator for $L = 1$ in both cases. In particular, there is a higher gain for 25-RB bandwidth than for 50-RB bandwidth. This is due to the fact that the estimation tap delays are changed with the sampling period. The best TDE performance is achieved when the estimation taps capture most of the multipath energy. In the cases under study, the periodic-tap 1D-JML estimator for $L > 1$ performs slightly better than the hybrid-tap 2D-JML estimator for $L > 1$. But, both estimators still achieve a very accurate ranging performance. Since the differences observed between the 1D- and 2D-JML estimator for $L > 1$ are small, different signal bandwidths and propagation models should be studied in order to assess if these performance results can be generalised.

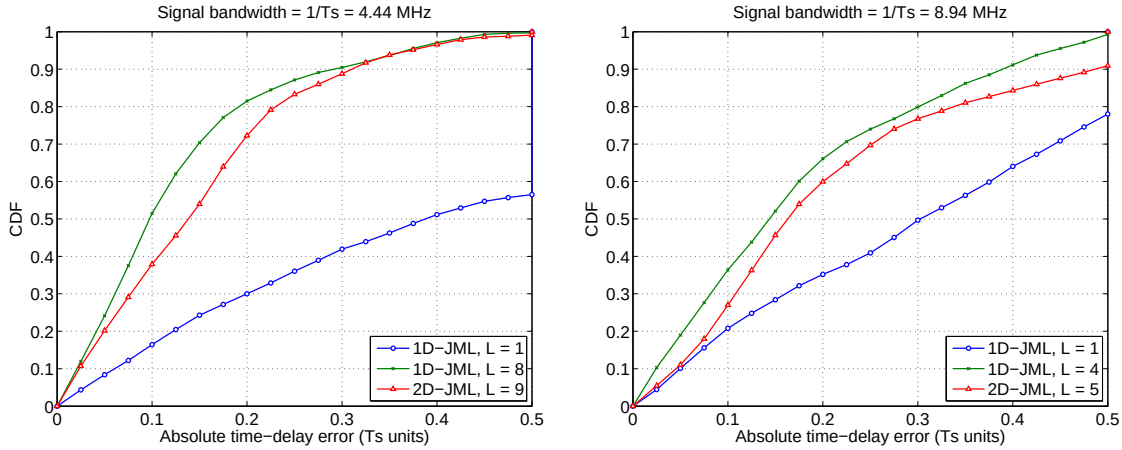


(a) Signal bandwidth equal to 25 RB.

(b) Signal bandwidth equal to 50 RB.

Figure 4.11: CDF of the 1D- and 2D-JML time-delay estimations using the ETU model with typical signal bandwidths. [1000 channel realisations are used.]

### 4.5.2 General assessment of the channel estimation models

The tap delay distribution has a significant importance on the resulting time-delay bias of the JML estimation. In the absence of noise, the optimal solution is to adaptively use a estimation model able to perfectly counteract the propagation channel. As it was introduced in Section 4.1, and assuming no prior knowledge of the channel, this can be ideally achieved using the arbitrary-tap model with an iterative method. However, this solution may imply a high computational burden, which may not be applicable for ranging applications in mass-market receivers. Thus, low-complexity JML estimators based on the single-, periodic- and hybrid-tap estimation models have to be considered. Using these channel estimation models, the MPEE in Figure 4.1 and the CDF in Figure 4.9(b) and 4.11 show that the performance of the 1D- and 2D-JML estimators is characterized by the signal bandwidth, the estimation model (including the number of taps to estimate), and the propagation channel. For instance, both JML estimators are unbiased if the tap delays of the estimation model match the propagation channel. Since specific conditions were only considered, this section aims to assess the performance of these 1D- and 2D-JML estimators in a wide variety of scenarios, defined by:

- LTE signal bandwidths, i.e. 6 RB, 15 RB, 25 RB, 50 RB, 75 RB and 100 RB,
- LTE channel models, i.e. EPA, EVA and ETU, and
- number of estimation taps $L$, i.e. from 1 to a maximum of 90.

The study is focused on the bias of the estimators induced only by the presence of multipath, thus AGW noise is not considered. For each scenario, the bias of the estimators is assessed with the CDF of the absolute and ordered TDE. Due to the high number of results, the CDF curves are compared using the area under curve as a metric, commonly known as area under the ROC (receiver operating characteristic) curve (AUC). Given the CDF of the time-delay estimations being defined by the equispaced points $Y_q$, the AUC metric is expressed as

$$\mathrm{AUC} = \frac{1}{\Delta Y} \sum_{q=1}^{Q} Y_q, \tag{4.5.2}$$

where $\Delta Y$ is the distance between points in the CDF, and $Q$ is the total number of points. The search interval of $\tau$ is limited within $[-1/2, 1/2]$ (in $T_\mathrm{s}$ units). Thus, the normalized AUC is between 0 and 1/2, which corresponds to a fully biased and unbiased estimation, respectively. The results obtained for the 1D-JML estimators (using single- and periodic-tap estimation models) and the 2D-JML estimator (using the hybrid-tap estimation model) are shown for EPA channel in Figure 4.12, EVA channel in Figure 4.13, and ETU channel in Figure 4.14. The three figures contain one sub-figure for each signal bandwidth (i.e. six in total), and three plots for each sub-figure. The structure of the plots is maintained along all sub-figures and figures. For instance, the plot at the top left in Figure 4.12(a) compares the CDF curves obtained with the 1D-JML estimator for $L = 1$ in blue color (i.e. single-tap model) and the 1D-JML estimator for $L > 1$ in red color (i.e. periodic-tap model). The plot at the top right in Figure 4.12(a) compares the CDF curves obtained with the 1D-JML estimator for $L = 1$ in blue color and the 2D-JML estimator for $L > 1$ in red color (i.e. hybrid-tap model). The plot at the bottom in Figure 4.12(a) depicts the AUC of the CDF curves as a function of the delay spread of the estimation model. This delay spread is defined by the delay position of the $L$-th tap. Thus, the delay spread is equal to $L - 2$ for the hybrid-estimation model, and equal to $L - 1$ for periodic-tap estimation model (in $T_\mathrm{s}$ units). For $L = 2$, the delay spread of the hybrid-tap model is approximated to 1/2 (in $T_\mathrm{s}$ units). Despite the delay spread of the single-tap model is equal to zero, as an exception, its AUC value is depicted for all the x-axis values, in order to be compared with the AUC values of the 1D- and 2D-JML estimators for $L > 1$. The tap delays of the propagation channel are also highlighted in the bottom plot with vertical dashed lines. In order to not result in a undetermined system, the number of unknowns (i.e. time delay $\tau$ and channel coefficients $\mathbf{h}$) must be equal or lower than the number of pilots. Thus, the maximum number of estimation taps is limited to $L_\mathrm{max} < 2 \cdot N_\mathrm{RB}$, due to the use of the PRS pilots. Since this number can be too high, $L_\mathrm{max}$ is equal to 90 for 50 RB, 75 RB and 100 RB cases.

Considering the EPA channel model, the 2D-JML estimator achieves the lowest bias for all the cases in Figure 4.12, because it obtains the highest AUC values from 6 RB (i.e. Figure 4.12(a)) to 100 RB (i.e. Figure 4.12(f)). The EPA model characterizes a close-in multipath channel, where the 2D-JML estimator outperforms the 1D-JML estimator. In this case, most of the multipath contribution is within 0 and $T_{\mathrm{s}}$, thus the 2D-JML estimator is able to capture most of this channel energy. The performance of the 1D-JML estimator is worse than the 2D-JML estimator, because only the first tap is able to capture most of the multipath energy. Given that the EPA delay spread is equal to 410 ns, the corresponding delay in $T_{\mathrm{s}}$ units is $\tau_s = \{0.42, 1.08, 1.82, 3.67, 5.51, 7.36\}$ for $N_{\mathrm{RB}} = \{6, 15, 25, 50, 75, 100\}$ (in the same order). As it can be seen, the bias of the estimators is independent of the number of taps $L$ (in the absence of noise), when the delay spread of the estimation model is larger than the delay spread of the channel $\tau_s$.

Considering the EVA channel model, the 2D-JML estimator still achieves the lowest bias for most of the cases in Figure 4.13. Nevertheless, this optimum performance is not necessarily obtained for a delay spread of the estimation model larger than the delay spread of the channel. The lowest bias of the 2D-JML estimator is obtained for specific values of $L$. Thus, the single-tap and periodic-tap 1D-JML estimator may have a better performance than the 2D-JML estimator for the rest of values of $L$, as it can be seen for 50 RB, 75 RB and 100 RB in Figure 4.13(d), 4.13(e) and 4.13(f). Indeed, the single-tap 1D-JML estimator outperforms the periodic-tap 1D-JML estimator for 50 RB. These results show that the performance of the 2D-JML estimator highly depends on the number of taps $L$ for the EVA channel.

Considering the ETU channel model, the 2D-JML estimator only achieves the lowest bias for certain values of $L$, and signal bandwidths of 6RB, 15 RB, 75 RB and 100 RB, as it is shown in Figure 4.14(a), 4.14(b), 4.14(a) and 4.14(b), respectively. In constrast, the 1D-JML estimator for $L > 1$ obtains the lowest bias for 25 RB and 50 RB, as it shown in Figure 4.14(c) and 4.14(d), respectively. The single-tap 1D-JML estimator shows the worst performance in all the cases. This mixture of results is due to the distribution of the ETU multipath rays, with short-delay multipath and a large delay spread.

The results obtained for each case, shown in Figure 4.12, 4.13 and 4.14, are summarized in Table 4.3. This summary indicates the optimum number of taps $L_{\mathrm{opt}}$ for both 1D- and 2D-JML estimators, using single-, periodic- and hybrid-tap estimation models. For every scenario, the estimator with the lowest bias is highlighted in blue. Using the optimum number of taps $L_{\mathrm{opt}}$, the 2D-JML estimator achieves the minimum bias in most of the cases. This optimum performance could be obtained with the following remarks:

- For low signal bandwidths (e.g. 6-RB bandwidth), the propagation rays jointly contribute to the multipath effect. Thus, the delay spread of the estimation model should coincide with the delay spread of the channel, in order to capture and counteract most of the multipath contribution.
- When the signal bandwidth is increased, the contribution of each propagation ray to the effect of multipath is more independent. Thus, the delay spread of the estimation model can be lower than the delay spread of the channel. In this case, the model order $L$ should be adjusted to capture those propagation rays with more channel energy.
- If there is no knowledge of the channel, as a rule-of-thumb, the number of estimated taps $L$ can be limited to the normal CP length $T_{CP}$, i.e. $L = \lceil T_{CP} \cdot N/T_{\mathrm{s}} \rceil = \{5, 13, 21, 43, 64, 85\}$ for $N_{\mathrm{RB}} = \{6, 15, 25, 50, 75, 100\}$, where $N = 12 \cdot N_{\mathrm{RB}} - 4$. Since this rule-of-thumb does not ensure the minimum achievable bias of any estimator, it is left for future work the adaptive selection of the model order $L$.

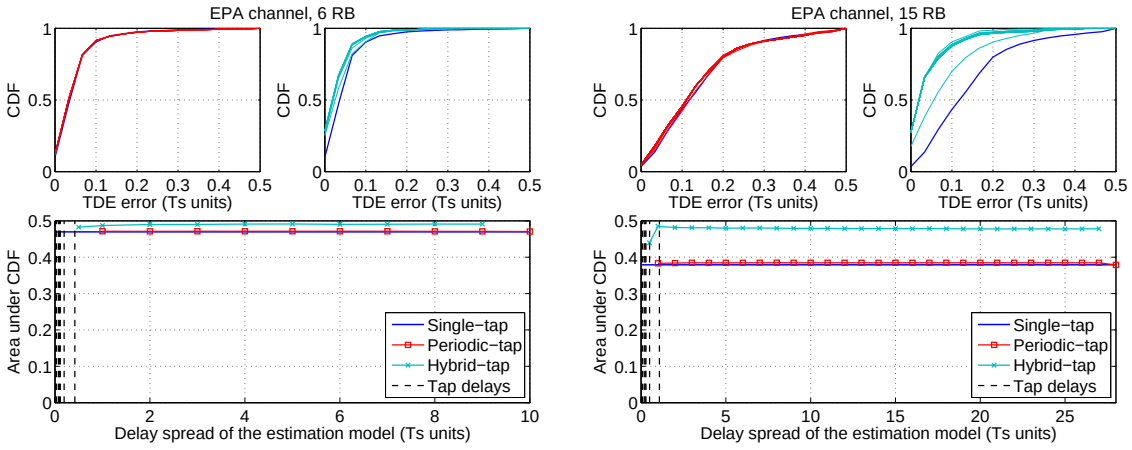


(a) BW = 6RB




(b) BW = 15RB

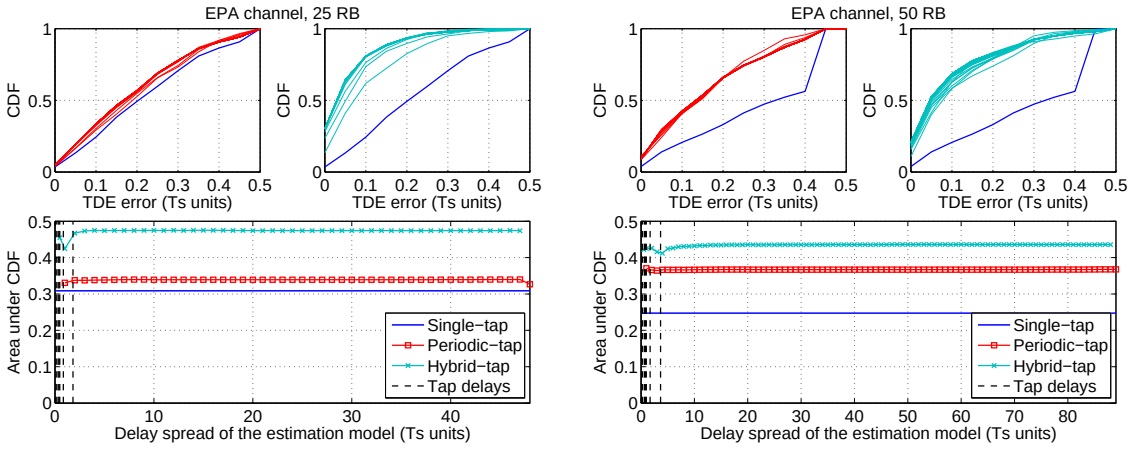


(c) BW = 25RB




(d) BW = 50RB

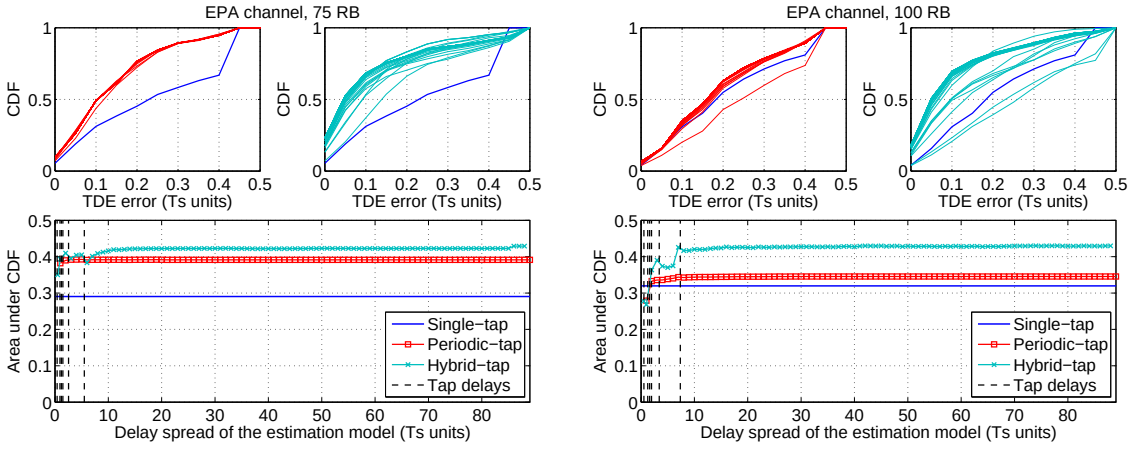


(e) BW = 75RB




(f) BW = 100RB

Figure 4.12: CDF and AUC of the 1D- and 2D-JML estimations for EPA channel model.

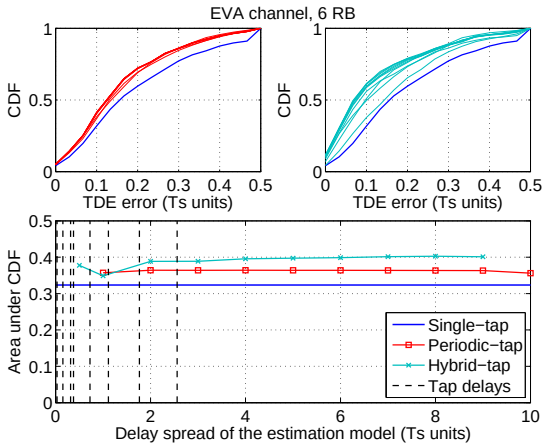


(a) BW = 6RB

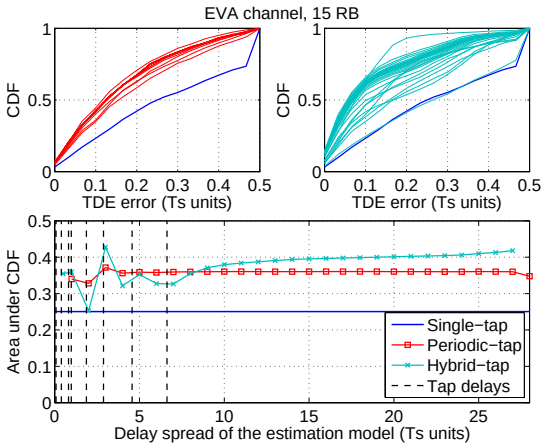


(b) BW = 15RB

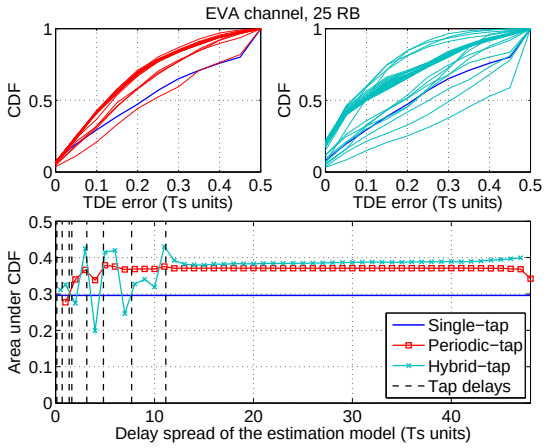


(c) BW = 25RB

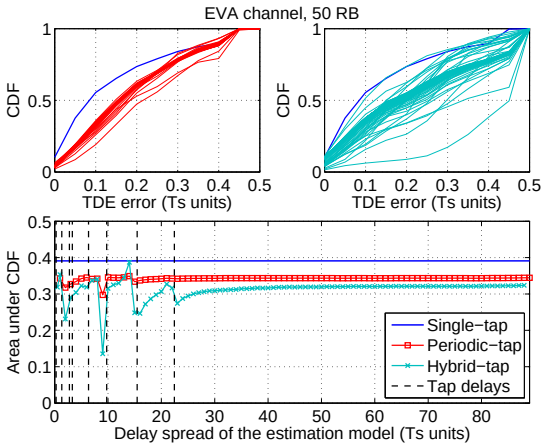


(d) BW = 50RB

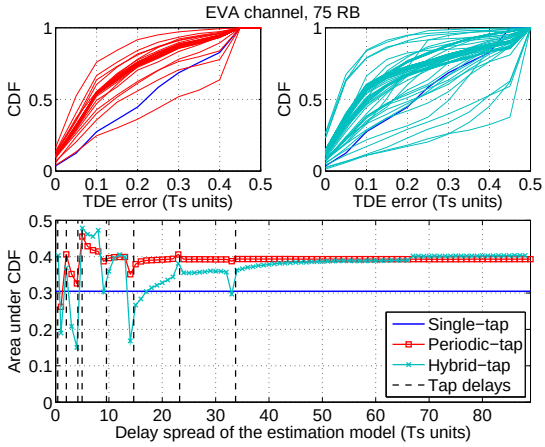


(e) BW = 75RB

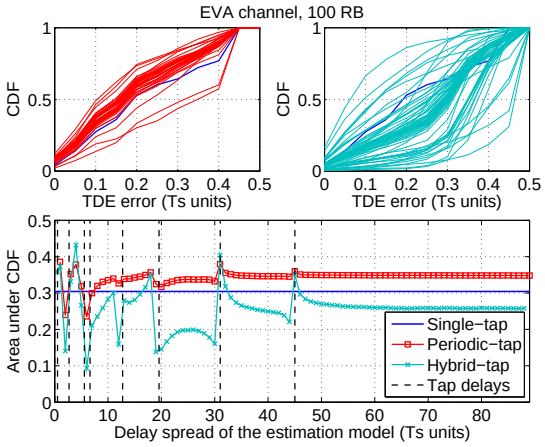


(f) BW = 100RB

Figure 4.13: CDF and AUC of the 1D- and 2D-JML estimations for EVA channel model.

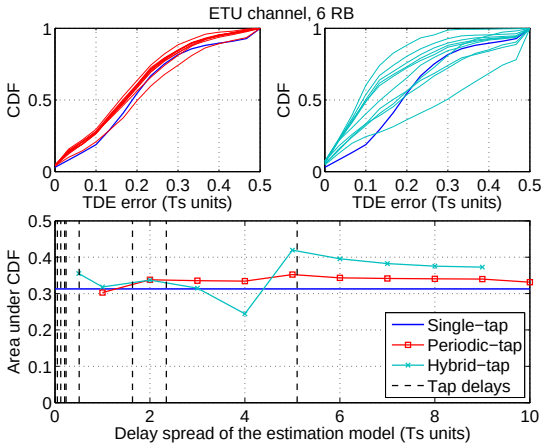


(a) BW = 6RB

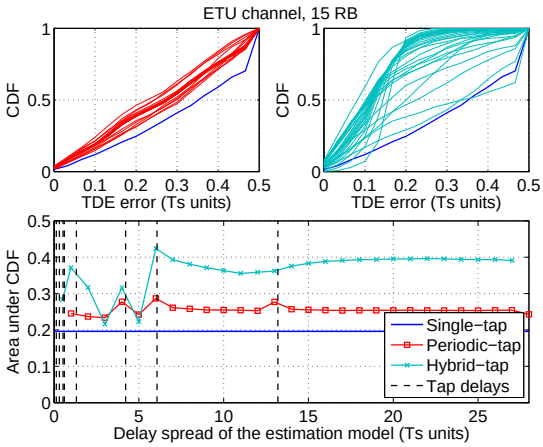


(b) BW = 15RB

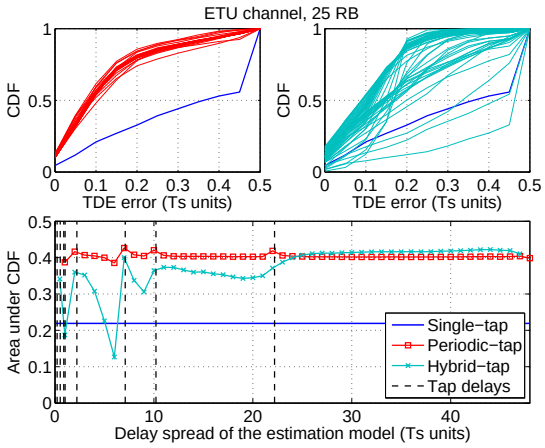


(c) BW = 25RB

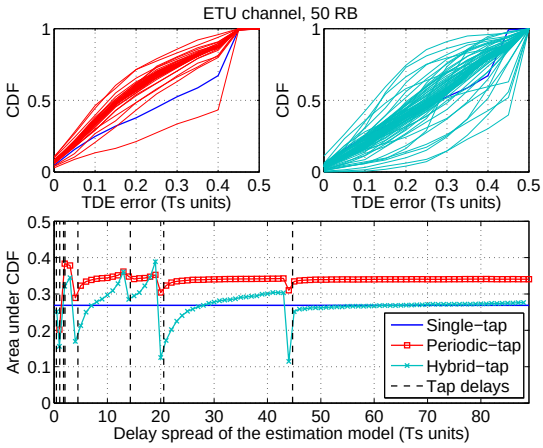


(d) BW = 50RB

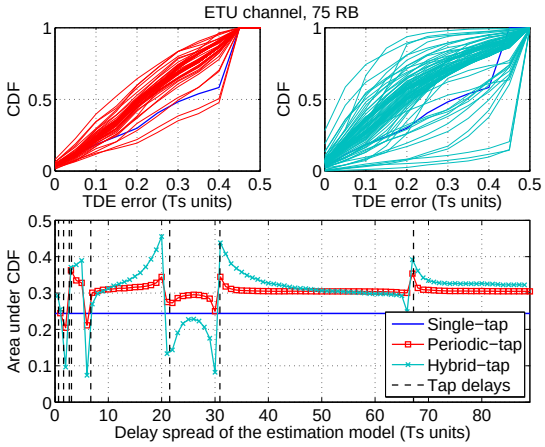


(e) BW = 75RB

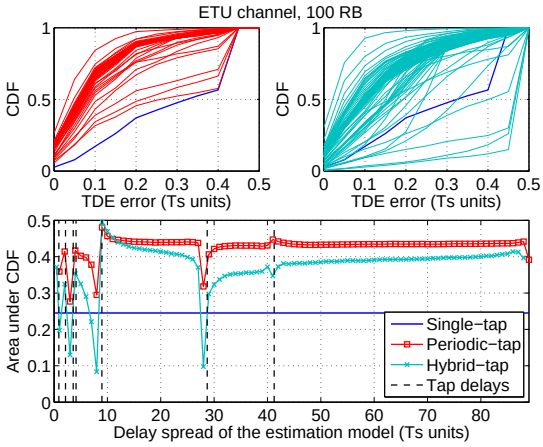


(f) BW = 100RB

Figure 4.14: CDF and AUC of the 1D- and 2D-JML estimations for ETU channel model.

Table 4.3: Optimum number of taps for the 1D- and 2D-JML estimators using single-, periodic- and hybrid-tap models for each LTE signal bandwidth and standard channel.

| Signal bandwidth | Estimation model | EPA | EVA | ETU |
|---|---|---|---|---|
| 6 RB | Single-tap | $L = 1$ | $L = 1$ | $L = 1$ |
| | Periodic-tap | $L_{\text{opt}} = \{2, \ldots, 11\}$ | $L_{\text{opt}} = \{2, \ldots, 11\}$ | $L_{\text{opt}} = \{3, \ldots, 11\}$ |
| | Hybrid-tap | $L_{\text{opt}} = \{2, \ldots, 11\}$ | $L_{\text{opt}} = \{2, \ldots, 11\}$ | $L_{\text{opt}} = \{7, \ldots, 11\}$ |
| 15 RB | Single-tap | $L = 1$ | $L = 1$ | $L = 1$ |
| | Periodic-tap | $L_{\text{opt}} = \{2, \ldots, 29\}$ | $L_{\text{opt}} = \{4, \ldots, 28\}$ | $L_{\text{opt}} = \{2, \ldots, 29\}$ |
| | Hybrid-tap | $L_{\text{opt}} = \{3, \ldots, 29\}$ | $L_{\text{opt}} = \{5, 12, \ldots, 29\}$ | $L_{\text{opt}} = \{3, 8, \ldots, 29\}$ |
| 25 RB | Single-tap | $L = 1$ | $L = 1$ | $L = 1$ |
| | Periodic-tap | $L_{\text{opt}} = \{2, \ldots, 49\}$ | $L_{\text{opt}} = \{6, \ldots, 48\}$ | $L_{\text{opt}} = \{2, \ldots, 49\}$ |
| | Hybrid-tap | $L_{\text{opt}} = \{4, \ldots, 49\}$ | $L_{\text{opt}} = \{5, 7, 8, 13\}$ | $L_{\text{opt}} = \{9, 25, \ldots, 49\}$ |
| 50 RB | Single-tap | $L = 1$ | $L = 1$ | $L = 1$ |
| | Periodic-tap | $L_{\text{opt}} = \{2, \ldots, 90\}$ | $L_{\text{opt}} = \{2, \ldots, 90\}$ | $L_{\text{opt}} = \{3, 4\}$ |
| | Hybrid-tap | $L_{\text{opt}} = \{2, \ldots, 90\}$ | $L_{\text{opt}} = \{3, 16\}$ | $L_{\text{opt}} = \{5, 15, 21\}$ |
| 75 RB | Single-tap | $L = 1$ | $L = 1$ | $L = 1$ |
| | Periodic-tap | $L_{\text{opt}} = \{2, \ldots, 90\}$ | $L_{\text{opt}} = \{3, \ldots, 90\}$ | $L_{\text{opt}} = \{4, 21, 32, 68\}$ |
| | Hybrid-tap | $L_{\text{opt}} = \{12, \ldots, 90\}$ | $L_{\text{opt}} = \{7, 8, 9, 10\}$ | $L_{\text{opt}} = \{7, 22, 33, 69\}$ |
| 100 RB | Single-tap | $L = 1$ | $L = 1$ | $L = 1$ |
| | Periodic-tap | $L_{\text{opt}} = \{3, \ldots, 90\}$ | $L_{\text{opt}} = \{2, 5, 32\}$ | $L_{\text{opt}} = \{3, \ldots, 90\}$ |
| | Hybrid-tap | $L_{\text{opt}} = \{9, \ldots, 90\}$ | $L_{\text{opt}} = \{6, 33\}$ | $L_{\text{opt}} = \{11, 12, 13\}$ |

## 4.6 RMSE and bias of the JML estimators over LTE channel models and AWGN

The bias of the 1D- and 2D-JML estimators has been assessed considering only the presence of multipath. Despite the results obtained help to design the JML estimators in multipath environments, noise has to be introduced in order to assess the achievable TDE performance in realistic conditions. Thus, this section considers the effect of multipath and noise on the time-delay estimation. The RMSE and bias of the 1D- and 2D-JML estimators are computed with Monte-carlo simulations to assess the ranging performance obtained. The RMSE of the 1D- and 2D-JML estimators is first used to confirm their attainability to the CRB for TDE. Then, the RMSE and bias of these estimators are obtained for the LTE signal bandwidths over the standard channel models to determine their achievable ranging accuracy.

### 4.6.1 Attainability of the CRB for TDE

The CRB with respect to $\tau$ was derived for the single-, periodic- and hybrid-tap channel estimation models in Section 4.2. In order to assess the attainability of the CRB expressions obtained, the RMSE of the 1D- and 2D-JML estimator is computed in two example cases, where the channel estimation model perfectly matches the propagation channel. Thus, the JML estimation should be unbiased given a certain $C/N_0$, and the resulting RMSE should attain the corresponding CRB for TDE. Since a particular case of the single-tap model for $h_0 = 1$ was studied in Section 3.2.4, this section focuses on the attainability of the CRB using periodic- and hybrid-tap models.

For sake of simplicity, and without loss of generality, let us consider a two-ray multipath channel with a counter-phase multipath contribution (i.e. $\phi_1 = \pi$) and SMR = 1 dB in both examples. The first example is characterized by a multipath delay $\tau_1$ equal to 1 (i.e. $\tau_{c,k} = \{0, 1\}$), while the second example is defined by a multipath delay $\tau_1$ equal to 0.5 (i.e. $\tau_{c,k} = \{0, 0.5\}$). Thus, the periodic-tap estimation model is assessed in the first example, and the hybrid-tap estimation model is assessed in the second example. As it is shown in Figure 4.15(a), the periodic-tap 1D-JML estimator for $L = 2$ attains the $\mathrm{CRB}_{\tau,\mathrm{PT}}$ in (4.2.20) with a $C/N_0$ threshold equal to 70 dB-Hz for the first example. The RMSE of this estimator departs from the $\mathrm{CRB}_{\tau,\mathrm{PT}}$ below this $C/N_0$ threshold due to outliers on the estimation, and the TDE becomes biased. In the second example, the hybrid-tap 2D-JML estimator for $L = 2$ attains the $\mathrm{CRB}_{\tau,\mathrm{HT}}$ in (4.2.32) for a $C/N_0$

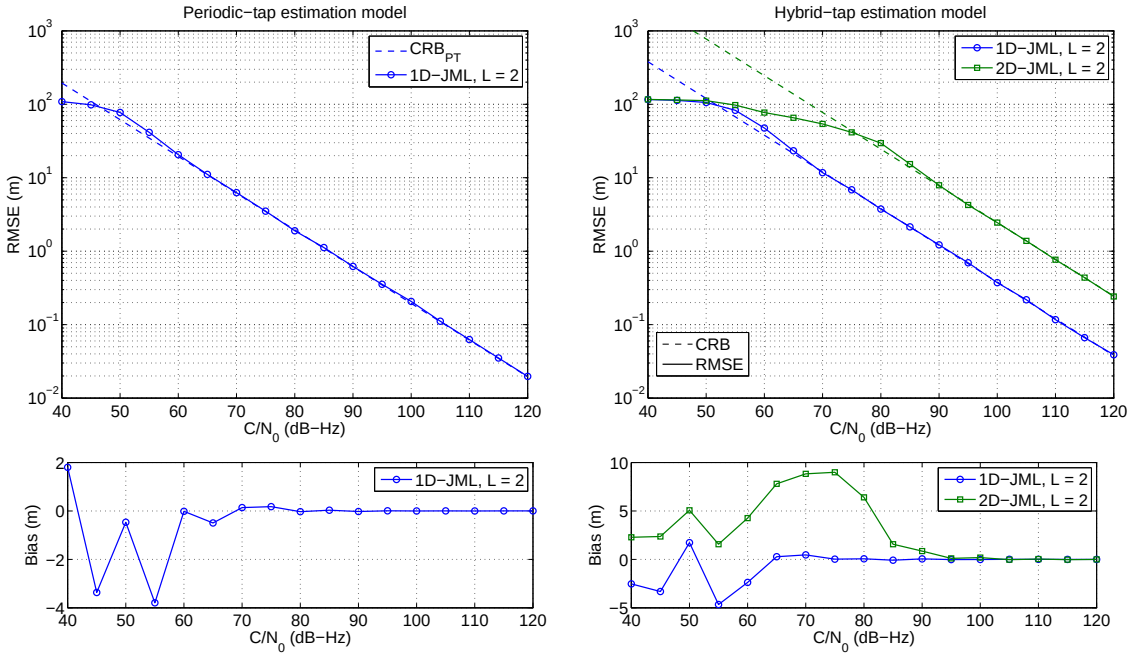


(a) Case 1: $\tau_{c,k} = \{0, 1\}$ (b) Case 2: $\tau_{c,k} = \{0, 0.5\}$

Figure 4.15: RMSE and bias of the 1D- and 2D-JML estimators and the corresponding $\text{CRB}_\tau$ in a two-ray channel with a multipath ray in counter-phase (i.e. $\phi_1 = \pi$) and SMR = 1 dB, considering a 6-RB PRS bandwidth. [1000 noise realisations per $C/N_0$ are used.]

threshold of 90 dB-Hz, as it is shown in Figure 4.15(b). The results obtained in the first and second examples cannot be compared among them, because these cases consider different channel realisations. Thus, the propagation channel model is used in the 1D-JML estimator to assess the performance of the 2D-JML estimator in the second example. This is done by introducing the delays of the propagation channel $\tau_{c,k} = \{0, 0.5\}$ in the Fourier matrix $\mathbf{F}_L$, which is then used to compute the 1D-JML estimator for $L = 2$ and the corresponding CRB, by following the same procedure as in the periodic-tap case. As it can be seen in 4.15(b), the 1D-JML estimator using the propagation model attains the corresponding CRB for a $C/N_0$ threshold of approximately 70 dB-Hz. In this particular case, there is a considerable difference in the ranging performance between the 1D- and 2D-JML estimators, because the 2D-JML estimator is more affected by noise than the 1D-JML estimator. This is due to the fact that the variance of the JML estimation (and any estimation in general) increases with the number of unknown parameters to estimate. Thus, there is a trade-off between the efforts to counteract multipath and the robustness against noise.

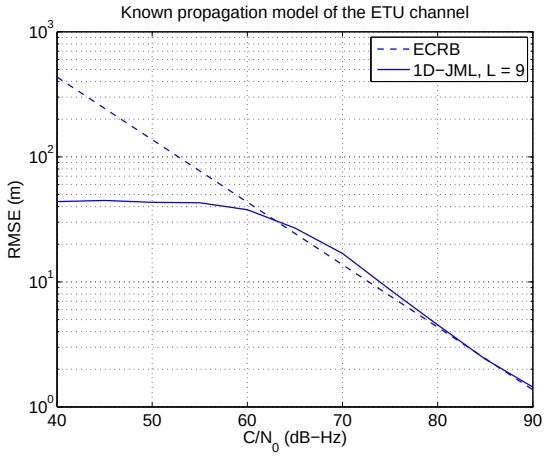


Figure 4.16: RMSE of the 1D-JML estimator for $L = 9$ assuming the known propagation model of the ETU channel and the corresponding $\mathrm{ECRB}_\tau$, with a 15-RB PRS bandwidth. [1000 ETU channel and noise realisations per $C/N_0$ are used.]

In general, the estimation of a parameter is unbiased if the correct estimation model is applied. Thus, the corresponding CRB is attained in these situations, as it shown in the previous example scenarios. In our ranging application, this implies to know the propagation channel model, which is an assumption barely applicable in realistic environments. The standard channel models, such as EPA, EVA or ETU, represent general scenarios that can be considered realistic navigation scenarios. Nevertheless, the main parameters of these channel models should not be assumed to be known, because they are only statistical values. In the same sense, the $\mathrm{CRB}_\tau$ is valid for a specific channel realisation, while the $\mathrm{ECRB}_\tau$ in (4.2.33) should be considered for multiple channel realisations. As an example of the attainability of the 1D-JML estimator to the $\mathrm{ECRB}_\tau$, let us consider the ideal case of knowing the propagation delays $\tau_{c,k}$ of the ETU channel. Using $\tau_{c,k}$ in the 1D-JML estimator, the resulting RMSE (computed over 1000 ETU channel realisations) attains the $\mathrm{ECRB}_\tau$ for a $C/N_0$ threshold of approximately 80 dB-Hz, as it is shown in Figure 4.16 with a 15-RB PRS bandwidth. However, this bound is not attained when using a different estimation model.

### 4.6.2 Achievable ranging accuracy in realistic navigation channels

The previous section has discussed the attainability of the 1D- and 2D-JML estimators to the CRB for TDE, which is possible if the channel estimation model matches the propagation channel model. However, the JML estimators usually have a model mismatch in realistic scenarios, and they cannot attain the CRB for TDE. Thus, this section aims

to assess the ultimate ranging performance of the 1D- and 2D-JML estimators in realistic navigation channels. These realistic environments are here considered to be characterized by standard channel models (i.e. EPA, EVA and ETU) and LTE signal bandwidths (i.e. 6 RB, 15 RB, 25 RB, 50 RB, 75 RB and 100 RB). The results are computed with 1000 channel realisations for every $C/N_0$ value within a range between 40 dB-Hz and 90 dB-Hz.

Since the performance of the estimators depends on the number of taps $L$, as it was discussed in Section 4.5.2, the optimum or nearly-optimum number of taps $L$ is considered for the 1D- and 2D-JML estimators in the different scenarios. For this purpose, the appropriate values of $L$ are taken for the periodic- and hybrid-tap models using Table 4.3. In case the bias of the JML estimator (in absence of noise) is similar for different values of $L$, the minimum $L$ among them is selected. Since $L$ can be different between the periodic- and the hybrid-tap models, $L_{\mathrm{p}}$ defines the number of taps in the periodic-tap model, and $L_{\mathrm{h}}$ defines the number of taps in the hybrid-tap model. Thus, the RMSE of the 1D- and 2D-JML estimators is shown in Figure 4.17, and the bias of these estimators is depicted in Figure 4.18. The results are grouped considering low signal bandwidths (i.e. 6 RB, 15 RB and 25 RB) and high signal bandwidths (i.e. 50 RB, 75 RB and 100 RB), for every LTE channel model. The values of $L_{\mathrm{p}}$ and $L_{\mathrm{h}}$ are written between brackets and ordered according to the signal bandwidths, i.e. $N_{\mathrm{RB}} = \{6, 15, 25\}$ or $N_{\mathrm{RB}} = \{50, 75, 100\}$.

In general terms, and for most of the cases, **the 2D-JML estimator for $\boldsymbol{L > 1}$ has a lower RMSE than the 1D-JML estimators for $\boldsymbol{L \geq 1}$ at moderate to high $\boldsymbol{C/N_0}$**, i.e. above $C/N_0$ values between 70 and 80 dB-Hz. This is fulfilled in 13 out of the 18 scenarios. For instance, given the EVA channel and signal bandwidths defined by 6 RB, 15 RB and 25 RB, the 2D-JML estimator outperforms the 1D-JML estimators for $C/N_0 = \{79.2, 72.7, 72.9\}$ dB-Hz, respectively, as it is shown in Figure 4.17(c). Considering these signal bandwidths, the $C/N_0$ values obtained correspond to SNR $= \{19.1, 8.5, 6.4\}$ dB. In addition, the 2D-JML estimator still has a better performance than the 1D-JML estimators for 6 RB and 75 RB over the EPA channel, but above a $C/N_0$ of 90 dB-Hz and 85 dB-Hz, as it is shown in Figure 4.17(a) and 4.17(b), respectively.

Let us consider a range of $C/N_0$ values that can be usually found in LTE scenarios, in order to assess the ranging performance obtained. For this purpose, the methodology introduced in Section 3.3.1 is followed to determine a common environment. The LTE scenario is defined by a urban macro-cell deployment, where three-sectorial base stations are located in a hexagonal grid. The main parameters of this scenario are taken from TR 36.942 [3GP12b], and they are summarized in Table 4.4. The inter-cell interference

Table 4.4: Base station simulation parameters according to [3GP12b].

| | |
|---|---|
| Maximum BS signal power | $P_{tx,max} = 43$ dBm |
| BS antenna radiation pattern | $G_{tx} = \bar{G}_{tx} - \min\left\{12 \cdot (\theta/\theta_{3dB})^2, A_{min}\right\}$ |
| BS antenna mean gain | $\bar{G}_{tx} = 15$ dBi |
| BS antenna model | 3 dB beam width, $\theta_{3dB} = 65$ degrees |
| BS antenna minimum attenuation | $A_{min} = 20$ dB |
| Minimum coupling loss | MCL = 70 dB |
| Path loss model[1] | $L_i = 128.1 + 37.6\log_{10}(R_i)$ dB |
| UE antenna model | Omnidirectional, $G_{rx} = 0$ dBi, NF = 9 dB |

[1] $R_i$ is the propagation distance to BS $i$ in kilometres.

is considered to be mostly removed by using the PRS. Following the recommendation in [3GP12b], log-normally distributed shadowing with standard deviation of 10 dB is added to the path loss model. Let us assume that the user is located in the main direction of the BS radiation pattern at a distance between 200 and 1000 meters, and the BS signal power is between 30 dBm (i.e. maximum power per downlink traffic channel [3GP12b]) and 43 dBm (i.e. maximum transmission power [3GP12b]). Taking into account these parameters in (3.3.4) and (3.3.5), the $C/N_0$ is between 71.9 dB-Hz and 84.9 dB-Hz at 1000 meters of distance, and between 98.2 dB-Hz and 111.2 dB-Hz at 200 meters of distance. Thus, considering these ranges of $C/N_0$ values, the 2D-JML estimator outperforms the 1D-JML estimators in most of the cases, according to the results obtained in Figure 4.17 and 4.18. Particularly, for $C/N_0 = 85$ dB-Hz (i.e. BS signal power of 30 dBm at approximately 450 meters of distance), the RMSE of the 2D-JML estimator using a 6-RB PRS bandwidth is equal to 29.7 meters for EPA channel, 57.4 meters for EVA channel, and 42.7 meters for ETU channel, and using a 100-RB PRS bandwidth is equal to 3.2 meters for EPA channel, 2.7 meters for EVA channel, and 1.4 meters for ETU channel. Therefore, **the achievable ranging accuracy of LTE using the 2D-JML estimator in realistic navigation channels over a typical $C/N_0$ of 85 dB-Hz (once inter-cell interference is removed) can be found around 30 and 60 meters for the lowest signal bandwidth (i.e. 1.4 MHz) and below 5 meters for the highest signal bandwidth (i.e. 20 MHz)**.

Nevertheless, there are still two scenarios where the 2D-JML estimator obtains a good ranging performance, but its RMSE is slightly higher than the 1D-JML estimators. First, the 1D-JML estimator for $L_\mathrm{p} = \{8, 10\}$ has a lower RMSE than the 2D-JML estimator for $L_\mathrm{h} = \{9, 11\}$ over the ETU channel with $N_\mathrm{RB} = \{25, 50\}$, as it can be seen in Figure 4.17(e) and 4.17(f), respectively. Second, the 1D-JML estimator for $L = 1$ achieves a

lower RMSE with respect to the 1D- and 2D-JML estimators for $L > 1$ over the EVA channel with 50 RB, as it can be seen in Figure 4.17(d).

The simulations conducted in this section have two sources of variability: noise and different channel realisations. At very high $C/N_0$ (i.e. above 90 dB-Hz), there are still variations due to the channel, thus the resulting RMSE is different than the bias. As it can be seen in Figure 4.18, the bias of the JML estimators is typically maintained above a $C/N_0$ of 80 dB-Hz. Considering the EPA channel at high $C/N_0$, the bias of the 2D-JML estimator is lower than 5 meters for all the bandwidths over the EPA channel, while the 1D-JML estimators can only achieve these values for high signal bandwidths, as it is shown in Figure 4.18(a) and 4.17(d). Considering channels with a large delay spread, such as EVA and ETU channels, at high $C/N_0$, the bias of the JML estimators is above 20 meters for a 6-RB PRS bandwidth, and below 5 meters for high signal bandwidths by using $L > 1$. In general terms, the 2D-JML estimator for $L > 1$ has a lower bias than the 1D-JML estimator for $L > 1$ using low signal bandwidths, and both 1D- and 2D-JML estimators for $L > 1$ obtain a similar bias using high signal bandwidths. The 1D-JML estimator for $L = 1$ achieves the highest bias in most of the cases.

In conclusion, the use of the novel 2D-JML estimator is essential to improve the time-delay performance with respect to the 1D-JML estimator, especially in scenarios with close-in multipath (typically found for low signal bandwidths). This enhancement is usually obtained for a specific number of taps $L$. Thus, the model order of the estimator should be designed accordingly. Considering the LTE channel models, the optimum values of $L$, indicated for every channel estimation model in Table 4.3, are valid and applicable in case a certain channel is characterized by one of the standard propagation models. In these realistic navigation channels with a typical $C/N_0$ of 85 dB-Hz (once inter-cell interference is removed), the 2D-JML estimator for $L > 1$ achieves a ranging accuracy around 30 and 60 meters for 1.4 MHz, and below 5 meters for 20 MHz, outperforming the 1D-JML estimators in most of the cases.

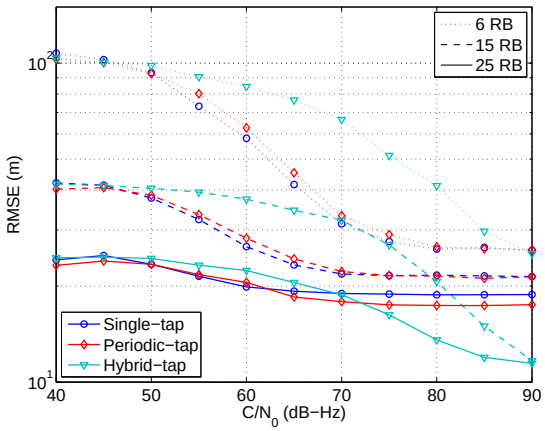


(a) EPA, $L_{\mathrm{p}} = \{2, 2, 2\}$, $L_{\mathrm{h}} = \{2, 3, 3\}$.

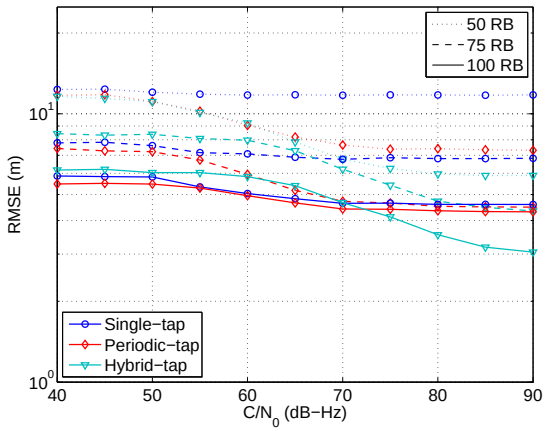


(b) EPA, $L_{\mathrm{p}} = \{2, 3, 4\}$, $L_{\mathrm{h}} = \{2, 4, 5\}$.

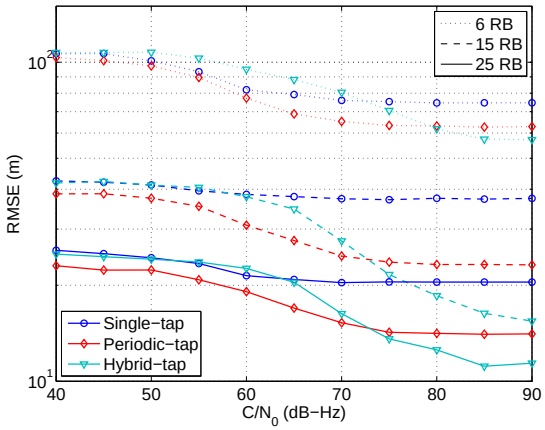


(c) EVA, $L_{\mathrm{p}} = \{2, 4, 6\}$, $L_{\mathrm{h}} = \{4, 5, 5\}$.

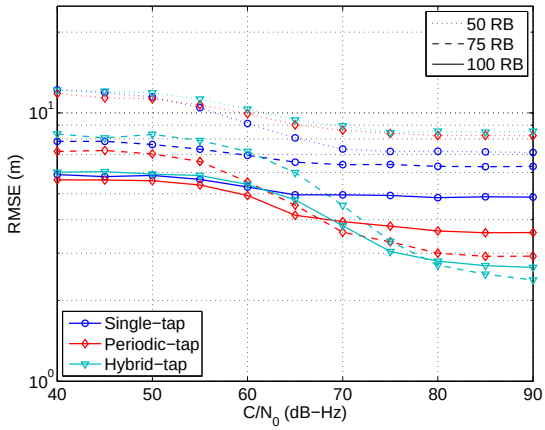


(d) EVA, $L_{\mathrm{p}} = \{2, 6, 2\}$, $L_{\mathrm{h}} = \{3, 7, 6\}$.

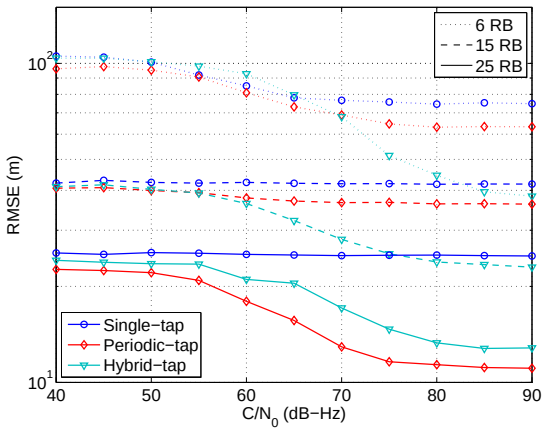


(e) ETU, $L_{\mathrm{p}} = \{6, 2, 8\}$, $L_{\mathrm{h}} = \{7, 3, 9\}$.

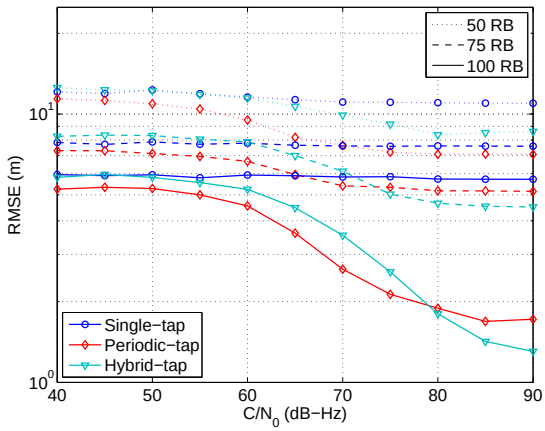


(f) ETU, $L_{\mathrm{p}} = \{3, 4, 10\}$, $L_{\mathrm{h}} = \{5, 7, 11\}$.

Figure 4.17: RMSE of the 1D- and 2D-JML estimator using single-, periodic- and hybrid-tap models for EPA, EVA and ETU channels, considering the LTE signals bandwidths.

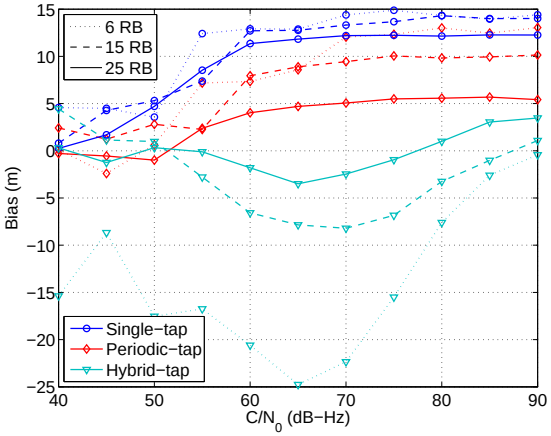


(a) EPA, $L_{\mathrm{p}} = \{2, 2, 2\}$, $L_{\mathrm{h}} = \{2, 3, 3\}$.

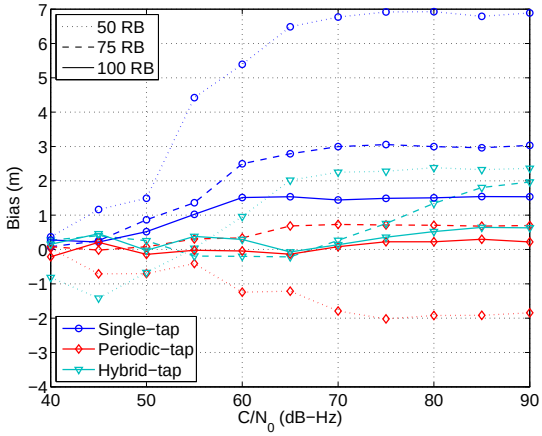


(b) EPA, $L_{\mathrm{p}} = \{2, 3, 4\}$, $L_{\mathrm{h}} = \{2, 4, 5\}$.

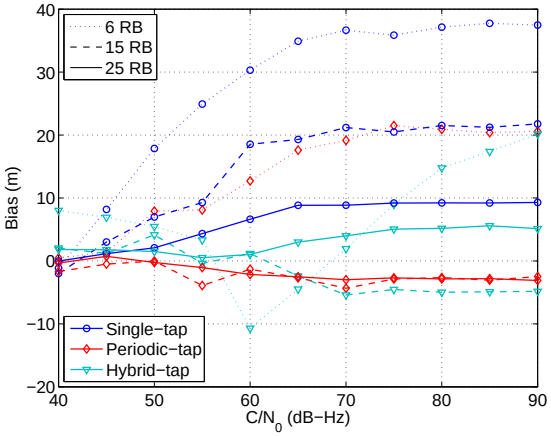


(c) EVA, $L_{\mathrm{p}} = \{2, 4, 6\}$, $L_{\mathrm{h}} = \{4, 5, 5\}$.

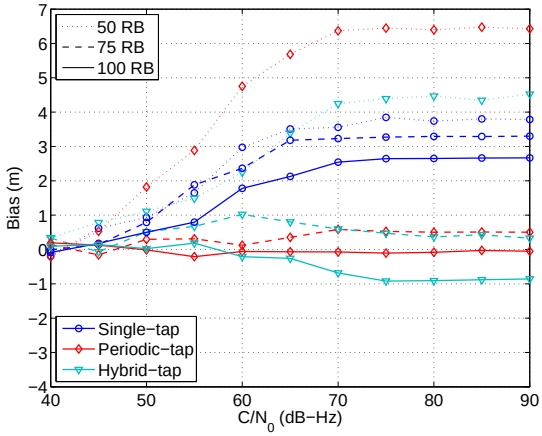


(d) EVA, $L_{\mathrm{p}} = \{2, 6, 2\}$, $L_{\mathrm{h}} = \{3, 7, 6\}$.

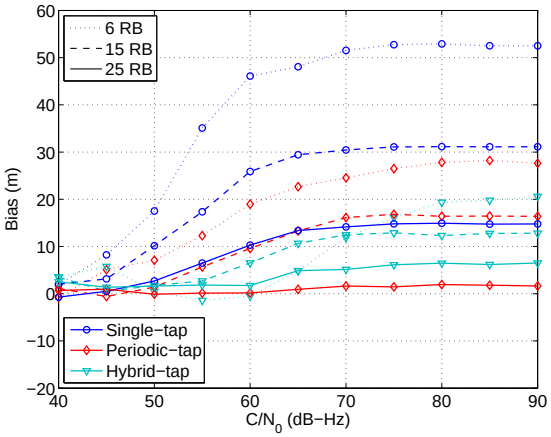


(e) ETU, $L_{\mathrm{p}} = \{6, 2, 8\}$, $L_{\mathrm{h}} = \{7, 3, 9\}$.

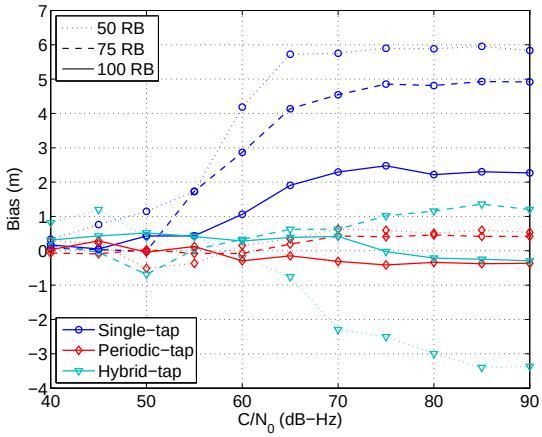


(f) ETU, $L_{\mathrm{p}} = \{3, 4, 10\}$, $L_{\mathrm{h}} = \{5, 7, 11\}$.

Figure 4.18: Bias of the 1D- and 2D-JML estimator using single-, periodic- and hybrid-tap models for EPA, EVA and ETU channels, considering the LTE signals bandwidths.

# Chapter 5

# Practical Validation of a LTE Positioning Receiver

The previous chapters have studied the achievable localization capabilities in LTE OTDoA, and proposed advanced techniques to counteract multipath. In this chapter, the practical validation of these results is accomplished by means of real LTE signals. In order to help on contributing to this goal, a tool is implemented to produce time-delay and position estimates in LTE networks. The tool to be presented is a software-defined radio (SDR) receiver that exploits the positioning capabilities of the LTE signals. The SDR LTE positioning receiver employs a Universal Software Radio Peripheral (USRP) platform and MATLAB to digitalize and process the signal, respectively. The receiver works at the physical layer by implementing accurate time and frequency synchronization methods for LTE signals. The time-delay estimation can be performed standalone without the positioning assistance data provided by LPP, but the precise location of the base stations is required to compute the user location. Results are presented in an AWGN static scenario to validate the positioning engine, and in a two-ray multipath environment to assess the ranging performance of the 1D- and 2D-JML estimators with real LTE signals. The ultimate ranging performance of these estimators for a system bandwidth of 1.4 MHz is finally analysed over a realistic navigation scenario by emulating the standard ETU channel in a real testbed.

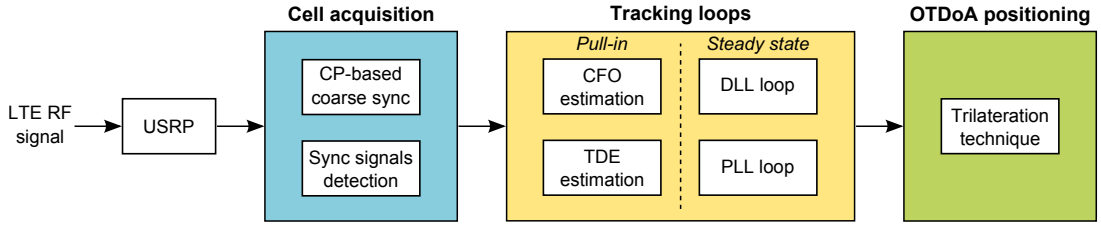


Figure 5.1: SDR LTE positioning receiver top-level block diagram.

## 5.1 SDR LTE positioning receiver

The software-defined radio LTE positioning receiver is implemented in MATLAB by post-processing the signal captured with a USRP platform. As it is shown in Figure 5.1, the SDR is based on three main modules: cell acquisition, tracking loops and OTDoA positioning.

### 5.1.1 Cell acquisition

In any LTE terminal, time and frequency synchronization are of paramount importance for cell acquisition. Generally, frequency synchronization has attracted more attention due to the sensitivity of OFDM receivers to carrier frequency offsets, but timing errors still have to be compensated in order to avoid severe performance degradation [Mor07]. Thus, the acquisition stage is based on the coarse time and frequency synchronization and the cell search procedure.

First, the start of the cyclic prefix is found by using the classical van de Beek algorithm [Bee97], which is a non-data-aided (NDA) maximum likelihood estimator written as

$$\tau_0 = \arg\max_{\tau} \left\{ |\gamma(\tau)| - \varepsilon \cdot \Phi(\tau) \right\}, \tag{5.1.1}$$

with

$$\gamma(m) \doteq \sum_{\ell=m}^{m+N_{\mathrm{CP}}-1} x(\ell) \cdot x^*(\ell+N), \tag{5.1.2}$$

$$\Phi(m) \doteq \frac{1}{2} \sum_{\ell=m}^{m+N_{\mathrm{CP}}-1} |x(\ell)|^2 + |x(\ell+N)|^2, \tag{5.1.3}$$

where $x(m)$ denotes the discrete-time signal samples, $\ell$ is the correlation lag, $N_{\mathrm{CP}}$ is the normal CP length in samples, and $\varepsilon$ is the correlation coefficient, which is approximated to

one for high SNR. As it can be seen, the algorithm takes advantage of the redundancy introduced by the cyclic prefix to coarsely estimate the time delay, using the auto-correlation function $\gamma(m)$, the energy $\Phi(m)$ and a sliding window size of $N_{\mathrm{CP}}$ samples. The complexity of the algorithm can be reduced with a recursive computation of $\gamma(m)$ and $\Phi(m)$ [Man09]. In addition, this estimation can be slightly refined by integrating several times the cost function of (5.1.1). Then, the frequency offset can be coarsely estimated as

$$\nu_0 = -\frac{1}{2\pi T} \arg\left\{\gamma(\tau_0)\right\}. \tag{5.1.4}$$

Given the CP-based estimates $\tau_0$ and $f_0$, the coarse synchronisation is completed by compensating these time and frequency shifts on the received signal. Now, the cell detection procedure can be started by removing the cyclic prefix and analysing the signal in the frequency domain. For this purpose, a discrete Fourier transform is applied to the OFDM signal as

$$r(n) = \mathcal{F}\left\{x(m+\tau_0) \cdot \exp\left(-j\frac{2\pi m f_0}{N}\right)\right\}. \tag{5.1.5}$$

Then, the received frequency samples $r(n)$ are cross-correlated with the PSS and SSS sequences in order to find the cell identity $N_{\mathrm{ID}}^{\mathrm{cell}}$. The applied circular cross-correlation can be expressed as

$$R_u(\ell) \doteq \sum_{n=-31, n\neq 0}^{31} r^*(n) \cdot d_u(n+\ell), \tag{5.1.6}$$

where $d(n)$ is a circular shifted version of the original pilot sequence and the subscript $u$ denotes the synchronisation sequence (i.e. PSS or SSS). The avoidance on the transmission of the DC subcarrier degrades the code properties of these sequences, where the ideal auto-correlation for the ZC codes is

$$R_{\mathrm{ZC}}(\ell) = \begin{cases} 1 & \text{if } \ell = 0, \\ 0 & \text{otherwise,} \end{cases} \tag{5.1.7}$$

and for the $m$-sequences is

$$R_M(\ell) = \begin{cases} 1 & \text{if } \ell = 0, \\ -1/M & \text{otherwise,} \end{cases} \tag{5.1.8}$$

being $\ell$ the correlation lag, and $M$ equal to 31. Finally, the peak of the correlation leads

to the cell identity detection, as follows,

$$N_{\mathrm{ID}}^{\mathrm{cell}} = 3 \cdot \arg\max_{N_{\mathrm{ID}}^{(1)}} \left\{ \left| R_{\hat{N}_{\mathrm{ID}}^{(1)}}(\ell) \right| \right\} + \arg\max_{N_{\mathrm{ID}}^{(2)}} \left\{ \left| R_{\hat{N}_{\mathrm{ID}}^{(2)}}(\ell) \right| \right\}. \tag{5.1.9}$$

where $N_{\mathrm{ID}}^{(1)}$ and $N_{\mathrm{ID}}^{(2)}$ are the detected cell identity group and sector, respectively.

### 5.1.2 Tracking loops

The residual errors resulting from the coarse synchronisation can severely degrade the time-delay estimation. Thus, a pull-in process is implemented in order to further reduce the acquisition errors. This process is based on integrating the outputs of a time-delay estimator and a carrier frequency offset estimator among several pilot symbols, to reduce the initial acquisition offsets. Conventional estimators are used for this purpose. Thus, the time-delay estimation is based on the matched filter, while the CFO estimator is based on the phase difference between OFDM pilot symbols [Moo94], which is defined as

$$\nu = \frac{N}{2\pi \cdot T \cdot (N + N_{\mathrm{CP}}) \cdot P} \cdot \arg\left\{ \sum_{n \in \mathcal{N}_{\mathrm{a}}} s_{k-P}^{*}(n) \cdot s_k(n) \right\}, \tag{5.1.10}$$

where $\mathcal{N}_{\mathrm{a}}$ is the subset of available pilot subcarriers, $k$ is the symbol index and $P$ is the index difference to the previous pilot symbol, and $s(n)$ denotes the OFDM signal after the wipe-off of the pilot code $d(n)$ in the frequency domain, i.e. $s(n) = r(n) \cdot d^{*}(n)$. Both time and frequency estimators are unbiased for those initial acquisition offsets that fulfil $|\tau| \leq T/2$ and $|\nu| \leq 1/(2T)$, respectively. Then, in order to further reduce the noise effect, several $\tau$ and $\nu$ estimates are averaged, and the resulting values are used to compensate most of the residual time and frequency errors.

Once the initial offsets are sufficiently reduced, tracking loops are implemented to filter the time-delay and frequency estimates. The tracking architecture is based on a first-order delay lock loop (DLL) with a second-order phase lock loop (PLL) assist [Bor07, War06], as it is shown in Figure 5.2. The resulting TDE of the matched filter in (3.2.3) is fed into the DLL. In addition, this TDE is used to compensate the time-delay offset and to estimate the phase of the pilot subcarriers,

$$\phi = \frac{1}{2\pi} \cdot \arg\left\{ \frac{1}{N_{\mathrm{a}}} \sum_{n \in \mathcal{N}_{\mathrm{a}}} s(n) \cdot \exp\left( j \frac{2\pi \cdot n \cdot \tau}{N} \right) \right\}, \tag{5.1.11}$$

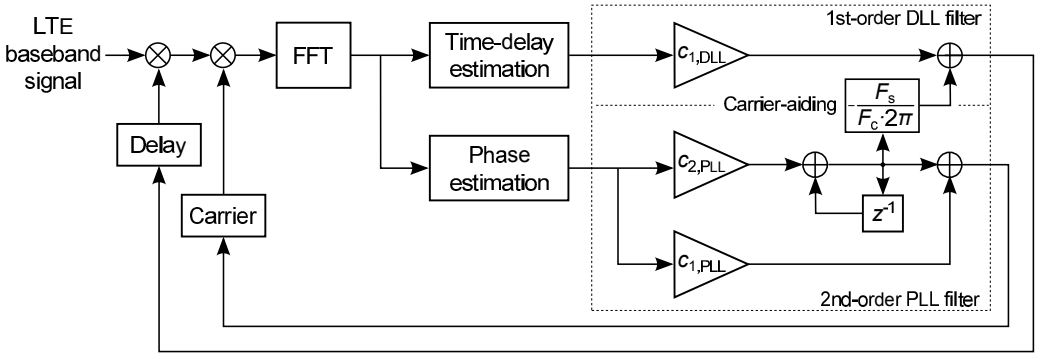


Figure 5.2: Tracking architecture based on a first-order DLL with a second-order PLL assist.

where $N_{\mathrm{a}}$ is the number of pilot subcarriers. Then, the phase estimate $\phi$ is introduced in the PLL. The DLL and PLL loop filter coefficients of first and second order, i.e. $c_1$ and $c_2$, respectively, are calculated according to [Bor07] as

$$c_1 = \frac{1}{K_0 K_{\mathrm{d}}} \cdot \frac{8\zeta\omega_{\mathrm{n}} T_{\mathrm{L}}}{4 + \zeta\omega_{\mathrm{n}} T_{\mathrm{L}} + \left(\omega_{\mathrm{n}} T_{\mathrm{L}}\right)^2}, \tag{5.1.12}$$

$$c_2 = \frac{1}{K_0 K_{\mathrm{d}}} \cdot \frac{4\left(\omega_{\mathrm{n}} T_{\mathrm{L}}\right)^2}{4 + \zeta\omega_{\mathrm{n}} T_{\mathrm{L}} + \left(\omega_{\mathrm{n}} T_{\mathrm{L}}\right)^2}, \tag{5.1.13}$$

where $K_0 K_{\mathrm{d}}$ is the loop gain, $\zeta$ is the damping ratio, $\omega_{\mathrm{n}}$ is the natural frequency, and $T_{\mathrm{L}}$ is the sampling period of the loop. Typical values of the loop design are a loop gain $K_0 K_{\mathrm{d}}$ equal to one and a damping ratio $\zeta$ equal to $\sqrt{2}/2$. Given this damping ratio, the natural frequency for the first order filter is $\omega_{\mathrm{n}} = 4B_{\mathrm{L}}$ and for the second order filter is $\omega_{\mathrm{n}} = 1.89B_{\mathrm{L}}$, where $B_{\mathrm{L}}$ is the noise bandwidth in the loop [War06]. The frequency shift estimated by the PLL is used to aid the DLL, known as *carrier-aiding*, with a scale factor $\alpha = F_{\mathrm{s}}/F_{\mathrm{c}}$ [War06], where $F_{\mathrm{c}}$ is the carrier center frequency. Finally, the output of the loop filters is integrated in order to track the signal in the next interval.

In parallel to the signal tracking, the SNR estimation is a metric that helps to assess the performance of the receiver. Many SNR estimators have been presented in the literature, as it is reviewed in [Pau00]. In order to take advantage of the empty and pilot subcarriers of the signal, the NDA SNR estimator proposed in [Li10] is implemented in the SDR receiver. Its SNR estimation $\rho$ is written as

$$\rho = \frac{\sum_{n \in \mathcal{N}_{\mathrm{a}}} |r(n)|^2}{\sum_{n \in \mathcal{N}_{\mathrm{e}}} |r(n)|^2} \cdot \eta - 1, \tag{5.1.14}$$

where the indexes of the $N_{\mathrm{e}}$ empty subcarriers are denoted in the subset $\mathcal{N}_{\mathrm{e}}$, and $\eta$ denotes the noise-to-noise ratio (NNR). The empty subcarriers are located in the guard bands of the system bandwidth, e.g. $N_{\mathrm{e}} = F_{\mathrm{s}}/F_{\mathrm{sc}} - 12 \cdot N_{\mathrm{RB}} - 1 = 55$ subcarriers for a sampling frequency $F_{\mathrm{s}}$ equal to 1.92 MHz and 6 RB. Considering an AWGN channel, the expected value of the NNR is defined by

$$\bar{\eta} = \frac{N_{\mathrm{e}}}{N_{\mathrm{a}}}. \tag{5.1.15}$$

The $C/N_0$ estimation can be obtained from the SNR estimates by considering the effective signal bandwidth, defined as $B_{\mathrm{eff}} = N \cdot F_{\mathrm{sc}}$.

### 5.1.3 OTDoA positioning

Once the receiver is in steady state tracking, its location is finally calculated with the OTDoA positioning method [3GP13b]. As it was introduced in Section 2.3, this method is based on the time-delay differences between the reference BS and the neighbour BSs to compute the position. As it is shown in Figure 5.3, the time-difference measurements follow hyperbolas that intersect in the UE location, which is then calculated with a trilateration technique. Taking as a reference the serving BS, i.e. BS 1, the difference between time-delay estimates (in seconds) of BS 1 and BS $i$ is defined by the following nonlinear equation [Bue12]:

$$t_1 - t_i = \frac{\sqrt{(x_1 - x)^2 + (y_1 - y)^2} - \sqrt{(x_i - x)^2 + (y_i - y)^2}}{c}, \tag{5.1.16}$$

where $x$ and $y$ are the user position coordinates, $x_1$ and $y_1$ are the BS 1 coordinates, $x_i$ and $y_i$ are the BS $i$ coordinates, and $c$ is the speed of light. As it can be seen, the user position unknowns $x$ and $y$ can be solved with at least two time-difference measurements. This computation only requires the knowledge of the BS locations and the time-delay offset between their transmission. Although OTDoA is implemented in LTE as a network-based positioning technology, the BS coordinates and their relative downlink timing are assisted to the SDR receiver, allowing the UE-based position calculation. The trilateration technique used in the positioning module is based on Fletcher s version of the Levenberg-Marquardt algorithm for minimization of a sum of squares of equation residuals [Fle71], which is implemented in a MATLAB function of the MathWorks File Exchange repository [Bal07].

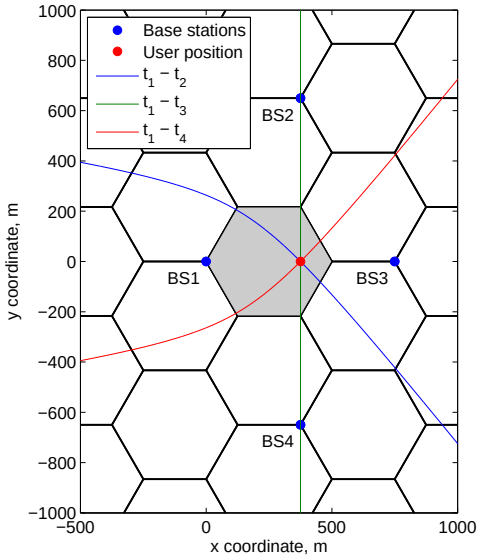


Figure 5.3: Example of hyperbolas obtained from the time-difference measurements, showing the possible locations of the user and its true position on the intersection of hyperbolas. The base station positions (blue dots) and user position (red dot) define the validation scenario.

## 5.2 Validation results of OTDoA positioning

The validation of the SDR LTE positioning receiver is performed with a static LTE scenario. The UE and BSs are fixed at specific positions in order to determine the specific time delay and power received for each signal. This scenario is emulated with equipment of the European Navigation Laboratory (ENL) at the European Space Agency (ESTEC, The Netherlands). An overall view of this equipment at ENL is shown in Figure 5.4. Then, the LTE received signal is captured with the USRP, and post-processed in MATLAB. Using the SDR receiver, the signal is acquired and tracked by means of a coarse and fine synchronisation. Finally, the SDR functionality is validated with the SDR position estimates.

### 5.2.1 Scenario definition

The setup of the validation scenario is based on a LTE network emulator, the USRP platform and the SDR positioning receiver, as it is depicted in Figure 5.5. The LTE network is emulated using two Spirent E2010S network emulators of the ENL facilities. These two emulators generate four synchronized LTE signals, each signal corresponding to a base station. The four BSs are assumed to belong to the same network operator, thus they

Figure 5.4: Testbench at the European Navigation Laboratory.

transmit in the same frequency channel, leading to intra-frequency RSTD measurements (i.e. time-delay differences at the same frequency). The band 3 at 1800 MHz is chosen for the downlink signal transmission, because it is the most popular spectrum for LTE commercial deployments [GSA14b]. Particularly, the E-UTRA Absolute Radio Frequency Channel Number (EARFCN) [3GP12c] is the 1750, corresponding to a carrier center frequency of 1860 MHz. The output of the emulators is then fed into a RF combiner, which combines the LTE RF signal from the base stations.

The physical layer of the network emulator is configured with a system bandwidth of 1.4 MHz. The PRS is transmitted in the whole bandwidth every 160 ms for six consecutives subframes and an offset of two subframes (i.e. $I_{\text{PRS}} = 2$). In addition, the network emulator requires as inputs the received power and time delay for each BS. Thus, an urban macro-cell deployment is emulated with a inter-site distance of 750 meters, as it was modelled in Section 3.3.1. The deployment is based on a hexagonal grid with three-sectorial base stations (i.e. 3-dB beamwidth of 65-degree). As it is shown in Figure 5.3, the UE is located at coordinates $\{x, y\} = \{\text{ISD}/2, 0\}$ in meters, and the BSs are at coordinates $\{x_i, y_i\} = \text{ISD}/2 \cdot \left\{0, 0; 1, \sqrt{3}; 2, 0; 1, -\sqrt{3}\right\}$ also in meters. Considering the parameters summarized in Table 4.4 of the previous chapter, and using them into (3.3.4), the resulting received power values are: $P_{\text{rx},i} = \{-54.08, -65.61, -64.31, -65.61\}$ in dBm. The potential inter-cell interference produced by the deployment of more base stations will not be considered. The application of shadowing or multipath are out of the scope of this section.

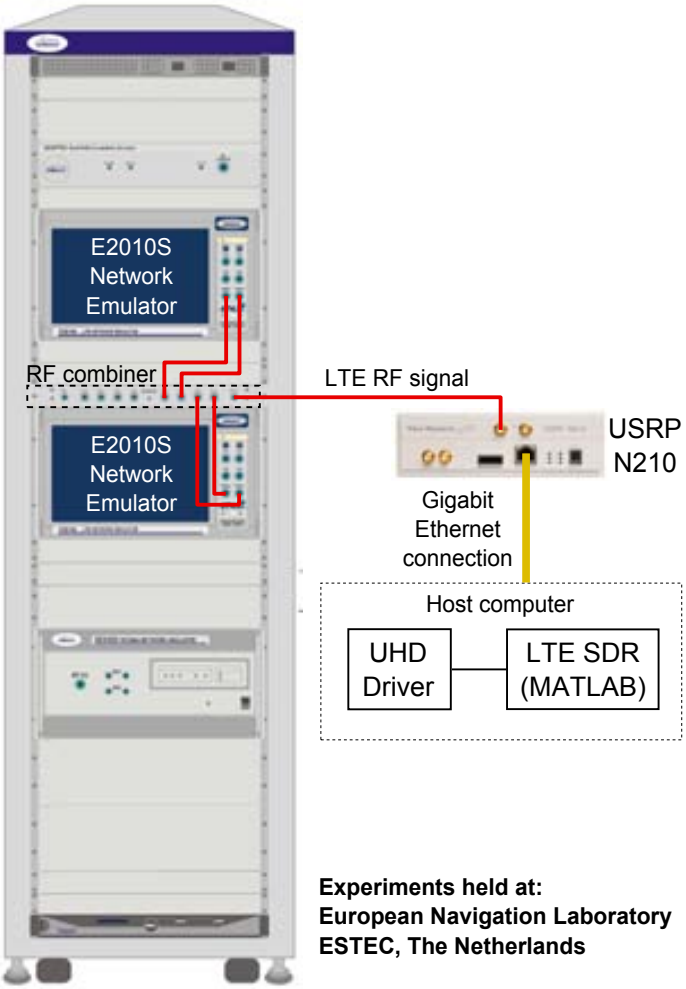


Figure 5.5: Schematic of the equipment for OTDoA tests.

Once the network emulators are configured, their RF outputs are combined and fed to a USRP N210 platform installed with a DBSRX2 daughterboard. The USRP is then connected through the Gigabit Ethernet port and controlled with the USRP hardware driver (UHD) from a computer. The UHD commands the recording of the complex baseband samples at a sampling ratio of 2 MHz. Finally, the samples are loaded with MATLAB and downsampled to 1.92 MHz, where the LTE signals are processed with the SDR receiver described in Section 5.1. The SDR receiver is assisted with the cell identities and relative time delays of the BSs emulated. The serving cell identity (i.e. BS 1) is first acquired and detected. Then, the assistance information is used to avoid the neighbour cell identification. Since the SDR receiver does not communicate with the network, no user data is transmitted by the emulated BSs. Thus, there are cell-specific reference signals without inter-cell interference. These CRS are used for tracking purposes and to validate the positioning module in absence of inter-cell interference and multipath, i.e. only in AWGN conditions.

### 5.2.2 Acquisition of the signal

Given the described scenario, the LTE RF signals are transmitted and captured using the equipment at ENL. An UHD example application, called `rx_samples_to_file`, is used to command the USRP to capture the signal and to store the received samples in the computer. This example application is described in [Ett12], where the main parameters are the carrier center frequency $F_{\mathrm{c}}$, the sampling frequency $F_{\mathrm{s0}}$, and the gain for the RF chain.

The analog-to-digital converter (ADC) of the USRP have a fixed sampling frequency of 100 MHz. This sampling frequency can be modified in the field-programmable gate array (FPGA) by applying a defined decimation rate. Once the signal is captured and stored in a file, it can be read in MATLAB and downsampled to the adequate sampling frequency specified in LTE. In this case, the LTE system bandwidth of 1.4 MHz is captured by the USRP with a sampling frequency $F_{\mathrm{s0}} = 2$ MHz, which is then downsampled to $F_{\mathrm{s}} = 1.92$ MHz, as it is shown in Fig. 5.6, in order to preserve the subcarrier spacing $F_{\mathrm{sc}} = 15$ kHz. The relation between these two sampling frequencies is an interpolation rate equal to 24 and a decimation rate equal to 25. Using this relation, the downconversion can be implemented introducing zero-padding in the frequency domain or using the MATLAB `resample` function, which has a lower computational load. The first captured samples are usually corrupted due to instabilities after locking to the signal frequency specified. Thus, it is recommended to skip a few hundreds of samples at the beginning of the file.

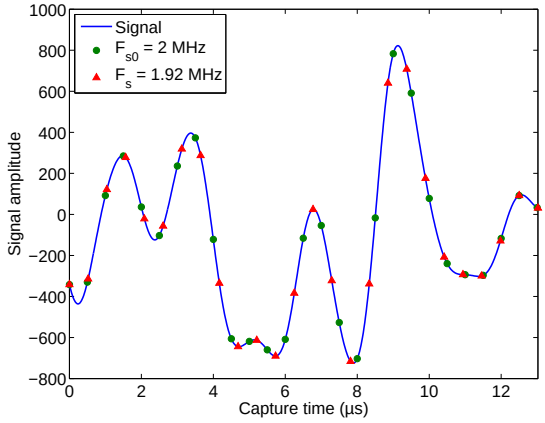


Figure 5.6: Downsampling of the received signal from a sampling frequency $F_{s0}$ of 2 MHz to a sampling frequency $F_s$ of 1.92 MHz.

Once the signal is captured and downsampled, the SDR receiver is able to acquire and synchronise the signals of four base stations, leading to the power spectral density shown in Figure 5.7(a). The captured signal is mainly defined by the pilot signals depicted in Figure 5.7(b). As it can be seen, the CRS and PRS pilots of different BSs do not overlap among them, because they use different allocation patterns mainly defined by the cell identity of each BS.

### 5.2.3 Coarse synchronisation

The coarse synchronisation is based on the acquisition of the LTE signal and the detection of the cell identity $N_{\mathrm{ID}}^{\mathrm{cell}}$, as it is described in Section 5.1.1. For this purpose, the redundancy of the CP is used with van de Beek algorithm [Bee97] to acquire the start of the OFDM symbol. Applying this algorithm, the maximum of the auto-correlation function corresponds to the coarse timing estimation, as it is shown in Figure 5.8(a). Then, the carrier frequency is coarsely synchronized using (5.1.5).

Once time and frequency are coarsely synchronized, the cell identity is detected by cross-correlating the received signal with the PSS and SSS. The cell identity sector $N_{\mathrm{ID}}^{(2)}$ is first detected with the PSS, as it shown in Figure 5.8(b), and the cell identity group $N_{\mathrm{ID}}^{(1)}$ is then detected with the SSS, as it can be seen in Figure 5.8(c). In this case, the cell detection is achieved at the fifth subframe (i.e. SF = 5). As it was discussed in Section 2.4.2, the ideal properties of the ZC sequences and $m$-sequences, which are highlighted with a black dashed line in Figure 5.8(b) and 5.8(c), respectively, cannot be achieved due to avoidance of the DC subcarrier.

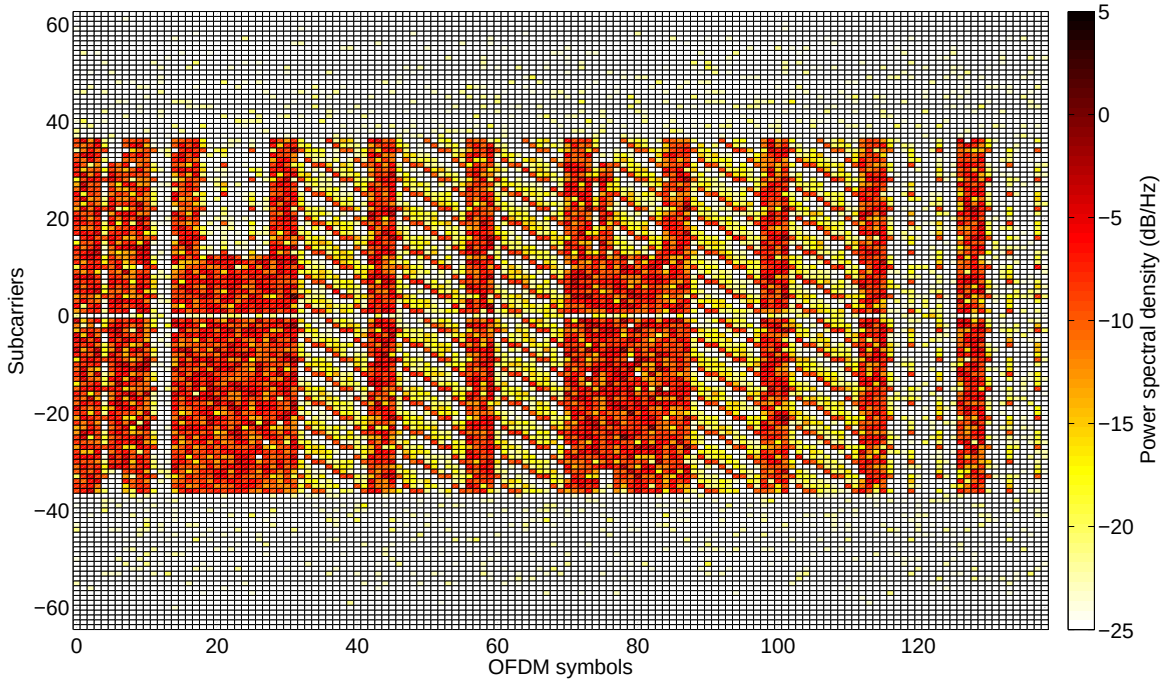


(a) Power spectral density of the received signal

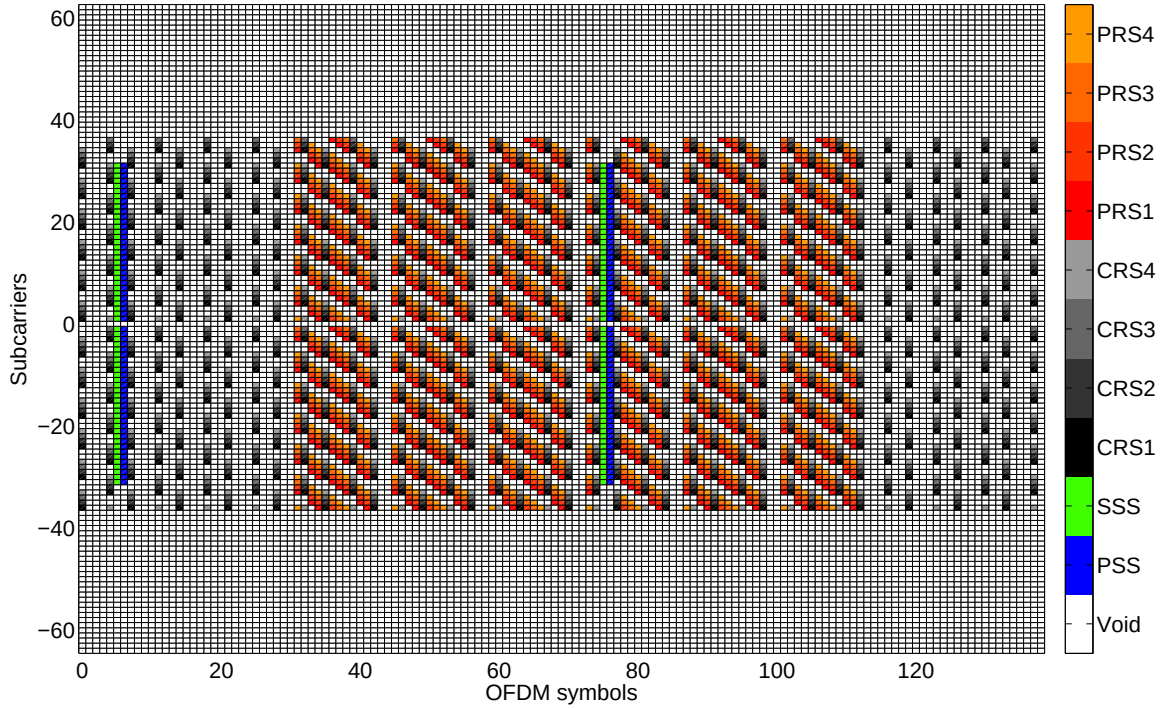


(b) LTE pilot signals

Figure 5.7: Time and frequency representation of the PSD with a PRS-enabled LTE radio frame for the validation scenario of four base stations.

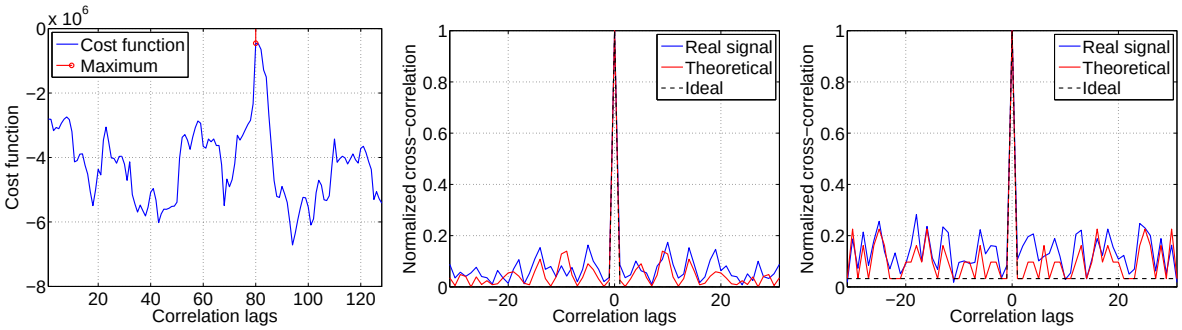


(a) CP-based coarse estimation (b) PSS, $N_{\mathrm{ID}}^{(2)} = 0$ (c) SSS, $N_{\mathrm{ID}}^{(1)} = 0$, SF $= 5$

Figure 5.8: Coarse synchronisation and cell identity detection.

### 5.2.4 Fine synchronisation

After the acquisition of the signal, the coarse time and frequency estimates are averaged over one radio frame to reduce the possible residual errors, which is here called pull-in process. Fine synchronization of time and frequency is then achieved using the tracking architecture shown in Figure 5.2. The noise bandwidth $B_{\mathrm{L}}$ of the DLL and PLL is set to 1 Hz and 20 Hz, respectively. In this case, the one CRS symbols every slot is used for time-delay and frequency estimation, because these OFDM symbols have no interference from data transmission. Thus, the sampling period of the loops $T_{\mathrm{L}}$ is equal to 0.5 ms.

The time-delay estimation obtained with the DLL is used to compute the time-differences between the serving BS and the neighbour BSs. The resulting OTDoA estimates are shown in Figure 5.9(a). The frequency shift estimates are obtained with the PLL, and they are depicted in Figure 5.9(b). As it can be seen, the DLL and PLL are able to track the incoming signal. However, the frequency shift has a noticeable oscillation due to the internal clock of the USRP. This clock instability can be reduced significantly by using an accurate external reference clock.

The SNR is also estimated for each BS by using one CRS symbol every slot. The mean of the SNR estimates is obtained every 200 ms, as it is shown in Figure 5.9(c), being the standard deviation of these SNR estimates depicted with error bars. The resulting SNR for the serving BS (i.e. BS 1) is approximately 19.8 dB, while the resulting SNR for the neighbour BSs (i.e. BS 2, BS 3 and BS 4) is approximately 8.7 dB, 9.9 dB and 8.7 dB, respectively. The standard deviation of the SNR for each BS is around 1 dB. As it can be seen, the differences between the SNR estimates obtained for each BS coincide approximately with the differences between the received power values $P_{\mathrm{rx},i}$ defined in Section 5.2.1. Thus, these results are in accordance with the scenario emulated.

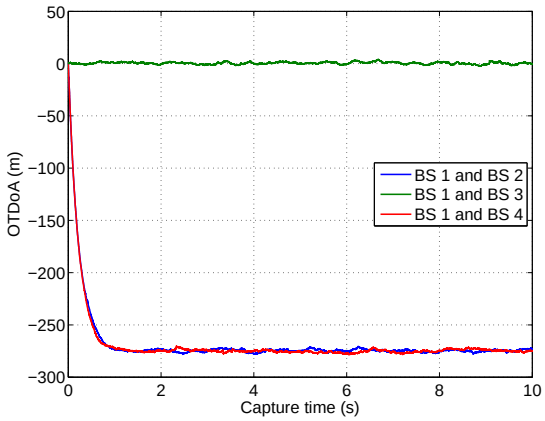


(a) OTDoA tracked by DLL

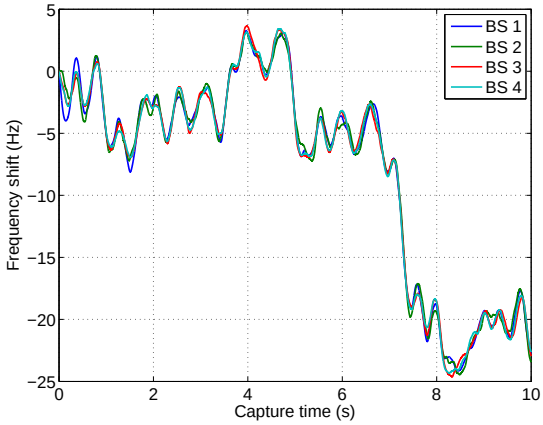


(b) Frequency shift tracked by PLL

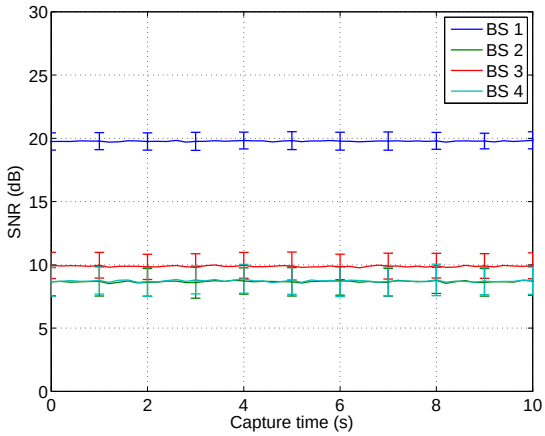


(c) SNR estimation for four BSs

Figure 5.9: Tracking results of the SDR LTE receiver for four LTE signals with a system bandwidth of 1.4 MHz in a static AWGN scenario.

### 5.2.5 Positioning

The user position is finally estimated using the OTDoA measurements, as it is shown in Figure 5.10(a). The estimated positions are obtained after the calibration of the relative time delays of the BSs emulated. However, there is still a bias on the mean value estimated with respect to the true user position, which is approximately equal to 34 cm. The standard deviation for $x$ and $y$ coordinates is plotted with an ellipse. As it can be seen, the position errors in the $x$ coordinate are lower than in the $y$ coordinate. This is due to the distribution of the base stations and the user position, depicted in Figure 5.3. The CDF of the position errors obtained with the SDR receiver are shown in Figure 5.10(b). Accurate position estimations with errors lower than three meters can be achieved for this static AWGN scenario with a system bandwidth of 1.4 MHz.

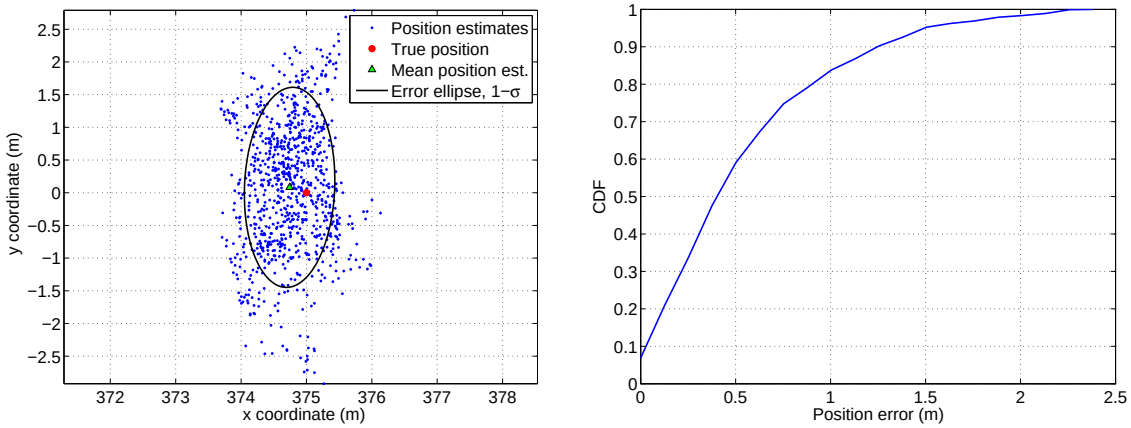


(a) Position estimations and true position

(b) CDF of position errors

Figure 5.10: Positioning results of the SDR LTE receiver for four LTE signals with system bandwidth of 1.4 MHz in a static AWGN scenario.

## 5.3 Multipath error envelope using real LTE signal

The previous section was aimed to validate the operation of the SDR LTE positioning receiver. Thus, a static scenario in absence of multipath was emulated using the equipment at ENL. In this section, the ranging performance of the 1D- and 2D-JML estimators is assessed with real LTE signals in a multipath scenario. In order to achieve a controlled environment, a two-ray multipath model is considered and the multipath error envelope is computed. This section describes the methodology followed and the MPEE results obtained for in-phase and counter-phase multipath cases.

### 5.3.1 Methodology

The current experiments in the presence of multipath are based on the ENL testbed of the previous section, which was shown in Figure 5.5. Since only ranging estimations are necessary to compute the MPEE, only one BS is emulated using a Spirent E2010S network emulator. The LTE signal is transmitted with a received power equal to $-50$ dBm in band 3 at a carrier center frequency of 1860 MHz (i.e. EARFCN equal to 1750). The system bandwidth is configured to 1.4 MHz, with the PRS-enabled every 160 ms with six consecutives subframes and an offset of two subframes (i.e. $I_{\text{PRS}} = 2$). Then, the Spirent VR5 HD spatial channel emulator is used to generate a two-ray multipath channel, which is based on a LoS signal with a power of $-40$ dBm and a multipath ray with SMR $= 1$ dB and $\phi_1 = \{0, \pi\}$. This multipath channel is convolved with the LTE signal fed from the network emulator. Once signal and multipath are emulated, the resulting

Table 5.1: Main equipment and configuration parameters of the testbed.

| | |
|---|---|
| *Equipment* | |
| Network emulator | Spirent E2010S |
| Channel emulator | Spirent VR5 HD |
| Software-defined radio | USRP N210 with DBSRX2 daughterboard |
| *Configuration parameters* | |
| Signal power | −40 dBm |
| LTE signal configuration | Normal CP with PRS-enabled |
| System bandwidth | 1.4 MHz |
| Carrier center frequency | 1860 MHz (band 3, EARFCN 1750) |
| USRP reference clock | 10-MHz external clock |
| USRP sampling frequency | 2 MHz |
| USRP gain | 40 dB |
| Receiver sampling frequency | 1.92 MHz |

RF signal is captured with the USRP N210 platform, which is mounted with a DBSRX2 daughterboard. The USRP is controlled with the `rx_samples_to_file` UHD application, which is configured with a gain of 40 dB and a sampling ratio of 2 MHz. An accurate external reference clock of 10 MHz is connected to the USRP in order to have a stable reference clock. Finally, the complex baseband samples of the LTE signal captured are downsampled to 1.92 MHz using the MATLAB `resample` function. The main equipment and configuration parameters of this testbed are summarized in Table 5.1.

Using this testbed, the MPEE is obtained with a single capture of the signal. This implies that the emulation and reception of the signal have to be coordinated in order to achieve adequate results. Thus, the methodology to compute the MPEE with real LTE signals is defined by three phases:

1. **Acquisition and tracking of the LoS signal**. During the first few seconds of the signal capture, the LoS signal is only transmitted in order to let the receiver to properly acquire and track the LTE signal. This procedure should avoid any bias on the time-delay estimation before adding a multipath ray to the channel. The CRS pilots are used every slot, i.e. every 0.5 ms, to update the estimates in the tracking loops, whose architecture was shown in Figure 5.2. The loop bandwidth of the DLL and the PLL is set to 0.8 Hz and 15 Hz, respectively.

2. **Ranging estimation in a two-ray multipath channel**. Once the SDR receiver is tracking the time delay and the frequency shift, a multipath ray is added to the

LoS ray by specifying a certain multipath delay $\tau_1$. The two-ray multipath channel induces a bias on the TDE in most of the cases. Thus, the time-delay estimates are not fed into the DLL, and the signal is tracked by using the carrier-aiding and the time delay filtered during the previous LoS-signal stage. In order to distinguish between different multipath channels, the value of the multipath delay $\tau_1$ is fixed during one second.

3. **MPEE computation**. Every point of the MPEE is finally obtained by averaging the time-delay estimates of the 1D- or 2D-JML estimator over one second. The standard deviation of the time-delay estimates is also computed.

Following this methodology, the MPEE results using real LTE signal can be compared with those results obtained in Section 4.4.1. This procedure should validate the ranging performance of the 1D- and 2D-JML estimators.

### 5.3.2 In-phase multipath ray

The MPEE is first computed considering an in-phase multipath contribution in the two-ray channel model. During the first ten seconds of the experiment, the LoS signal is only transmitted in order to help the acquisition and tracking of the signal. The time delay is estimated with the 1D-JML estimator for $L = 1$, and the phase is estimated with the four-quadrant arctangent of the frequency-correlated samples. Both time-delay and phase estimates are obtained by using the CRS pilots of one OFDM symbol every slot. These CRS pilots are also used to estimate the $C/N_0$ with (5.1.14). After the tenth second, the in-phase multipath ray is introduced in the channel, and the multipath delay is increased at a rate of approximately $0.02 \cdot T_\mathrm{s}$ per second, where $T_\mathrm{s}$ is equal to 980.39 ns. Considering both emulation stages, the RF signal is captured during 100 seconds, and its frequency shift is continuously tracked, as it shown in Figure 5.11(a). Since the external reference clock of 10 MHz is connected to the USRP, the variance of the frequency shift is considerably lower than in Section 5.2.4, where the internal clock was used. The standard deviation of the current frequency tracking (during the total capture) is equal to 0.38 Hz. Once the in-phase multipath ray is added, the time-delay estimates are not fed into the DLL (to avoid disturbances on the resulting MPEE), thus the DLL is only driven by the previous filtered estimate and the carrier-aiding from the PLL. The signal is sufficiently stable to maintain tracking during this multipath stage.

Among the total time of the signal capture, 75 seconds are used to obtain the MPEE, by using multipath delays within $[0, 1.5]$ in $T_\mathrm{s}$ units. Since the multipath delay is fixed

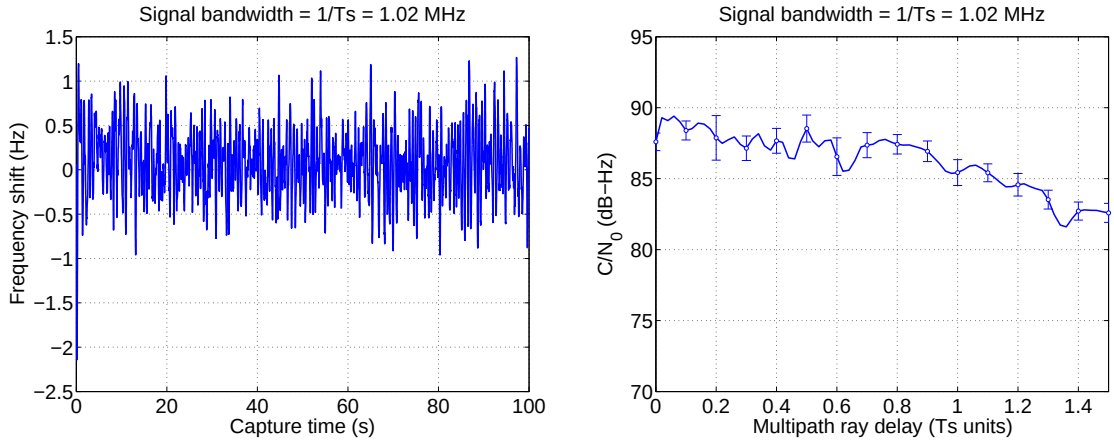


(a) Frequency shift tracked over capture time (b) $C/N_0$ estimation over multipath delay $\tau_1$

Figure 5.11: Tracking results of the real emulated signal, considering the 6-RB CRS without data transmission and an in-phase multipath ray with 1 dB of SMR.

during one second, 200 estimates of the time delay, phase, frequency shift and $C/N_0$ are obtained. As it is shown in Figure 5.11(b), the mean of the $C/N_0$ estimates decreases as the multipath delay increases. The standard deviation of these estimates is depicted in this figure by error bars with values around 1 dB. The MPEE using the 1D-JML estimator for $L = \{1, 8\}$ and the 2D-JML estimator for $L = 8$ is then obtained with the real LTE signal, as it is shown in Figure 5.12. These results are compared with the MPEE computed (in absence of noise) with a simulated LTE signal in Section 4.4.1. Since the multipath error is obtained for the 1D- and 2D-JML using the mean of 200 estimates per point, the standard deviation of these estimates is depicted with error bars. The resulting MPEE with the 1D-JML estimator for $L = \{1, 8\}$ is very similar in both real and simulated cases. In addition, the standard deviation of these estimators is smaller than the 2D-JML estimator for $L = 8$. Still, the 2D-JML estimator achieves mean values close to a multipath error equal to zero. The overall performance of the estimators can be assessed by computing the CDF of the multipath errors. Considering the time-delay estimates used to obtain the MPEE, the CDF of these estimates is shown in Figure 5.13. The 2D-JML estimator for $L = 8$ obtains a considerable improvement with respect to the 1D-JML estimators. For instance, the 2D-JML estimator for $L = 8$ produces an absolute TDE error of $0.08{\cdot}T_s$ (i.e. 23.5 meters) for 67% of the cases, while the 1D-JML estimators obtain (for the same percentage of the cases) an error of $0.29{\cdot}T_s$ (i.e. 85.3 meters) with $L = 1$ and $0.18{\cdot}T_s$ (i.e. 52.9 meters) with $L = 8$. However, the ranging performance of the 2D-JML estimator is degraded due to the impact of noise, as it can be seen from an absolute TDE error lower or equal to $0.5{\cdot}T_s$ (i.e. 147.1 meters) for 95% of the cases.

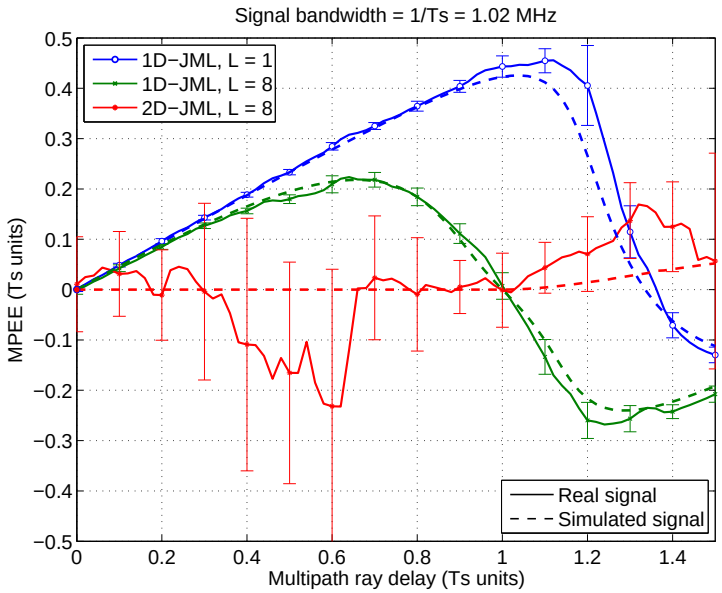


Figure 5.12: MPEE of the 1D- and 2D-JML estimators using the single-tap, periodic-tap and hybrid-tap models for the real emulated signal (solid lines) and the simulated signal (dashed lines), considering the 6-RB CRS without data transmission and an in-phase multipath ray with 1 dB of SMR.

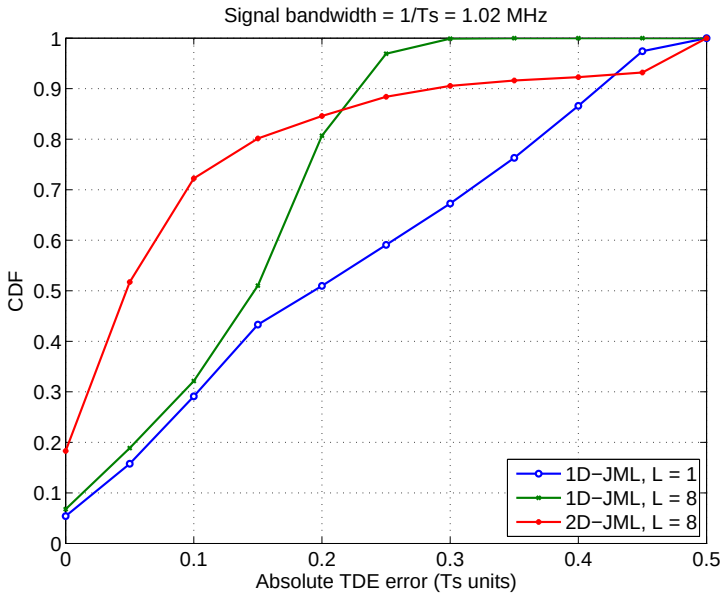


Figure 5.13: CDF of ranging errors of the 1D- and 2D-JML estimators using the single-tap, periodic-tap and hybrid-tap models for the real emulated signal, considering the 6-RB CRS without data transmission and an in-phase multipath ray with 1 dB of SMR.

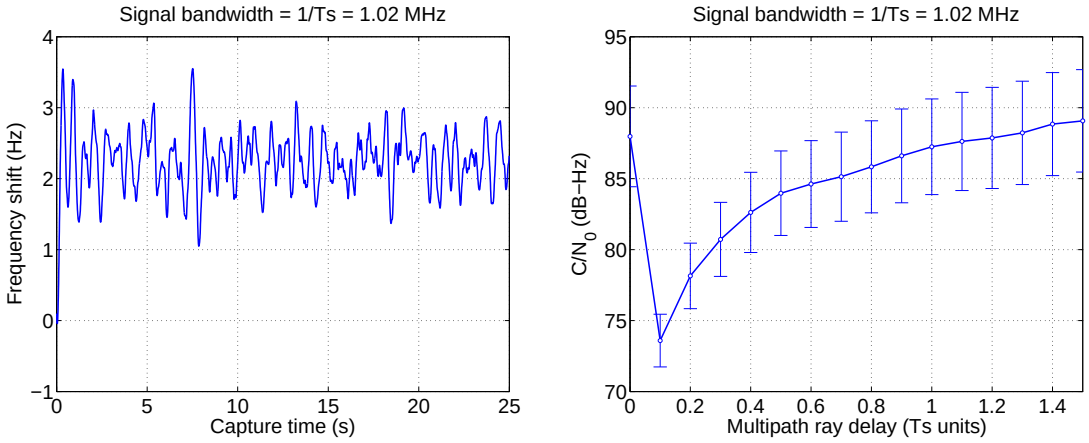


(a) Frequency shift tracked over capture time (b) $C/N_0$ estimation over multipath delay $\tau_1$

Figure 5.14: Tracking results of the real emulated signal, considering the 6-RB CRS without data transmission and a counter-phase multipath ray with 1 dB of SMR.

### 5.3.3 Counter-phase multipath ray

Following the same procedure as in the previous section, a counter-phase multipath ray is considered in the channel model. During the first 2.5 seconds, the signal is properly acquired and tracked due the transmission of only LoS signal. The estimation process is implemented considering the CRS pilots of one symbol every slot, thus 200 estimates are obtained every second. After 2.5 seconds of capture time, the multipath delay of the counter-phase ray is added and increased at a rate of approximately $0.1 \cdot T_s$ per second, where $T_s$ is equal to 980.39 ns. The RF signal is captured during 25 seconds, and the frequency shift is continuously tracked, as it shown in Figure 5.14(a). As in the previous section, the 10-MHz external clock provides an stable reference, leading to a standard deviation of the frequency shift equal to 0.42 Hz (during the total capture time).

The MPEE is computed using 15 seconds of the signal capture, considering multipath delays within $[0, 1.5]$ in $T_s$ units. For each point, 200 estimates of the time delay, phase, frequency and $C/N_0$ are obtained. The mean of the $C/N_0$ estimates is shown in Figure 5.14(b), depicting the standard deviation of these estimates with error plots. As it can be seen, the mean $C/N_0$ of the counter-phase case is lower than the mean $C/N_0$ of the in-phase case, shown in Figure 5.11(b). In addition, the standard deviation of the $C/N_0$ estimation is higher than in the previous case, with values from 1.8 dB to 3.6 dB. The MPEE is then computed using the 1D-JML estimators for $L = \{1, 8\}$ and the 2D-JML estimator for $L = 8$ considering the real and simulated LTE signal, as it shown in Figure 5.15. The results obtained with the 1D-JML estimators are very similar for both real and simulated cases. In contrast, noise severely degrades the ranging performance of the

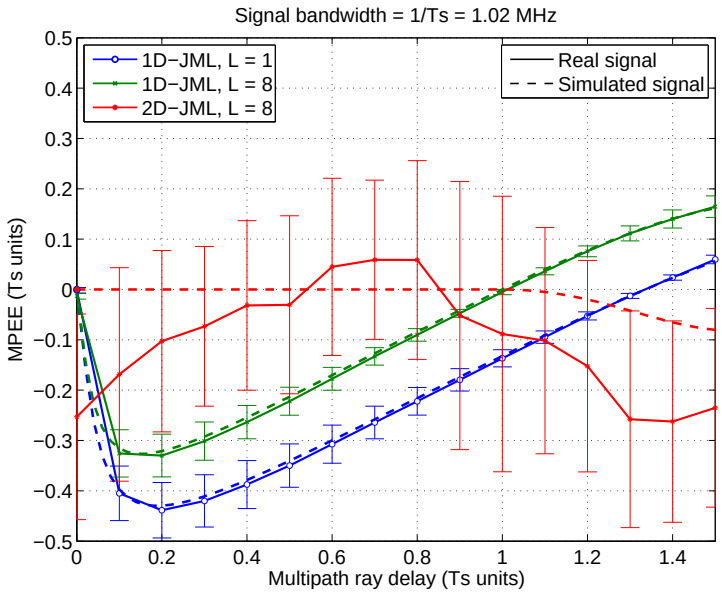


Figure 5.15: MPEE of the 1D- and 2D-JML estimators using the single-tap, periodic-tap and hybrid-tap models for the real emulated signal (solid lines) and the simulated signal (dashed lines), considering the 6-RB CRS without data transmission and a counter-phase multipath ray with 1 dB of SMR.

2D-JML estimator, by introducing a notable bias. The standard deviation of the 2D-JML estimation (shown with error bars) is also relatively high. Considering the TDE errors of these estimators, the corresponding CDF curves are shown in Figure 5.16. Both 1D- and 2D-JML estimators for $L = 8$ achieve similar absolute TDE errors for the 67% of the cases, i.e. the 1D-JML estimator achieves an error of $0.146{\cdot}T_s$ (i.e. 42.9 meters) and the 2D-JML estimator obtains an error of $0.154{\cdot}T_s$ (i.e. 45.3 meters). Nevertheless, the ranging performance of the 2D-JML estimator is still degraded due to noise, as it can be seen for error values obtained in the 95% of the cases.

Let use recall the results obtained in Section 4.6.1 for a two-ray channel with $\tau_1 = 0.5$, $\phi_1 = \pi$ and SMR = 1 dB. In that case, the $C/N_0$ threshold of the 2D-JML estimator for $L = 2$ is 90 dB-Hz. Below this $C/N_0$, outliers estimations introduce a certain bias and the RMSE departs from the $\text{CRB}_{\tau,\text{HT}}$ in (4.2.32). These results can justify the ranging performance obtained by the 2D-JML estimator for $L = 8$ in this section. Since the multipath ray is added destructively to the LoS ray, the $C/N_0$ decreases to a level below the threshold suggested in Section 4.6.1, producing a notable bias on the 2D-JML estimation. In addition, the increase of the noise effect due to the destructive ray introduces a higher variance on the 2D-JML estimation than in the constructive case. In contrast, the 1D-JML estimators are less affected by the impact noise on the TDE.

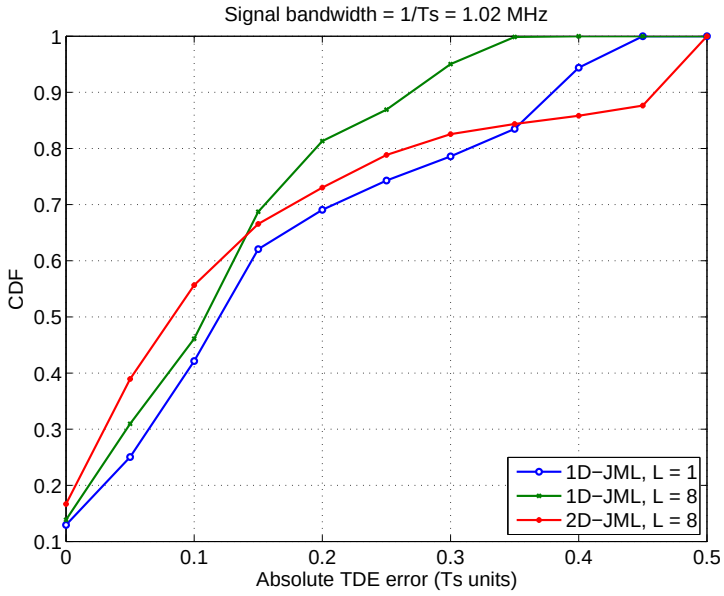


Figure 5.16: CDF of ranging errors of the 1D- and 2D-JML estimators using the single-tap, periodic-tap and hybrid-tap models for the real emulated signal, considering the 6-RB CRS without data transmission and a counter-phase multipath ray with 1 dB of SMR.

In conclusion, the MPEE of the 2D-JML estimator is shown to be less biased for close-in multipath than the 1D-JML estimators, considering a real LTE signal. Indeed, the 2D-JML estimator has a notable improvement on the ranging estimation with respect to the 1D-JML estimators in the case of constructive multipath, as it is shown by computing the CDF of the multipath errors. However, the impact of noise over the 2D-JML estimation is more severe than in the 1D-JML estimation, resulting in a higher variance on the ranging estimation.

## 5.4 Achievable ranging performance in urban channels

The ranging performance of the 1D- and 2D-JML estimators has been assessed using real LTE signal over a two-ray multipath channel. Nevertheless, this scenario does not represent general urban environments, characterized by dense multipath and a delay spread larger than $T_s$. Thus, this section uses the ETU channel model to determine the achievable ranging accuracy of 1D- and 2D-JML estimators in urban channels. This standard channel model provides a realistic navigation channel in order to assess the ultimate ranging performance, considering a system bandwidth of 1.4 MHz.

The methodology followed in this experiment is similar to the procedure conducted in the previous section, by using the same testbed summarized in Table 5.1. In the current experiment, the ETU channel model is emulated with a Doppler shift of 300 Hz, by using Spirent VR5. During the first ten seconds of the experiment, the multipath energy is kept very low in order to ease the acquisition and tracking of the LTE signal. Then, multipath is applied according to the ETU model during a time of 25 seconds. Since multipath induce a bias on the TDE, the time-delay estimates are not fed into the DLL, thus the DLL is driven only by carrier-aiding and the time delay filtered in the previous stage.

Using the CRS pilots of one symbol every slot, 200 estimates of the time delay, phase, frequency and $C/N_0$ are obtained every second. The LTE signal is successfully tracked during the capture time, as it is shown in Figure 5.17(a) by the frequency shift tracking. As it can be seen, the impact of ETU multipath increases the variance of the frequency estimates with respect to the MPEE experiments. In addition, the mean $C/N_0$ estimates are obtained over 200 ms with values between 80 dB-Hz and 90 dB-Hz, as it is depicted in Figure 5.17(b). The standard deviation of these $C/N_0$ values is around 2.5 dB, similarly to the counter-phase multipath case. Given these conditions, the time-delay estimates are computed during 25 seconds by using the 1D-JML estimators for $L = \{1, 6\}$ and the 2D-JML estimator for $L = 7$. The CDF of these ranging errors is then depicted in Figure 5.18. The 2D-JML estimator outperforms the 1D-JML estimators, as it can be seen in Table 5.2 with the ranging errors for the 67% of the cases, $\epsilon_{67\%}$, and for the 95% of the cases, $\epsilon_{95\%}$. These results are in accordance to the CDF curves shown in Figure 4.9(b) of Section 4.5. In that case, the ranging errors were computed in absence of noise and with different channel realisations of the ETU model. Nevertheless, the ranging performance of the 1D- and 2D-JML estimators is still validated by this experiment with real LTE signal. In order to further analyse this case, the RMSE and bias of the estimators is shown in Figure 5.19, computing these metrics over 1 second (depicted with dots) and over 25 seconds (depicted with dashed lines). The results obtained in this section are also in accordance with the RMSE and bias obtained in Section 4.6.2. In that section, given a $C/N_0$ of 85 dB-Hz, the RMSE of the 1D-JML estimations for $L = \{1, 6\}$ is equal to 75.3 m and 63.4 m, respectively, and the RMSE of the 2D-JML estimations for $L = 7$ is equal to 39.6 m; while the bias of the 1D-JML estimations for $L = \{1, 6\}$ is equal to 52.5 m and 28.2 m, respectively, and the bias of the 2D-JML estimations for $L = 7$ is equal to 19.8 m. Although the channel realisations of the real and simulated studies are different, the ranging performance of the estimators is very similar among them. Thus, this experiment validates the performance improvement introduced by the 2D-JML estimator with respect to the 1D-JML estimators in a ETU channel with a system bandwidth of 1.4 MHz.

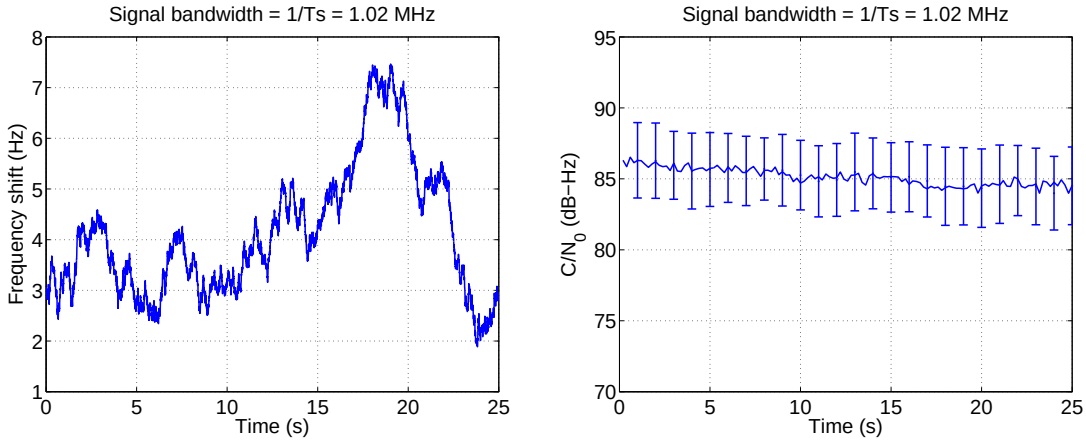


(a) Frequency shift tracking

(b) $C/N_0$ estimation

Figure 5.17: Tracking results of the real emulated signal, considering the 6-RB CRS without data transmission and ETU channel with Doppler shift equal to 300 Hz.

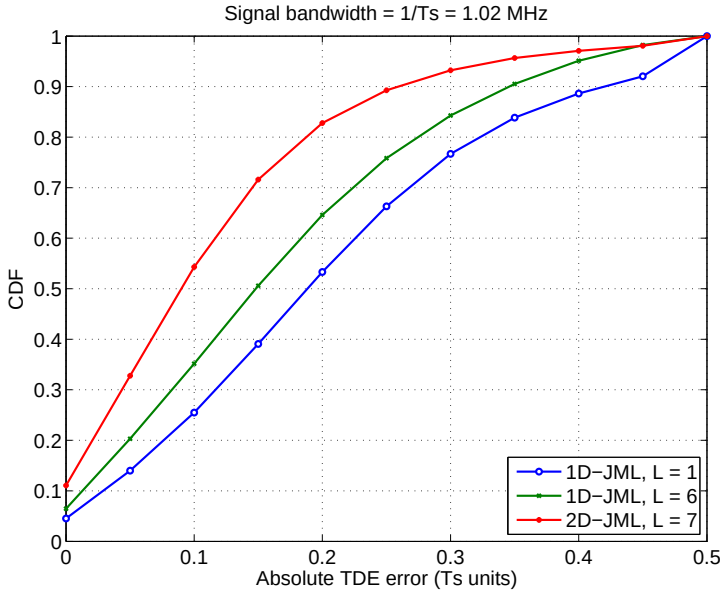


Figure 5.18: CDF of ranging errors of the 1D-JML estimators for $L = \{1, 6\}$ and 2D-JML estimator for $L = 7$ with real emulated signal, considering the 6-RB CRS without data transmission and ETU channel with Doppler shift of 300 Hz.

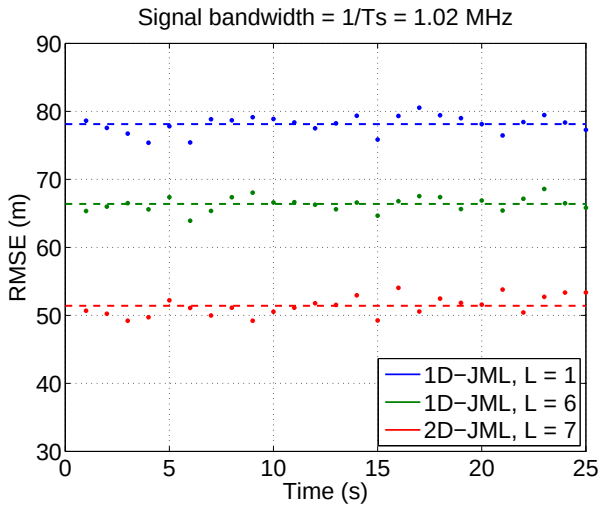


(a) RMSE of the ranging estimations

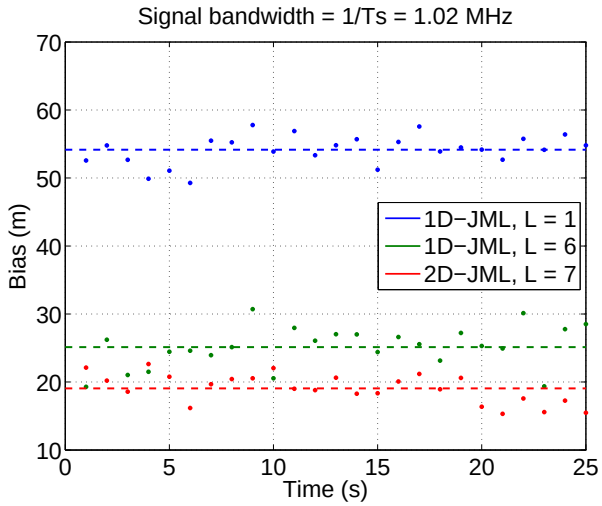


(b) Bias of the ranging estimations

Figure 5.19: RMSE and bias of the 1D-JML estimators for $L = \{1, 6\}$ and 2D-JML estimator for $L = 7$ with real emulated signal, considering the 6-RB CRS without data transmission and ETU channel with Doppler shift of 300 Hz. The RMSE and bias is computed over 1 s (shown with dots) and over 25 s (shown width dashed line).

Table 5.2: Ranging errors (for the 67% and 95% of the cases), RMSE and bias of the 1D-JML estimators for $L = \{1, 6\}$ and the 2D-JML estimator for $L = 7$, considering the 6-RB CRS without data transmission and ETU channel with Doppler shift of 300 Hz.

| Time-delay estimator | $\epsilon_{67\%}$ ($T_s$ units) | $\epsilon_{95\%}$ ($T_s$ units) | $\epsilon_{67\%}$ (m) | $\epsilon_{95\%}$ (m) | RMSE (m) | Bias (m) |
|---|---|---|---|---|---|---|
| 1D-JML, $L = 1$ | 0.253 | 0.467 | 74.4 | 137.4 | 78.1 | 54.2 |
| 1D-JML, $L = 6$ | 0.211 | 0.399 | 62.1 | 117.4 | 66.4 | 25.1 |
| 2D-JML, $L = 7$ | 0.137 | 0.337 | 40.3 | 99.1 | 51.4 | 19.1 |

In this section, a realistic navigation channel is emulated by using the standard ETU model. The ranging performance of the 1D- and 2D-JML estimators has been evaluated for a LTE system bandwidth of 1.4 MHz. Thus, the experiment has reproduced a harsh environment with close-in multipath. In accordance with the simulation results, the 2D-JML estimator outperforms the 1D-JML estimators. The achievable ranging accuracy of the 2D-JML estimator is around 50 m for a 1.4-MHz bandwidth, given a $C/N_0$ of approximately 85 dB-Hz. Since these results are obtained for the lowest signal bandwidth, the ranging performance is expected to improve for higher signal bandwidths.

# Chapter 6

# Conclusions and Future Work

This thesis has explored the potential of multicarrier signals to adopt advanced techniques to counteract the effect of multipath in ranging applications. The time-delay estimation (TDE) of conventional receivers has a notable bias in harsh environments with dense multipath. Thus, countermeasures against multipath have to be introduced in order to achieve the ultimate positioning performance. An optimum solution is based on the joint estimation of time delay and channel. This joint estimation can be easily applied in multicarrier signals, due to the straightforward implementation of the channel estimation in the frequency domain. In order to assess this attractive capability, the practical case of the Long Term Evolution (LTE) standard has been considered. This technology specifies the downlink transmission of orthogonal frequency-division multiplexing (OFDM) signals, which are multicarrier formats. Thus, the LTE signal formats have been used to study a new joint time-delay and channel estimator, which can further counteract the effect of multipath. The achievable TDE performance of this joint estimation has been assessed in realistic navigation channels, which can be characterized by the presence of close-in multipath that critically affects the ranging performance. The work has been completed with a validation of the new joint time-delay and channel estimation using a software-defined radio (SDR) receiver with real LTE signals. The conclusions of the thesis are drawn in this section, along with the open issues pending for future work.

## 6.1 Conclusions

In Chapter 2, the main features of LTE technology for ranging applications have been described. The LTE standard have been reviewed to show two main enabling capabilities

of LTE for positioning: the transmission of wideband signals, and the tight synchronisation among base stations. In addition, the standard supports a dedicated downlink multicarrier signal for observed time difference of arrival (OTDoA) positioning, i.e. the positioning reference signal (PRS). Since the PRS is aimed to avoid inter-cell interference, this reference signal has been used in this thesis to assess the ranging capabilities of multicarrier signals. To understand the evolution of the standard, a brief historical survey on cellular positioning has been provided. This survey has shown that LTE inherits from its predecessor technologies, i.e. CDMA systems such as UMTS or CDMA2000, the use of the matched filter or correlation-based techniques, as the conventional estimator for ranging. The downlink physical layer of LTE has also been introduced in this chapter.

In Chapter 3, the achievable localization capabilities of LTE have been assessed using the conventional receiver. This receiver is based on the matched filter, which is the maximum likelihood (ML) estimator in additive white Gaussian noise (AWGN) channels. But, two main impairments for TDE have been found in LTE navigation environments: inter-cell interference and multipath. In order to consider these effects, the link budget of the five most powerful base stations with respect to the user location have been computed for every position in a standard LTE macro-cell layout. The resulting signal-to-interference plus noise ratio (SINR) values have been used to determine the AWGN level, which has been added to the PRS. Three realistic scenarios have been distinguished whether an interference cancellation technique, a smart transmission scheme, or no interference mitigation is applied. Considering the absence of multipath, the position errors achieved exceed 100 meters around the base stations due to the near-far effect (i.e. when no interference mitigation is applied), but these results can be improved up to the centimetre level if a coordinated transmission scheme is implemented by enabling the full capability of the PRS. Despite the expected poor performance of the matched filter in the presence of multipath, multipath channels have been included to complete the achievable positioning performance assessment with a conventional receiver in LTE. Considering a coordinated scheme, the results have shown a notable bias on the TDE for standard LTE channel models (e.g. EPA, EVA and ETU). The best position accuracy is around the barycentre of every three close base stations. In the case of a pedestrian channel (i.e. EPA model), the lowest position error using a system bandwidth of 1.4 MHz has been shown to be around 12 and 30 meters in the 67% and 95% of the cases, while these position errors have been improved to around 4 and 10 meters in the 67% and 95% of the cases by using the highest system bandwidth (i.e. 20 MHz). However, position errors around 10 meters have only been obtained for high bandwidth in harsh environments (i.e. characterized by ETU model).

In Chapter 4, a new technique for joint time-delay and channel estimation has been presented to improve the ranging performance in channels with close-in multipath. First, the channel estimation models typically used have been studied. Excluding the arbitrary-tap model, which leads to a high computational burden in the joint estimation, the Cramér-Rao bound (CRB) has been derived for the single- and periodic-tap models and the novel hybrid-tap model. Using these three models, the joint maximum likelihood (JML) has been applied for the TDE. The one-dimensional JML (1D-JML) has been obtained with single- and periodic-tap models, while the proposed two-dimensional JML (2D-JML) has been obtained with the hybrid-tap model, which is defined by equi-spaced or periodic taps and an arbitrary tap between the first two equi-spaced taps. This novel channel parameterization helps to counteract close-in multipath, by solving a two-dimensional optimization problem with relative low complexity. The technique has been studied using the PRS in usual LTE working conditions, represented by the standard channel models and signal bandwidths in LTE. Considering these conditions, the optimum number of taps has been obtained in absence of noise for the JML estimators. Then, the optimality of these JML estimators has been validated by attaining the CRB, when the channel estimation model matches the propagation channel model. The use of the novel 2D-JML estimator is essential to improve the time-delay performance with respect to the 1D-JML estimator, especially in scenarios with close-in multipath (typically found for low signal bandwidths). This enhancement has been usually obtained for a specific number of taps $L$. Thus, the model order of the estimator should be designed accordingly. Considering the LTE channel models, the optimum values of $L$ have been obtained for every channel estimation model, and they are valid and applicable in case a certain channel is characterized by one of the standard propagation models. In these realistic navigation channels with a typical $C/N_0$ of 85 dB-Hz (once inter-cell interference is removed), the 2D-JML estimator for $L > 1$ achieves a ranging accuracy around 30 and 60 meters for 1.4 MHz, and below 5 meters for 20 MHz, outperforming the 1D-JML estimators in most of the cases.

In Chapter 5, the joint time-delay and channel estimators has been validated with real LTE signals emulated at the European Navigation Laboratory (ENL). For this purpose, a software LTE positioning receiver has been presented with a detailed description of its architecture. A preliminary scenario with four synchronised base stations has been used to confirm the correct operation of the software receiver to perform LTE OTDoA positioning. Then, the multipath error envelope (MPEE) of the 1D- and 2D-JML estimators has been compared between the simulations and the experiments with real signal. Finally, a realistic navigation channel has been emulated by using the standard ETU model. In accordance

with the simulation results, the 2D-JML estimator outperforms the 1D-JML estimators. The achievable ranging accuracy of the 2D-JML estimator is around 50 m for a 1.4-MHz bandwidth, given a typical $C/N_0$ of approximately 85 dB-Hz. Since these results have been obtained for the lowest signal bandwidth, the ranging performance is expected to improve for higher signal bandwidths.

One of the main insights obtained during this thesis is the importance of the tap delay distribution on the joint time-delay and channel estimation. Thus, we propose a contribution that takes advantage of this to counteract the critical effect of multipath in ranging applications, by exploiting the structure of multicarrier signals. Positive results have been obtained through simulations, and they have been validated through the emulation of a realistic navigation scenario by using real LTE signals.

## 6.2 Future work

The open issues addressed for future work are described in this section. In Chapter 3, the following extension could be addressed:

- To assess the positioning capabilities of LTE with non-synchronized networks, such as those operated by different network providers. This introduces clock and frequency offsets that produce additional ranging errors.
- To consider different cell layout scenarios in order to assess the impact of the locations of base stations and user equipment on the position error.
- To consider advanced propagation channels, which include shadowing effects or variable tap delay distributions.

In Chapter 4, the following research actions can be considered:

- To estimate adaptively the model order of the JML estimators. Since the periodic- and hybrid-tap estimation models sample the channel impulse response, they may also be used iteratively to adjust the model order in order to obtain the ultimate ranging performance.
- To improve the robustness of the 2D-JML estimator against noise, for instance by integrating several OFDM symbols in the same time-delay estimation.
- To assess the minimum mean square error (MMSE) criterion instead of the maximum likelihood, given a certain prior knowledge of the propagation channel.

Finally, further contributions after the work in Chapter 5 are:

- To assess the performance of hybrid GNSS and LTE positioning systems using the SDR LTE receiver, and its adaptation to any hybrid fusion of satellite and terrestrial signals.
- To achieve a real-time implementation of the SDR receiver to test LTE positioning capabilities in real LTE deployments.
- To assess the performance of the JML estimators in dynamic real channels.

# Bibliography


[3GP99a] 3GPP TS 03.71, Location services (LCS); Functional description; Stage 2 , Rel. 98, V7.0.0, June 1999.

[3GP99b] 3GPP TS 25.305, Stage 2 functional specification of user equipment (UE) positioning in UTRAN , Rel. 99, V3.0.0, December 1999.

[3GP01] 3GPP2 C.S0022-0, Position determination service standard for dual mode spread spectrum systems , V3.0, February 2001.

[3GP03] 3GPP TS 25.996, Spatial channel model for multiple input multiple output (MIMO) simulations , Rel. 6, V6.1.0, September 2003.

[3GP05] 3GPP TS 22.071, Location services (LCS); Service description; Stage 1 , Rel. 7, V7.4.0, December 2005.

[3GP06] 3GPP TR 25.913, Requirements for evolved UTRA (E-UTRA) and evolved UTRAN (E-UTRAN) , Rel. 7, V7.3.0, March 2006.

[3GP10] 3GPP TS 36.211, Evolved universal terrestrial radio access (E-UTRA); Physical channels and modulation , Rel. 9, V9.1.0, March 2010.

[3GP11] 3GPP TS 05.05, Radio transmission and reception , Rel. 99, V8.20.0, November 2011.

[3GP12a] 3GPP, Overview of 3GPP release 9 , September 2012.

[3GP12b] 3GPP TR 36.942, Evolved universal terrestrial radio access (E-UTRA); Radio frequency (RF) system scenarios , Rel. 9, V9.3.0, July 2012.

[3GP12c] 3GPP TS 36.104, Evolved universal terrestrial radio access (E-UTRA); Base station (BS) radio transmission and reception , Rel. 9, V9.13.0, September 2012.

[3GP12d] 3GPP TS 37.571-1, Universal terrestrial radio access (UTRA) and evolved UTRA (E-UTRA) and evolved packet core (EPC); User equipment (UE) conformance specification for UE positioning; Part 1: Conformance test specification , Rel. 9, V9.3.0, December 2012.

[3GP13a] 3GPP TS 23.271, Functional stage 2 description of location services (LCS) , Rel. 9, V9.8.0, March 2013.

[3GP13b] 3GPP TS 36.305, Evolved universal terrestrial radio access network (E-UTRAN); Stage 2 functional specification of user equipment (UE) positioning in E-UTRAN , Rel. 9, V9.10.0, January 2013.

[3GP14a] 3GPP TS 36.101, Evolved universal terrestrial radio access (E-UTRA); User equipment (UE) radio transmission and reception , Rel. 9, V9.18.0, January 2014.

[3GP14b] 3GPP TS 36.133, Evolved universal terrestrial radio access (E-UTRA); Requirements for support of radio resource management , Rel. 9, V9.18.0, January 2014.

[3GP14c] 3GPP TS 36.355, Evolved universal terrestrial radio access (E-UTRA); LTE positioning protocol (LPP) , Rel. 9, V9.13.0, January 2014.

[Abe10] S. Abeta, M. Tanno, M. Iwamura, Standardization trends in LTE enhancement , *NTT DOCOMO Technical Journal*, Vol. 12, nº 1, pags. 42 44, June 2010.

[Ala05] B. Alavi, K. Pahlavan, Analysis of undetected direct path in time of arrival based UWB indoor geolocation , *Proc. IEEE 62nd Vehicular Technology Conference (VTC-2005-Fall)*, Vol. 4, pags. 2627 2631, Dallas, Texas, USA, 25 28 September 2005.

[Als04] N. Alsindi, X. Li, K. Pahlavan, Performance of TOA estimation algorithms in different indoor multipath conditions , *Proc. IEEE Wireless Communications and Networking Conference (WCNC)*, Vol. 1, pags. 495 500, Atlanta, Georgia, USA, 21 25 March 2004.

[Aud02] C. Audet, J.E. Dennis, Analysis of generalized pattern searches , *SIAM Journal on Optimization*, Vol. 13, nº 3, pags. 889 903, 2002.

[Baj08] W.U. Bajwa, J. Haupt, G. Raz, R. Nowak, Compressed channel sensing , *Proc. 42nd Annual Conference on Information Sciences and Systems (CISS)*, pags. 5 10, Princeton, New Jersey, USA, 19 21 March 2008.

[Bal07] M. Balda, LMFsolve.m: Levenberg-Marquardt-Fletcher algorithm for nonlinear least squares problems , MathWorks, File Exchange, ID 16063, 2007.

[Bee97] J.J. van de Beek, M. Sandell, P.O. Borjesson, ML estimation of time and frequency offset in OFDM systems , *IEEE Trans. on Signal Processing*, Vol. 45, nº 7, pags. 1800 1805, July 1997.

[Bia12] O. Bialer, D. Raphaeli, A.J. Weiss, Efficient time of arrival estimation algorithm achieving maximum likelihood performance in dense multipath , *IEEE Trans. on Signal Processing*, Vol. 60, nº 3, pags. 1241 1252, 2012.

[Bor07] K. Borre, D.M. Akos, N. Bertelsen, P. Rinder, S.H. Jensen, *A software-defined GPS and Galileo receiver: a single-frequency approach*, Birkhauser, 2007.

[Bou09] G. Boudreau, J. Panicker, N. Guo, R. Chang, N. Wang, S. Vrzic, Interference coordination and cancellation for 4G networks , *IEEE Communications Magazine*, Vol. 47, nº 4, pags. 74 81, April 2009.

[Bue12] R.M. Buehrer, S. Venkatesh, Fundamentals of time-of-arrival-based position locations , S.A. Zekavat, R.M. Buehrer (eds.), *Handbook of Position Location: Theory, Practice, and Advances*, chap. 6, pags. 175 212, John Wiley & Sons, Inc., 1st ed., 2012.

[Bur14] F Burkhardt, E Eberlein, S Jaeckel, G Sommerkorn, R Prieto-Cerdeira, MIMOSA A dual approach to detailed land mobile satellite channel modeling , *International Journal of Satellite Communications and Networking*, 2014, DOI: 10.1002/sat.1045.

[Caf98] J.J. Caffery, G.L. Stuber, Overview of radiolocation in CDMA cellular systems , *IEEE Communications Magazine*, Vol. 36, nº 4, pags. 38 45, 1998.

[Cha94] Y. T. Chan, K. C. Ho, A simple and efficient estimator for hyperbolic location , *IEEE Trans. on Signal Processing*, Vol. 42, nº 8, pags. 1905 1915, August 1994.

[Che03] N. Chen, M. Tanaka, R. Heaton, OFDM timing synchronisation under multipath channels , *Proc. IEEE 57th Vehicular Technology Conference (VTC 2003-Spring)*, Vol. 1, pags. 378 382, Jeju, South Korea, 22 25 April 2003.

[Che13] S.S. Cherian, A.N. Rudrapatna, LTE location technologies and delivery solutions , *Bell Labs Technical Journal*, Vol. 18, nº 2, pags. 175 194, 2013.

[Com99] Communication from the Commission to the European Parliament, the Council, the Economic and Social Committee and the Committee of the Regions, The 1999 communications review: Towards a new framework for electronic communications infrastructure and associated services , *European Commision*, September 1999.

[Com03] Commission of the European Communities, Commission recommendation of 25 July 2003 on the processing of caller location information in electronic communication networks for the purpose of location-enhanced emergency call services , *Official Journal of the European Union*, July 2003.

[Cor06] L. Correia (ed.), *Mobile Broadband Multimedia Networks*, Academic Press, 2006.

[CSR11] CSRIC Working Group 4C, Technical options for E9-1-1 location accuracy , Final report, Communications Security, Reliability and Interoperability Council (CSRIC), March 2011.

[CSR13] CSRIC III Working Group 3, E9-1-1 location accuracy: Indoor location test bed report , Final report, Communications Security, Reliability and Interoperability Council (CSRIC) III, March 2013.

[Dai10] L. Dai, Z. Wang, J. Wang, Z. Yang, Positioning with OFDM signals for the next-generation GNSS , *IEEE Trans. on Consumer Electronics*, Vol. 56, nº 2, pags. 374 379, 2010.

[Dam10] A. Dammann, C. Mensing, S. Sand, On the benefit of location and channel state information for synchronization in 3GPP-LTE , *Proc. European Wireless Conference (EW)*, pags. 711 717, Lucca, Italy, 12 15 April 2010.

[Dam11] A. Damnjanovic, J. Montojo, Y. Wei, T. Ji, T. Luo, M. Vajapeyam, T. Yoo, O. Song, D. Malladi, A survey on 3GPP heterogeneous networks , *IEEE Wireless Communications*, Vol. 18, nº 3, pags. 10 21, 2011.

[Dam13] A. Dammann, G. Agapiou, J. Bastos, L. Brunelk, M. García, J. Guillet, Y. Ma, J. Ma, J.J. Nielsen, L. Ping, R. Raulefs, J. Rodriguez, D. Slock, D. Yang, N. Yi, WHERE2 location aided communications , *Proc. 19th European Wireless Conference (EW)*, pags. 1 8, Guildford, UK, 16 18 April 2013.

[Dar09] D. Dardari, A. Conti, U. Ferner, A. Giorgetti, M.Z. Win, Ranging with ultra-wide bandwidth signals in multipath environments , *Proceedings of the IEEE*, Vol. 97, nº 2, pags. 404 426, 2009.

[Dha11] S. Dhar, U. Varshney, Challenges and business models for mobile location-based services and advertising , *Communications of the ACM*, Vol. 54, nº 5, pags. 121 128, 2011.

[Dra98] C. Drane, M. Macnaughtan, C. Scott, Positioning GSM telephones , *IEEE Communications Magazine*, Vol. 36, nº 4, pags. 46 54, 1998.

[Ebe13] E Eberlein, F Burkhardt, G Sommerkorn, S Jaeckel, R Prieto-Cerdeira, MIMOSA Analysis of the MIMO channel for LMS systems , *Space Communications*, Vol. 22, nº 2, pags. 145 158, 2013.

[EIA90] EIA/TIA Interim Standard IS-54, Cellular system dual-mode mobile station base station compatibility standard , May 1990.

[EIA92] EIA/TIA Interim Standard IS-95, Cellular system recommended minimum performance standards for full-rate speech codes , May 1992.

[Emm11] A. Emmanuele, M. Luise, J.-H. Won, D. Fontanella, M. Paonni, B. Eissfeller, F. Zanier, G. Lopez-Risueno, Evaluation of filtered multitone (FMT) technology for future satellite navigation use , *Proc. 24th International Technical Meeting of The Satellite Division of the Institute of Navigation (ION GNSS)*, pags. 3743 3755, Portland, Oregon, USA, 20 23 September 2011.

[eSa04] eSafety Forum, eCall Driving Group, Memorandum of understanding for realisation of interoperable in-vehicle eCall , Tech. rep., European Commission, May 2004.

[ETS92] ETSI-SMG, GSM TS 05.10, Radio subsystem synchronization , Ph2, V4.0.1, April 1992.

[Ett12] Ettus Research, Examples provided with the USRP hardware driver , Application note, 2012.

[Eur87] European Conference of Postal and Telecommunications Administrations (CEPT), GSM memorandum of understanding , 1987.

[Eur13] European Commision, Proposal for a regulation of the European Parliament and the Council concerning type-approval requirements for the deployment of the eCall in-vehicle system and amending Directive 2007/46/EC , Tech. rep., European Commision, June 2013.

[Far05] T. Farley, Mobile telephone history , *Telektronikk*, Vol. 101, nº 3/4, pags. 22, 2005.

[FCC96] FCC, Report & order and futher notice of proposed rulemaking (FCC 96-264) on revision of the FCC rules to ensure compatibility with enhanced 911 emergency calling systems , Tech. rep., 1996.

[FCC99] FCC, Third report and order on E-911 phase II requirements , Tech. Rep. FCC 99-245, September 1999.

[FCC07] FCC, Report and order on wireless E911 location accuracy requirements , Tech. Rep. FCC 07-166, September 2007.

[FCC14] FCC, Third futher notice of proposed rulemaking on wireless E911 location accuracy requirements , Tech. rep., February 2014.

[Fis98] S. Fischer, H. Grubeck, A. Kangas, H. Koorapaty, E. Larsson, P. Lundqvist, Time of arrival estimation of narrowband TDMA signals for mobile positioning , *Proc. 9th IEEE International Symposium on Personal, Indoor and Mobile Radio Communications (PIMRC)*, Vol. 1, pags. 451 455, Boston, Massachusetts, USA, 8 11 September 1998.

[Fit91] M.P. Fitz, Planar filtered techniques for burst mode carrier synchronization , *Proc. IEEE GLOBECOM*, Vol. 1, pags. 365 369, Phoenix, Arizona, USA, 2 5 December 1991.

[Fle71] R. Fletcher, A modified Marquardt subroutine for non-linear least squares. , Tech. rep., Atomic Energy Research Establishment, Harwell, England, 1971.

[Fly10] G. Flynn, The role of standards and progress made , presentation given at the 2nd Invitational Workshop on Opportunistic RF Localization for Next Generation Wireless Devices, Worcester, USA, 14 June 2010.

[Ged10] K. Gedalyahu, Y.C. Eldar, Time-delay estimation from low-rate samples: A union of subspaces approach , *IEEE Trans. on Signal Processing*, Vol. 58, nº 6, pags. 3017 3031, 2010.

[Gen12] C. Gentner, E. Munoz, M. Khider, E. Staudinger, S. Sand, A. Dammann, Particle filter based positioning with 3GPP-LTE in indoor environments , *Proc. IEEE/ION Position Location and Navigation Symposium (PLANS)*, pags. 301 308, Myrtle Beach, South Carolina, USA, 23 26 April 2012.

[Gen13] C. Gentile, N. Alsindi, R. Raulefs, C. Teolis, Cellular localization , *Geolocation Techniques*, pags. 137 159, Springer, 2013.

[Gez08] S. Gezici, A survey on wireless position estimation , *Wireless Personal Communications*, Vol. 44, nº 3, pags. 263 282, 2008.

[Gla14] V. Gladkikh, A. Klimovskiy, Technical regulation in the scope of ERA-GLONASS emergency response system deployment , Seminar on ERA GLONASS, Accident Emergency Call System (AECS), 25 February 2014, Moscow, Russia.

[Gol73] G.H. Golub, V. Pereyra, The differentiation of pseudo-inverses and nonlinear least squares problems whose variables separate , *SIAM Journal on Numerical Analysis*, Vol. 10, nº 2, pags. 413 432, 1973.

[GOS12] GOST R 54620-2011, Global navigation satellite system. Emergency response system in case of accidents. Car system call emergency services. General technical requirements , September 2012.

[GSA14a] GSA Global mobile Suppliers Association, Evolution to LTE report , Tech. rep., 17 February 2014.

[GSA14b] GSA Global mobile Suppliers Association, GSA status of the LTE ecosystem report: 1563 LTE user devices launched by 154 suppliers , Tech. rep., 19 March 2014.

[Gus05] F. Gustafsson, F. Gunnarsson, Mobile positioning using wireless networks: Possibilities and fundamental limitations based on available wireless network measurements , *IEEE Signal Processing Magazine*, Vol. 22, nº 4, pags. 41 53, 2005.

[Guv09] I. Guvenç, C.-C. Chong, A survey on TOA based wireless localization and NLOS mitigation techniques , *IEEE Communications Surveys & Tutorials*, Vol. 11, nº 3, pags. 107 124, 2009.

[Hat80] M. Hata, T. Nagatsu, Mobile location using signal strength measurements in a cellular system , *IEEE Transactions on Vehicular Technology*, Vol. 29, nº 2, pags. 245 252, 1980.

[Hei00] G. Hein, B. Eissfeller, V. Oehler, J.O. Winkel, Synergies between satellite navigation and location services of terrestrial mobile communication , *Proc. 13th International Technical Meeting of the Satellite Division of The Institute of Navigation (ION GPS)*, pags. 535 544, Salt Lake City, Utah, USA, 19 22 September 2000.

[Hen07] L. Hentila, P. Kyosti, M. Kaske, M. Narandzić, M. Alatossava, MATLAB implementation of the WINNER Phase II Channel Model ver1.1 , *IST-WINNERII Project*, December 2007.

[Hil13] F Hillebrand, The creation of standards for global mobile communication: GSM and UMTS standardization from 1982 to 2000 , *IEEE Wireless Communications*, Vol. 20, nº 5, pags. 24 33, 2013.

[ITU97] ITU-R M.1225, Guidelines for evaluation of radio transmission technologies for IMT-2000 , 1997.

[ITU08] ITU-R M.2135-1 International Telecommunication Union, Guidelines for evaluation of radio interface technologies for IMT-Advanced , 2008.

[Kau11] R. Kaune, J. Horst, W. Koch, Accuracy analysis for TDOA localization in sensor networks , *Proc. 14th International Conference on Information Fusion (FUSION)*, pags. 1 8, Chicago, Illinois, USA, 5 8 July 2011.

[Kay89] S.M. Kay, A fast and accurate single frequency estimator , *IEEE Trans. on Acoustics, Speech and Signal Processing*, Vol. 37, nº 12, pags. 1987 1990, December 1989.

[Kay98] S.M. Kay, *Fundamentals of Statistical Signal Processing: Estimation Theory*, Prentice-Hall PTR, 1993 1998.

[Kha09] F. Khan, *LTE for 4G Mobile Broadband: Air Interface Technologies and Performance*, Cambridge University Press, 2009.

[Kyo07] P. Kyosti, J. Meinila, L. Hentila, X. Zhao, T. Jamsa, C. Schneider, M. Narandzić, M. Milojević, A. Hong, J. Ylitalo, V.-M. Holappa,

M. Alatossava, R. Bultitude, Y. de Jong, T. Rautiainen, WINNER II channel models , IST-WINNER II project deliverable D1.1.2, 30 September 2007.

[Lar01] E.G. Larsson, G. Liu, J. Li, G.B. Giannakis, Joint symbol timing and channel estimation for OFDM based WLANs , *IEEE Communications Letters*, Vol. 5, nº 8, pags. 325 327, 2001.

[Lar11] M.D. Larsen, G. Seco-Granados, A.L. Swindlehurst, Pilot optimization for time-delay and channel estimation in OFDM systems , *Proc. IEEE International Conference on Acoustics, Speech and Signal Processing (ICASSP)*, pags. 3564 3567, Prague, Czech Republic, 22 27 May 2011.

[Li04] X. Li, K. Pahlavan, Super-resolution TOA estimation with diversity for indoor geolocation , *IEEE Trans. on Wireless Communications*, Vol. 3, nº 1, pags. 224 234, 2004.

[Li10] Y. Li, Blind SNR estimation of OFDM signals , *Proc. International Conference on Microwave and Millimeter Wave Technology (ICMMT)*, pags. 1792 1796, Chengdu, China, 8 11 May 2010.

[Liu07] H. Liu, H. Darabi, P. Banerjee, J. Liu, Survey of wireless indoor positioning techniques and systems , *IEEE Trans. on Systems, Man, and Cybernetics, Part C: Applications and Reviews*, Vol. 37, nº 6, pags. 1067 1080, 2007.

[LS13] J.A. López-Salcedo, E. Gutiérrez, G. Seco-Granados, A.L. Swindlehurst, Unified framework for the synchronization of flexible multicarrier communication signals , *IEEE Trans. on Signal Processing*, Vol. 61, nº 4, pags. 828 842, 2013.

[Lud02] B. Ludden, A. Pickford, J. Medland, H. Johnson, F. Brandon, L.E. Axelsson, K. Viddal-Ervik, B. Dorgelo, E. Boroski, J. Malenstein, Report on implementation issues related to access to location information by emergency services (E112) in the European Union , Tech. rep., Coordination Group on Access to Location Information for Emergency Services (CGALIES), February 2002.

[Lui95] M. Luise, R. Reggiannini, Carrier frequency recovery in all-digital modems for burst-mode transmissions , *IEEE Trans. on Communications*, Vol. 43, nº 234, pags. 1169 1178, February/March/April 1995.

[Man09] K. Manolakis, D.M. Gutiérrez-Estévez, V. Jungnickel, W. Xu, C. Drewes, A closed concept for synchronization and cell search in 3GPP LTE systems ,

*Proc. IEEE Wireless Communications and Networking Conference (WCNC)*, pags. 1 6, Budapest, Hungary, 5 8 April 2009.

[Mar11] P. Marsch, G.P. Fettweis, *Coordinated Multi-Point in Mobile Communications: From Theory to Practice*, Cambridge University Press, 2011.

[Mat13a] MathWorks, *MATLAB Global Optimization Toolbox User's Guide*, Vol. R2013b, 2013.

[Mat13b] MathWorks, *MATLAB Optimization Toolbox User's Guide*, Vol. R2013b, 2013.

[ME02] I. Martin-Escalona, F. Barceló, J. Paradells, Delivery of non-standardized assistance data in E-OTD/GNSS hybrid location systems , *Proc. of IEEE International Symposium on Personal, Indoor and Mobile Radio Communications (PIMRC)*, Vol. 5, pags. 2347 2351, Lisbon, Portugal, 15 18 September 2002.

[Med09] J. Medbo, I. Siomina, A. Kangas, J. Furuskog, Propagation channel impact on LTE positioning accuracy: A study based on real measurements of observed time difference of arrival , *Proc. IEEE 20th International Symposium on Personal, Indoor and Mobile Radio Communications (PIMRC)*, pags. 2213 2217, Tokyo, Japan, 13 16 September 2009.

[Meh11] C. Mehlfuhrer, J. Colom-Ikuno, M. Šimko, S. Schwarz, M. Wrulich, M. Rupp, The Vienna LTE simulators Enabling reproducibility in wireless communications research , *EURASIP Journal on Advances in Signal Processing*, Vol. 2011, nº 1, pags. 1 14, 2011.

[Men97] U. Mengali, A.N. D Andrea, *Synchronization Techniques for Digital Receivers*, Plenum, New York, 1997.

[Men08] C. Mensing, A. Dammann, Positioning with OFDM based communications systems and GNSS in critical scenarios , *Proc. 5th Workshop on Positioning, Navigation and Communication (WPNC)*, pags. 1 7, Hannover, Germany, 27 March 2008.

[Men09] C. Mensing, S. Sand, A. Dammann, W. Utschick, Interference-aware location estimation in cellular OFDM communications systems , *Proc. IEEE International Conference on Communications (ICC)*, pags. 1 6, Dresden, Germany, 14 18 June 2009.

[Men10] C. Mensing, S. Sand, A. Dammann, Hybrid data fusion and tracking for positioning with GNSS and 3GPP-LTE , *International Journal of Navigation and Observation*, Vol. 2010, pags. 1 12, 2010.

[Men13] C. Mensing, *Location Determination in OFDM Based Mobile Radio Systems*, PhD Thesis, Technische Universitat Munchen, 2013.

[Moe98] M. Moeglein, N. Krasner, An introduction to SnapTrack® server-aided GPS technology , *Proc. 11th International Technical Meeting of the Satellite Division of The Institute of Navigation (ION GPS)*, pags. 333 342, Nashville, Tennessee, USA, 15 18 September 1998.

[Mol06] A.F. Molisch, H. Asplund, R. Heddergott, M. Steinbauer, T. Zwick, The COST259 directional channel model Part I: Overview and methodology , *IEEE Trans. on Wireless Communications*, Vol. 5, nº 12, pags. 3421 3433, December 2006.

[Mon13] R. Montalbán, J.A. López-Salcedo, G. Seco-Granados, A.L. Swindlehurst, Power allocation method based on the channel statistics for combined positioning and communications OFDM systems , *Proc. IEEE International Conference on Acoustics, Speech and Signal Processing (ICASSP)*, pags. 4384 4388, Vancouver, Canada, 26 31 May 2013.

[Moo94] P.H. Moose, A technique for orthogonal frequency division multiplexing frequency offset correction , *IEEE Transactions on Communications*, Vol. 42, nº 10, pags. 2908 2914, 1994.

[Mor98] M. Morelli, U. Mengali, Feedforward frequency estimation for PSK: A tutorial review , *Eur. Trans. on Telecommunications*, Vol. 9, nº 2, pags. 103 116, March/April 1998.

[Mor07] M. Morelli, C.-C.J. Kuo, M.-O. Pun, Synchronization techniques for orthogonal frequency division multiple access (OFDMA): A tutorial review , *Proceedings of the IEEE*, Vol. 95, nº 7, pags. 1394 1427, 2007.

[Pan13] M. Panchetti, C. Carbonelli, M. Horvat, M. Luise, Performance analysis of PRS-based synchronization algorithms for LTE positioning applications , *Proc. 10th Workshop on Positioning Navigation and Communication (WPNC)*, pags. 1 6, Dresden, Germany, 20 21 March 2013.

[Pau00] D.R. Pauluzzi, N.C. Beaulieu, A comparison of SNR estimation techniques for the AWGN channel , *IEEE Trans. on Communications*, Vol. 48, nº 10, pags. 1681 1691, 2000.

[Pop92] B.M. Popovic, Generalized chirp-like polyphase sequences with optimum correlation properties , *IEEE Trans. on Information Theory*, Vol. 38, nº 4, pags. 1406 1409, July 1992.

[Pro00] J.G. Proakis, *Digital Communications*, McGraw-Hill, 4th ed., 2000.

[Pun06] M.-O. Pun, M. Morelli, C.-C.J. Kuo, Maximum-likelihood synchronization and channel estimation for OFDMA uplink transmissions , *IEEE Trans. on Communications*, Vol. 54, nº 4, pags. 726 736, 2006.

[R1-08] R1-084490, Support for emergency services , 3GPP, Nortel, RAN1-55, Prague, Czech Republic, October 2008.

[R1-09a] R1-090053, Improving the hearability of LTE positioning service , 3GPP, Qualcomm Europe, RAN1-55bis, Ljubljana, Slovenia, January 2009.

[R1-09b] R1-090353, On OTDOA in LTE , 3GPP, Qualcomm Europe, RAN1-55bis, Ljubljana, Slovenia, January 2009.

[R1-09c] R1-090768, Performance of DL OTDOA with dedicated LCS-RS , 3GPP, Alcatel-Lucent, RAN 1-56s, Athens, Greece, February 2009.

[R1-09d] R1-090918, On OTDOA method for LTE positioning , 3GPP, Ericsson, RAN 1-56s, Athens, Greece, February 2009.

[R1-09e] R1-091648, Way forward on OTDOA positioning , 3GPP, Ericsson, Alcatel-Lucent, Huawei, LGE, Motorola, Nokia, Nokia Siemens Networks, Nortel, Qualcomm, Samsung, RAN 1-56bis, San Francisco, USA, March 2009.

[R1-09f] R1-091789, Further considerations on PRS design for LTE Rel-9 , 3GPP, Huawei, RAN 1-57, San Francisco, USA, May 2009.

[R1-09g] R1-091930, Evaluation of PRS-assisted OTDOA-based positioning for LTE , 3GPP, Motorola, RAN 1-57, San Francisco, USA, May 2009.

[R1-09h] R1-092307, Analysis of UE subframe timing offset measurement sensitivity to OTDoA performance , 3GPP, Alcatel-Lucent, RAN1-57bis, Los Angeles, USA, June 2009.

[R4-06] R4-060334, LTE channel models and simulations , 3GPP, Ericsson, Elektrobit, Nokia, Motorola, Siemens, RAN4-38, February 2006.

[R4-07] R4-070572, Proposal for LTE channel models , 3GPP, Ericsson, Nokia, Motorola, Rohde & Schwarz, RAN4-43, May 2007.

[RA10] K. Ranta-Aho, Performance of 3GPP Rel-9 LTE positioning methods , presentation given at the 2nd Invitational Workshop on Opportunistic RF Localization for Next Generation Wireless Devices, Worcester, USA, 14 June 2010.

[Rap02] T. S. Rappaport, *Wireless Communications: Principles and Practice*, Prentice Hall, Upper Saddle River, NJ, 2002.

[Rau08] R. Raulefs, S. Plass, Combining wireless communications and navigation the WHERE project , *Proc. IEEE 68th Vehicular Technology Conference (VTC 2008-Fall)*, pags. 1 5, Calgary, Canada, 21 24 September 2008.

[Rau13] R. Raulefs, S. Zhang, C. Mensing, Bound-based spectrum allocation for cooperative positioning , *Trans. on Emerging Telecommunications Technologies*, Vol. 24, nº 1, pags. 69 83, 2013.

[Ree98] J.H. Reed, K.J. Krizman, B.D. Woerner, T.S. Rappaport, An overview of the challenges and progress in meeting the E-911 requirement for location service , *IEEE Communications Magazine*, Vol. 36, nº 4, pags. 30 37, 1998.

[RP-08a] RP-080995, Positioning support for LTE , 3GPP, Alcatel-Lucent, AT&T, CMCC, Ericsson, KDDI, Nokia Siemens Networks, Nortel Networks, Qualcomm Europe, Spirent TeleCommunication Systems, US Cellular Corporation, Verizon, RAN-42, Athens, Greece, December 2008.

[RP-08b] RP-081140, Support for IMS emergency calls over LTE , 3GPP,Alcatel-Lucent, Verizon Wireless, Nortel, AT&T, Qualcomm, Motorola, Nokia, Nokia Siemens Networks, Ericsson, Samsung, RAN-42, Athens, Greece, December 2008.

[San11] L. Sanguinetti, M. Morelli, An initial ranging scheme for IEEE 802.16 based OFDMA systems , *Proc. 8th International Workshop on Multi-Carrier Systems & Solutions (MC-SS)*, pags. 1 5, Herrsching, Germany, 3 4 May 2011.

[Say05] A.H. Sayed, A. Tarighat, N. Khajehnouri, Network-based wireless location: challenges faced in developing techniques for accurate wireless location information , *IEEE Signal Processing Magazine*, Vol. 22, nº 4, pags. 24 40, 2005.

[Sch07] J. Schroeder, S. Galler, K. Kyamakya, K. Jobmann, NLOS detection algorithms for ultra-wideband localization , *Proc. 4th Workshop on Positioning, Navigation and Communication (WPNC)*, pags. 159 166, Hannover, Germany, 22 March 2007.

[Sch12] K. Schmeink, R. Adam, P.A. Hoeher, Performance limits of channel parameter estimation for joint communication and positioning , *EURASIP Journal on Advances in Signal Processing*, Vol. 2012, nº 178, pags. 1 18, 2012.

[Ses11] S. Sesia, I. Toufik, M. Baker, *LTE – The UMTS Long Term Evolution: From Theory to Practice*, John Wiley & Sons, 2011.

[Sol02] S.S.. S Soliman, C.E. Wheatley, Geolocation technologies and applications for third generation wireless , *Wireless Communications and Mobile Computing*, Vol. 2, nº 3, pags. 229 251, 2002.

[Sor05] T.B. Sorensen, P.E. Mogensen, F. Frederiksen, Extension of the ITU channel models for wideband (OFDM) systems , *Proc. IEEE 62nd Vehicular Technology Conference (VTC-2005-Fall)*, Vol. 1, pags. 392 396, Dallas, Texas, USA, 25 28 September 2005.

[Sun05] G. Sun, J. Chen, W. Guo, K.J.R. Liu, Signal processing techniques in network-aided positioning: A survey of state-of-the-art positioning designs , *IEEE Signal Processing Magazine*, Vol. 22, nº 4, pags. 12 23, 2005.

[Tek98] S. Tekinay, E. Chao, R. Richton, Performance benchmarking for wireless location systems , *IEEE Communications Magazine*, Vol. 36, nº 4, pags. 72 76, 1998.

[VD09] F.S.T. Van Diggelen, *A-GPS: Assisted GPS, GNSS, and SBAS*, Artech House, 2009.

[Ver10] M. Vergara, F. Antreich, M. Meurer, G. Seco-Granados, Spreading code design for a MC-CDMA based GNSS pilot signal , *Proc. 5th ESA Workshop on Satellite Navigation Technologies and European Workshop on GNSS Signals and Signal Processing (NAVITEC)*, pags. 1 6, Noordwijk, Netherlands, 8 10 December 2010.

[Ver11] R. Verdone, A. Zanella (eds.), *Pervasive Mobile and Ambient Wireless Communications: COST Action 2100*, Springer, Berlin, Germany, 2011.

[Vid02] J. Vidal, M. Nájar, R. Játiva, High resolution time-of-arrival detection for wireless positioning systems , *Proc. IEEE Vehicular Technology Conference (VTC)*, Vol. 4, pags. 2283 2287, Vancouver, Canada, 24 28 September 2002.

[Wan09] Y. Wang, G. Leus, A.-J. van der Veen, Cramér-Rao bound for range estimation , *Proc. IEEE International Conference on Acoustics, Speech and Signal Processing (ICASSP)*, pags. 3301 3304, Taipei, Taiwan, 19 24 April 2009.

[Wan12a] D. Wang, M. Fattouche, F.M. Ghannouchi, Multicarrier code for the next-generation GPS , *EURASIP Journal on Wireless Communications and Networking*, , nº 1, pags. 185, 2012.

[Wan12b] W. Wang, T. Jost, A. Lehner, U.-C. Fiebig, Physical-statistical channel model for joint GNSS and mobile radio based positioning , *Proc. 25th International Technical Meeting of The Satellite Division of the Institute of Navigation (ION GNSS)*, pags. 953 959, Nashville, Tennessee, USA, 17 21 September 2012.

[War06] P.W. Ward, J.W. Betz, C.J. Hegarty, Satellite signal acquisition, tracking, and data demodulation , E.D. Kaplan, C.J. Hegarty (eds.), *Understanding GPS: Principles and Applications*, chap. 5, pags. 153 241, Artech House Publishers, Boston, London, 2nd ed., 2006.

[Xia04] Y.-C. Xiao, P. Wei, X.-C. Xiao, H.-M. Tai, Fast and accurate single frequency estimator , *Electronics Letters*, Vol. 40, nº 14, pags. 910 911, July 2004.

[Yan12] J. Yang, X. Wang, S.I. Park, H.M. Kim, Direct path detection using multipath interference cancellation for communication-based positioning system , *EURASIP Journal on Advances in Signal Processing*, Vol. 2012, nº 188, pags. 1 18, 2012.

[Yuc08] T. Yucek, H. Arslan, Time dispersion and delay spread estimation for adaptive OFDM systems , *IEEE Trans. on Vehicular Technology*, Vol. 57, nº 3, pags. 1715 1722, 2008.

[Zag98] J.M. Zagami, S.A. Parl, J.J. Bussgang, K.D. Melillo, Providing universal location services using a wireless E911 location network , *IEEE Communications Magazine*, Vol. 36, nº 4, pags. 66 71, 1998.

[Zan08] F. Zanier, M. Luise, Fundamental issues in time-delay estimation of multicarrier signals with applications to next-generation GNSS , *Proc. 10th Inter-*

*national Workshop on Signal Processing for Space Communications (SPSC)*, pags. 1 8, Rhodes Island, Greece, 6 8 October 2008.

[Zek11] R. Zekavat, R.M. Buehrer, *Handbook of Position Location: Theory, Practice and Advances*, Vol. 27, Wiley-IEEE Press, 2011.

[Zha02] Y. Zhao, Standardization of mobile phone positioning for 3G systems , *IEEE Communications Magazine*, Vol. 40, nº 7, pags. 108 116, 2002.

[Zho09] H. Zhou, Y.-F. Huang, A maximum likelihood fine timing estimation for wireless OFDM systems , *IEEE Trans. on Broadcasting*, Vol. 55, nº 1, pags. 31 41, 2009.

[Zhu11] C. Zhu, *High Accuracy Multi-link Synchronization in LTE Downlink*, Master Thesis, Technische Universitat Munchen, 2011.

[Zhu12] C. Zhu, High accuracy multi-link synchronization in LTE: Applications in localization , *Proc. 16th IEEE Mediterranean Electrotechnical Conference (MELECON)*, pags. 908 913, Hammamet, Tunisia, 25 28 March 2012.